

GEOHERMAL MICROFLUIDIC  
SYSTEMS FOSTER  
PREBIOTIC CHEMISTRY

THOMAS MATREUX



MÜNCHEN 2024



---

Geothermal microfluidic systems  
foster prebiotic chemistry

**Thomas Matreux**

---

**Dissertation**

zur Erlangung des Grades  
Doktor der Naturwissenschaften

an der Fakultät für Physik  
der Ludwig-Maximilians-Universität München

vorgelegt von  
Thomas Matreux  
aus München

München, Mai 2024

Erstgutachter: Prof. Dr. Dieter Braun  
Zweitgutachter: Prof. Dr. Hannes Mutschler  
eingereicht am: 29.05.2024  
Tag der mündlichen Prüfung: 31.07.2024

# Zusammenfassung

Leben ist ein Phänomen fern vom thermodynamischen Gleichgewicht, und auch seine Entstehung wurde vermutlich entscheidend von den vor etwa 4 Milliarden Jahren vorhandenen Nichtgleichgewichtssystemen geprägt und vorangetrieben. Dazu gehören geothermische Systeme mit Wärmeströmen durch dünne, wassergefüllte Gesteinsspalten, die zur Konvektion des Wassers und der Thermophorese der gelösten Stoffe führen. Meine Dissertation zeigt, dass ihr Zusammenspiel eine hochselektive Anreicherung von Komponenten antreibt, die einzigartige Möglichkeiten für präbiotische Systeme auf dem Weg zur Entstehung des Lebens bietet.

Die präbiotische Chemie erfordert in der Regel spezifische Zusammensetzungen und oftmals hohe Konzentrationen an Ausgangsstoffen, damit am Ende der teils komplexen Synthesewege die gewünschten Produkte gebildet und unerwünschte Nebenreaktionen unterdrückt werden. Eine mögliche Lösung hierfür bietet die thermophoretische Akkumulation, welche Aminosäuren, Nukleotide und RNA-Bausteine (Kapitel 3, [1]) selbst für massenidentische Verbindungen robust auftrennen kann. Netzwerkartig miteinander verbundene Gesteinskammern, wie sie in natürlichen Systemen vorliegen, verbessern hierbei die Aufreinigung deutlich. Die daraus resultierende Vielfalt an Zusammensetzungen steigert die Reaktionsausbeute beispielsweise einer wichtigen Peptidpolymerisation um bis zu vier Größenordnungen und zeigt somit die Bedeutung für präbiotische Reaktionen.

Die meisten wichtigen aufkommenden Biopolymere wie RNA, DNA und Phospholipide enthalten Phosphor als zentralen Baustein, obwohl dieser in der Erdkruste einen überraschend geringen Masseanteil hat. Zudem ist das als häufigst angenommene (Kalzium-)Phosphatmineral, Apatit, unter neutralen oder alkalischen Bedingungen, wie sie für die meisten präbiotischen Synthesereaktionen erforderlich sind, unlöslich. Geothermale Systeme bieten eine Lösung, da Wärmeströme Phosphat von seinem Fällungspartner Kalzium im saurem Milieu räumlich trennen können. Hierdurch bleiben große Mengen an Phosphat auch nach der pH-Neutralisierung gelöst und stehen zur Erzeugung reaktiver Phosphatarten für die präbiotische Chemie bereit (Kapitel 4, [2]).

Selbst nach Erreichen der für die sogenannte RNA-Welt Hypothese zentralen katalytischen RNA-Strängen ergeben sich weitere Probleme. RNA-Enzyme benötigen für ihre Funktion spezifische Salinitätsbedingungen wie zum Beispiel viel Magnesium- und wenig Natriumionen. Auslaugungsexperimente mit präbiotisch relevanten Basalten führen jedoch zu hohen Natrium- und nur geringen Magnesiumkonzentrationen. Dieses Verhältnis kann durch thermophoretische Akkumulation umgekehrt werden, so dass in den erzeugten magnesiumreichen Lösungen ein optimales Habitat für RNA-Enzyme geschaffen wird (Kapitel 5, [3]).

Eine wichtige Herausforderung bei der RNA-basierten Replikation ist die Templatblockade durch das gebildete Produkt, das mit Schmelztemperaturen über 100 °C einhergeht und durch die fehlende Freigabe des Templates die weitere Replikation verhindert. Eine Lösung hierfür können Salz- und pH-Oszillationen sein, da saure, salzarme Bedingungen die Schmelztemperatur absenken. Interessanterweise führt der Ionengradient von thermisch akkumuliertem Meereswasser zur Bildung von pH Gradienten. In einem präbiotisch motivierten Modellsystem aus Ameisensäure und Natriumhydroxid bestätigen Experimente eine auf Zeitskalenseparation basierte Theorie, und zeigen, dass durch Wärmeflüsse erzeugte pH Gradienten je nach Zusammensetzung der Lösung variiert und sogar invertiert werden können (Kapitel 6, [4]).



# Abstract

Life is a phenomenon far from equilibrium, which suggests that its emergence was also decisively shaped and driven by the non-equilibrium systems present around 4 billion years ago. These include geothermal systems with heat flows through thin, water-filled rock fractures, which drive the convection of water and the thermophoresis of dissolved substances. My thesis shows that their interplay drives a highly selective enrichment of components that offers unique opportunities for prebiotic systems on the path to the emergence of life.

Prebiotic chemistry usually requires specific compositions and high concentrations of compounds for the desired products to form at the end of sometimes complex synthesis pathways whilst suppressing undesired side reactions. A possible solution for this is provided by thermophoretic accumulation, which can robustly separate amino acids, nucleotides and RNA building blocks (Chapter 3, [1]) even for mass-identical compounds. In networks of connected rock cracks, as found in natural systems, this purification is further enhanced. The resulting diversity of compositions increases reaction yields by up to four orders of magnitude, for example for peptide polymerization, thus demonstrating how temperature gradients in rock cracks can foster prebiotic chemistry.

Most of the emerging important biopolymers such as RNA, DNA and phospholipids contain phosphorus as a central building block, even though it has a surprisingly small abundance in the Earth's crust. In addition, the presumably most common (calcium) phosphate mineral, apatite, is insoluble at the neutral or alkaline pH values required for most prebiotic synthesis reactions. Geothermal systems provide a solution as heat flows can spatially separate phosphate from its precipitation partner calcium in acidic environments. As a consequence, large amounts of phosphate remain in solution even after pH-neutralization and can be used to generate reactive phosphate species for prebiotic chemistry (Chapter 4, [2]).

After addressing above milestones, further problems arise for catalytic RNA strands, which are central to the so-called RNA world hypothesis. These require specific salinity conditions for their function, such as high magnesium and low sodium concentrations. However, leaching experiments using prebiotically relevant basalts show high sodium but only low magnesium concentrations. Thermophoretic accumulation can reverse this ratio, naturally creating a habitat for RNA enzymes (Chapter 5, [3]). In systems of connected rock cracks, the strength and stability of the selective enrichment is further enhanced.

An important challenge in RNA-based replication is template inhibition by the formed product, as melting temperatures can rise to above 100 °C thus preventing further replication. Salt and pH oscillations can drive an environmental solution, as acidic, low-salt conditions lower the melting temperature significantly. Interestingly, the ion gradients of thermally accumulated seawater lead to the formation of pH gradients. In a prebiotically motivated model system of formic acid and sodium hydroxide, experiments confirm a theoretical approach based on the separation of timescales, and show that pH gradients generated by heat fluxes can be varied and even inverted by changes in the initial composition of the solution (Chapter 6, [4]).





# Table of contents

<b>Zusammenfassung</b>	<b>v</b>
<b>Abstract</b>	<b>vii</b>
<b>1 Introduction</b>	<b>1</b>
1.1 Origins of life research . . . . .	1
1.1.1 Environmental conditions . . . . .	1
1.1.2 Prebiotic chemistry . . . . .	2
1.1.3 Scenarios and promising environments . . . . .	2
1.1.4 Heat flows across rock cracks . . . . .	3
1.2 Heat-flow-driven enrichment . . . . .	4
1.2.1 1D – Thermophoresis . . . . .	4
1.2.2 2D – Thermogravitational accumulation . . . . .	5
1.2.3 3D – Large convective fluxes . . . . .	5
1.3 Research questions . . . . .	6
<b>2 Methods</b>	<b>7</b>
2.1 Experimental setup . . . . .	7
2.1.1 Thermo-microfluidic cell . . . . .	7
2.1.2 Implementation of a thermal gradient . . . . .	9
2.1.3 Implementation of large convective fluxes . . . . .	10
2.2 Extraction protocols . . . . .	10
2.3 Analysis . . . . .	12
2.3.1 Ion chromatography . . . . .	12
2.3.2 Liquid chromatography . . . . .	13
2.3.3 pH measurements . . . . .	14
2.4 Leaching and dissolution of geomaterials . . . . .	14
<b>3 Separation and purification of molecules and boosting of reactions</b>	<b>17</b>
3.1 Introduction . . . . .	18
3.2 Results . . . . .	18

3.2.1	Enrichment of small molecules . . . . .	18
3.2.2	Separation in an experimental 3-chamber-network . . . . .	19
3.2.3	Purification in a large network . . . . .	21
3.2.4	Reactions in chambers . . . . .	22
3.3	Outlook . . . . .	23
3.3.1	Habitat of chemical reaction networks . . . . .	23
<b>4</b>	<b>Solubilization of apatite and local enrichment of phosphate</b>	<b>25</b>
4.1	Introduction . . . . .	26
4.2	Phosphate from apatite . . . . .	26
4.2.1	Leaching behaviour of apatite . . . . .	26
4.2.2	Dissolution and fractionation by heat flows . . . . .	27
4.2.3	Solubilization of phosphate and utility for prebiotic chemistry . . . . .	28
4.2.4	Modelling precipitation and solubility . . . . .	28
4.3	Other phosphate sources . . . . .	30
4.3.1	Compatibility of geomaterials with phosphate polymerization . . . . .	31
4.3.2	Phosphate-enriched basalts . . . . .	31
4.4	Selective precipitation of magnesium phosphates . . . . .	32
<b>5</b>	<b>Ribozyme habitats from basalt leachates</b>	<b>35</b>
5.1	Introduction . . . . .	36
5.2	Experimental results . . . . .	37
5.3	Outlook . . . . .	39
5.3.1	Salty pH gradients . . . . .	39
5.4	Applications beyond origins of life . . . . .	40
5.4.1	General principle of fractionation by heat flows . . . . .	40
5.4.2	Thermogravitational desalination . . . . .	41
<b>6</b>	<b>Formation mechanism of thermally controlled pH gradients</b>	<b>43</b>
6.1	Introduction . . . . .	44
6.2	Experimental results . . . . .	45
6.3	Selective retention of molecules in a flow setting . . . . .	47
6.4	Outlook . . . . .	52
<b>A</b>	<b>Heat flows in rock cracks naturally optimize salt compositions for ribozymes</b>	<b>53</b>
	Article . . . . .	53
	Methods . . . . .	62
	Extended Data . . . . .	64
	Supplementary Information . . . . .	71

---

<b>B Formation mechanism of thermally controlled pH gradients</b>	<b>109</b>
Article . . . . .	109
Supplementary Information . . . . .	119
<b>C Heat flows enrich prebiotic building blocks and enhance their reactivity</b>	<b>129</b>
Article . . . . .	129
Methods . . . . .	137
Extended Data . . . . .	142
Supplementary Information . . . . .	154
<b>Bibliography</b>	<b>179</b>
<b>List of figures</b>	<b>199</b>
<b>List of tables</b>	<b>201</b>
<b>List of my publications</b>	<b>203</b>
PhD-related first author publications . . . . .	203
PhD-related contributing author publications . . . . .	203
Other publications . . . . .	203
<b>Acknowledgements</b>	<b>205</b>



# Chapter 1

## Introduction

### 1.1 Origins of life research

The question of the emergence of life has puzzled mankind for centuries [5]. In the 19th century, Adolph Strecker found that alanine is an intermediary product en-route to lactic acid and discovered that amino acids can be formed by the reaction of potassium cyanide, ammonium chloride, and an aldehyde, simple and presumably prebiotically plausible molecules [6,7], a synthesis approach now known as Strecker reaction. In 1861, Alexander Butlerov discovered the formose reaction [8–11] to form sugars from formaldehyde with a base and a divalent metal ion as catalysts, having previously reported the formation of formaldehyde [12]. In the 1950s, Stanley Miller and Harold Urey exposed water and a gas mixture of methane, ammonia and hydrogen, which at the time was considered a hypothetical early Earth atmosphere, to electrical discharges in a glass flask. Organic molecules are formed and gradually accumulated in another collection flask in the circuit, yielding for example some amino acids and formic acid [13,14]. More fundamentally, the question how to approach the origins of life has puzzled researchers [15–18], triggering debates on what is life itself [19,20].

#### 1.1.1 Environmental conditions

In this context, a crucial question is how the Earth might have been like when life emerged. First early life forms are supposed to have existed around 3.5-3.8 billion years [21–23] with higher estimates going up to 4 billion years [21] ago. A definite boundary for the oldest possible emergence of still-existing life is the moon forming impact around 4.4-4.5 billion years ago as this would have erased all hypothetically possible earlier life [24–31]. Subsequent cooling provided conditions for nascent life. However, atmospheric and environmental models vary between different scenarios [32–34], for instance ranging from the methane-ammonia-hydrogen-rich atmosphere used by Miller and Urey [13,14,35,36] with longer residence times of methane [37] to more carbon dioxide-rich atmosphere [38,39], oxygen-depleted [40] and various others such as hydrogen-rich [41] with intrinsic consequences for prebiotic chemistry [33,38]. Similarly, the composition of early oceans is discussed [42–44], affecting for instance the sulphur cycle [37,45] and phosphate concentrations [46,47]. Also, overall salinity, composition and pH modify reaction rates [48] and stability of molecules such as RNA [3,49–53] and peptides [54–56].

### 1.1.2 Prebiotic chemistry

The "RNA world" hypothesis [57–60] is based on RNA's capacity to both store information and be catalytically active. Even in today's biology, RNA plays a variety of roles, from catalyzing biochemical reactions over temporary information storage in mRNAs and in the regulation of gene expression [61]. Towards the first functional RNAs, a lot of progress has been achieved over recent year. The evident starting point is the formation of the individual mononucleotides [62–70] from simple, presumably prebiotically relevant molecules such as glycolaldehyde which has been confirmed to exist in interstellar dust [71]. From these RNA monomers and activating agents, the de-novo strand formation has been studied [72–74], for instance using a preactivation of monomers with imidazoles [73, 75–78] as well as 2',3'-cyclic phosphorylated RNA monomers [74, 78–80] and 3',5'-cyclic phosphorylated RNA guanosine monomers [81–84]. However, as discussed in more detail in chapter 3 [1], this runs into the question of the plausibility of pure feedstocks that are mixed in standard laboratory experiments [67] as reactions would otherwise easily produce a plethora of unwanted side-products [85, 86]. In addition, usually high reactant concentrations are required, which could be envisioned for instance by drying processes [87, 88], by localization in compartmentalized systems such as vesicles or coacervates [89–91], by adsorption on mineral surfaces [92–94] or by thermogravitational accumulation as studied here [1, 78, 95–99].

One critical piece in this puzzle is phosphate, integral for life as we know it, for instance in the backbone of DNA and RNA, in the biological nucleoside-polyphosphate energy currencies and in phospholipids in cell membranes [100, 101]. Given this prominence and its function, phosphate is assumed to have been used early on in the emergence of life, no matter what scenario for an emergence of life is considered. However, phosphate precipitates with a variety of divalent ions, such as calcium, to form apatite. This presumably kept phosphate levels far below millimolar to molar concentrations required in prebiotic chemistry [62, 102–105], posing the so-called phosphate problem. Various phosphate minerals have been studied for their potential as prebiotic phosphate source [106]. Important examples include apatite minerals [107–114], including hydroxyapatite and fluorapatite, and other calcium minerals such as brushite [107, 111, 115, 116] and whitlockite [107, 114–116]. Further, the iron phosphate vivianite [106] and magnesium phosphates such as newberyite [111, 116], bobierrite [117] and struvite [107, 111] have been hypothesized to play a role. This however poses the question as to in what environment they could be found and would be used, with an interesting setting found in carbonate-rich lakes that permit higher absolute phosphate levels [87, 88, 118] by carbonate-calcium precipitation at the cost of increased total salinities.

### 1.1.3 Scenarios and promising environments

Over the decades, various scenarios and environments for the emergence of life have been proposed. Famously introduced by Darwin, one of the more studied ones are 'warm little ponds', compatible with various processes relevant for prebiotic chemistry [111, 119]. Here, the molecules needed for prebiotic chemistry are present and exposed to wet and dry phases during day-night cycles. These cyclic evaporation and rehydration cycles can drive nucleotide polymerization [80, 81, 120], enhance efficiency of phosphorylation [121, 122] and various other processes [123–128]. Inherently, the evaporation leads to an up-concentration of all solutes, however without compositional changes. Another environment are shallow and deep hydrothermal vents or chimneys [129–132] which

provide various temperatures and mineral compositions [133, 134] over small space and can drive gradients in temperature [98], pH and ion concentrations [129, 135–137]. These gradients have been supposed to generate potential differences of up to 180 mV and potentially drive the conversion of inorganic carbon into organic material [138, 139], a process crucial during the emergence of life.

In addition, and compatible with the former environments, delivery of exogenous material has been widely discussed [140–148] as various molecules have been observed in outer space [71], in interstellar clouds [149] and in the atmosphere of Titan [150]. In line with the previously discussed phosphate problem, delivery of meteoritic schreibersite ((Fe, Ni)<sub>3</sub>P), a reduced iron-nickel phosphorus mineral [151–155], has been studied, showing phosphorylation and formation of reactive phosphate species such as trimetaphosphate (TMP) and diamidophosphate (DAP). Similarly, as mentioned above, geomaterial surfaces have been discussed to play a pivotal role, as feedstock for ions [3], as catalytically active surface [156–159] and by (selective) adsorption for instance for amino acids [160–162], nucleotides and RNA and DNA [92, 163–166] or other prebiotically relevant molecules [167, 168]

#### 1.1.4 Heat flows across rock cracks

In my doctoral research, we investigated heat flows across water-filled rock fractures and their potential for emerging prebiotic chemistry. Temperature itself is an important factor for nascent life, for instance driving or favouring chemical reactions and imposing stronger or weaker evaporation. The overall temperature is partially driven by global heating by solar radiation [169, 170], in addition to more local processes such as the radiogenic decay of thorium, potassium and uranium isotopes [171]. Heat flows have been described over large scales [172], in the context of tidal heating [173], volcanic activity [174], meteoritic impacts [143, 175, 176], geothermal settings, as a thermoareole around magmatic intrusions [174] and many more chemical and petrological processes, as by the second law of thermodynamics, heat is a general waste product. In the context of relevant reactions, we study water-filled geothermal habitats where water-filled rock fractures are exposed to temperature gradients. Such fractures are generated for instance by internal stresses in glass state [177, 178]. They typically form large networks of microfluidic systems and were presumably widely present on the early Earth, for instance in geothermal or hydrothermal systems, in mafic to ultramafic rocks in volcanic complexes, sedimentary layers and in shallow submarine or lacustrine environments [174, 178, 179]. When under water and depending on their permeability [180], the networks of fractures would be exposed to large-scale flows which in addition can further drive thermal heterogeneity inside the system.

## 1.2 Heat-flow-driven enrichment

In such heat-flow-exposed water-filled cracks, solutes exhibit thermophoresis (1D), convection (2D) and large-scale fluxes (3D) as shown in Figure 1.1.

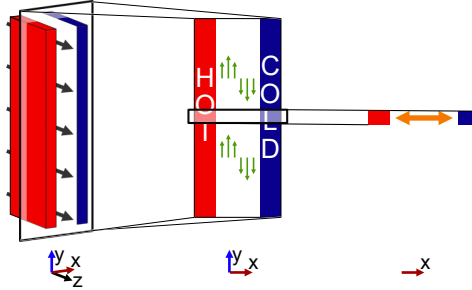


Figure 1.1: 3D Large-scale convective fluxes lead to transport through networks of cracks, 2D convection boosts the accumulation provided by 1D thermophoresis (from left to right, adapted from [4]).

### 1.2.1 1D – Thermophoresis

The directed movement of particles along a temperature gradient is called thermophoresis [181]. Over the past decades, this was for instance successfully used for microscale thermophoresis (MST) [182, 183]. The substance property related to this movement is called thermodiffusion coefficient  $D_T$ , yielding a drift velocity  $v = -D_T \cdot \nabla T$ . The thermodiffusive flux writes

$$J_{D_T} = -c \cdot D_T \cdot \nabla T \quad (1.1)$$

with counteracting ordinary diffusion that can be described by Fick's first law as follows

$$J_D = -D \cdot \nabla c \quad (1.2)$$

with  $J$  being the diffusive flux of particles, the diffusion constant  $D$  and the concentration  $c$ . In steady state ( $J = 0$ ), the total flux can thus be written as  $\frac{\nabla c}{c} = -\frac{D_T}{D} \cdot \nabla T$ . The fraction of diffusion coefficient yields the Soret coefficient  $S_T$  that is defined as

$$S_T = \frac{D_T}{D} \quad (1.3)$$

For most substances, this parameter is positive, meaning that a net movement of particles towards the cold side takes place. The resulting concentration profile follows an exponential depletion law:

$$\frac{c(x)}{c(x_0)} = \exp(-S_T \cdot (T(x) - T(x_0))) \quad (1.4)$$

with line coordinate  $x$  in the direction of the temperature gradient.



### 1.2.2 2D – Thermogravitational accumulation

For the two-dimensional case, a superposition of thermophoresis and convection occurs. This effect was first described by Clusius and Dickel for gases [184] and also occurs in aqueous solvents, for instance for the dissolved organic molecules and inorganic salts studied in this thesis. Convection is induced by temperature differences that lead to a thermal expansion of water which is different on the hot/cold side of the chamber and thereby creates a convection roll (see also Figure 1.1). The superposition with thermophoresis as described above leads to an accumulation of dissolved solutes in the bottom cold corner of the chamber. To describe this situation analytically, we thus add a convective flux

$$J_C = \mathbf{v} \cdot c \quad (1.5)$$

with convection velocity  $\mathbf{v}$ , depending for instance on the thickness of the chamber and the angle relative to gravity [185]. The total flux is thus given by

$$J(t) = J_D + J_{D_T} + J_C = -D \cdot \nabla c - c \cdot S_T \cdot D \cdot \nabla T + \mathbf{v} \cdot c \quad (1.6)$$

In our case, the temperature gradient can be assumed to be linear across the thickness of the chamber  $w$ . Due to the large aspect ratio (height/thickness), the turning points of the convective flow can be neglected in an approximation, so that the flow speed is constant along the height ( $h$ ). This leads to a drift-diffusion type equation:

$$\frac{\partial c}{\partial t} = D \left( \frac{\partial^2 c}{\partial x^2} + \frac{\partial^2 c}{\partial y^2} \right) + D \cdot S_T \cdot \frac{\Delta T}{w} \cdot \frac{\partial c}{\partial x} - v(x) \frac{\partial c}{\partial y} \quad (1.7)$$

with  $x$  and  $y$  as shown in Figure 1.1. An approximative approach can be found in literature [95, 186] and is partially discussed in the Supplementary Information of appendix B. As shown, for an optimal pore thickness and ratio, a concentration ratio between bottom ( $c_{bottom}$ ) and top ( $c_{top}$ ) of

$$\frac{c_{bottom}}{c_{top}} = \exp \left( 0.42 \cdot S_T \cdot \Delta T \cdot \frac{h}{w} \right) \quad (1.8)$$

can be achieved for a temperature difference  $\Delta T$ .

### 1.2.3 3D – Large convective fluxes

The accumulation in a single chamber is combined with large-scale fluxes [180], connecting chambers of geological networks of connected fractures. As they are typically slow, they do not impair the thermophoretic accumulation but act on a separate timescale [4]. Connected chambers can on the contrary further enhance accumulation and separation by repeated exposure to thermally driven enrichment in subsequent cells in a network [1, 3].

### 1.3 Research questions

Using the interplay of above effects, in my doctoral work, we studied the thermophoretic separation of prebiotically relevant salts and molecules. The separation stems from different strengths of accumulation due to different Soret coefficients (see for instance [1]). We used this to tackle multiple questions related to the origins of life, detailed in the following chapters.

- Chapter 3: Separation and purification of molecules and boosting of reactions. Prebiotic chemistry usually requires pure starting solutions and defined mixing steps. We show that heat flows can spatially separate and purify more than 50 small organic, prebiotically relevant molecules, boosting prebiotic chemistry.
- Chapter 4: Solubilization of apatite and local enrichment of phosphate. Apatite, the presumably most abundant phosphate mineral on early Earth, is inaccessible under the pH conditions of nascent life. Heat flows can fractionate acidic-dissolved apatite and enrich dilute phosphate, thereby circumventing the phosphate problem.
- Chapter 5: Ribozyme habitats from basaltic leachates. Basaltic leachates, oceans and ponds typically contain insufficient magnesium and more sodium than magnesium, hindering ribozyme activity. We show that heat flows selectively enrich divalent ions and thereby establish natural habitats for ribozymes.
- Chapter 6: Formation mechanism of thermally controlled pH gradients. Prebiotically relevant acid-base mixtures are selectively accumulated by heat flows, thereby inducing pH gradients. Predicted by a theoretical framework, these can be modulated in amplitude and inverted for different initial compositions.

**Future perspectives** A crucial question for the emergence of life is the emergence of functional molecules, for instance simple ribozymes or autocatalytic RNA reaction networks [187–197]. However, nature would have to screen a plethora of non-functional sequences to find the suitable fit [198, 199], asking for some prebiotically relevant selection pressure. Similarly, selection for compartmentalization in vesicles [200–204] or coacervates [91, 167, 205–208] from randomized ingredients provides an interesting perspective for future research.

# Chapter 2

## Methods

As the following chapters use the same thermo-microfluidic chambers and similar and overlapping analysis techniques, the description of the methods is given here in a unified version. Details per project are also attached in the Methods and Supplemental Information of the papers [1, 3, 4], see appendices A-C.

### 2.1 Experimental setup

An extensive review of the evolution of thermo-microfluidic chambers is given in A. Kühnlein's dissertation [209]. Whilst the construction design has changed over the years, from laser-induced thermal gradients [96, 210] to cryostat-Ohmic heater driven gradients with polylactic acid (PLA) printed [211, 212], resin printed and various versions of FEP-foil cutout-based designs as used in this and other recent work [78, 80, 132, 213–215], the general working principle remained the same. A schematic depiction of the different elements is shown in Figure 2.1 and explained in the following.

#### 2.1.1 Thermo-microfluidic cell

The thermo-microfluidic cell was constructed and exposed to a thermal gradient as shown in Figure 2.1. The microfluidic structure was designed using CAD-software (Autodesk Inventor, USA) and cut out of fluorinated ethylene propylene (FEP) foil (Holscot, Netherlands) using an industrial plotter device (CE6000-40 Plus, Graphtec, Germany). For the different experiments, various foil thicknesses between 100  $\mu\text{m}$  and 340  $\mu\text{m}$  were used. This thin cutout foil was then sandwiched between two sapphires (KYBURZ, Switzerland) of 0.5 mm thickness (towards the cooling side of the setup) and of 2 mm (on the heated side). Here, sapphire was used to ensure high heat conductivity, optical access and chemical inertness. The sapphires were coated before each experiment using a hydrophobic coating (ProSurf MT-5, Surfactis, France) to avoid interaction with the sample (especially relevant for RNA and precipitation experiments) and to facilitate extraction of frozen samples. For fluid access, the thin, cooled sapphire has four holes of 1 mm diameter.

The thereby constructed sapphire-FEP-sapphire sandwich was then placed on a heat-conducting graphite foil (25  $\mu\text{m}$ , 1,600  $\text{W}\cdot\text{mK}^{-1}$ , Panasonic, Japan) which was placed on an aluminum base (see part 2 in Figure 2.1). For homogeneous force distribution and reproducibility, the sandwich was held in place by six torque-controlled steel screws, connecting a holding steel frame (part 7 in Figure 2.1) to said aluminum base. The height

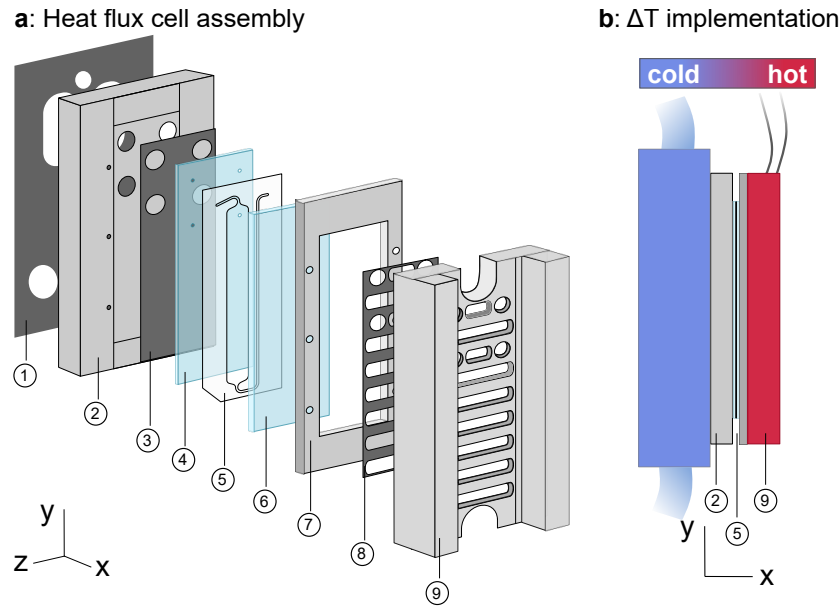


Figure 2.1: Experimental implementation: **(a)** The microfluidic FEP structure (5) is sandwiched between two sapphires, one of thickness  $500\ \mu\text{m}$  (4), in contact with the cooling back (2), and one of thickness  $2000\ \mu\text{m}$  (6), in contact with the heating elements (9). This sapphire–FEP–sapphire sandwich is placed with an intermediary layer of heat-conducting foil (3) on an aluminum base (2) which in turn is covered by a heat-conducting foil (1) on its back for optimal connection to the cooling system and the cryostat. The sandwich is held in place by a steel frame (7), connected to the base by torque-controlled screws for a homogeneous force distribution. A resistance heating element (9) is mounted on top with another intermediary layer of heat-conducting foil (8) with torque-controlled screws. **(b)** The fully assembled chamber is mounted onto a cooled aluminum block which is connected to a cryostat for cooling. The heaters are connected to power supplies controlled by Arduino boards that change applied power via solid state relays. (adapted from [1])

of the partially built chamber was then measured using a confocal micrometer (CL-3000 series with CL-P015, Keyence) to ensure homogeneous height of the chamber which was later used to determine the Soret coefficient of accumulated molecules (see [1]).

Heating was done using an Ohmic heating element (part 9 in Figure 2.1, for more details see next section) which was mounted onto the steel frame with another layer of heat-conducting graphite foil (EYGS0811ZLGH,  $200\ \mu\text{m}$ ,  $400\ \text{W}\cdot\text{mK}^{-1}$ , Panasonic, Japan). For this, again torque-controlled screws were used for homogeneous force distributions.

On the back side, microfluidic connections were attached as required for filling the chamber. For this, we used (all from Techlab, Germany): connectors (UP P-702-01), end caps (UP P-755), screws (VBM 100.823-100.828), ferrules (VBM 100.632) and tubings (Teflon (FEP), KAP 100.969). For flushing and for control of fluid flow, we used syringes with volumes between  $50\ \mu\text{l}$  and  $10\ \text{ml}$  (all from ILS, Germany, acquired from Göhler-HPLC Syringes, Germany) 2606614, 2606714, 2606814, 2606914, 2606015, 2606035, 2606055 and 2606075. Before experiments, chambers were pre-flushed using low-viscosity, fluorinated oil (3M Novec 7500 Engineered Fluid, USA) to push out gas inclusions, facilitate the loading of the chamber and to check for tightness. In static

experiments (see later), the sample was loaded by using a syringe to push fluorinated oil through the chamber and pull in the sample through the same tubing as this technique showed to best avoid the inclusion of air bubbles. After that, the tubings were closed with end caps to avoid drying and pressure effects.

### 2.1.2 Implementation of a thermal gradient

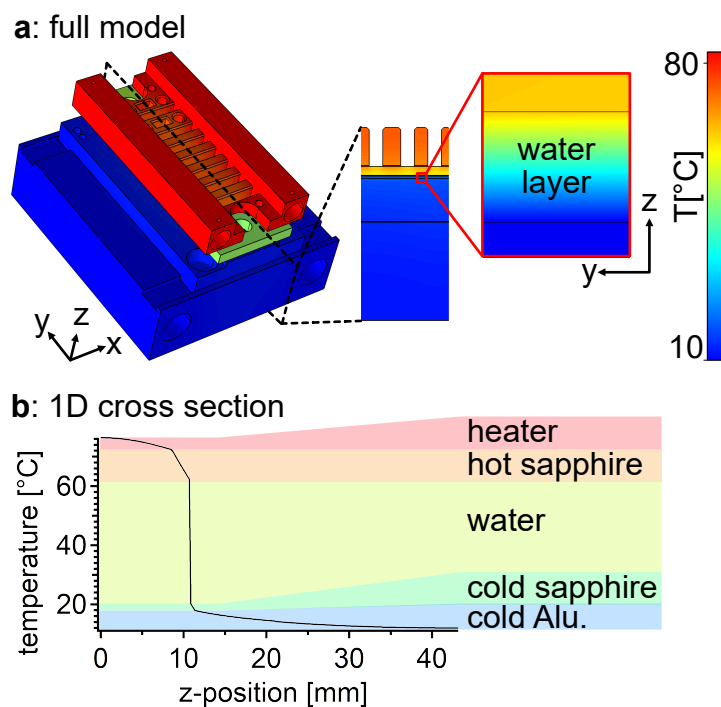


Figure 2.2: Finite-element simulation model of the temperature profile in the experimental setup. **(a)** shows the full structure for an externally applied temperature gradient between 10°C and 80°C. Using known thermal conductivities, the model determines the temperature profile, showing that the gradient is strongly reduced in the aluminum/steel parts, with only 40 K arriving at the water layer. **(b)** shows this in more detail, with temperature gradients across each layer (adapted from [3]).

### Heating

The Ohmic resistance heaters inside the steel parts (see Figure 2.1) are connected to a 480 W, 24 V (in later versions also 320 W, 24 V) power supplies (all from MEAN WELL Enterprises Co., Taiwan) with intermediary solid state relays (SSR) that are controlled by an arduino board with ramps 1.4. To read the temperature sensor signals and control the SSR, we use a customized version of the open-source firmware “Repetier” (Germany). On the technical side, in a recent iteration we changed to LAN cables (cat 6A) for signal transport from the temperature sensor to the arduino as this improves compatibility to future applications in fume hoods or under protected atmosphere in glove boxes, for instance to work with  $\text{Fe}^{2+}$  under oxygen exclusion.

## Cooling

The entire chamber was then mounted onto a precooled aluminum block (see Figure 2.1 b). For cooling, this was connected to a cryostat. Depending on the application and strength of cooling required, we used multiple different cryostats, mostly Grant Optima TXF200 R5 and Julabo DYNEO DD-1000F. To connect the cryostat to the trapping setup, we relied on EPDM tubings (Watercool Heatkiller EPDM Schlauch 16/10mm, acquired from caseking, Germany) for their good isolation whilst ensuring continuous fluid flow thanks to their rigidity. In addition, we used quick connectors (Koolance QD3 Schnellverschluss, acquired from caseking, Germany) to switch between setups and for transport purposes. In order to make the cooling of triplicate runs more efficient and the temperature profile more uniform, we constructed a new triple base, combining 3 individual units into a single unit where the cooling fluid is distributed by a serpentinizing shape.

## Measuring temperatures

After equilibration, temperatures were measured on the heated and cooled sapphires using a heat imaging camera (ShotPRO, Seek Thermal, USA). To determine the effective thermal gradient on the inside (i.e. at both edges of the water layer), finite-element simulations (COMSOL 5.4, Sweden) were used, exemplarily shown in Figure 2.2.

### 2.1.3 Implementation of large convective fluxes

We implemented large convective fluxes as occurring in geological settings both for experimental studies in flow [1, 3] and extraction of samples for measurements [3, 4]. This is shown in Figure 2.3, in this case for salty solutions, adapted from [3]. The sample solution is stored in the syringe and tubing named "in" and continuously flushed through the thermo-microfluidic chamber (in the middle of the sketch). The thermal gradient (orthogonal to the sketch) selectively accumulates solutes towards the bottom. Via three distinct outlets ("top", "middle" and "bottom"), the fractionated fluid is recovered and can be analysed or used for further experiments. Here, the "top" and "bottom" tubings are connected to syringe pumps, controlling the outflow speed (usually each between 5% and 12% of the inflow volume rate). The "middle" outlet is left open inside a falcon to avoid under- or overpressure inside the chamber. This specific design was used for chapters 5 and 6. In chapter 4, a modified version with only two outlets was used, while in chapter 3 a three-chamber-on-one-chip version was used.

To control the fluid flow, we used syringe pumps (Low Pressure Syringe Pump neMESYS 290N with Quadruple Syringe Holder Low-Pressure, Cetoni, Germany) and various syringes as listed above (Chemically Resistant Heavy Duty Syringes with PTFE seals from ILS, Germany, acquired from Göhler-HPLC Syringes, Germany).

For the microfluidic connections, as described above for filling the chamber, we used FEP tubings, connectors, tefzel end caps, delrin screws and ferrules (all from techlab, Germany).

## 2.2 Extraction protocols

Over the projects, three different extraction protocols were used: full recovery (chapters 3.3 and 4.4), freeze extraction (chapters 3 and 4) and flow-through (chapters 3-6).

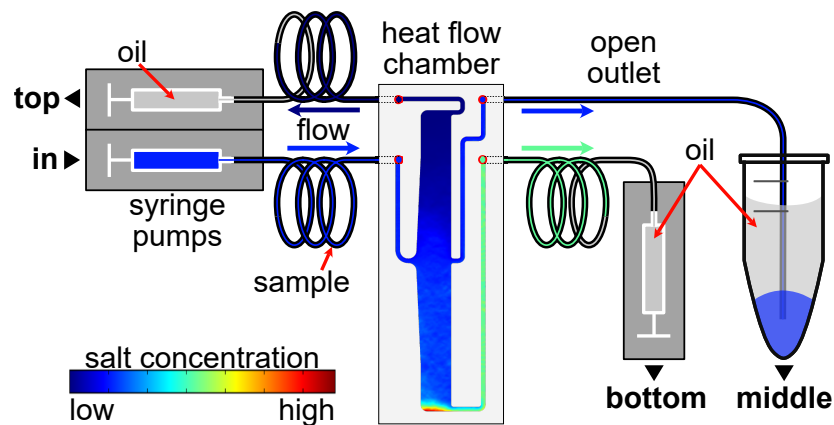


Figure 2.3: Implementation of large convective fluxes. The sample solution ("in") was continuously supplied to chamber and subjected to the thermal gradient (orthogonal to view plane), leading to fractionation of solutes. This separation was recovered by three outlet tubings, the "top" and "bottom" being pulled out with for example 10% of the inflow volume rate, thereby mimicking a geological network of connected cracks and recovering the accumulated resp. depleted fraction for analysis. The "middle" outlet was left open and recovered in a falcon tube to avoid pressure problems (adapted from [3]). For more details on finite-element simulations as shown here, see appendices A and C and a short version in chapter 6.3

### Full recovery

For precipitation samples and in some testing experiments, chambers with low volume were used where freeze extraction would be complicated due to volume limitations. Therefore the entire chamber was opened after the experiment and analysed as such.

### Freeze extraction

In order to see the distribution of solutes along the height (i.e. the direction of gravitation), a freeze extraction protocol was developed and implemented (see Figure 2.4). Heaters were turned off and the cryostat was set to 5 °C. The chamber was directly recovered from the setup and frozen at -80 °C for at least 15 minutes. After that, the chamber could be unscrewed on an aluminum block previously cooled to -80 °C and the sapphire sandwich could be opened without melting. Then, the frozen interior was cut into 4-8 fractions, according to volume requirements for analysis. Here, a specifically designed piece was used and 3D-printed to obtain fractions of equal volume. Mostly, four fractions were used as fewer fractions would lead to lower resolution of analysis by averaging over a larger fraction of the chamber while more fractions suffer from a larger positional error by volume uncertainties.

### Recovery by flow-through

The flow-through extraction protocol is depicted in Figure 2.3. The premixed solution is continuously supplied through an inlet tubing controlled by a syringe pump to the chamber ("in"), where the flow is subjected to the heat flow (orthogonal to view plane). This leads to the thermally driven fractionation of solutes, with little to no disturbance of the accumulation by the applied flow. The established separation is then recovered

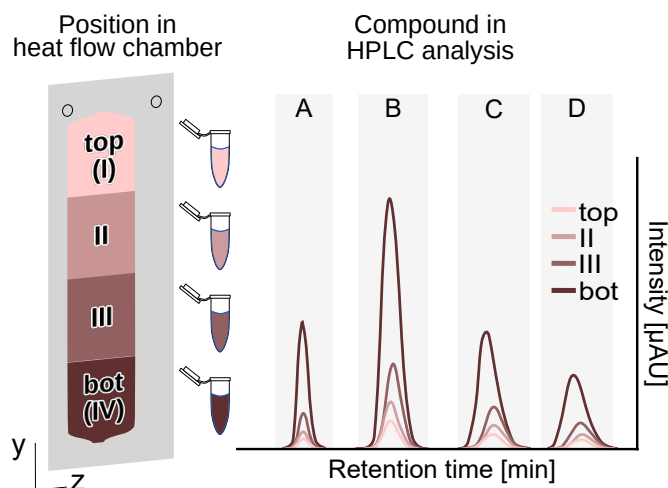


Figure 2.4: Freeze extraction procedure. As detailed in the text, the frozen chamber was cut into four fractions which were then separately molten by gradual transfer to a heated aluminum block and analysed, for instance by HPLC (adapted from [1]).

by three outlets, connected to tubings. The "top" and "bottom" outlet are controlled by syringe pumps, used to pull out for example 10% of the inflow volume rate. The "middle" outlet is left open to avoid pressure problems and recovered in a vial.

## 2.3 Analysis

As analysis methods overlap between the different chapters, they will be presented here and referenced accordingly.

### 2.3.1 Ion chromatography

For the analysis of (poly-)phosphates (in chapter 3), of various anions and cations (in chapters 4-5) and of formate and sodium (in chapter 6), concentrations and compositions of ions were measured with ion chromatography. We used two connected ion chromatography machines to measure cations and anions simultaneously. Samples were injected using an autosampler (AS-DV, ThermoFisher Scientific, USA) which was connected to a first ion chromatography system used for cation measurements (Dionex Aquion, ThermoFisher Scientific, USA) which in turn was connected to a second ion chromatography system for anion measurements (Dionex Integriion, ThermoFisher Scientific, USA).

For cations, we used an isocratic elution system as no larger or higher charged compounds were measured which would require gradient elution. For methods details, see individual publications, for instance an analytical column (Dionex IonPac CS12A), a guard column (Dionex IonPac CG18) and a suppressor (Dionex CDRS 600) were used and a flow of 0.25 ml/min of 15.45 mM MSA (Methanesulfonic acid) was applied with 12mA suppression, a cell temperature of 40 °C and a column temperature of 35 °C. Eluted ions were detected with a conductivity detector (DS6 Heated Conductivity Cell). For anions, a gradient system was used, specifically for the detection of polyphosphates. Again, method details are given in the publications but a reference method used an



analytical column (Dionex IonPac AS16 2mm), a guard column (Dionex IonPac AG16 2mm), a suppressor (Dionex ADRS 600 2mm), an eluent generator (EGC 500 KOH) and a trap column (Dionex CR-ATC 600). With a flow of 0.325 ml/min, the elution protocol started with 57.5 mM KOH (for 10 min), followed by a linear increase to 62.5 mM KOH over 2 min, isocratic elution with 62.5 mM KOH for 5 min, a direct step to 57.5 mM and equilibration for 8 min. Suppression was set to 47 mA, cell temperature to 40 °C and column temperature to 35 °C. Eluted anions were measured using a conductivity detector (DS6 Heated Conductivity Cell). For both machines, data was analysed with Chromeleon 7.2.10 (ThermoFisher Scientific, USA) and calibrations were done using commercially available standard solutions except for formate and polyphosphates where hand-mixed standard solutions were used.

### 2.3.2 Liquid chromatography

For measurements of organic molecules such as amino acids, nucleobases, nucleotides and 2-aminoazoles, two different LC systems were used. In addition, for confirmation and analysis of glycine dimerization and detection of non-proteogenic amino acids, an orbitrap MS was used.

#### System 1

For nucleobases, nucleosides, cytidine monophosphates, adenosine monophosphates, 5'-ribonucleotides, 2',3'-cyclic ribonucleotides, 3',5'-cyclic ribonucleotides, deoxyribonucleotides and di-glycine, the following system was used: Vanquish Flex (VF-S01-A) equipped with a binary pump (VF-P10-A-01), a heated column compartment (VH-C10-A) and a variable-wavelength detector (VF-D40-A) (all Thermo Fisher Scientific, USA). For separation of analytes, we used a Symmetry C18 column (3.5 µm pore size, 2.1 mm diameter, 150 mm length, 100 Å particle size, WAT106005, Waters, USA) and as eluents water with 0.1 % v/v formic acid (eluent A) and acetonitrile with 0.1 % v/v formic acid (eluent B). Further, we applied a flow of 0.3 ml/min with a column temperature of 30 °C (still air) and detected the UV absorption at 260 nm with 50 Hz. The detailed protocols can be found in the publication, but typically started with an isocratic elution step, followed by a gradient elution with an increasing fraction of B and ended by a washing step with 40 % B for 1 min and equilibration at starting concentration for 6 min. For the cases listed above, we analysed mass spectra (for details see next section).

#### System 2

For the analysis of 2-aminoazoles and mixtures of proteogenic amino acids, we relied on the following system: Vanquish Core (VC-S01-A-02) equipped with a quaternary pump (VC-P20-A-01), a heated column compartment (VC-C10-A-03), a diode array detector (VC-D11-A-01) and a fluorescence detector (VC-D50-A-01) (all Thermo Fisher Scientific, USA).

For the separation of 2-aminooxazole, 2-aminoimidazole and 2-aminothiazole, we adapted a method from literature [216] and used an isocratic with 90 % water with 10 mM ammonium formate and 10 % acetonitrile. For 5 min, we applied 1.5 ml/min flow over a InertSustain Amide column (100 Å, 5 µm, 4.6 × 150 mm, GL5020-88631, GL Sciences, Japan) with a column temperature of 40 °C and UV detection at 225 nm.

For the separation of all 20 proteogenic amino acids, we adapted a method from the literature [217] using pre-column derivatization of samples with 6-aminoquinolyl-N-hydroxysuccinimidyl carbamate (AQC, S041, Synchem, USA). This preparation step was done by mixing 7 parts of 50 mM borate buffer (28341, Thermo Fisher Scientific, USA) with 1 part of sample. Then, 2 parts of freshly prepared AQC (4 mg/ml) in anhydrous acetonitrile (43166, Alfa Aesar, USA) were added and carefully mixed by pipette. To complete the reaction, samples were incubated for 10 min at 55 °C. For separation in the LC, we used a ACCLAIM Vanquish C18 column (2.2  $\mu$ m, 2.1 mm  $\times$  150 mm, Thermo Fisher Scientific, USA) with water with 50 mM ammonium formate (17843, Honeywell, USA) and 0.8% v/v formic acid (A117-50, Fisher Scientific, USA) as eluent A and acetonitrile as eluent B. For elution, we used a column temperature of 45 °C and measured the UV absorption at 260 nm as well as the fluorescence emission at 473 nm under excitation at 266 nm (both with 50 Hz). A flow of 0.65 ml/min was applied. For the elution protocols, see publication. For peak identification, we prepared samples containing individual amino acids. As background levels in the fluorescence channel are lower, we used this for all amino acids except for tryptophan, where fluorescence is suppressed, and tyrosine, which yields by-products [217].

### Mass spectrometry

For mass analysis, we used a Q Exactive Plus Orbitrap HR/AM (Thermo Fisher Scientific, USA), under positive ionization with a resolution of 70k, an AQC target of  $3 \times 10^6$  and a maximum IT of 200 ms. A sheath gas flow rate of 2 was chosen on the HESI source, together with a spray voltage of 2.9 kV, 320 °C capillary temperature, 50 °C auxiliary gas heater temperature and a S-lens RF level of 50. For analysis in Chromeleon 7.2.10, the main isotope mass  $\pm 0.075$  m/z was extracted.

We both used mass spectrometry to confirm the masses in selected peaks, for instance for phosphorylation experiments, and for quantification of non-proteogenic amino acids and glycine dimerization with reference mixtures of defined concentrations for calibration.

### 2.3.3 pH measurements

For the pH measurements in all chapters, a Versa Star Pro device equipped with a Thermo Scientific Orion 8220BNWP pH Electrode and, for even smaller volumes in chapter 5.3, a Thermo Scientific Orion 9810BN pH Electrode (all Thermo Fisher Scientific, USA) was used.

## 2.4 Leaching and dissolution of geomaterials

In multiple parts of this thesis, we study the interactions of geomaterials with liquids. Chapter 4 investigates how apatite can be rendered accessible in prebiotically plausible natural pathways by thermal gradients as well as the potential of various other geomaterials as phosphate source for prebiotic chemistry. In chapter 5, the leaching of ions from basaltic materials and its compatibility with ribozyme activity is analysed.

As used in literature, we use the expression "leaching" to describe a closed, bulk setting (see Figure 2.5) where we expose a geological sample to a solution with a pre-set pH (and salinity) and leave it untouched until an equilibrium pH and ion concentration

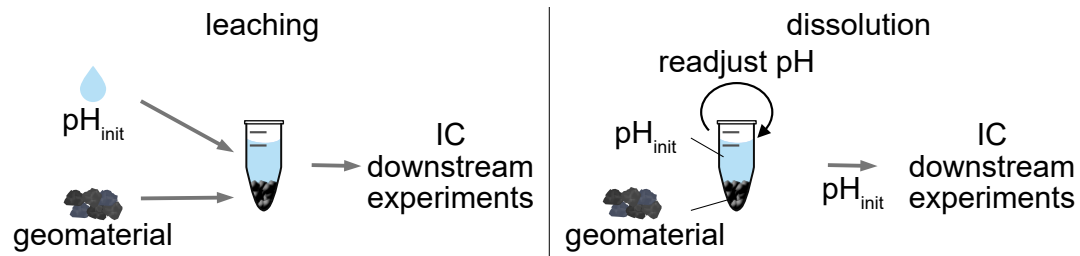


Figure 2.5: Leaching and dissolution experiments. While for leaching (left), geomaterial is exposed to a solution of preadjusted pH and left to equilibrate in ion concentration and pH, for dissolution experiments (right), we readjusted the pH until the pH of the solution equilibrated at the desired value, only leaving the ion concentration to equilibrate freely.

are reached. Typically after 3-5 days, we recover the supernatant for subsequent analysis in ion chromatography or experiments.

In an open geological setting, however, inflows continuously set the pH (and salinity) to a constant value. To do so experimentally, we readjusted pH repeatedly until an equilibrium at the target pH and salinity was reached. As evidently the pH would vary and dissolution would rarely be as completely as in our experiments for instance due to parabolic flow profiles, in chapter 4, we dilute 1 fraction of dissolved sample with 3 fractions of water, adjusted to the same pH.



# Chapter 3

## Heat flows enrich prebiotic building blocks and enhance their reactivity

This chapter corresponds to the paper from Matreux, Aikkila, *et al.* published in *Nature* in 2024 (appendix C) [1] and another project en route.

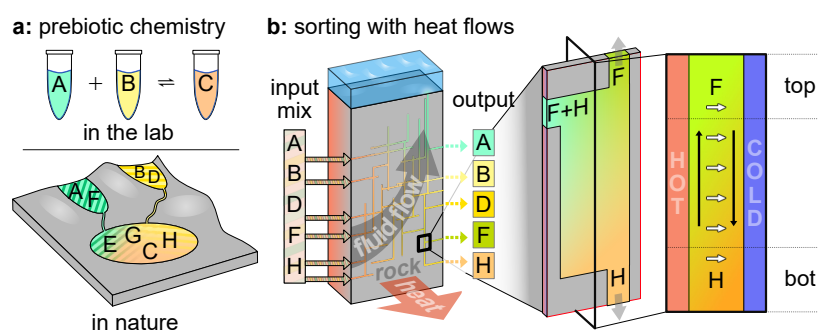


Figure 3.1: Prebiotic chemistry reactions often rely on pure reagents and defined sequences of mixing steps. However, in a natural setting, starting materials are typically mixed which massively impairs yields and leads to the formation of many by-products. In this project, we could establish that heat flows through rock cracks can drive the spatial sorting of simple, prebiotically relevant molecules such as amino acids, nucleobases and precursors. In a geological network of connected cracks, many different starting conditions for ensuing chemical reactions can be reached simultaneously and even mass-identical species be separated (adapted from [1]).

## 3.1 Introduction

A crucial step during the origins of life was the formation of the building blocks of life such as nucleotides, lipids and amino acids from simple substance presumably available for prebiotic chemistry [63, 64, 139, 218–220]. To explore these reactions and to ensure reproducibility, however, experiments are typically started with well-defined concentrations of pure reagents [62, 86, 221, 222]. In a multi-step reaction pathway, this can lead to the need for a well-defined sequence of steps, including the addition of new reagents or the purification of products. Without some intermediary purification, mainly by-products or clutter will be created and - if at all - vanishingly small concentrations of the desired product [85, 223, 224].

Even though intermediary purification steps seem artificial in a prebiotic context, some examples of such processes have been found. These include the crystallization of aminooxazolines [211, 225], the precipitation of aminonitriles [226], the selective interconversion of products [227], physical selection pressures such as UV light [228], or the selective sequestration of ribose using cyanamide [229]. Further, length selective adsorption of RNA on minerals [166] and RNA building blocks on surfaces [230] have been shown but require adequate washing steps to further use the adsorbed material. Phase-separated systems such as coacervates can segregate molecules, for instance for ribozyme activity [231] and other reactions [91]. However, all these mechanisms only work for specific sets of prebiotic compounds and may require (mutually exclusive) environmental conditions.

The results from past literature [95, 98, 181, 232] and other studies in this thesis (chapters 5-6) made us wonder whether heat-flow-driven enrichment could provide a widely available purification and separation mechanism. Our results show that heat flows through water-filled rock cracks can spatially separate and purify over 50 prebiotically relevant organic compounds. This specificity is made possible by the strongly varying strength of molecules, depending on charge, size, solvent interaction and others [233–237].

## 3.2 Results

The full description of results can be found in appendix C, here, a shortened version of the main findings is given.

### 3.2.1 Enrichment of small molecules

We started from dilute mixtures of compounds, mostly 20-50  $\mu\text{M}$  to avoid interactions. After the experimental time (18 h), the content of the chamber was frozen and separated into four fractions (see chapter 2 and for a more detailed description appendix C). The values were then internally normalized by the average concentration of the chamber and the concentration profile was plotted (see Figure 3.2) over chamber height. By comparing the obtained "relative" concentrations, the enrichments of one species against another were calculated by

$$\text{enrichment} = \frac{c_A - c_B}{c_B} \quad (3.1)$$

with the "relative" concentrations  $c$  of species A and B. For instance, the different local concentrations of 2-aminoimidazole and 2-aminooxazole transfer to 32% stronger

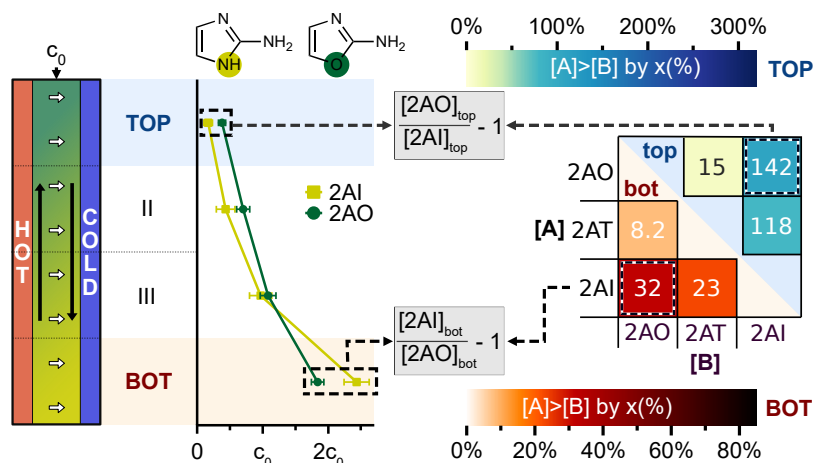


Figure 3.2: Enrichment of 2-aminoazoles in a heat flow chamber. On the left, the chamber and extracted fractions are shown. Analysis of the individual fractions by HPLC yields the normalized concentration profiles shown in the middle, showing a higher concentration of 2-aminoimidazole (2AI) than 2-aminoxazole (2AO) in the bottom fraction. This is represented by a 32 % enrichment of 2AI over 2AO by comparing their concentration as shown on the right side (adapted from [1]).

concentration of 2AI in the bottom fraction (see Figure 3.2).

We extended the analysis of these separations to various groups of molecules, including all 20 proteogenic amino acids. These were again mixed at dilute concentrations and exposed to the thermal gradient. The following extraction shows a strong selection (see Figure 3.3) the aliphatic amino acids leucine, isoleucine and valine are enriched in the bottom fraction (up to 81 % over glycine). In the top fraction, the strongly accumulated species are depleted, leading to relative excesses of small amino acids such as glycine. Even mass-identical isoleucine and leucine are separated up to 12 %.

For various other thermal fractionation patterns, see appendix C. The same separation effect is observed for nucleobases, nucleosides and differently phosphorylated nucleosides, distinguishing mass-identical compounds. The separation works over a wide range of pH (at least 3–11) and salinities (at least 0–100 mM NaCl) and for mixtures of solvents, for instance including 10 % formamide solution or phosphate-rich buffers.

### 3.2.2 Separation in an experimental 3-chamber-network

As we had started to look into networks of connected cracks before [3] (see appendix A), this made us wonder how strong the separation would be in a geologically more relevant setting. As our microfluidic setups are limited in size, we decided to investigate this in a 3-chamber-network, shown in Figure 3.4. Here, a continuous inflow of a mixture is supplied through the inlet and accumulated in a first thermo-microfluidic chamber. However, once it has passed this first chamber, it goes to a second chamber, either flowing through the top outlet into the upper chamber or through the bottom outlet into the lower chamber. Here again, thermophoretic accumulation takes place. After the experiment (60 h), the entire 3-chamber-network was frozen and extracted into 12 parts, 4 fractions per chamber.

The resulting concentrations for a mixture of amino acids are shown in Figure 3.4, indicating the individual chambers with a certain colour and the position inside the chamber by lighter/darker tones. It is clearly visible that the enrichment is strongly

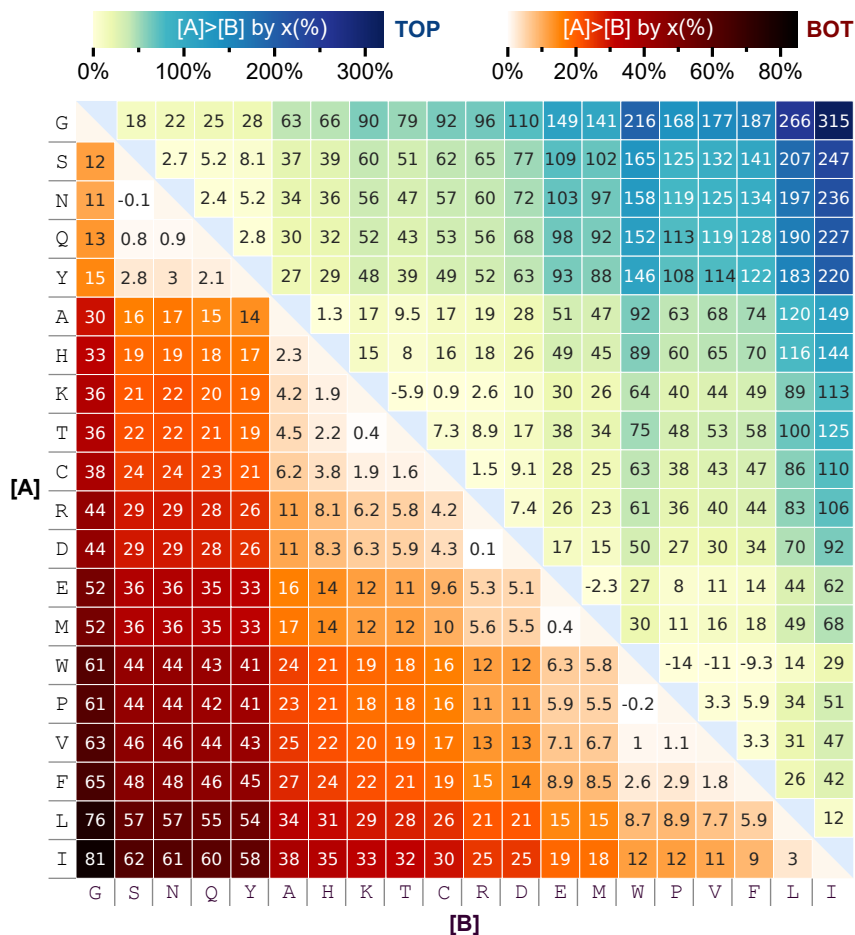


Figure 3.3: Enrichment of amino acids in a heat-flow chamber. The bottom left triangle shows the lower part of the chamber, the top right triangle the upper part (see Figure 3.2). For instance, isoleucine is accumulated 81 % stronger than glycine in the bottom fraction, while in the top fraction, glycine is 315 % overrepresented compared to isoleucine (adapted from [1]).

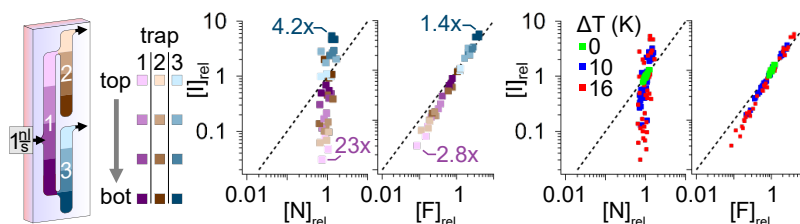


Figure 3.4: Separation in an experimental 3-chamber-network, shown on the left side. The enrichment between amino acids is strongly enhanced, even separating thermophoretically similar amino acids such as phenylalanine (F) and isoleucine (I). The separation is temperature gradient-dependent, showing stronger deviation from equimolarity (dotted line) for a 16 K gradient (adapted from [1]).

boosted, instead of the 61 % reached in the bottom fraction of a single chamber, isoleucine (N) is now 4.2-fold overconcentrated compared to asparagine (N) in the bottom part of the lower second chamber (blue). The same enhancement takes place in the upper parts, effectively yielding up to 95 % purity of individual compounds.



For thermophoretically more similar amino acids (for instance phenylalanine (F) and isoleucine (I)), the separation is also enhanced but stays at lower absolute values. Stronger temperature gradients further the separation, as depicted in Figure 3.4 on the right side.

### 3.2.3 Purification in a large network

To analyse how species behave in a larger, geologically more relevant network, we used finite-element simulations (for details see Methods in appendix C). However, for the numerical modelling, the Soret coefficients of all participating molecules were required which for the largest part were not determined before.

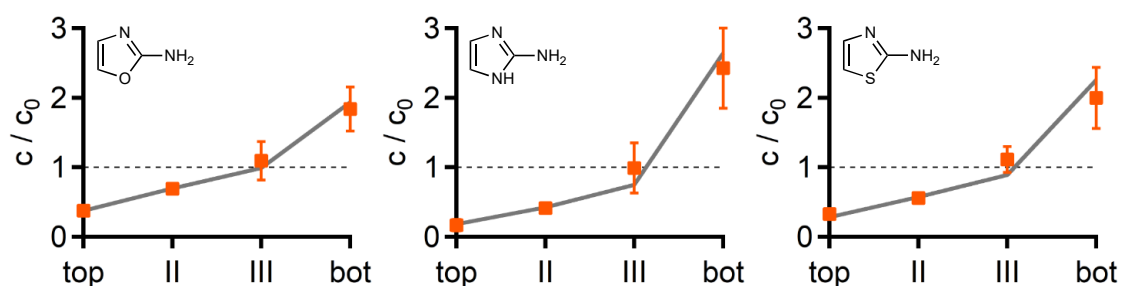


Figure 3.5: Examples of determination of Soret coefficients. From left to right: 2-aminooxazole, 2-aminoimidazole, 2-aminothiazole. The measured concentration profiles (orange) are fitted to finite-element simulations, yielding thermophoretic properties. For comparison, the concentration profiles with fitted Soret coefficients are plotted in grey (adapted from [1]).

So far, methods for example rely on fluorescent labels which however importantly alter the diffusive and thermophoretic properties of molecules, especially for small compounds such as nucleotides and amino acids [238]. Holographic measurement techniques, on the other hand, require high solute concentrations that lead to pH shifts and only permit the measurement of one compound at a time [239]. This made us think about how we could use the concentration profiles obtained (see Figure 3.2) to determine the thermophoretic strength of compounds in complex mixtures. Using finite-element simulations sweeping over various Soret coefficients, we could fit the concentration profiles and simultaneously measure the thermophoretic properties of all compounds in solution, only limited by analytical detection. An example of this fitting procedure is shown in Figure 3.5 for 2-aminooxazole, 2-aminoimidazole and 2-aminothiazole.

For one of the few compounds used here with previously investigated thermophoretic properties, 3',5'-AMP, our result agreed with literature values within error margins [240]. Using the obtained properties, we simulated networks of randomly connected cracks (always allowing for channels staying at the same height or ascending/descending one row, see Figure 3.6 left) and found a strongly enhanced separation of molecules. As an example, in Figure 3.6, the concentrations of glycine and isoleucine are depicted in a network of 40 x 20 chambers. This network is fed by a mixture of compounds at 1 nl/s which translates to flow volume rates between 0.1 and 10 nl/s per input channel due to randomly assigned throughputs.

Figure 3.6 shows the strong enhancement of separation, yielding chambers with either high excesses of isoleucine or of glycine. More examples of this separation are shown in the publication in appendix C.

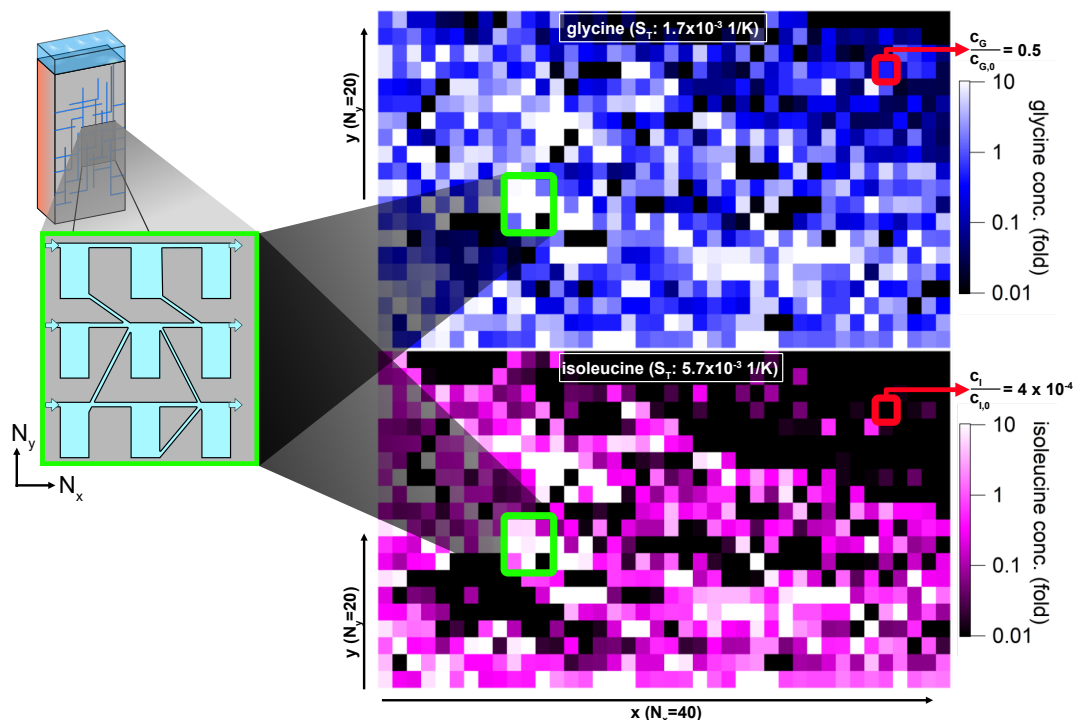


Figure 3.6: Local concentrations in a simulated network of 40x20 chambers. The thermophoretically stronger accumulating isoleucine is visibly dragged down over the course of the flow, locally reaching high enrichment. On the other hand, glycine, thermophoretically weak, is present throughout the network and thus has strong excesses in downstream parts on the right (adapted from [1]).

### 3.2.4 Reactions in chambers

Given the strong colocalization of molecules, this triggered the question to what extent this could benefit for prebiotic chemistry. We chose to investigate this on the example of glycine dimerization. While standard protocols do this upon heated drying [241], the reaction also works in water when catalysed by the reactive condensed phosphate trimetaphosphate (TMP). However, trimetaphosphate is supposed to be scarce on the early Earth (also see next chapter for a possible formation from apatite).

As shown in Figure 3.7, in the absence of heat-flow-driven accumulation and for 1 mM of TMP and 1 mM (or 10 mM) of glycine, no di-glycine is formed. In contrast, for the heat-flow case, TMP is strongly accumulated and locally provides an environment where the dimerization is catalysed for both glycine concentrations (rose and purple).

This boost once again is strongly enhanced in a network of connected cracks, increasing the yield by up to four orders of magnitude, with substantial effects even for weak temperature gradients (see appendix C for more details).

**Boosting polymerization** Another beneficial aspect of thermogravitational accumulation of small molecules was shown by Dirscherl *et al.*: The selective accumulation of activated nucleotides enhances polymerization and can trigger a greater sequence variety of formed oligomers [78]. This was shown for both aminoimidaole-activated adenosine deoxyribonucleotides and 2',3'-cyclic cytidine and guanosine ribonucleotides.

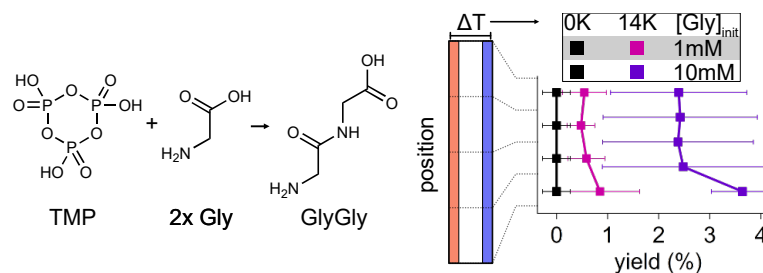


Figure 3.7: TMP-catalysed dimerization of glycine in water (shown on the left). The reactive condensed phosphate trimetaphosphate (TMP) is supposed to be scarce on an early Earth. While without heat-flow-driven TMP-enrichment, for 1 mM TMP and 1 mM / 10 mM glycine no dimer is formed, the selective accumulation locally provides suitable conditions and thereby drives the formation of di-glycine, even for low starting concentrations (adapted from [1]).

### 3.3 Outlook

A curious aspect to further explore will be other solvents, both for emergence of life [242] and for instance towards chiral selection which is not provided by thermogravitational accumulation in water. As the polymerization of 2',3'-cyclic ribonucleotides strongly depends on pH [80], another interesting prospect could be the combination of pH gradients with nucleotide polymerization, potentially creating favourable habitats. Furthermore, nucleoside or amino acid formation with simple components such as described by Powner *et al* and Liu *et al* would provide an interesting starting point [6, 62, 69, 243–250]. Towards more complex systems, the selective accumulation and colocalization of molecules provides an interesting scenario for combinations of proteins, nucleotides and other molecules crucial for life in order to overcome dilution and provide proto-cellular compartments only by physical non-equilibria [251–258].

#### 3.3.1 Habitat of chemical reaction networks

Complex reaction networks are a key component of living systems, for example in metabolic networks that help cells function and maintain stability. Hence, understanding how such networks emerged during the origins of life is crucial [11, 218, 250]. In contemporary biology, the Krebs cycle in eukaryotes is performed in the mitochondrial matrix, made possible by sustained spatial heterogeneity. However, on an early Earth and in absence of highly-evolved cell machinery, environmental non-equilibria need to achieve this spatial organization of reaction systems. Given the previous results for geologically plausible, heat-flow-driven crack systems, we decided to try to incorporate the formose reaction in such a system.

While the Breslow cycle (or formose reaction) has been known since 1861, first described by Butlerov, the analytical developments of the last years, led to an unprecedented understanding of this reaction network [11, 259–262]. It tackles the crucial question of synthesizing and interconverting sugars and polysaccharides from simple initial compounds. The system of chemical reactions synthesizes C4-C6 sugars from simple C1-C3 building blocks by formaldehyde-driven chain growth. In addition, the network exhibits strong responses to varying environmental conditions, allowing the compositional complexity to be analysed as a function of input parameters such as

feedstock and catalyst availability. Recently, the Huck group has shown a detailed understanding of this complex reaction network [11, 259–261], increasing analysability and predictability using machine learning approaches.

In a project underway, we explore the formose reaction as an ideal model system to explore its vast chemical reaction space in prebiotically plausible, thermal non-equilibrium systems. The geologically-inspired network of connected heat-flow cells provides niches of highly variable chemical compositions, showing how first-principle processes lead to spatially organized reaction networks, as required by living systems. Homogeneous heat flows and geological structures lead to a complex spatial organization and enrichment of the prebiotic solutes despite the system’s simple and homogeneous initial condition.

In the future, this will further open the door to study other systems such as the reverse Krebs cycle [218] in a multi-chamber approach with potentially naturally occurring widely spread salt compositions which reflect the highly diverse requirements per reaction step.

# Chapter 4

## Heat flows solubilize apatite and boost phosphate availability on the early Earth

This chapter corresponds to a preprint from Matreux, Schmid, *et al.* [2] and two other projects en route.

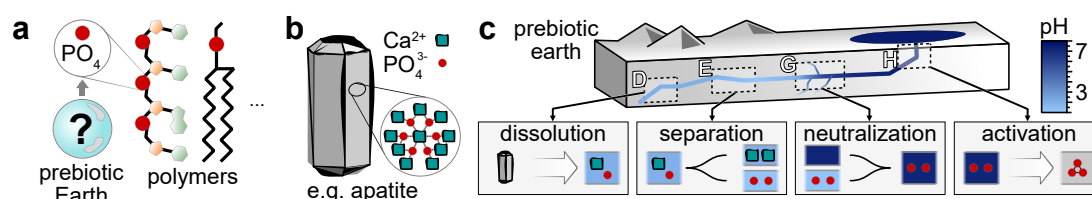


Figure 4.1: Summary of the phosphate problem at the origins of life and heat-flow-driven approach to use apatite for prebiotic chemistry. **(a)** Phosphate is integral to various biomolecules, from the backbone of RNA and DNA over phospholipids to many other occurrences. However, its prebiotic availability poses major problems as, for instance, one of the presumably most abundant phosphate minerals (apatite, **b**) is insoluble under the pH conditions relevant to nascent life. **(c)** In a heat-flow setting, the acidic-dissolved apatite is naturally fractionated, yielding a highly phosphate-enriched fraction. Upon pH-neutralization, this leaves up to 15 mM of phosphate in solution, boosted by up to 100-fold compared to the absence of heat flows and facilitating the formation of more reactive condensed phosphate species such as trimetaphosphate upon heating.

## 4.1 Introduction

Phosphate is essential to all life, be it in the backbone of RNA or DNA, in energy-carriers such as polyphosphates (ATP and GTP), phospholipids in cell membranes or various other occurrences. However, its prebiotic availability poses major problems as in the presence of divalent ions, phosphate is highly insoluble over a wide range of pH values, including those required for prebiotic chemistry. Most prominently, this is the case for calcium phosphates such as apatite, assumed to be among the most abundant phosphate minerals on the early Earth. The usage for prebiotic chemistry is further rendered problematic by the low reactivity of orthophosphate, leading to high millimolar to molar required concentrations, for instance, for the phosphorylation of nucleosides and their precursors as well as for the synthesis of more reactive phosphate species such as trimetaphosphate (TMP).

In this project, we use natural, geologically most relevant fluorapatite as phosphate source [2], thus an apatite with a fraction of fluoride. Using known dissolution characteristics, we acidic-dissolve the grains by repeated addition of hydrochloric acid (see chapter 2 for a detailed description of the methods and the dissolution experiments).

Upon exposure of the acidic solution to thermo-microfluidics, we observe a selective over-accumulation of phosphate relative to its precipitation partner calcium, shifting the Ca:P ratio from 5:3 as found stoichiometrically in apatite to 1:1 [2]. As a consequence, even upon pH-neutralization by alkaline inflows closer to the surface, high concentrations of orthophosphate remain in solution, enhancing solubility 100-fold. Interestingly, the resulting concentrations are sufficient to trigger the formation of low concentrations of trimetaphosphate, which itself has a comparatively high Soret coefficient (see chapter 3) and would thus easily accumulate, outcompeting orthophosphate to form local reactive niches.

As pure fluorapatite would be rather rare in nature but mostly incorporated in other geomaterials, we screened the leaching behaviour of a range of geomaterials and observed ion concentrations of  $<100\ \mu\text{M}$  in solution. By local accumulation, we could detect an up to 130-fold increase, and show the natural establishment of phosphate habitats.

Another geological possibility to provide phosphate to nascent life are phosphate-enriched basalts, assumed to be more relevant on an early Earth. In another project, we thus looked into their leaching characteristics and to what point they work as phosphate source for prebiotic reactions.

Together with the strong accumulation of magnesium over sodium (chapter 5), this opens the door to studies on precipitation in thermal gradients, exemplarily shown with a complete shift in precipitation dynamics for a simple, magnesium-sodium-phosphate-based model system.

## 4.2 Phosphate from apatite

### 4.2.1 Leaching behaviour of apatite

In a first step, we tested the leaching behaviour of 3 different geological apatite samples (Ipirá complex, Brazil, Durango, Mexico and Ontario, Canada) of various compositions (see Table 4.1). As described in the Methods in chapter 2, for these experiments, we exposed defined masses of apatite to water with a preadjusted pH, see Figure 4.2 for results. As expected from literature [263], we found a strongly pH dependent behaviour

Origin	Country	CaO (%)	P <sub>2</sub> O <sub>5</sub> (%)	F (ppm)
Ipirá complex	Brazil	54.6	39.0	2.9
Ontario	Canada	55.1	41.5	2.4
Durango	Mexico	54.0	41.4	3.2

Table 4.1: Composition of natural apatites, measured by X-ray fluorescence.

(Fig. 4.2 a-c) but did not observe any dependence on mass:volume ratio, temperature or any other parameter (Fig. 4.2 d-g).

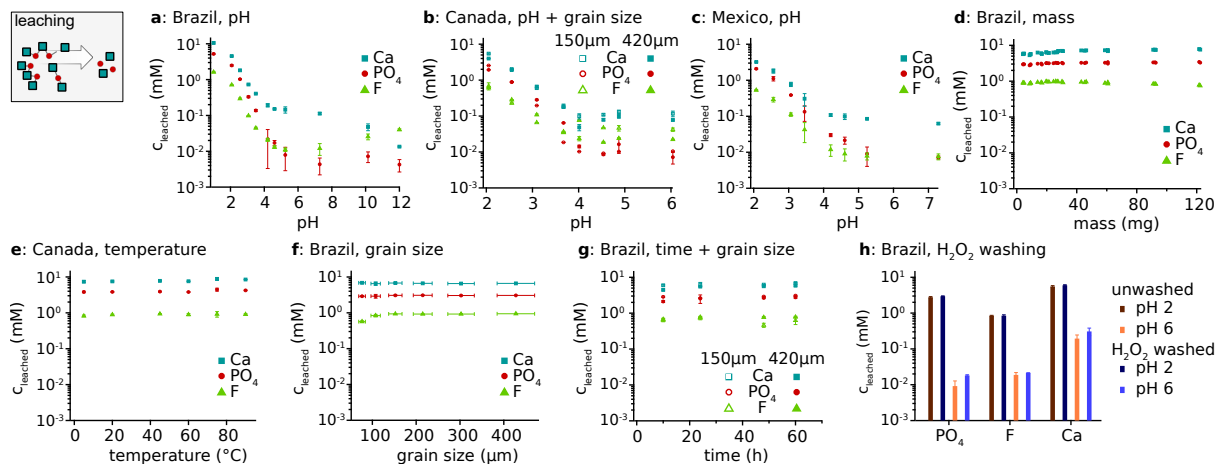


Figure 4.2: Leaching from different natural apatites and dependence on parameters. **(a-c)** Apatites from different sampling locations were exposed to various pH solutions and the main released ions were measured using ion chromatography, showing similar concentration-pH profiles and compositions in all experiments. **(d-h)** Neither mass:volume ratio, nor temperature, grain size or prior washing changed leached concentrations and compositions.

### 4.2.2 Dissolution and fractionation by heat flows

In a more realistic geological flow scenario where the pH is externally set and kept stable as for example in crack networks, dissolved concentrations are strongly increased for acidic pHs (see Figure 4.3 a). Here, as introduced in the Methods in chapter 2, the geomaterial is immersed in water that is repeatedly readjusted to the desired pH (see Figure 2.5). However, this does not change the Ca:P ratio (see Figure 4.3 a/c) and thus results in precipitation of phosphate upon reneutralization, keeping the phosphate inaccessible for prebiotic chemistry (see Figure 4.4 a-b). To mimic the flow scenario and include for example parabolic flow profiles changing local dissolution dynamics, we diluted the acidic-dissolved solution with 3 fractions of water that was previously adjusted to the same pH.

Thermal non-equilibria across rock cracks drastically change the situation. Using a similar approach as shown in the Methods, but with a closed middle outlet (shown in Figure 4.3). We applied a flow of 15 nl/s and recovered 5% through the bottom outlet which is indicated as  $\Delta T$  in all figures. By molecule-selective thermophoresis, phosphate ions are up to 70% stronger enriched than chelating calcium ions. The positively charged calcium is replaced by a shift in pH towards more acidic values (see Figure 4.3 b-c), keeping

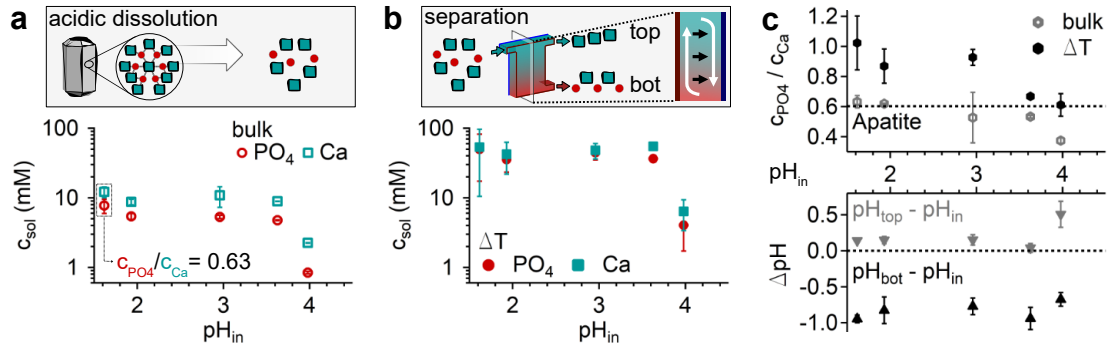


Figure 4.3: Dissolution of apatite and thermally driven separation. **(a)** Apatite dissolves at the characteristic 5:3 Ca:P ratio, yielding up to 10 mM after 4-fold dilution. **(b)** Heat-flow-driven fractionation accumulates both species but increases phosphate concentrations to the calcium levels. **(c)** This massively changes the ratio of calcium to phosphate by 70 %, effectively removing calcium ions per phosphate ion which is balanced by a shift in pH.

electrostatic neutrality. As a consequence, this balances the Ca:P ratio to equimolar values, massively changing the outcome of following geological neutralization.

### 4.2.3 Solubilization of phosphate and utility for prebiotic chemistry

To mimic alkaline or neutral inflows closer to surface, we repeatedly added sodium hydroxide to neutralize the acidic solutions. This repeated addition is validated by geochemical modelling using phreeqc [264, 265] as subsequent precipitation of apatite lowers the pH (see modelling results in Figure 4.4 a). In the model, the precipitation is achieved by analysing oversaturated species, in our case mostly hydroxyapatite (for more details see next section).

After this neutralization, we measured phosphate concentrations in bulk (i.e. inflow samples which were not exposed to a thermal gradient) and in the thermally fractionated samples, see Figure 4.4 b. Phosphate concentrations are boosted by up to 100-fold by prior heat-flow-driven separation, reaching 15 mM in solution at neutral pH and thus accessible for prebiotic chemistry. This is consistent with geochemical modelling (in black/grey).

Crucially, this facilitates the polymerization of phosphate, for instance boosting the formation of reactive trimetaphosphate (TMP) up to 250-fold [56, 266–272], see Figure 4.4 c.

### 4.2.4 Modelling precipitation and solubility

For modelling the precipitation and resulting concentrations in solution, we used PHREEQC 3.7.3 [264], as well as the python implementation of PHREEQC, phreeqpython [265].

Using standard databases for all ions in solution, possible mineral precipitates are analysed and the saturation index (SI) is calculated.

$$SI = \log(IAP/K_{sp}) \quad (4.1)$$

with the ion activity product IAP of the dissolved ions of the mineral and their solubility product  $K_{sp}$ . If this index is larger than 0, the mineral species is oversaturated



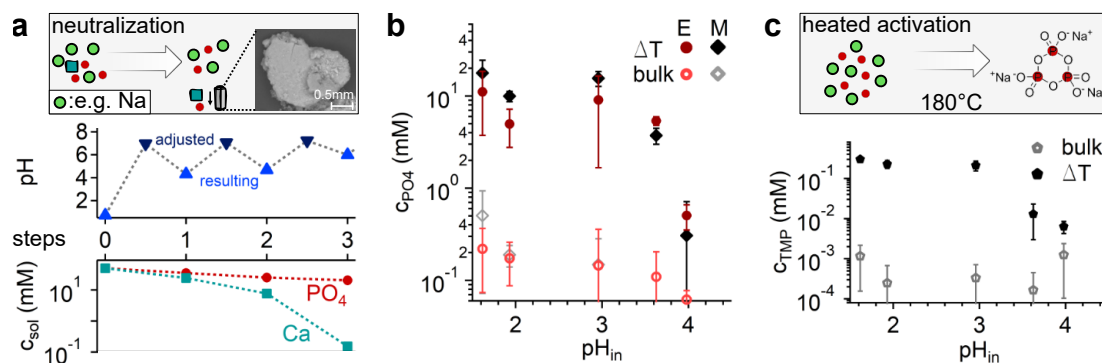


Figure 4.4: pH-neutralization of solution and accessibility for prebiotic chemistry. **(a)** Repeated alkaline additions for instance by inflows closer to the surface drive precipitation of calcium phosphates and limit the phosphate accessibility at neutral pH. **(b)** While in bulk (rose), only submillimolar concentrations of phosphate remain in solution after neutralization, the heat-flow-driven removal of calcium enhances the phosphate solubility 100-fold, yielding up to 15 mM in solution. This is validated by geochemical modelling based on initial concentrations (black/grey). **(c)** The phosphate concentration present are sufficient to trigger the formation of more reactive condensed phosphate species such as trimetaphosphate, boosted 250-fold in comparison to the case of absent heat flows.

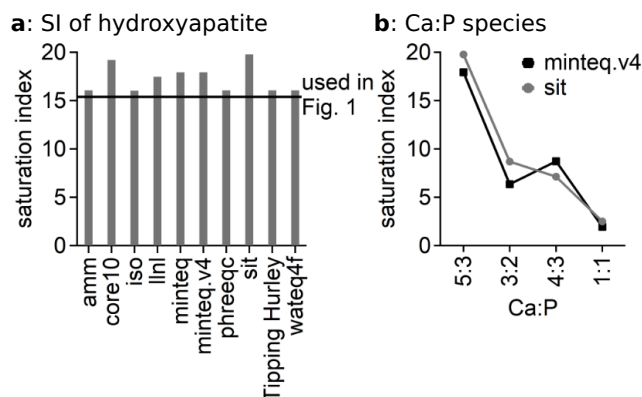


Figure 4.5: Saturation indices for different databases. **(a)** Starting with 50 mM phosphate, 50 mM calcium, 20 mM chloride at pH 1 under an addition of 300 mM sodium hydroxide, all databases show the oversaturation of hydroxyapatite, the black line indicates the database used in previous figures. **(b)** Where present, we compared the saturation indices of different calcium phosphate minerals and found a dominant oversaturation of a Ca:P ratio of 5:3, for instance apatite.

and will naturally precipitate.

In Figure 4.5 exemplary saturation indices are shown, using the composition measured by ion chromatography in our samples, 50 mM phosphate, 50 mM calcium, 20 mM chloride under an addition of 300 mM sodium hydroxide. Here, the chloride stems from the acidic dissolution of apatite but is also realistic in a natural setting [42–44]. The concentration of sodium hydroxide was calculated to neutralize the samples, taking into account both the initial pH and the  $pK_a$ 's of phosphate that need to be overcome on the way to neutrality.

In Figure 4.5 a, different databases are compared which show small differences but a general strong trend towards precipitation of hydroxyapatite. This is further validated

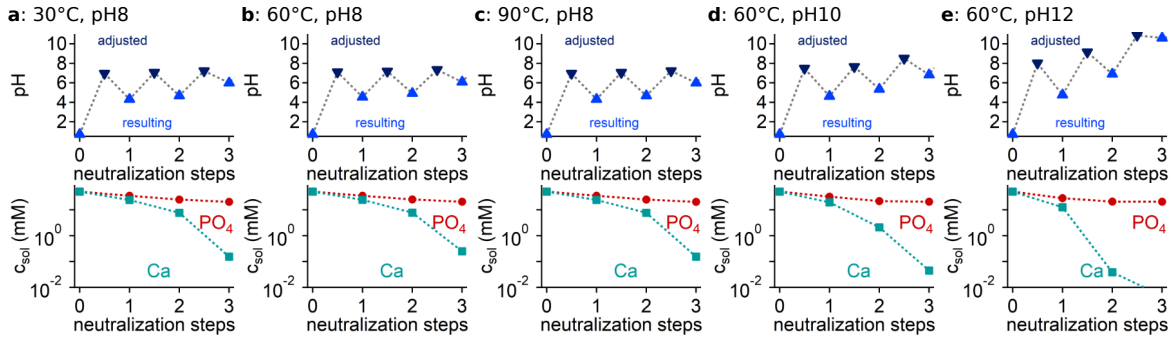


Figure 4.6: Impact of temperature and inflow pH on neutralization and precipitation. (a-e) As used in Figure 4.4, we modelled the resulting pH and ion concentrations after multiple neutralization steps and found that neither the temperature nor the neutralizing inflow pH (in the range 8-12) changes the outcome. As expected, a higher pH accelerates the precipitation and thus reduces the number of required steps, i.e. in a natural setting the combined volume of incoming neutralizing fluid.

by two databases that take into account various calcium phosphate mineral species and predict the precipitation of mainly  $\text{Ca:P} = 5:3$  species such as apatite.

To test the influence of environmental conditions, we tested the precipitation dynamics for various temperatures and pH values of inflows but found only minor changes (see Figure 4.6, mostly accelerating the process for increased pH values which seems reasonable).

### 4.3 Other phosphate sources

While apatite is assumed to be the most abundant phosphate mineral on early Earth, most phosphate is presumably contained either in small layers with up to 10 molal % of apatite [273], phosphate mineral inclusions [117, 274] or non-crystalline phosphate containing materials.

Name	Abbreviation	Phosphate content (wt %)
Siliclastic sand	SCS	0.22 %
Illite	ILL	0.37 %
Carbonate sand	CAS	0.05 %
Kaolinite	KAO	0.45 %
Basaltic sand	BSS	0.05 %
Volcanic glass	VCG	0.48 %
Montmorillonite	MON	0.03 %
Volcanic clay	VCC	0.06 %
Zeolite	ZEO	0.02 %

Table 4.2: Phosphate content of various geomaterials. Measurement was done using EDS (energy dispersive X-ray spectroscopy) to measure composition of elements on the surface. After measurements, values with more than 10 % total mass were normalized and used to calculate above weight percent.

To evaluate such geomaterials as phosphate source on an early Earth, we tested different phosphate-bearing geomaterials for phosphate leaching at various initial pH

values (see Figure 4.7 b). These contained between 0.02 wt% and 0.5 wt% phosphate, see Table 4.2. The obtained phosphate leachate concentrations ranged from 0-0.1 mM, thus far below those required for prebiotic chemistry.

In a similar setting as in the previous section, we analysed how well phosphate can be drawn into and retained in small rock fractures, thereby providing a local phosphate niche habitat. For this, we closed the bottom outlet of the prior setup (shown in Figure 4.7) and flushed a dilute solution of 500  $\mu\text{M}$  phosphate with 30 nl/s over the pore. The experiments showed that in the entire fracture, phosphate concentrations increase up to 40-fold after one week with up to 130-fold in the lowest quarter of the fracture.

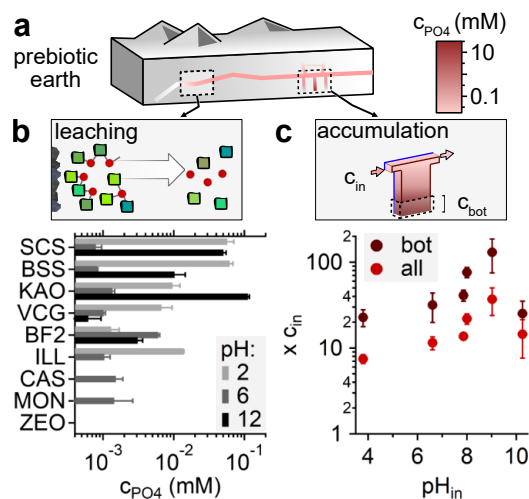


Figure 4.7: Geological flow setting for heat-flow-driven enrichment of phosphate from dilute sources. **(a)** In a network, phosphate containing geomaterial is leached into a flow which en-suite flows over a heated pore. By the interplay of convection and thermophoresis, phosphate is strongly drawn into the pore, providing a local phosphate habitat. **(b)** Leached phosphate concentrations from a variety of sands, basalts and clays remain below 0.1 mM. **(c)** Such low concentrations can be locally enriched up to 130-fold by heat flows through rock cracks that take up the phosphate from a solution flowing over a closed pore.

### 4.3.1 Compatibility of geomaterials with phosphate polymerization

As geomaterial was shown to influence prebiotic reactions, we tested the compatibility of heated polymerization of phosphate with the used geomaterials, see Figure 4.8. While for diphosphate all geomaterials at least slightly reduce concentrations, the formation of trimetaphosphate and linear triphosphate are enhanced on some surfaces such as Kaolinite. Other geomaterials, such as the clays Montmorillonite and Illite seem to hinder the cyclization of TMP or the resorption of TMP.

### 4.3.2 Phosphate-enriched basalts

An interesting other aspect is the usage of geological phosphate sources beyond apatite on the early Earth. In a publication currently in preparation, we explore the reactivity and utility of phosphate-enriched basaltic rock, assumed to be more realistic on an early

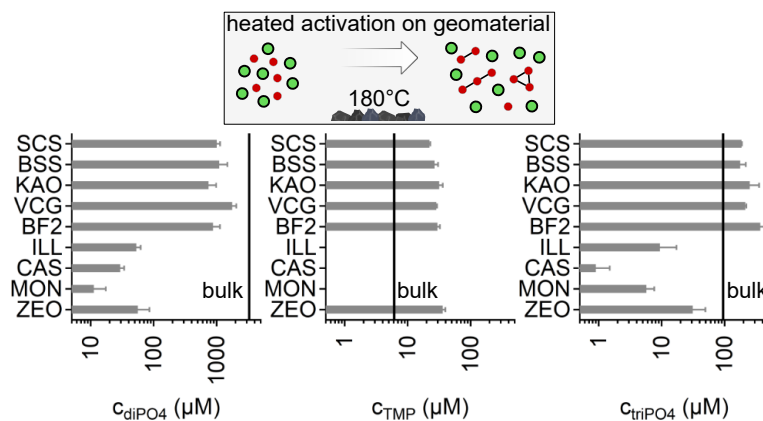


Figure 4.8: Compatibility of phosphate polymerization with geomaterial. For a range of clays, sands and basalts, we heated 10  $\mu\text{l}$  of 10 mM of phosphate at 180  $^{\circ}\text{C}$  and found that for instance the formation of TMP can benefit from the presence of kaolinite and some other geomaterials while in general, less diphosphate is in solution after reelution than for the non-geomaterial case.

Earth even though geomaterial with up to 4% phosphate content was still detected recently [273].

#### 4.4 Selective precipitation of magnesium phosphates

The shown strong local enrichment of phosphate by heat flows introduced in this chapter raises the question whether thermal gradients could also drive the selective precipitation of otherwise unfavourable species.

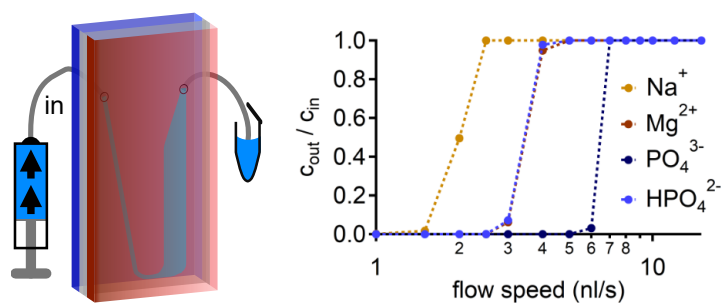


Figure 4.9: Experimental setup. A continuous flow is supplied through "in" and exposed to the thermogravitational accumulation. While in the thin inlet channel, flow speeds are high and thus reduce heat-driven precipitation, in the broad outflow channel (on the right in the thermo-microfluidic chamber) the applied flow and the thermal accumulation are in competition. This leads to a highly selective retention of molecules as exemplarily shown for the model system. The ion with weakest accumulation (sodium) is only retained for small volume flow rates while highly charged phosphate is strongly retained and thus enriched.

In collaboration with François Guyot (MNHN Paris), we investigated the behaviour of mixtures of sodium phosphate and magnesium chloride. Using a simple flow through a channel as shown in Figure 4.9, we found a drastic shift in precipitating phases. This

is driven by the selective retention of ions, in our case magnesium and phosphate over sodium, determined by the competition between thermogravitational accumulation and applied flow. As shown in Figure 4.9, this leads to defined cut-off values for each ion, here simulated for a gradient of 40 K over a width of 170  $\mu\text{m}$ . A more detailed discussion of this effect and the simulational approach are shown in chapter 6.3, where we first came across the strong selectivity of this effect. Due to stability reasons, the simulation was ran without electrostatic interactions which reduces the steepness of the cut-off as ions interact but is still consistent with experimental results.

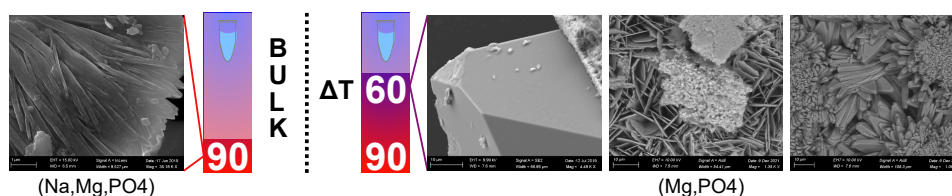


Figure 4.10: Precipitation behaviour in a model system of sodium phosphate and magnesium chloride. While in bulk, high temperatures are required but only yield formation of mixed-ion precipitates (left), selective accumulation in temperature gradients leads to formation of pure magnesium phosphates at lower temperatures (right).

While in absence of temperature gradients, mixed phases precipitate, the presence of heat flows lead to a lowering of precipitation temperature induced by the strong accumulation of ions and to precipitation of pure magnesium phosphate phases such as newberyite, bobierite and baricite (see Figure 4.10 for scanning electron microscopy images of resulting phases). Experiments here were done with a 4 mm broad channel of 170  $\mu\text{m}$  thickness and with a volume flow rate of 3.2 nl/s as obtained from Figure 4.9. Phase identification was done using X-ray diffraction.



## Chapter 5

# Heat flows in rock cracks naturally optimize salt compositions for ribozymes

This chapter corresponds to the paper from Matreux, Le Vay, *et al.* published in *Nature Chemistry* in 2021 (appendix A) [3].

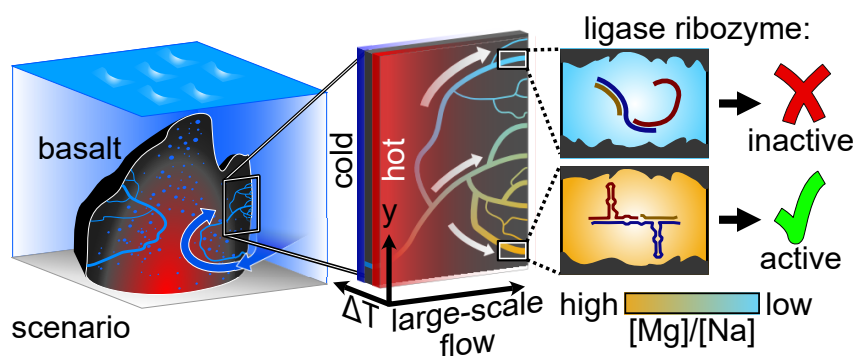


Figure 5.1: Heat flows in rock cracks naturally optimize salt compositions for ribozymes. While basaltic leachate concentrations and compositions are not suitable for ribozyme function, heat flows through connected water-filled rock cracks establish ribozyme habitats by selective accumulation of divalent ions (adapted from [3]).

## 5.1 Introduction

On an early Earth, the emergence and sustainment of enzymatic function was crucial for catalysis and information storage, and on the long run for the emergence of first self-replicating systems. As introduced, one candidate for functional activity is RNA as it can both self-replicate and fold into complex structures with catalytic activity, similar to modern biology's protein. As this makes RNA a good match to initiate a self-sustaining evolution, an "RNA world" has been hypothesized [57, 275], but research also extends towards pre-RNA [276] and mixed [277] systems. However, RNA requires high concentrations of magnesium ions (10 to 200 millimolar) in order to correctly fold into their active state [278–282] and limited concentrations of other ions such as sodium that can lead to displacement of divalent ions and misfolding and inactivity [283–287].

Typical basalts however contain only limited amounts of magnesium, and other proposed geological environments such as salt-rich ponds typically have Na:Mg ratios of 100:1 to 1000:1 [87]. Whilst drying can increase absolute concentrations, it cannot alter the composition of salts in solution. Even more, the hydrolysis of RNA is worsened thereby, with even stronger degradation at increased temperatures and high pH. Also in a more general setting, wet-dry cycles [288, 289] are a powerful mechanism but do not allow the relative concentration ratio of solution components to be altered. In addition, salt concentration increases exponentially with decreasing liquid volume, which may lead to extremely high divalent metal ion concentrations that promote RNA hydrolysis. The problem of RNA hydrolysis is mitigated during up-concentration in frozen water ice above the eutectic point, but the ratio of monovalent to divalent salt ions in solution is largely preserved in the remaining liquid phase. Furthermore, high initial concentrations of salts generally reduce the magnitude of up-concentration as less volume reduction by water ice formation is required to reach the equilibrium salt concentration that prevents further freezing [191, 290, 291].

This poses the important question what environment could provide high concentrations of divalent metal ions all while avoiding high concentrations of monovalent ions such as sodium. In this project, we showed how a geothermal setting can alter the ratio and naturally establish local ribozyme habitats (see Figure 5.1).

Starting from a geological perspective, we investigated the leaching of salts from synthesized basaltic glass and natural ground basaltic rock [292], using samples from the tholeiitic magma series stemming from the Krafla eruptions on Iceland. Basaltic glass is an ideal material for this prebiotic scenario due to its high alteration kinetics for the efficient liberation of cations, its characteristic high surface area due to quench granulation, and efficient pathways for fluid circulation [293–296]. Alteration products of basalt, such as Montmorillonite clays, are commonly used in prebiotic scenarios. Using ion chromatography, we characterized the amount of salts leached under various conditions such as temperature and grain size of the geomaterial with a focus on magnesium and sodium.

We then tested the efficiency of RNA-catalysed ligation reactions in the resulting salt conditions. We used the R3C replicator ribozyme as a model system, as it is a simple RNA-only self replicator, and shares its catalytic mechanism with prebiotically relevant RNA polymerases which are particularly affected by sodium inhibition [297]. We explored how heat flows can optimize the salt content for these ligation reactions. By locally increasing salt concentrations from starting conditions obtained from leaching, and by boosting the concentration ratio between divalent and monovalent salts, conditions can



be improved to such an extent that RNA-catalysed reactions can take place in otherwise inhibitory environments. As in a geological system, connected rock cracks would be the typical situation, we experimentally and by simulation investigated the situation in networks of cracks and observed that even initially inhibitory conditions can be naturally optimized by heat flows (shown in chapter 5.4 as an example of desalination).

## 5.2 Experimental results

### Leaching from basaltic rock

The leaching from tholeiite basalt (for compositional analysis see appendix A) was studied for various parameters (see Figure 5.2). However, magnesium concentrations do not exceed 0.1-0.2 mM, insufficient to drive ribozyme reactions. In addition, especially for the rock samples, much more sodium is leached which in turn, upon drying to increase magnesium concentrations, would inhibit ribozyme activity (see later section).

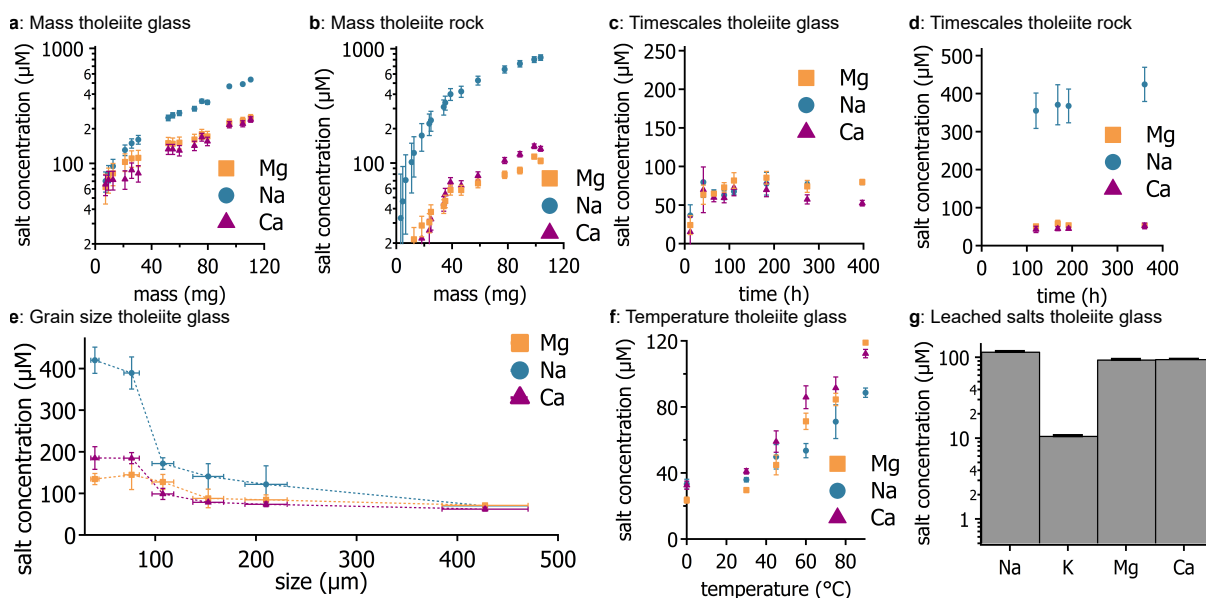


Figure 5.2: Leaching from basaltic rock. Except if stated otherwise, 30 mg of geomaterial were leached at  $60^{\circ}\text{C}$  for 36-48 h in 150  $\mu\text{l}$  ultrapure water. **(a-b)** Both for molten and quenched (a) and natural (b) tholeiite basalt, the leached ion concentrations increase with higher mass-to-volume ratios. **(c-d)** Time evolutions shown an equilibration after around 30 h. **(e)** The grain size massively changes leaches concentrations, as intuitively expected due to increased surface. For smallest grain sizes, wetting becomes less efficient and leached concentrations decrease. **(f)** Increased temperatures lead to more leaching. **(g)** The main cations leached (and detected) are sodium, magnesium and calcium, with potassium concentrations already one order of magnitude lower (adapted from [3]).

### Selective thermogravitational accumulation of magnesium

To explore the selective accumulation of ions, we used the setup introduced in chapter 2 and shown in Figure 5.3. This mimics a heated rock crack which is continuously supplied with a premixed solution (in this case 1 mM of sodium chloride and of magnesium

chloride). A flow of 11.8 nl/s was applied and pushed the solution through the thermal chamber where it was exposed to the gradient. The accumulation drives ions towards the bottom of the chamber, where the bottom outlet and syringe draws them out at a controlled flow rate to recover for example 5% of the inflow volume rate. The same is the case for the top part, leaving the middle 90% to flow through an open outlet into a falcon tube. The three fractions and the inlet are then analysed by ion chromatography, showing local accumulation and depletion.

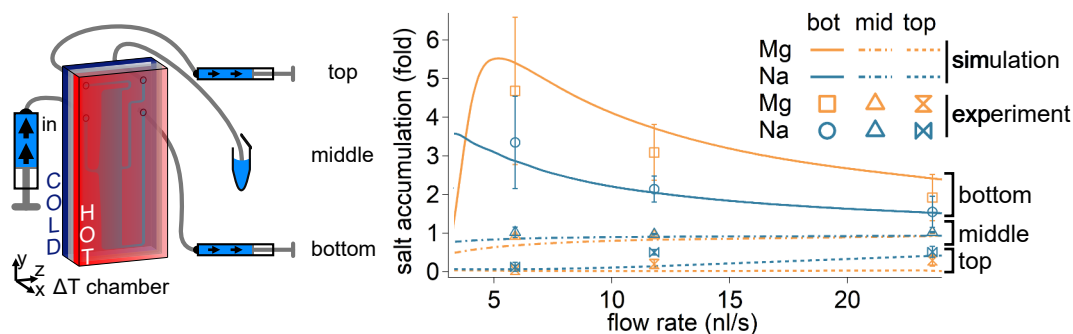


Figure 5.3: Separation of magnesium versus sodium ions in a thermophoretic flow cell. The supplied inflow solution ("in") is separated into 3 different parts after thermophoretic accumulation, with the "bottom" and "top" syringes each pulling 5% of the inlet volume flow rate. The accumulation of ions is measured by ion chromatography and depicted on the right side for various flow speeds (symbols) against finite-element simulations (lines) (adapted from [3, 4]).

The results for various flow rates are shown in Figure 5.3. The symbols show the experimental data while the lines show results from finite-element simulations. Magnesium is accumulated up to 2-fold stronger than sodium, with up to 5-fold absolute up-concentrations. When the flow rate gets too low, the outflow volume flow is not fast enough to counteract the secondary heat flow chamber in the outlet channel (see also chapter 6.3), leading to a complete breakoff of ions leaving the chamber. Beyond that limit, lower flow rates lead to higher accumulations as the timescales of large flows (used for measurement) and thermophoretic accumulation are stronger separated and thereby permit a strong enrichment at the bottom of the chamber.

### Ribozyme activity with varied salt conditions

In close collaboration with the Mutschler lab (now TU Dortmund) and Kristian Le Vay, we explored to what point leachate salt conditions before and after thermal accumulation permit ribozyme activity. For this, we used two version of the R3C ribozyme [207], one simple ligase and one ladder ribozyme (shown here).

As depicted in Figure 5.4, the ribozyme activity strongly depends on salt conditions, requiring 4 mM magnesium ions to reach 20% yield. In the presence of heat flows and by the selective accumulation of magnesium, this is lowered to 0.5 mM for 12% yield, reflecting the local enrichment.

In addition, drying the original leachates would harm the activity as even 10-fold excess of sodium lowers the yield, with 1000-fold completely inhibiting the reaction.

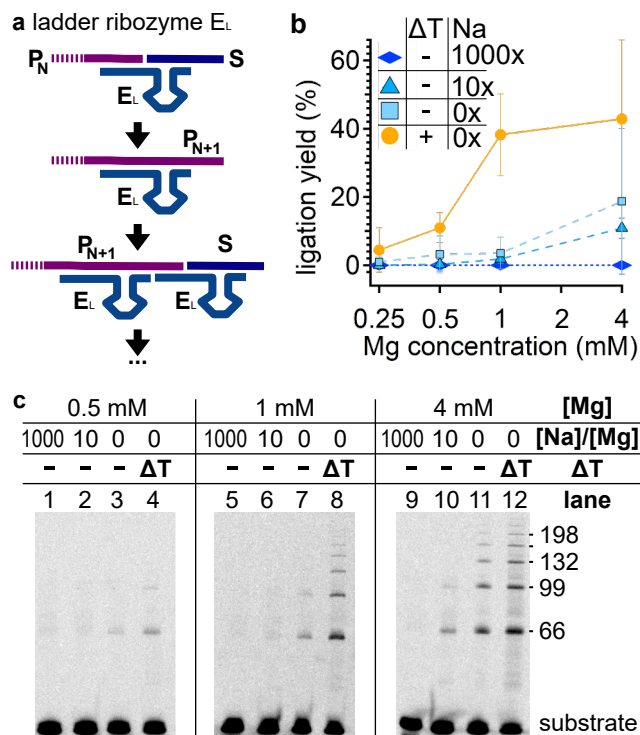


Figure 5.4: Ribozyme activity for various salt conditions. **(a)** The basic working principle of the R3C ladder ribozyme.  $E_L$  catalyses the ligation of a substrate strand (S) to a product strand (P) which was previously assembled in the same manner, making all product strands length multiplicates of 33, the length of the substrate. **(b)** From the electrophoresis gels, the yield is determined for various salt conditions with and without a thermal gradient, showing the effective accumulation of magnesium ions and lowering the yield per concentration approximately 4-fold. **(c)** PAGE gels show the ligated products for various salt conditions, with the calculated yield shown in (b) (adapted from [3]).

## 5.3 Outlook

An interesting other pairwise separation would be the fractionation of potassium and sodium, now established in cells and also probably required at some stage during the origins of life [298, 299]. These gradients could also be incorporated into phase-separated systems such as coacervates and vesicles by cycling through different local habitats. Beyond origins of life, another exploratory potential application is thermodiffusive desalination as detailed in chapter 5.4.

### 5.3.1 Salty pH gradients

Interestingly, when using salt concentrations closer to those presumed in prebiotic oceans [42–44], we found that the selective accumulation of ions induces proton gradients. We tested this for various salts (see Figure 5.5) and curiously found close to no dependence on the cationic species involved.

The induced pH gradients are consistent with 1-dimensional finite-element simulations with included electrostatic interactions and hint to a stronger effective thermophoretic accumulation strength of anionic species (i.e. chloride) even though its Soret coefficient in past measurements was estimated lower [300]. The project and the understanding of

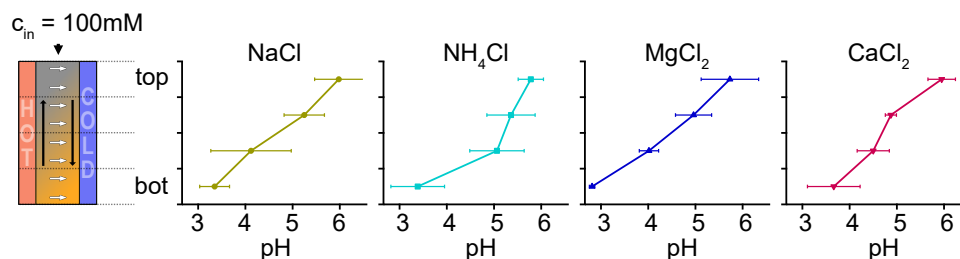


Figure 5.5: Salty solutions of 100 mM of the listed salts were exposed to a thermal gradient for 18 hours and freeze extracted. Interestingly, in addition to the ionic gradients described in this chapter, a pH gradient occurs which is independent of the cationic species.

the underlying mechanism are still underway but might lead to the natural emergence of habitats where RNA is protected at low pH but can cycle towards regions of replication and function. For a model acid-base system using prebiotically relevant formic acid and sodium hydroxide [301, 302], we could experimentally validate a theoretical framework based on the separation of timescales (see next chapter).

## 5.4 Applications beyond origins of life

In this thesis, the selective accumulation of ions and molecules by thermal gradients is used to explore the potential of heat flows for the origins of life. However, applications go far beyond the field and include for instance thermodiffusive or thermogravitational desalination, gas separation for CO<sub>2</sub> removal and various other possible fractionation processes.

### 5.4.1 General principle of fractionation by heat flows

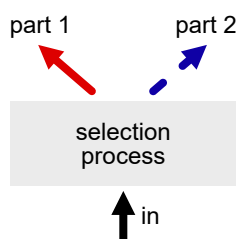


Figure 5.6: General principle of separation cells, consisting of one inflow into the chamber where some selection process differentiates solutes, yielding different properties or concentrations in two outflows.

On a general basis, the fractionation is achieved by simple separation cells (depicted in Figure 5.6), also called Burgers cells. Here, an incoming fluid (or gas) is split into 2 (or more) parts by a selection process which in our case is driven by temperature gradients.

#### Orthogonal temperature gradient

When using thermophoresis as selection force, this yields a setting as shown in Figure 5.7 with different possible orientations of the thermo-microfluidic cell. In part a, the

separation process is depicted as for instance used in [303]. Here, gravity is parallel to the thermal gradient and thus accumulation and selection is only driven by thermophoresis.

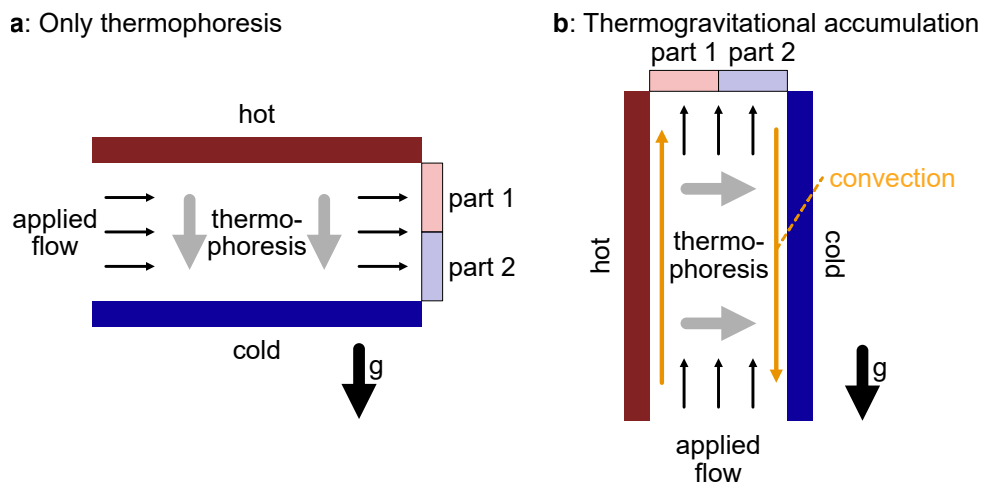


Figure 5.7: Example of individual cell for thermodiffusive versus thermogravitational separation. **(a)** Thermodiffusive separation. The side view show the externally applied flow through the cell. The temperature gradient is orthogonal to the flow direction but parallel to gravity, limiting separation and enrichment. **(b)** Thermogravitational separation. Upon orthogonality between gravity and temperature gradient, the enrichment is boosted by convection. For the case of externally applied flow that is antiparallel to gravity, the separation is strongest.

As introduced before, the accumulation of solutes and the strength of fractionation is amplified upon orthogonality of temperature gradient and gravity. In addition, the applied flow should be antiparallel to gravity to have a competition between thermally driven accumulation and externally applied flow for strongest selection. This case is shown in part b, with the same working principle as used in many of the prior chapters. As the aspect ratio (height, i.e. length in flow direction divided by width, i.e. dimension of the temperature gradient) should be large enough, this could also be regarded as a Hele-Shaw flow.

### Selection in a network of connected cells

Figure 5.8 shows a small network of connected separation cells, typically called Burgers networks and for example used for the generation of gradient hydrogels [304] and to enhance standard column gradient separation with intrinsically set gradients [242]. As shown in chapters 3 and 5, the fractionation aspect is boosted for connected heat-flow chambers. In a thermodiffusive setting, thermophoresis accumulates species selectively in each cell, where the diluted upper part is transported to one side and the accumulated part to the other column of cells.

### 5.4.2 Thermogravitational desalination

As shown in chapters 4 and 5, salts are strongly accumulated in thermal gradients. For the origins of life, the up-concentrated (bottom) fraction is of most interest as there, for instance, magnesium or phosphate ions are overrepresented. In contrast, for an industrial

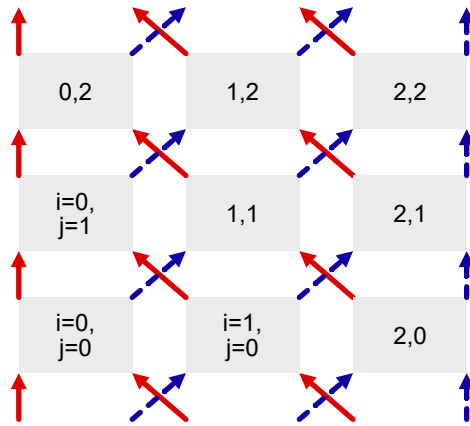


Figure 5.8: Example of 2D burgers network.

application, the upper fraction with depleted salinity is highly useful. The depleted concentration of ions can be observed for instance in the publication from chapter 5 in appendix A [3] where after 3 connected chambers sodium levels are damped 25-fold and magnesium levels approximately 250-fold (see Figure 5.9).

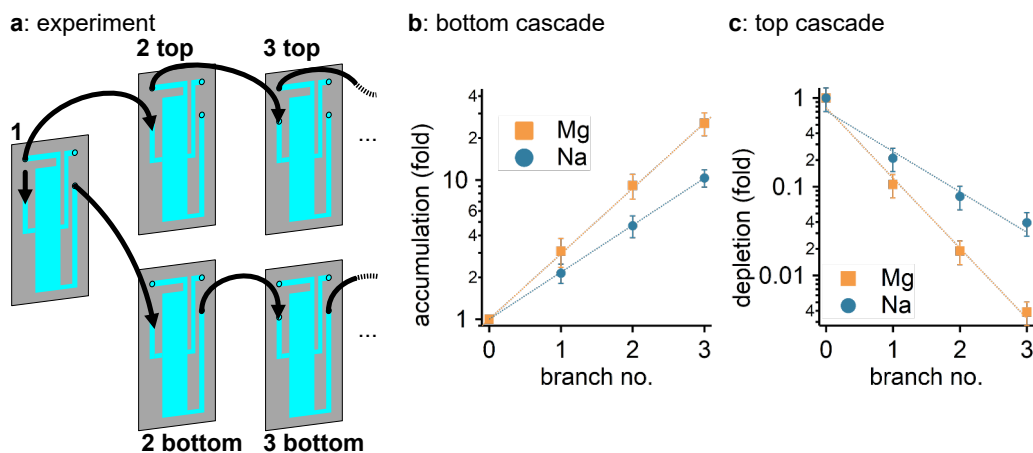


Figure 5.9: Thermogravimetric salt concentration and desalination. **(a)** Cascades of thermo-microfluidic chambers further increase the absolute concentration/depletion. **(b)** For instance, when feeding the bottom outlet into the next chamber and so on, ions are highly concentrated. **(c)** The same is true for the top outlet, leading to strong thermogravimetric desalination (adapted from [3]).

Based on the same effect, Xu *et al* recently showed that thermogravimetric desalination [303] can slowly desalinate sea water but needs many meters of connected channel. However, this study used a temperature gradient parallel to gravitation which leads to highly weakened accumulations. Using flows over pores or against accumulation (see chapter 4) or separating flows (see chapters 5-6) could massively increase desalination efficiency and would be possible to implement for instance in proximity to factories where large amounts of heat are produced as by-product. The same process could inherently also be used to remove organics or other non-desirable substances from water, as most substances will have a sufficiently large Soret coefficient (see chapters 3 and 6) and could even be applied for gaseous selection [305].

# Chapter 6

## Formation mechanism of thermally controlled pH gradients

This chapter corresponds to the paper from Matreux, Altaner, Raith, *et al.* published in *Communications Physics* in 2023 (appendix B) [4].

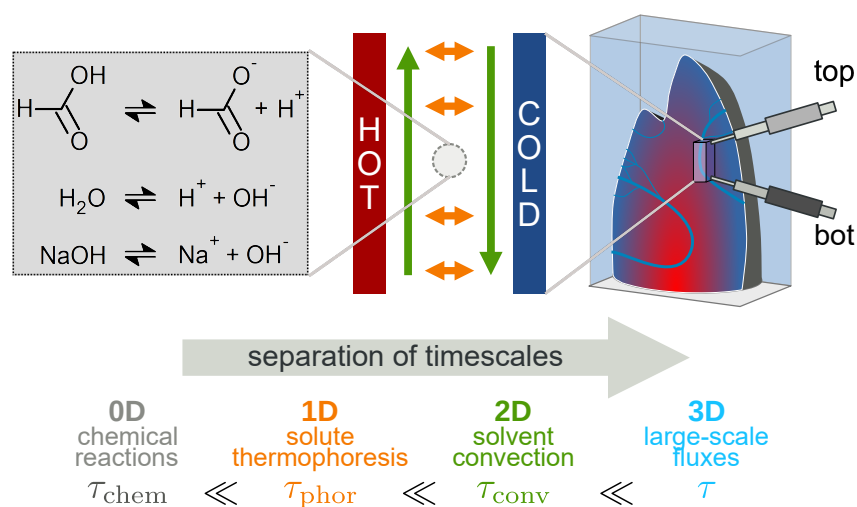


Figure 6.1: Selective accumulation of solutes drives pH gradients in simple, prebiotically relevant acid-base mixtures such as the model system formic acid and sodium hydroxide. The separation of timescales which is also reflected in the different dimensionalities allowed the formulation of a theoretical framework that was experimentally validated (adapted from [4]).

## 6.1 Introduction

Life on Earth is a non-equilibrium phenomenon that requires chemical gradients across biomembranes to maintain its working state. One well-known example are proton gradients [306], which are used to produce the central energy currency ATP [307]. Modern cells create such gradients with the help of sophisticated membranes and proton pumps, storing chemical energy obtained during photosynthesis or oxidation of organic compounds. The formation of local chemical gradients was presumably also a prerequisite for life in its early stages. Otherwise, early replication or metabolism would have come to an instant standstill. The question remains open as to which processes might have driven the formation of non-equilibria without membranes and complex machinery.

In the "RNA world" hypothesis, the autocatalysed replication of RNA is based on the template production of a complementary strand and its subsequent separation from the template to start a new round of replication. Interestingly, it turns out that separation is comparatively hard to achieve. This manifests in high melting temperatures which might not have been accessible in prebiotic environments or could have led to strand hydrolysis. Worse still, as introduced in the previous chapter, most currently known RNA enzymes require high amounts of salt to ensure proper folding into the functional state. These high salt concentrations however lead to even higher hydrolysis rates. A possible solution to this issue was presented by Mariani and co-workers [308]. They could show that lowering the pH by 3.5 units resulted in a drop of the melting temperature of 30 K even in the high salt regime required by RNA enzymes. Accordingly, the replication of RNA strands could be achieved by cycling the local pH between a bound and unbound state at low temperatures, thus avoiding the hydrolysis of RNA strands.

pH oscillations are also beneficial for other chemical reactions relevant to the origins of life. One example is the synthesis of phosphoroaminonitriles on the way to amino acids via (Phosphoro-)Strecker reactions, as shown by Ashe and co-workers [226]. Varying pH conditions may also have helped to avoid the destruction of nucleosides during their synthesis steps in for example acidic environments [309] and could have enhanced the functional repertoire of ribozymes [279]. The effects of pH changes on montmorillonite clay are well known [310] as well as changes of the strength of adsorption of nucleotides and similar molecules changes with pH [163], giving access to the pH-driven selective binding of for example purine over pyrimidine nucleotides.

On an early Earth, however, the question arises how to create and sustain large pH gradients and drive pH cycles on a small scale without the complex, protein-driven machinery found in modern cells. This has been investigated in oxidation reactions in metallo-complexes [311], which allows the possibility of establishing pH gradients locally across membranes as well as in the context of (alkaline) hydrothermal vents [129,135,312], for instance to provide a prebiotic proton-motive force to drive early metabolisms [313]. Here, it has been reported that pH gradients can lead to the precipitation of different minerals [134,136] and could be able to generate potential differences of 180 mV and greater, driving carbon fixation [135–137].

In a geothermal setting, it was shown that temperature differences across micron-sized pores form pH gradients of 2 units spanning across few millimeters [212]. Considerable pH gradients were found for various buffers, including prebiotically plausible amino acids as buffer agents.

In this project, we derived an analytical model of a coupled drift-diffusion reaction system that can predict the formation of pH gradients driven by thermal gradients and



experimentally validated the findings. For this, we used a prebiotically relevant acid-base system, formic acid and sodium hydroxide, thus a weak acid which only has two protonation states and a strong base which will remain dissociated under the relevant pH conditions.

**Why formic acid and sodium hydroxide?** The formation of formic acid under early Earth conditions has been reported by Miller [301], from CO [314] and in alkaline solution via the Cannizzaro reaction [302]. The synthesis of formic acid from CO<sub>2</sub> has been described with and without ferrous sulfate [315], by hydrogenation in acidic medium [316] and under catalysed photoelectric reduction [317]. Furthermore, the hydrolysis pathway of HCN to formamide and formic acid is known [230], linking to formamide-based reactions [318]. The formation of formamide from simple compounds such as NH<sub>3</sub>, formic acid, formic acid ester derivatives, CO and alcohols, as well as the reaction of formamide to thymine in the presence of titanium dioxide with a formic acid-mediated reduction step have been proposed [319]. Further roles of formic acid include for instance the conversion of uracil to thymine [320], as reagent in the formation of FaPys from aminopyrimidines [321], as base material for the formation of pyruvic acid [302,322] and together with formaldehyde in the methylation of amines [323]. The existence of formic acid has been reported on comets [310,324–327] and has been supposed to be plausible on primitive Early Earth [301,320]. The used base, sodium hydroxide, is present in oceans and various environments [42–44].

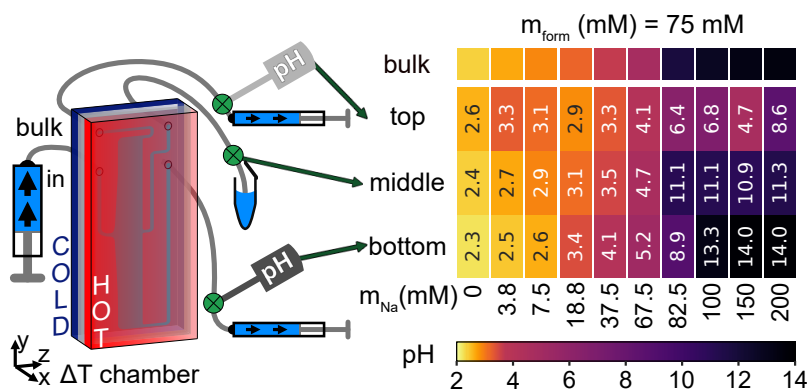


Figure 6.2: The experimental setup is shown on the left, using one inflow syringe to push a premixed solution of formic acid and sodium hydroxide through the thermo-microfluidic chamber. Via three outlets (the top and bottom outlets controlled by syringe pumps), the thermally induced pH gradient is extracted and can be analysed by standard pH meters. On the right side, the measured values for 75 mM formic acid and varied sodium hydroxide concentrations are shown, clearly showing the inversion and strong changes in amplitude of the gradient between top and bottom part of the chamber (adapted from [4]).

## 6.2 Experimental results

Based on the theoretical framework developed in the Gerland group (TU Munich) by Bernhard Altaner and Johannes Raith, we aimed to experimentally validate the predictions and explore the different features. The framework used an approach that allows a generalized analysis and predictions of outcomes of heat flow experiments

involving an arbitrary amount of species being subject to arbitrary chemical reactions. In the adiabatic limit of fast reactions, this allows for the derivation of expressions to predict the magnitude and direction of chemical gradients at the interplay of a multitude of species.

As pH dependent, ratiometric fluorescent dyes [212] only allow the measurement of pH over a limited range and can be chemically damaged or altered by the solution, we implemented a continuous flow system that allows the usage of reliable pH meters. Throughout the experiment, the sample is pushed into the thermal chamber where it is separated into three parts that are extracted at a well-defined outflow ratio of 12 % (top), 76 % (middle) and 12 % (bottom), see Figure 6.2. The timescale of thermal accumulation and the protonation reaction is fast compared to the extraction, which results in a quasi-in-situ measurement of the pH (see Figure 6.1).

The stocks of acid and base were titrated using ion chromatography water. For each stock, the pH value was measured prior to the experiment (see "bulk" in Figure 6.2). After loading the sample into the inlet tubing, the thermal gradient and the syringe pumps were switched on simultaneously so that the sample could enter the thermal chamber during active thermal accumulation. After sufficient sample for pH measurement was gathered in the outlet tubings, the temperature gradient was switched off and the samples were recovered for subsequent measurement using a low-volume pH meter (see chapter 2). The resulting values are shown in Figure 6.1 for the different fractions.

From this, the pH difference between top and bottom fraction was calculated (i.e.  $\text{pH}_{\text{top}} - \text{pH}_{\text{bottom}}$ ) and plotted in Figure 6.3 (blue data points). The experimental data showed to be in good quantitative agreement with the theoretical results (orange lines, for details on the derivation see appendix B).

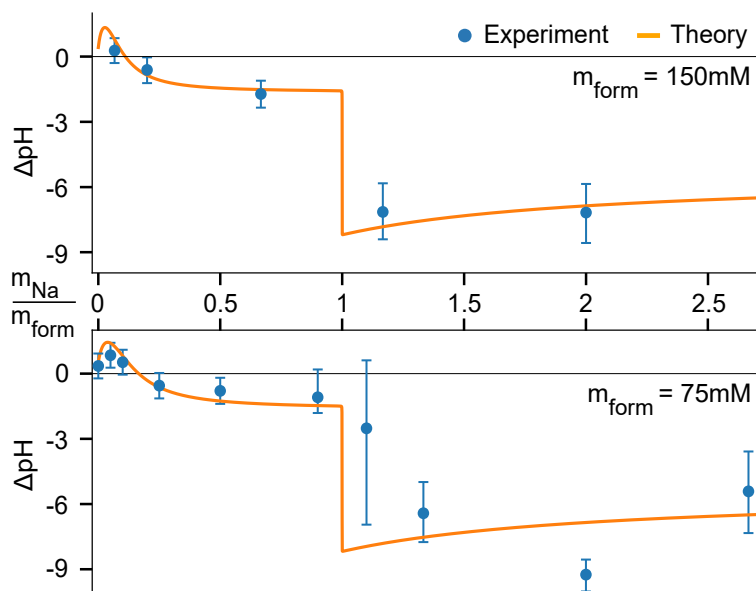


Figure 6.3: Resulting pH gradients. Both for 75 mM and 150 mM formic acid, the experimental results (blue) show to be in good agreement with theoretical results (orange lines) (adapted from [4]).

## 6.3 Selective retention of molecules in a flow setting

**Background** In this project, we designed the experimental setup to determine the pH value as good as possible inside the heat flow cell. For this purpose, the pH values were measured with a standard laboratory pH meter and no pH-dependent dyes were used, which are not designed for use in these extreme temperature conditions and are not compatible with measurements in the entire pH range. Since measurement directly inside the cell using a pH meter is not possible due to the small dimensions of the microfluidic system, we slowly and continuously extract the cell volume at the top, middle and bottom of the cell respectively to obtain the necessary measurement volume. By splitting the outflow into three portions as mentioned above and balancing the outflows with respect to each other, the cell volume is split into three fixed volume portions, of which the contents are extracted through the respective outlet. At the same time, we allow the appropriate amount of stock solution to flow through the input channel so that the cell is completely filled with fluid at all times. The aim of the considerations described below was now to keep the effects of this slow drift flow on the actual experiment as small as possible and thus to obtain an unbiased picture of the pH distribution inside the cell.

**Residence time** An important parameter for describing this situation is the so-called residence time, which indicates how long a volume element introduced into the cell by the drift flow remains in the cell on average until extraction. If this residence time is greater than the relaxation time of the accumulation process occurring in the heat flow cell, i.e. if the drift flow is sufficiently small, it can be assumed that the accumulation remains essentially undisturbed as discussed in the Supplementary Information of appendix B. If the drift flux is correspondingly too fast, the accumulation will be disturbed (see also the flow speed variation in the prior chapter). The following problem arises with the extraction at the lower outlet: If the outlet is placed at the level of the bottom of the cell, it would always lead to a diffusive loss of accumulated material. In our experiment, we therefore placed the exit hole for the lower output channel sufficiently high (as shown in Figure 6.3). However, this requires the to-be extracted material to overcome a thermogravitational accumulation in the exit channel, since its vertical part has a convection flow and thermophoresis similar to the main chamber. Thus, if the drift velocity through this channel is too low, the material to be extracted will remain at the bottom of the heat flow cell and cannot be recovered (see for example chapter 4.4 where we use this retention as selection pressure). The situation here is thus exactly the inverse of the above consideration, so that a trade-off must be found between undisturbed extraction and the lowest possible retention of the material to be extracted in the exit channel.

These considerations made us choose an inflow speed of 3.28 nl/s. The resulting residence time was validated in a static trap by measurements with a ratiometric dye for a similar molecule. In order to avoid a too high retention of the material, we chose an outflow speed of 0.39 nl/s, thus averaging over the bottom-most 12%. The value was still kept relatively low to keep as close as possible to the maximal pH difference present inside the heat flow cell as larger values would lead to significant averaging. As shown in Figure 6.3, this seems to have introduced a more substantial error bar for the value close to equimolarity which can be explained by a stability consideration as introduced in the Supplementary Information of the publication (see appendix B).

**Definition of retention** We tried to quantify this trade-off by first having a look at the bottom-trap concentrations at the bottom of the chamber, then analyse the changes in the exit channel induced by thermogravitational accumulation for which we introduced a step factor  $\kappa_i$  of species  $i$ , determined by finite element simulation. This step factor is defined as

$$\kappa_i = \frac{c_{i, \text{bottom out}}}{c_{i, \text{bottom trap}}} \quad (6.1)$$

with the bottom-trap concentration  $c_{i, \text{bottom trap}}$  at the bottom of the trap and the outflow concentration  $c_{i, \text{bottom out}}$  at the outlet of the trap. This allows us to calculate effective outflow concentrations (measured in our experimental setup) and relate this to the pH measured accordingly.

**Initial pH and concentrations** For a fixed concentration of formic acid (in the following 0.075 M will be used where not explicitly stated otherwise) and varying amounts of sodium hydroxide, the initial pH was calculated. These conditions represent the situation at the bottom of the chamber, thus after the accumulation and establishment of the pH gradient described by the theoretical framework, but before the outflow process. For all graphs, the quantities will be plotted against  $\frac{c_{\text{NaOH}}}{c_{\text{HCOOH}}}$  (and thus "equivalents" of sodium hydroxide and not concentrations) to make it more intuitive.

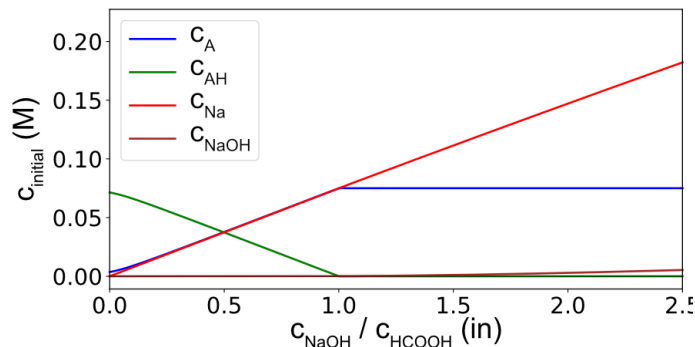


Figure 6.4: Initial concentrations of different species after equilibration for 0.075 M formic acid and varying equivalents of sodium hydroxide, calculated from the initial pH via Henderson-Hasselbalch equation and conservation of moieties.

Via Henderson–Hasselbalch equation, for all pH values and for fixed moieties of formic acid and sodium hydroxide, the initial concentrations at the bottom of the trap of each species can be calculated, shown in Figure 6.4, exemplarily written in Equation 6.2.

$$\text{pH} = \text{p}K_{a, \text{formic acid}} + \log_{10} \left( \frac{C_{\text{formate}}}{C_{\text{formic acid}}} \right) \quad (6.2)$$

**Soret and diffusion coefficients** We used these concentrations for the finite-element simulations. These in addition required the Soret and diffusion coefficients of all species involved which are shown in Table 6.1.

The Soret coefficients of the uncharged species are not found in literature but (after comparison to the Soret coefficients of charged and uncharged types from similar species [212]) are assumed to be an order of magnitude smaller than the Soret coefficient of their corresponding free form.

Species $j$	Charge	$S_{T,j}$ [1/K]	$D_j$ [ $10^{-9} m^2/s$ ]
OH <sup>-</sup>	-1	0.02327 [300]	5.273 [328]
H <sup>+</sup>	+1	0.01809 [300]	9.311 [328]
COOH <sup>-</sup>	-1	0.0055 [329]	1.454 [328]
Na <sup>+</sup>	+1	0.00468 [300]	1.334 [328]
HCOOH	0	0.00055	1.49 [330]
NaOH	0	0.0004	1.49

Table 6.1: Values of Soret and diffusion coefficients.

**Finite-element simulation** The full 3D simulation of the outflow process was done using finite-element software (COMSOL 5.4). For this, both the full heat flow cell geometry and a replication of the bottom outflow channel were analysed (shown in Figure 6.5).

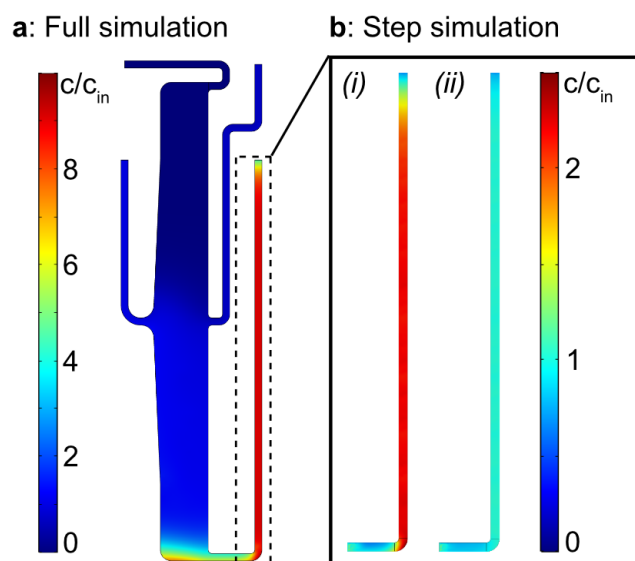


Figure 6.5: Simulation of thermophoretic retention in a flow (results exemplarily shown for formate). (a) Simulation of full flow-through cell. A continuous inflow with defined flow rate is supplied through the left inlet. Top and bottom outlet pull out material at 12% of the inflow volume rate. A clear accumulation through the bottom outflow channel is visible with the highest concentration retained at the bottom. (b) Outflow channel geometry as created for the finite-element simulation including the bottom arm of the full geometry for two different Soret coefficients. (i) shows results assuming a Soret coefficient of  $5.5E-3$  1/K, (ii) for  $1.25E-3$  1/K. Again, not all concentration accumulated in the arm reaches the output. This effect is stronger for higher Soret coefficients due to enhanced accumulation.

We chose to analyse the effects of the competition in the outflow channel via a replicate of the lower channel as we try to quantify the retention caused by the experimental procedure. The main was to understand what happens between the lower edge of the trap and the measurement point (thus the end of the bottom channel). As the accumulation also drives an up-concentration, we will analyse potential concentration-dependent factors later.

To reproduce the experimental situation, the modules "heat transfer in solids", "laminar flow" and "transport of diluted species" were used. In the stationary state

and under assumption of insulation, the heat transfer is calculated from

$$\rho \cdot C_p \cdot \mathbf{u} \cdot \nabla T + \nabla \cdot (-\mathbf{k} \cdot \nabla T) = Q \quad (6.3)$$

with  $\rho$  the density,  $C_p$  the specific heat capacity,  $\mathbf{u}$  the velocity of the fluid,  $T$  the temperature,  $\mathbf{k}$  the thermal conductivity  $k_{\text{H}_2\text{O}} = 0.62 \frac{\text{W}}{\text{mK}}$  of water and  $Q$  the heat flow. In the experiment, temperatures on cold and hot side are measured by a thermistor and a IR camera respectively (as described above), giving us the lateral temperature distribution. The result is then coupled to the Navier-Stokes equation:

$$\rho(T) (\mathbf{u} \cdot \nabla) \mathbf{u} = \nabla \cdot \left[ -p + \eta(T) (\nabla \mathbf{u} + (\nabla \mathbf{u})^T) - \frac{2}{3} \cdot \eta(T) (\nabla \cdot \mathbf{u}) \right] - \mathbf{e}_y \cdot \mathbf{g} \cdot \rho(T) \quad (6.4)$$

with the temperature dependent density  $\rho(T)$  and viscosity  $\eta(T)$ , the velocity vector of the solution  $\mathbf{u}$ ,  $p$  the local pressure,  $\mathbf{e}_y$  the unit vector in y-direction and  $\mathbf{g}$  the gravitational acceleration. Setting the fluid to compressible and non-slip boundaries except for in- and outlet, this yields a solution for the velocity field  $\mathbf{u}$ . To couple diffusion and thermophoresis to the velocity field, a transport component was added as shown in Equation 6.5.

$$\nabla \cdot (-D_i \nabla c_i + (\mathbf{u} + S_{T,i} D_i \nabla T) c_i) = 0 \quad (6.5)$$

For each species  $i$ , the diffusion coefficient ( $D_i$ ), the local concentration ( $c_i$ ) and the Soret coefficient ( $S_{T,i}$ ) are plugged in. The values for  $D_i$  and  $S_{T,i}$  are taken from literature (see Table 6.1).

Using this simulation, we can obtain the concentration values required for the step factor  $\kappa_i$  for all species. We found a step factor of 0.781 for formic acid ( $\text{HCOOH}$ ), 0.683 for formate ( $\text{HCOO}^-$ ), 0.696 for sodium ( $\text{Na}^+$ ) and 0.782 for sodium hydroxide ( $\text{NaOH}$ ). Taking the example of formic acid, 0.781 means that 78.1% of the formic acid present at the bottom of the thermal trap arrives at the outlet. The step factors of hydronium and hydroxide ions are  $< 2\text{E-}5$ , meaning that neither of those leave the trap. This was expected, as they have very high Soret and diffusion coefficients and will self-(de-)ionize to establish local electroneutrality.

As the uncharged species (formic acid and sodium hydroxide) are less affected by the counter trap, we expect potential changes between the pH at the bottom of the chamber and in the outlet to be determined by the competition between charged sodium and charged formate. This makes it probable that the strongest effects occur around 1 equivalent (thus  $c_{\text{NaOH}}(\text{in}) = c_{\text{HCOOH}}(\text{in})$ ) as there a massive pH change happens and only the charged types of each moiety are present.

Upon varying the Soret and diffusion coefficients of formate in our simulation (shown in Figure 6.6), we observe a (falling) linear pattern for increasing Soret coefficients, intersecting the given step factor of sodium at  $4.9\text{E-}31/\text{K}$ . The Soret coefficient of formate is supposed to be in a similar regime as other ions of the same size and charge, leaving us with the region between  $1 - 6.5\text{E-}31/\text{K}$ . For the diffusion coefficient, variation in the possible range does not lead to a massive change in the step factor of formate.

**Outflow concentrations and pH** Using these step factors, outflow concentrations for all species are calculated by multiplying the concentration of each species with its step factor. The concentrations then allow us to calculate the pH at every point (similar to the calculation done to find the initial pH).

This gives us the results shown in Figure 6.7. We characterize this difference between the situation at the bottom of the trap and the measured outflow by  $\delta\text{pH}$ :

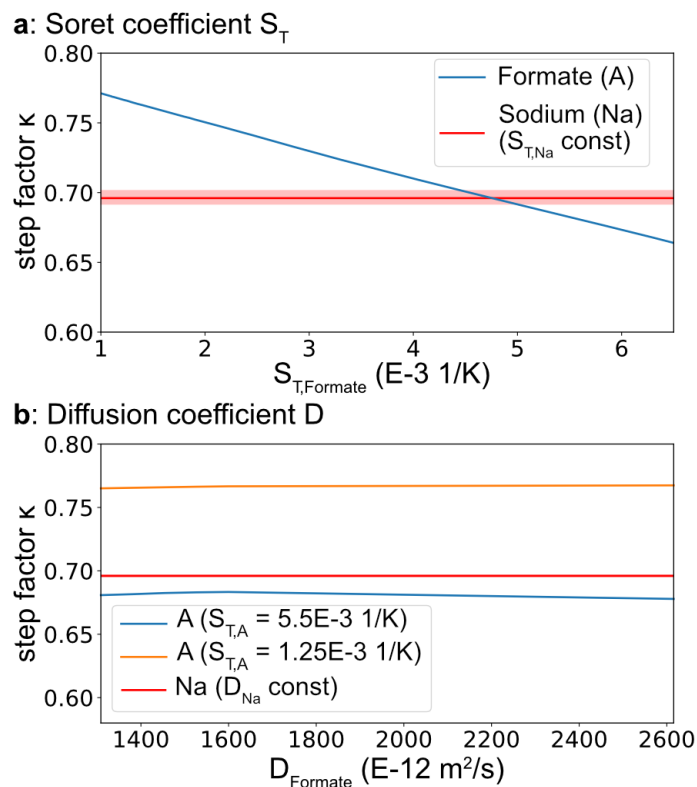


Figure 6.6: Step factor for varying  $S_{T,Formate}$  and  $D_{Formate}$ . (a) Step factor of formate (blue) for a range of Soret coefficients compared to the step factor of sodium (red) for its Soret coefficient with 5% error. (b) Step factor of formate (blue) for a range of diffusion coefficients for two different Soret coefficients, compared to the step factor of sodium (red).

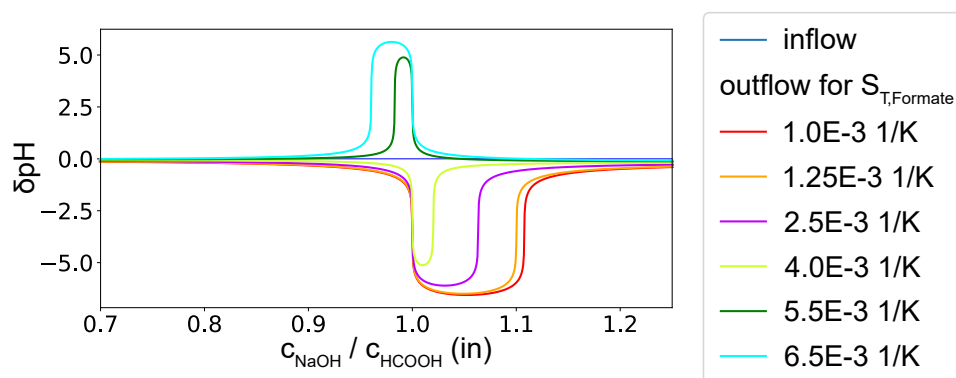


Figure 6.7: Comparison of inflow and outflow pHs for different equivalents of sodium hydroxide (always with 0.075 M formic acid). The differences from the inflow pH are depicted, showing different signs, broadnesses and amplitudes for different Soret coefficients of formate

$$\delta pH = pH_{out} - pH_{in} = pH_{measured}^{bottom} - pH_{trap}^{bottom} \quad (6.6)$$

As expected, the results reflect the competition between sodium and formate and thus show different effects when trapping of formate is stronger than when sodium is more strongly accumulated. This leads to a situation where, between 1 and 1.1 equivalents

of sodium hydroxide, a much lower pH is detected than present at the inflow (thus the bottom of the trap).

**Concentrations of species** As described in chapter 2, we measured outflow concentrations by ion chromatography as an estimation of the concentrations for the different measurements. This yielded accumulations of around 3-4 fold at the outflows, thus still higher concentrations at the bottom of the trap. However, as shown in Figure 6.8, this does not change the broadness of the effect and only leads to small deviations in amplitude.

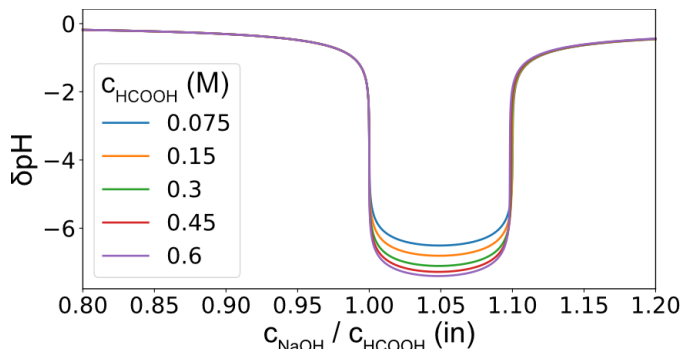


Figure 6.8: Difference in pH for multiple initial concentrations of formic acid for  $S_{T,Formate} = 1.25E-31/K$ , showing little concentration dependence.

In summary, this clearly shows a selective retention of material in the outflow which also strongly affects the outflow pH. The exposure of the accumulated solution to another trapping process, this time with flow against accumulation, leads to even stronger and more selective retention.

## 6.4 Outlook

Interesting future perspectives include the further analysis of 2-dimensional salt and pH gradients which inherently occur as the accumulation of the ionic species drives the pH gradient. This could provide a natural habitat for RNA as partially introduced in the previous chapter but with an additional melting/reannealing cycle or a protective environment against hydrolysis. Cycling of proto-cellular systems through various pH and salt conditions will open the door to studies on content reshuffling [331] and observations of coacervate properties in thermal gradients. An additional dimension beyond ionic and pH gradients would be redox gradients, which are considered to be important in a geo-evolutionary context [332–334], for instance for replication processes [335] and activation.

The selective retention shows the strong effect of a flow-accumulation competition with a geologically highly relevant geometry as it only requires a flow against gravity with an orthogonal temperature gradient; the inflow can also come directly from below. Inherently, this effect is not limited to pH gradients but was also used in other projects, such as the study of chemical reaction networks (chapter 3.3) and selective precipitation of minerals (chapter 4.4). In addition, it provides an interesting setting to apply thermogravitational desalination (chapter 5.4) and maximize selective retention of all ions.



# Appendix A

## Heat flows in rock cracks naturally optimize salt compositions for ribozymes

Published in *Nature Chemistry* in August 2021.

**Matreux, T.\***, Le Vay, K.\*, Schmid, A., Aikkila, P., Belohlavek, L., Çalışkanoglu, A.Z., Salibi, E., Kühnlein, A., Springsklee, C., Scheu, B., Dingwell, D. B., Braun, D., Mutschler, H. & Mast, C. B.

Heat flows in rock cracks naturally optimize salt compositions for ribozymes

*Nature Chemistry*

**13**, 1038–1045

2021

<https://doi.org/10.1038/s41557-021-00772-5>

According to Springer Nature, the ownership of copyright in original research articles remains with the author, who retains the non-exclusive rights to reproduce the contribution in whole or in part in any printed volume (book or thesis) of which they are the author(s).

As the Supplementary Information contains numerous pages of source images of gels, they are omitted here and can be found online.



# Heat flows in rock cracks naturally optimize salt compositions for ribozymes

T. Matreux<sup>1,5</sup>, K. LeVay<sup>2,5</sup>, A. Schmid<sup>1</sup>, P. Aikkila<sup>1</sup>, L. Belohlavek<sup>3</sup>, A. Z. Çalışkanoglu<sup>3</sup>, E. Salibi<sup>2</sup>, A. Kühnlein<sup>1</sup>, C. Springsklee<sup>3</sup>, B. Scheu<sup>3</sup>, D. B. Dingwell<sup>3</sup>, D. Braun<sup>1</sup>, H. Mutschler<sup>4</sup> and C. B. Mast<sup>1</sup>

**Catalytic nucleic acids, such as ribozymes, are central to a variety of origin-of-life scenarios. Typically, they require elevated magnesium concentrations for folding and activity, but their function can be inhibited by high concentrations of monovalent salts. Here we show that geologically plausible high-sodium, low-magnesium solutions derived from leaching basalt (rock and remelted glass) inhibit ribozyme catalysis, but that this activity can be rescued by selective magnesium up-concentration by heat flow across rock fissures. In contrast to up-concentration by dehydration or freezing, this system is so far from equilibrium that it can actively alter the Mg:Na salt ratio to an extent that enables key ribozyme activities, such as self-replication and RNA extension, in otherwise challenging solution conditions. The principle demonstrated here is applicable to a broad range of salt concentrations and compositions, and, as such, highly relevant to various origin-of-life scenarios.**

Several origin-of-life hypotheses posit that nucleic acid catalysis and information storage led to the first self-replicating system capable of open-ended evolution. Foremost among these is the RNA world hypothesis<sup>1,2</sup>, but hypotheses centred on ‘pre-RNA’ worlds<sup>3</sup> and mixed nucleic acid systems<sup>4</sup> are also widespread. Nucleic acid enzymes can catalyse a broad range of reactions in solution and are able to tolerate a wide range of conditions thanks to their resistance to irreversible aggregation, but are typically less powerful than their modern protein-based counterparts. To realize their full catalytic potential, nucleic acid catalysts require specific environmental conditions that promote folding and substrate binding while they limit hydrolytic degradation. In particular, wet-dry cycling and freezing were shown to dramatically enhance nucleic acid enzyme activity, and to facilitate catalysis in otherwise inactive systems<sup>5</sup>. However, almost all ribozyme systems in solution require a high magnesium salt concentration (10–200 mM) to fold into their active state<sup>6–10</sup>, and some require site-specific divalent metal ions as a catalytic cofactor. These requirements conflict with the susceptibility of RNA to hydrolysis catalysed by metal ions, especially at high temperatures and high pH. A further challenge is that not all salts favour the function of ribozymes. For example, ubiquitous monovalent salts can displace the divalent metal ions required for folding and activity<sup>11</sup>. This effect can occur when the sodium ion concentration exceeds the magnesium ion concentration by as little as a factor ten<sup>11–15</sup>. Ribozymes that rely on Mg<sup>2+</sup> as a catalytic cofactor, a group that includes prebiotically relevant polymerases and the R3C self-replicator, can be particularly affected by sodium ion inhibition<sup>13</sup>. It is therefore important to identify environmental mechanisms through which the requirement for extremely high concentrations of divalent metal ions can be circumvented, and through which inhibition by monovalent ions can be ameliorated.

Accordingly, the question arises as to which environments on early Earth might have provided suitable salt conditions for such prebiotic processes. One geologically probable process that

produces saline environments is the leaching of salts from basalt. As a primary partial melt of the Earth’s mantle, basalt is one of the most abundant rock types to be expected in the Earth’s early crust, as well as the crust of other terrestrial planets in our solar system<sup>16</sup>. However, the solutions that result from basalt leaching are typically dilute, with MgCl<sub>2</sub> concentrations below a few hundred micromoles, whereas concentrations of monovalent sodium salts can be up to a factor of ten greater than those of the leached magnesium, as shown in this work. Salt concentrations in the high millimolar range have been found in carbonate lakes which, due to their high concentrations of dissolved phosphate, are also promising environments for prebiotic processes, such as nucleotide synthesis<sup>17</sup>. However, the concentration of monovalent sodium salts in these environments can be up to 1,000-fold higher than that of magnesium salts, which again precludes an effective ribozyme function.

Wet-dry cycles were previously proposed as a solution to low salt concentrations, in which up-concentration is driven by evaporation<sup>18,19</sup>. This mechanism, although powerful, does not allow the relative concentration ratio of solution components to be altered. In addition, salt concentration increases exponentially with decreasing liquid volume, which may lead to extremely high divalent metal ion concentrations that promote RNA hydrolysis. The problem of RNA hydrolysis is mitigated during up-concentration in frozen water ice above the eutectic point, but the ratio of monovalent to divalent salt ions in solution is largely preserved in the remaining liquid phase. Furthermore, high initial concentrations of salts generally reduce the magnitude of up-concentration as less volume reduction by water ice formation is required to reach the equilibrium salt concentration that prevents further freezing<sup>20–22</sup>.

In this work, we show how these problems can be solved in conditions that are sufficiently far from equilibrium, but which should still have occurred frequently enough on the prebiotic Earth to have had a relevant effect. We investigated how heat fluxes across small water-filled cracks in rock can change both the absolute

<sup>1</sup>Systems Biophysics, Ludwig Maximilians University Munich, Munich, Germany. <sup>2</sup>MPI für Biochemie, Biomimetische Systeme, Martinsried, Germany.

<sup>3</sup>Earth and Environmental Sciences, Ludwig Maximilians University Munich, Munich, Germany. <sup>4</sup>TU Dortmund University, Dortmund, Germany. <sup>5</sup>These authors contributed equally: T. Matreux, K. LeVay. ✉e-mail: [hannes.mutschler@tu-dortmund.de](mailto:hannes.mutschler@tu-dortmund.de); [christof.mast@physik.uni-muenchen.de](mailto:christof.mast@physik.uni-muenchen.de)

concentrations and the concentration ratios of different salt species simultaneously. Heat flow as a driving factor is interesting, because heat generation is a near ubiquitous process in such scenarios. Traversing water-filled cracks with a size of some 100  $\mu\text{m}$ , such heat flows can drive both thermal microconvection and thermophoresis, two processes which, in combination, can concentrate dissolved molecules depending on their charge, size and interaction with the surrounding solution<sup>23–25</sup>. It was previously shown that such systems are applicable in the context of the origin of life as they, for example, drive exponential replication in DNA-based model systems<sup>26,27</sup>, create local pH differences of several units<sup>28</sup> or concentrate formamide<sup>29</sup>. At air–water interfaces, heat fluxes can enrich, crystallize, dry, phosphorylate and encapsulate prebiotic molecules, enhance ribozyme catalysis<sup>30</sup> and even facilitate duplex melting and strand release by cyclically varying the salinity via recondensation<sup>31</sup>. Such heat flow cells were also used to enrich fatty acids locally to form protocell-like vesicles<sup>32</sup>.

Here we pursued an interdisciplinary approach. Starting from a geological perspective, we investigated the leaching of salts from basalt, the most common volcanic rock on Earth. Basaltic glass is an ideal material for this prebiotic scenario due to (1) its high alteration kinetics for the efficient liberation of cations, (2) its characteristic high surface area due to quench granulation and (3) efficient pathways for fluid circulation<sup>33–36</sup>. The alteration products of basalt, such as montmorillonite clays, are commonly used in prebiotic scenarios of basalt, but are less suitable as they do not liberate ions into solution in sufficient quantity, and nor do they possess the required microstructure for thermophoresis. We then tested the efficiency of RNA-catalysed ligation reactions in the resulting salt conditions. We use the R3C replicator ribozyme as a model system, as it is the first reported RNA-only self replicator and shares its catalytic mechanism with prebiotically relevant RNA polymerases, which are particularly affected by sodium inhibition<sup>37</sup>. We explored how heat flows can optimize the salt content for these ligation reactions. By locally increasing salt concentrations from the starting conditions obtained from leaching, and by boosting the concentration ratio between divalent and monovalent salts, conditions can be improved to such an extent that RNA-catalysed reactions can take place in otherwise inhibitory environments (Fig. 1).

## Results

**Salt leaching from tholeiitic basalt.** We initially investigated the enrichment of salt-free pure water with salts by geological processes (Fig. 1b). To this end, we mimicked the salt-leaching process by placing basalt samples (Supplementary Table 1) of different sizes, states and masses in different aqueous solvent conditions (Supplementary Method 1) with varying physical conditions of temperature, agitation and leaching time (Fig. 2, Extended Data Fig. 1, Supplementary Table 2 and Supplementary Fig. 1), and determined the concentrations of different salt types using ion chromatography (IC; Supplementary Methods 2 and 3).

As noted above, we focused on tholeiitic basalt in these experiments, and explored two different states of this basalt to understand the effect of the physical and phase states on the leaching process: (1) sampled holocrystalline basaltic rock, which consists of different mineral phases (for example, olivine, pyroxene and feldspars) in a micrometre-scale groundmass of these and other phases, and (2) synthesized glass, remelted from the powdered tholeiite and quenched to a homogeneous amorphous (glassy) state without any crystalline mineral phases (Supplementary Table 1). Initially, the leaching of salts from tholeiitic basalt was investigated by varying the mass of the basaltic glass or rock (Fig. 2b,c, respectively) in a fixed volume (150  $\mu\text{l}$ ) of ultrapure water. The basaltic samples were sieved to a size of 90–125  $\mu\text{m}$ , the temperature was adjusted to 60 °C and the leaching time was set to 36 hours, which should be sufficient to reach the preliminary equilibrium concentration (Fig. 2e).

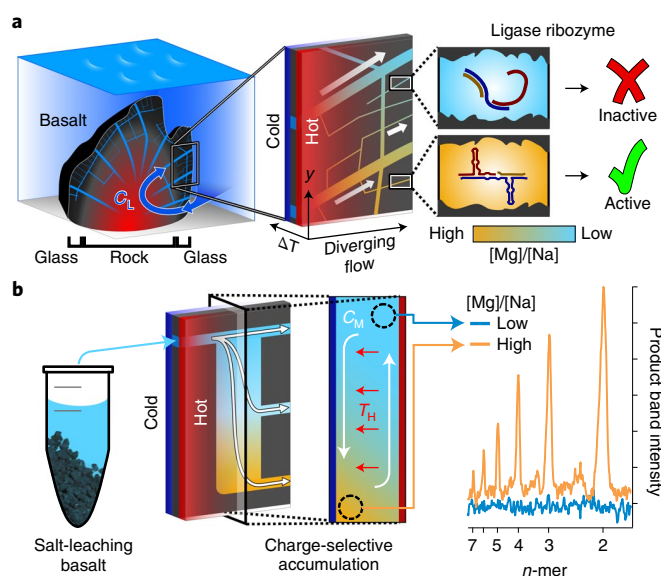


**Fig. 1 | Schematic diagrams of the proposed prebiotic scenario and the experimental set-up. a**, The proposed prebiotic scenario: connected, water-filled cracks in a basaltic complex form a natural microfluidic system. Within this, salt ions leach from the surrounding rock and/or glass into the water, which is continuously replenished by large-scale convection ( $C_L$ ). However, the salt concentration and composition are initially not sufficient to host prebiotic chemistry, for example, RNA enzyme catalysis. Nearby heat sources, such as the core of the basaltic complex, create a heat flux through the water-filled cracks, which leads to a thermophoretic accumulation of the leached salt ions. This process selectively increases the abundance of divalent ions over inhibitory monovalent salts at the bottom of the cracks, where it provides a suitable working environment for ribozymes. **b**, The experimental set-up: the salt leaching from basaltic rock and glass was characterized. The large excess of monovalent ions detected inhibits ribozyme function. The application of a heat flow through a thin sample-containing cell, which mimics water-filled cracks of a basaltic complex, leads to simultaneous convection ( $C_M$ , white arrows) and thermophoresis ( $T_H$ , red arrows), and as a result to the accumulation of divalent ions, which thus creates a suitable habitat for ribozymes. The plot shows the amount of ligated ribozyme product versus product length.

A wider temperature range is covered in Supplementary Fig. 1. The results show that even with a mass ratio of up to 1:1 of basalt to water, the maximum achievable concentrations for sodium salts range from 500  $\mu\text{M}$  (glass) to 1,000  $\mu\text{M}$  (rock), but the amount of magnesium salts remains below 200  $\mu\text{M}$ . The same applied to measurements over a wide particle size range (Fig. 2d). To determine the time at which the salt leaching reached equilibrium, we measured the salt concentrations for 30 mg of basaltic glass with a grain size of 355–500  $\mu\text{m}$  at 60 °C over a period of 423 hours. To check different plausible solution conditions for leaching, we performed this measurement for ultrapure water (MilliQ) and for water with a presumed prebiotic composition<sup>38</sup> (Supplementary Method 1) and thus obtained  $\tau_{\text{pure}} = 30$  h and  $\tau_{\text{prebio}} = 27$  h as time constants from a monoexponential fit (Fig. 2e). Differences in the repeats of measurements  $N$  (Fig. 2d,e) resulted from overlapping datapoints in the series of measurements within the multidimensional parameter space. The previously shown measurements were performed accordingly in this time period. In water with a hydrothermal composition<sup>39</sup>, no measurable leaching of magnesium ions was obtained (Supplementary Table 2). In all the measurements shown, the magnesium concentration remains in the three-digit micromolar range.

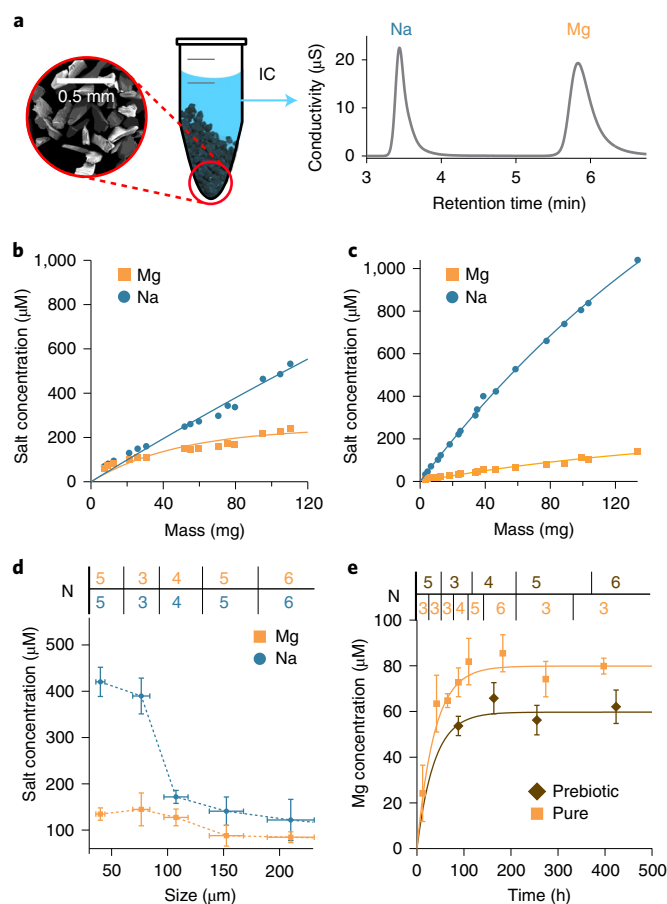


**Fig. 2 | Leaching of salts from basaltic rock.** **a**, Basaltic rock and glass samples were crushed and sieved to different sizes and incubated with a leaching solution (pure or prebiotic water<sup>38</sup>) for several weeks under a wide range of conditions (Extended Data Fig. 1, Supplementary Fig. 1 and Supplementary Table 2). Inset: scanning electron microscopy image. The supernatant was analysed using IC. **b**, Basaltic glass samples with particle sizes of 90–125  $\mu\text{m}$  and a weight of up to 120 mg were leached at 60 °C in 150  $\mu\text{l}$  of pure water (MilliQ) until an equilibrium salt concentration was reached. The sodium concentration exceeded that of the leached magnesium by up to three times, with the latter remaining at low values (200  $\mu\text{M}$ ). Each point corresponds to one measurement and the mean deviation from a simple exponential saturation (line) is  $\overline{\Delta c_{\text{Mg}}} = 31 \mu\text{M}$  and  $\overline{\Delta c_{\text{Na}}} = 70 \mu\text{M}$ . **c**, The same treatment as used for **b** was used to leach salt from basaltic rock samples 90–125  $\mu\text{m}$  in size. The sodium concentration was ten times higher than that of magnesium, the latter being 100  $\mu\text{M}$ . The mean deviation from a simple exponential saturation (line) is  $\overline{\Delta c_{\text{Mg}}} = 20 \mu\text{M}$  and  $\overline{\Delta c_{\text{Na}}} = 46 \mu\text{M}$ . **d**, Size dependence of the leached salt concentrations at 60 °C over 100 h. The total mass of basaltic glass was 30 mg in 150  $\mu\text{l}$  of pure water. The table at the top shows the number of repeats  $N$ . **e**, Characteristic equilibration timescales for leaching glass with pure and prebiotic water at 30 and 27 h, respectively (for rock, see Extended Data Fig. 1 and Supplementary Fig. 1). Error bars calculated from the s.d. from data provided in Supplementary Table 2. The table at the top shows the number of repeats  $N$ .

**Selective concentration of salt ions by thermal gradients.** The results shown in Fig. 2 demonstrate that the resulting sodium salt concentrations clearly exceed the concentrations of the divalent salts under consideration. This situation is not only found here, but in even more extreme but prebiotically relevant environments, such as carbonate lakes<sup>17</sup>. We therefore investigated how a heat flow

through water-filled cracks in a rock complex and the resulting temperature gradients could improve such inhibiting salt conditions to favour prebiotic processes, such as RNA catalysis. Temperature gradients cause two simultaneous effects: thermophoresis and natural convection. The first, thermophoresis, causes the drift of solutes along the temperature gradient, which in the case of ions usually leads to an accumulation on the cold side. The latter, convection, is triggered by the temperature-induced density differences of the solvent and transports the ions along the cold side downwards, where they are concentrated even more. We expect this effect to be more efficient for larger or more highly charged substances due to their stronger thermophoresis<sup>40–42</sup>.

To determine if thermophoresis in a microfluidic system can alter the ionic composition, we prepared salt solutions with compositions found in our leaching experiments and introduced them into a heat flow cell. This cell was defined by a microfluidic structure cut into a 170  $\mu\text{m}$  thick fluorinated ethylene propylene (FEP) film, covered on both sides by a sapphire window. One window was cooled by a cryostat and the other electrically heated so that a linear temperature gradient between 20 and 60 °C prevailed in the cell (Fig. 3a; see Extended Data Figs. 2–4, Supplementary Methods 4–7, Supplementary Figs. 2–6 and Supplementary Table 3 for details). Through four holes in the back sapphire, we applied a drift flow up to 23  $\text{nls}^{-1}$  to simulate a slow, large-scale convection (Fig. 1a). Such small drift flows through the heat flow cell should not interfere with the thermophoretic accumulation, as their velocity is far below that of microscale convection (Fig. 1a). The resulting throughflow into three outlets (top, middle and bottom) allowed us to determine the concentration (bottom) or depletion (top) of the different salt species independently of each other using IC (Fig. 3b). The set-up minimizes surface effects (for example, adsorption) and temperature fluctuations that would prevent the full modelling and understanding of the system, and it geometrically mimics the frequent interconnected cracks in the carapace of a basaltic complex that are subject to thermally driven, slow, large-scale convection. In the outer rim of this carapace, the basaltic magma is usually quenched in a glassy state due to the high cooling rates of the aqueous environment<sup>43,44</sup>. The concomitant high thermal stresses result in the shattering of the outermost magma into small clasts (hyaloclastites) and thermal cracking of the carapace<sup>45,46</sup>.

Results from the IC measurements were compared with a three-dimensional finite element simulation (Extended Data Fig. 3, Supplementary Method 7 and Supplementary Figs. 4 and 5) that uses thermophoretic and diffusive mobilities taken from the literature and therefore does not require any free parameters (Supplementary Table 4). We found the experimental results to be in good agreement within the error ranges and could show a clear separation of magnesium from sodium ions up to a factor of two at the bottom output (Fig. 3c). Accordingly, the upper outlet delivers a solution with a reduced salt concentration by a factor of ten for magnesium ions and a factor of two for sodium ions.

**Effect of salt concentration and thermal accumulation on ribozyme activity.** Next, we examined the dependency of ribozyme catalysis on different salt conditions and tested how activity in the heat flow cell can be improved within an experimental time window of two hours. For more extreme salt conditions, such as those found in carbonate lakes, we extrapolated the findings using a numerical model.

The first ribozyme system we used is a variant of the R3C ligase, which catalyses the 5'-triphosphate-dependent joining of oligonucleotide substrates to form additional copies of itself<sup>7</sup> ( $E_R$  in Fig. 4a; see Extended Data Fig. 5, Supplementary Methods 8–11, Supplementary Fig. 7 and Supplementary Tables 5 and 6 for details). We first sought to investigate the ability of the heat flow cell to rescue ribozyme self-replication in limiting the magnesium

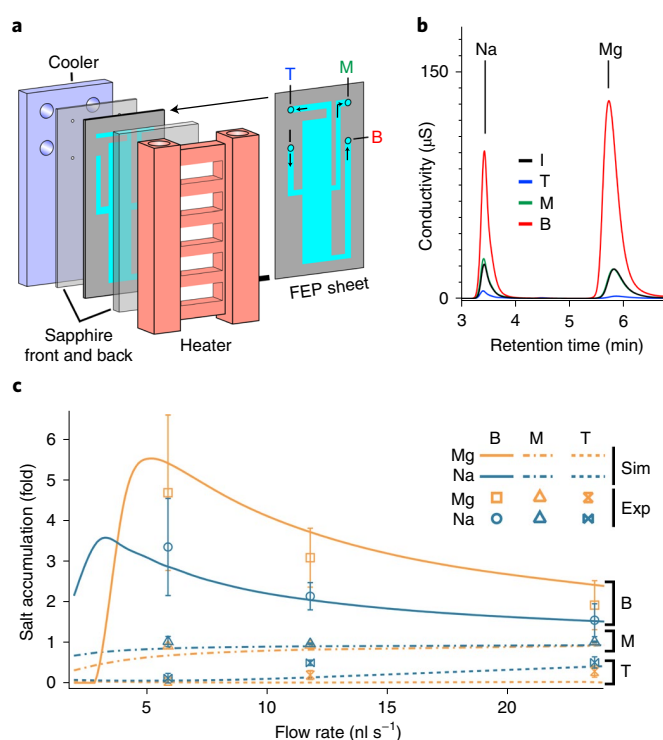


**Fig. 3 | Thermal microfluidic set-up and numerical control.** **a**, For the heat flow cell, a microfluidic structure was cut from a 170  $\mu\text{m}$  thick FEP film and placed between two sapphire plates. The front sapphire was heated by an electric heater (red) and the rear sapphire was tempered by a water-bath-cooled aluminium plate (blue). During the experiment, the samples were injected at a constant flow velocity on one side and simultaneously sampled on the opposite side to create a dynamic flow system that mimics large-scale convection through cracks in natural rock. Access to the microfluidic system was provided by four laser-cut holes in the back of the sapphire, which created one inlet (I) and three outlets (top (T), middle (M) and bottom (B)). **b**, The extracted samples from the different outlets were analysed against standards by IC. **c**, In the numerical model, thermal convection, flow and thermophoresis were simulated in a coupled drift-diffusion system using finite element methods (lines). We were able to reproduce the magnesium and sodium salt concentrations measured experimentally (symbols) in the catchment basins within the error thresholds without using free parameters. The coefficients of thermal and diffusive mobility we used are from the literature<sup>40,41</sup>. Error bars calculated from the s.d. from triplicate measurements, also provided in Supplementary Table 3. Sim, simulation; exp, experiment.

concentrations in the absence of NaCl (Supplementary Fig. 8). As expected, ligation efficiency only increased with high magnesium concentrations under bulk conditions at 35 °C (Fig. 4b,c (lanes 1–6) and Supplementary Fig. 9). Carrying out the same reaction in our heat flow set-up (Fig. 4c, lanes 7–12) strongly increased the ligation efficiency at very low initial  $\text{Mg}^{2+}$  concentrations. Intriguingly, the set-up enabled a small amount of replication even at a 0.25 mM  $\text{Mg}^{2+}$  bulk concentration (lane 8), which is typically insufficient for this type of reaction (lane 2). Greater enhancements relative to the control and reduced hydrolysis were observed at lower magnesium concentrations (Supplementary Fig. 9d,e). For a single cell, the optimal magnesium concentration is 1–2 mM. In this range, moderate enhancement factors lead to final ligation yields that are close to the maximum, but hydrolysis is limited. Taken together, these results clearly show that RNA catalysis can be initiated through ionic enrichment caused by thermophoresis even under limiting magne-

sium concentrations. With regard to the sensitivity of the replicator ribozyme to sodium, we observed a moderate decrease in activity in presence of a tenfold excess of NaCl over  $\text{MgCl}_2$ . In presence of a 1,000-fold excess of NaCl, ribozyme activity was completely abolished (Supplementary Fig. 9).

To test the influence of the different physical scenarios on the RNA ligation efficiency, we compared the simple replicator performance in the heat flow cell, in free solution and in a wet-dry scenario (Fig. 4d,e, respectively; Supplementary Fig. 10). For the latter experiment, we prepared reaction mixtures with different volumes (5, 10, 30 and 60  $\mu\text{l}$ ) and heated them for two hours at 35 or 60 °C. The former temperature corresponds to the optimum solution reaction temperature, the latter to the maximum temperature in the heat flow cell and the incubation time was set to be identical to that of the previous heat flow chamber experiments. During incubation, the cap remained open to allow evaporation, which led to visibly dry (red symbols in Fig. 4d,e) or still suspended samples (black symbols) depending on temperature and volume. The incubated sample was refilled to the initial volume with  $\text{H}_2\text{O}$ , and then the ligation yield and amount of hydrolysed product was determined by urea-polyacrylamide gel electrophoresis (PAGE) (Fig. 4d,e). The temperatures used are plausible for the Archean period, as suggested from oxygen isotopic ratio measurements of Archean marine cherts<sup>47,48</sup>. More recent work suggests a cooler ambient temperature, but even in this case the temperature in drops of liquid can easily reach 60 °C due to solar radiation<sup>49</sup>. The results show that the correct balance of reaction time, temperature and salt content must be achieved for ribozyme activity. For example, if the volume is too large (10–60  $\mu\text{l}$ ), 35 °C is not sufficient for an adequate evaporation and hence accumulation of  $\text{MgCl}_2$  within two hours. At 60 °C, the high temperature and magnesium up-concentration leads to the hydrolysis of RNA and thus loss of function (obtained from the bottom of the gel shown in Supplementary Fig. 10 according to data analysis shown in Supplementary Method 9). Activity enhancement comparable to that of the heat flow cell was only observed with a volume of 5  $\mu\text{l}$  at 35 °C. However, the large variation in activity over three replicates shows that even small, random variations in experimental parameters, such as humidity, can strongly influence the outcome. In general, the heat flow cell provides a stable and reproducible enhancement in activity for larger volumes of material when compared with drying under similar conditions.

Next, we set out to model the effect of thermal gradients and ion composition on the prebiotically relevant synthesis of long RNA molecules from short precursors. To this end, we modified the R3C ribozyme in such a way that it was capable of concatenating short substrate strands (S) into long RNA chains ( $P_n$ ) to investigate the ability of the various environments to promote the formation of longer RNA products ( $E_L$  in Fig. 4f; details in Extended Data Fig. 5, Supplementary Method 8, Supplementary Fig. 7 and Supplementary Tables 5 and 6). In this RNA concatemer ligation assay, we found a substantially higher sensitivity towards sodium, although  $E_L$  and  $E_R$  differ by only five point mutations. Under the optimal bulk conditions at 35 °C in the presence of 1 mM  $\text{MgCl}_2$ , on average about two RNA segments were incorporated into the product chains (Fig. 4g,h, lane 7, and Supplementary Figs. 11 and 12). Under the same conditions in the presence of a tenfold excess of NaCl over  $\text{MgCl}_2$  barely any RNA concatemer ligation activity was detectable (lane 6) and a fourfold increase in  $\text{MgCl}_2$  levels was necessary to achieve the main average product length, albeit with much lower yields (lane 10). With a 1,000-fold sodium surplus, no detectable ligase activity could be observed for any tested magnesium concentrations (lanes 1, 5 and 9, 0.25–8 mM; see Supplementary Table 11 for all the data). We then investigated the influence of temperature gradients on the RNA concatemer ligation system under different ionic compositions. Overall, we observed a higher substrate turnover in the heat flow cell (20–60 °C, no throughflow, two hours of duration; lanes 4,

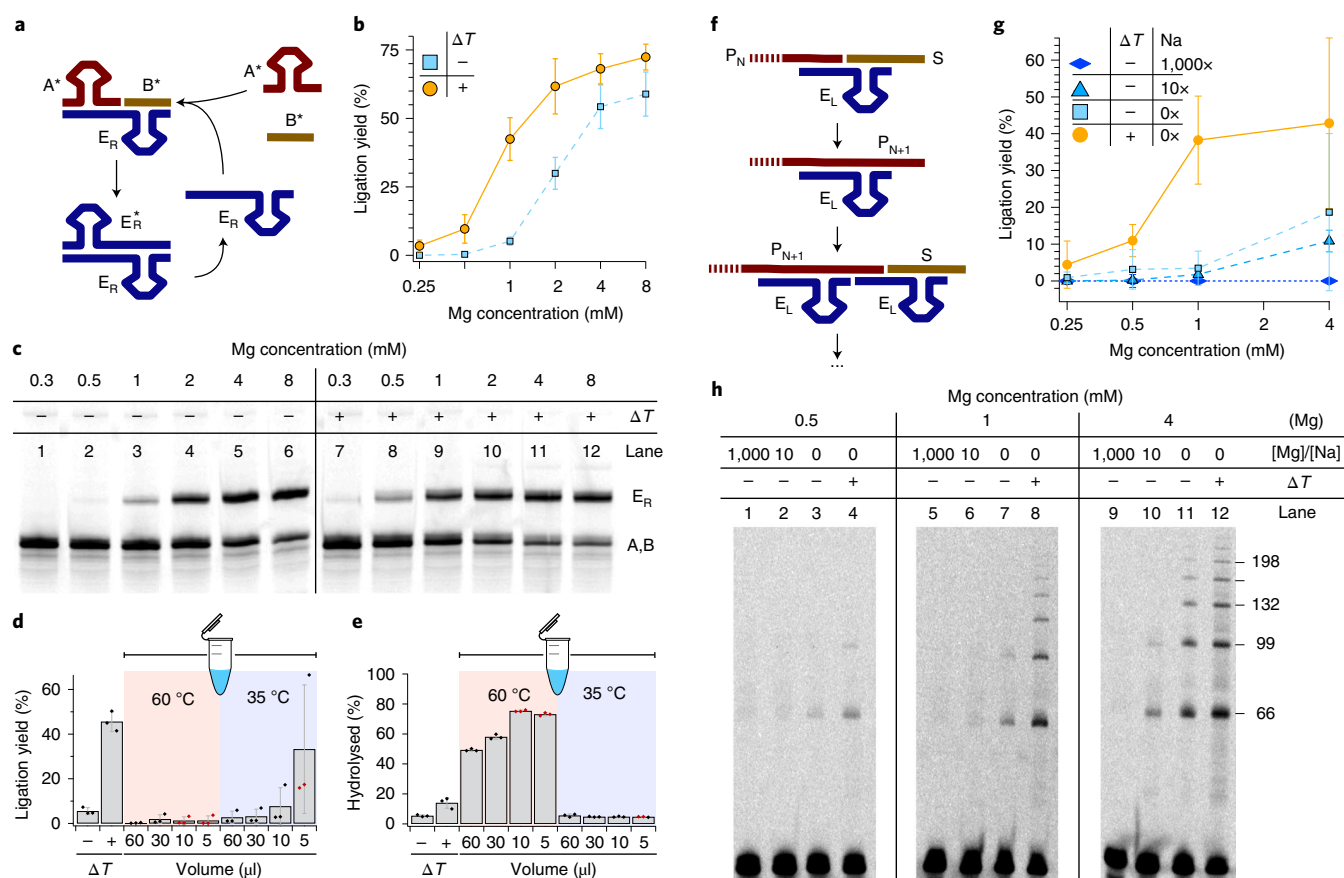


**Fig. 4 | Influence of salt conditions and thermal trapping on a replicator ribozyme  $E_R$  and a ladder-building ribozyme  $E_L$ .** **a–e**, Replicator ribozyme  $E_R$ . **a**, Schematic showing the replication cycle of the ribozyme R3C ( $E_R$ ), ligating the substrate strands  $A^*$  and  $B^*$ , yielding  $E_R^*$ . **b**, Ligated product yields in a vial at the optimal reaction temperature of 35 °C ( $\Delta T$ , –) and in the heat flow cell ( $\Delta T$ , +) based on the gel results in **c**. Error bars calculated from the s.d. of triple repeats, also shown in Supplementary Fig. 9. **c**, Urea–PAGE gel showing R3C replicator activity at varying magnesium concentrations both in solution and in the heat flow cell. **d,e**, Ligation yield (**d**) and amount of hydrolysed RNA polymer (**e**) after incubation of the R3C replicator for 2 h at 35 °C in a closed vial ( $\Delta T$ , –) and in the heat flow cell ( $\Delta T$ , +) (as in **b**) compared with the incubation in an open vial with evaporation at 35 and 60 °C and a 1 mM  $MgCl_2$  concentration. The symbol colour represents the visually determined state after 2 h: black indicates that the liquid was still visible, and red that the sample had dried up (Supplementary Fig. 10). **f–h**, A ladder-building RNA enzyme ( $E_L$ ). **f**,  $E_L$  catalyses the ligation of a substrate strand (S) to a product strand (P), which in turn was previously assembled from the substrate in the same manner. The length of the product strands is therefore a multiple of the length of the substrate (31 nucleotides). **g**, From the fluorescence signal in **h**, the ligation yield was calculated as a function of the magnesium concentration relative to the amount of sodium ( $x$ -fold) in a vessel at a homogeneous temperature ( $\Delta T$ , –), and in a heat flow cell ( $\Delta T$ , +). The inhibiting effect of even moderate amounts of sodium on the ligases is clearly visible. In a heat flow the efficiency of the ligases is substantially increased by the thermophoretic concentration of magnesium. Error bars calculated from the s.d. of triple repeats, also shown in Supplementary Fig. 11. **h**, Urea–PAGE gel showing ribozyme activity for different absolute  $MgCl_2$  concentrations (4–0.125  $\mu M$ ; Supplementary Fig. 11) in free solution ( $\Delta T$ , –) and in a thermogradient ( $\Delta T$ , +). In addition, the amount of NaCl relative to the magnesium concentration varied between no NaCl, 10 times more NaCl than  $MgCl_2$ , and 1,000 times more NaCl than  $MgCl_2$ .

8 and 12) at all the magnesium concentrations when compared with that of the free solution (lanes 3, 7 and 11; Fig. 4g,h). Ligation yield in the heat flow cell was on average 43% at 4 mM  $MgCl_2$ , compared to 18% in the bulk solution without added NaCl, and only 11% in the bulk solution in the presence of a tenfold excess of NaCl. The heat flow cell effectively preserved its activity at limiting magnesium concentrations, with ligation observed for both ribozymes even at 0.25 mM  $MgCl_2$ . The enhanced activity in the heat flow cell is due to several factors. First, the magnesium and RNA concentrations are increased by a factor of about ten due to thermophoretic accumulation (Supplementary Methods 7 and 9). Second, the RNA is trapped at the cold side of the cell by thermophoresis, which, in addition to a low average magnesium concentration, reduces hydrolysis. Also, pH is known to have a considerable impact on ribozyme function. It is already known from previous work that a pH difference between

the top and bottom of the chambers can be generated in the heat flow cells when used in conjunction with a buffer system such as Tris<sup>28</sup>. Specifically, it has been shown experimentally that the pH at the bottom of the chamber does not exceed about 8.5 under comparable conditions, which keeps the ribozyme within its working range. In an unbuffered system, the same effect for sodium, for example, would only account for a pH difference of about 0.6 and is therefore negligible (Supplementary Method 6).

**Salt separation in networks of interconnected heat flow cells.** Finally, we sought to investigate how our system might be applicable to even more extreme salt conditions. The brine of carbonate lakes, for example, contains an up to 1,000-fold excess of NaCl over  $MgCl_2$  (ref. 17). To provide suitable salt conditions for ribozymes from such extreme salt concentrations, a series of connected heat flow cells

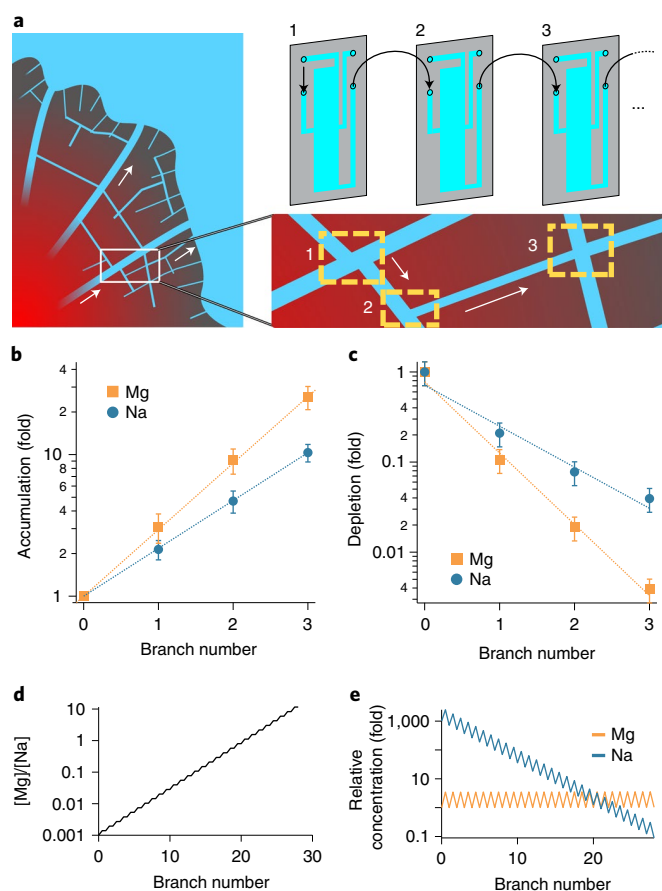


**Fig. 5 | Interconnected channels in a basaltic complex allow a variety of possible salt conditions.** **a**, The water flows through the basaltic complex by large-scale convection ( $v_{\text{drift}} = 11.8 \text{ nl s}^{-1}$ ). At any point where the fluid is merged or branched, the salinity can change by mixing or thermal concentration, which in our experiment is simulated by heat flow cells placed one after the other. **b**, Experimental results show the sequential thermophoretic purification, because the salt content in the concentration centres (lower channels) increases exponentially with the size of the system. Owing to the higher Soret coefficient of magnesium compared to sodium, the relative concentration changes in favour of divalent magnesium. Error bars calculated from the s.d. from triplicate measurements, also provided in Supplementary Table 3. **c**, Accordingly, the salt concentration is reduced at the depletion sites (upper channels). As a result, even water with a high salt content can be purified into low-salt water. **d**, The numerical extrapolation to a 28-fold larger system shows how the concentration ratio Mg:Na could be increased from 1:1,000 to 10:1 by thermophoretic purification. **e**, Infiltrating fresh water (rate of 2.4x per junction) could keep the absolute magnesium concentration at a constant level.

is required. Although this is challenging to realize in our set-up, it could occur quite naturally in a rock system of fissures and cracks (Fig. 5a). Under an applied heat flow and a slow throughflow from large-scale convection, liquid could be flushed through these cells in a similar manner to through our heat flow cells, and thus successively increase the magnesium content. We have implemented this scenario experimentally with three cells, in which we collected the upper and lower outflow of one cell, analysed it with IC and then injected a reconstituted solution into the inlet of another cell (Fig. 5a). Reinjection of the bottom output resulted in a gradual enrichment of  $\text{Mg}^{2+}$  over  $\text{Na}^+$ , whereas reinjection of the top output resulted in depletion. Starting from a solution with 1.5 mM of  $\text{MgCl}_2$

and  $\text{NaCl}$  each, the salt concentrations obtained in this way were increased by a factor of 25 ( $\text{MgCl}_2$ ) or 10 ( $\text{NaCl}$ ) at the lower outlets after 3 runs (Fig. 5b) and decreased by a factor of 260 ( $\text{MgCl}_2$ ) or 25 ( $\text{NaCl}$ ) at the upper outlets (Fig. 5c). A direct coupling of multiple cells was not possible due to the experimental timescales required to achieve the necessary volume for analysis (months).

This finding implies that a scaled-up network of connected cells should enable ion ratios compatible with ribozyme catalysis even in the case of a 1,000-fold sodium surplus. Indeed, a numeric model with 28 connected heat cells altered a  $\text{Na}^+:\text{Mg}^{2+}$  input ratio from 1,000:1 to a 1:10 an output ratio (Fig. 5d,e). In this model, we assumed the experimentally found separation of sodium and magnesium at the lower outlet of a heat flow cell under the conditions described above mixed with a 2.4-fold volume rate of continuously seeping fresh water fed into the next cell. It is worthwhile mentioning that this separation based on 28 individual cells can also be achieved with a single cell that is 28 times longer than the single cells used in this study<sup>23,50</sup>. This translates into a geologically plausible crack of about 1.6 m in length. To underline the plausibility of the selection effect in natural, extended systems, we also modelled and statistically evaluated the more general case of hundreds of randomly connected heat flow cells for a variety of boundary conditions, such as temperature gradient or flow rate (Extended Data Fig. 6, Supplementary Method 13 and Supplementary Figs. 13–19). The results show that, despite the assumed complete mixing of all species before entering a heat flow cell through, for example, chaotic advection<sup>51</sup>, on average a large accumulation and selection effect can be achieved. We also compared different ions, such as sodium, magnesium, calcium and potassium, and observe the greatest potential for selective enrichment in the competition between monovalent and divalent ions. Selection between monovalent ions, for example, due to the higher Soret coefficient of sodium compared with that of potassium, is possible, but occurs relatively rarely and only at larger temperature differences.

## Discussion

In this work, we demonstrated the positive influence of heat fluxes through geometrically confined water layers on prebiochemical systems, starting from the geological accumulation of salts. Under close-to-equilibrium conditions, most common geological processes may provide unfavourable salt conditions for ribozyme activity. In contrast, heat fluxes across fracture-like compartments push the system sufficiently out of equilibrium that microconvection and thermophoresis can accumulate the magnesium ions required for ribozyme function, while simultaneously depleting inhibitory sodium ions.

Notably, the two closely related ribozyme systems show different tolerances to sodium ion inhibition. Consequently, high sodium levels may block the exploration of promising evolutionary trajectories towards higher or new catalytic activities. Our findings imply that access to such otherwise blocked pathways could have been provided through simple and abundant heat fluxes across rock fissures. Establishing suitably ionic conditions may have therefore been critical for the emergence of key ribozyme activities, such as template-dependent copying of RNA sequences, which shows a similar sensitivity to high sodium levels<sup>13</sup>. In this context, other pre-homeostatic biosystems, for example, based on peptides or primitive protein enzymes, may have also benefited from such confined heat-flow environments. Indeed, many modern  $\text{Mg}^{2+}$ -dependent enzymes, such as kinases, are also vulnerable towards monovalent ions such as sodium<sup>52</sup>. Finally, high salinities, mainly due to high sodium chloride levels, also hinder the formation of potential protocellular systems based on single-chain amphiphiles or membrane-free compartments<sup>53–55</sup>. Thus, thermophoretic alterations of the ion composition have the potential to create ecological niches for both early biocatalysis and precellular compartments.

As thermophoresis and convection are universal and also exist, albeit slower<sup>50</sup>, at much smaller temperature gradients than those used in this work, active demixing of salt solutions may occur in many different natural environments for a wide range of different salt mixtures beyond mixtures of NaCl and MgCl<sub>2</sub>. As noted in Supplementary Fig. 6 and Supplementary Table 3, many metal ions, such as potassium and calcium, show thermophoresis of different strengths, which indicates that these could be selectively enriched depending on the fluidic system. By randomly combining different flow paths, almost any salt conditions could be implemented by nature, as shown in the Supplementary Method 12.

Another interesting side effect of the thermophoresis-based accumulation of salts is that, in contrast to typical dehydration, an excessive up-concentration of salts is impaired by a negative feedback mechanism. This is a direct consequence of the Soret coefficient of ions, which is a measure of the strength of the thermophoretic accumulation, being dependent on the local salt concentration and becoming smaller but non-zero at higher salt concentrations<sup>56</sup>. In the prebiotic context, this has already been demonstrated by Szostak and co-workers, who found a substantial reduction of the possible thermogravitational accumulation in such heat flow cells at higher initial salt concentrations<sup>32</sup>. On the one hand, this effect prevents extremely high salt concentrations that would be obtained by, for example, evaporation and, in the case of magnesium, can lead to an increased hydrolysis of RNA. On the other hand, the depletion of salts at the upper fluid passages occurs even at extremely high initial salt concentrations due to the non-zero Soret coefficient, which should result in a behaviour similar to that shown in Fig. 5, assuming a sufficiently large system. Although salt concentration by dehydration or the formation of eutectic phases are non-equilibrium mechanisms, only the combination of heat flows and the geometric boundary conditions formed, for example, by geomaterial allow the emergence of a system far enough from equilibrium to enable the selection effects reported here. In a large network of rock fractures, there is also the possibility that products formed in locations with high magnesium concentrations can reach chambers with lower magnesium concentrations due to drift through the system, and thus be protected from hydrolysis in the long term. Hence, the selective up-concentration of the prebiotically relevant species reported here provides further compelling evidence that thermal gradients across narrow rock fissures were an ideal habitat for the first life-relevant reactions.

### Online content

Any methods, additional references, Nature Research reporting summaries, source data, extended data, supplementary information, acknowledgements, peer review information; details of author contributions and competing interests; and statements of data and code availability are available at <https://doi.org/10.1038/s41557-021-00772-5>.

Received: 28 August 2020; Accepted: 13 July 2021;

Published online: 26 August 2021

### References

- Gilbert, W. Origin of life: the RNA world. *Nature* **319**, 618 (1986).
- Neveu, M., Kim, H.-J. & Benner, S. A. The 'strong' RNA world hypothesis: fifty years old. *Astrobiology* **13**, 391–403 (2013).
- Hud, N. V. Searching for lost nucleotides of the pre-RNA world with a self-refining model of early Earth. *Nat. Commun.* **9**, 5171 (2018).
- Bhowmik, S. & Krishnamurthy, R. The role of sugar-backbone heterogeneity and chimeras in the simultaneous emergence of RNA and DNA. *Nat. Chem.* **11**, 1009–1018 (2019).
- Kazakov, S. A., Balatskaya, S. V. & Johnston, B. H. Ligation of the hairpin ribozyme in *cis* induced by freezing and dehydration. *RNA* **12**, 446–456 (2006).
- Denesyuk, N. A. & Thirumalai, D. How do metal ions direct ribozyme folding? *Nat. Chem.* **7**, 793–801 (2015).
- Le Vay, K., Salibi, E., Song, E. Y. & Mutschler, H. Nucleic acid catalysis under potential prebiotic conditions. *Chem. Asian J.* **15**, 214 (2020).
- Freisinger, E. & Sigel, R. K. O. From nucleotides to ribozymes—a comparison of their metal ion binding properties. *Coord. Chem. Rev.* **251**, 1834–1851 (2007).
- Wu, Y.-Y., Zhang, Z.-L., Zhang, J.-S., Zhu, X.-L. & Tan, Z.-J. Multivalent ion-mediated nucleic acid helix–helix interactions: RNA versus DNA. *Nucleic Acids Res.* **43**, 6156–6165 (2015).
- Erat, M. C., Coles, J., Finazzo, C., Knobloch, B. & Sigel, R. K. O. Accurate analysis of Mg<sup>2+</sup> binding to RNA: from classical methods to a novel iterative calculation procedure. *Coord. Chem. Rev.* **256**, 279–288 (2012).
- Xi, K., Wang, F.-H., Xiong, G., Zhang, Z.-L. & Tan, Z.-J. Competitive Binding of Mg<sup>2+</sup> and Na<sup>+</sup> ions to nucleic acids: from helices to tertiary structures. *Biophys. J.* **114**, 1776–1790 (2018).
- Fischer, N. M., Poléto, M. D., Steuer, J. & van der Spoel, D. Influence of Na<sup>+</sup> and Mg<sup>2+</sup> ions on RNA structures studied with molecular dynamics simulations. *Nucleic Acids Res.* **46**, 4872–4882 (2018).
- Attwater, J. et al. Chemical fidelity of an RNA polymerase ribozyme. *Chem. Sci.* **4**, 2804–2814 (2013).
- Heilman-Miller, S. L., Pan, J., Thirumalai, D. & Woodson, S. A. Role of counterion condensation in folding of the *Tetrahymena* ribozyme. II. Counterion-dependence of folding kinetics. *J. Mol. Biol.* **309**, 57–68 (2001).
- Koculi, E., Hyeon, C., Thirumalai, D. & Woodson, S. A. Charge density of divalent metal cations determines RNA stability. *J. Am. Chem. Soc.* **129**, 2676–2682 (2007).
- Shellnutt, J. G. Derivation of intermediate to silicic magma from the basalt analyzed at the Vega 2 landing site, Venus. *PLoS ONE* **13**, e0194155 (2018).
- Toner, J. D. & Catling, D. C. A carbonate-rich lake solution to the phosphate problem of the origin of life. *Proc. Natl. Acad. Sci. USA* **117**, 883–888 (2020).
- Gangidine, A., Havig, J. R., Hannon, J. S. & Czaja, A. D. Silica precipitation in a wet–dry cycling hot spring simulation chamber. *Life* **10**, 3 (2020).
- Damer, B. & Deamer, D. The hot spring hypothesis for an origin of life. *Astrobiology* **20**, 429–452 (2020).
- Attwater, J., Wochner, A., Pinheiro, V. B., Coulson, A. & Holliger, P. Ice as a protocellular medium for RNA replication. *Nat. Commun.* **1**, 76 (2010).
- Monnard, P.-A., Kanavarioti, A. & Deamer, D. W. Eutectic phase polymerization of activated ribonucleotide mixtures yields quasi-equimolar incorporation of purine and pyrimidine nucleobases. *J. Am. Chem. Soc.* **125**, 13734–13740 (2003).
- Mutschler, H., Wochner, A. & Holliger, P. Freeze–thaw cycles as drivers of complex ribozyme assembly. *Nat. Chem.* **7**, 502–508 (2015).
- Baaske, P. et al. Extreme accumulation of nucleotides in simulated hydrothermal pore systems. *Proc. Natl. Acad. Sci. USA* **104**, 9346–9351 (2007).
- Debye, P. Zur Theorie des clusiuschen trennungsverfahrens. *Ann. Phys.* **428**, 284–294 (1939).
- Clusius, K. & Dickel, G. Neues verfahren zur gasentmischung und isotopentrennung. *Naturwissenschaften* **26**, 546 (1938).
- Kreysing, M., Keil, L., Lanzmich, S. & Braun, D. Heat flux across an open pore enables the continuous replication and selection of oligonucleotides towards increasing length. *Nat. Chem.* **7**, 203–208 (2015).
- Mast, C. B. & Braun, D. Thermal trap for DNA replication. *Phys. Rev. Lett.* **104**, 188102 (2010).
- Keil, L. M. R., Möller, F. M., Kieß, M., Kudella, P. W. & Mast, C. B. Proton gradients and pH oscillations emerge from heat flow at the microscale. *Nat. Commun.* **8**, 1897 (2017).
- Niether, D., Afanasenkau, D., Dhont, J. K. G. & Wiegand, S. Accumulation of formamide in hydrothermal pores to form prebiotic nucleobases. *Proc. Natl. Acad. Sci. USA* **113**, 4272–4277 (2016).
- Morasch, M. et al. Heated gas bubbles enrich, crystallize, dry, phosphorylate and encapsulate prebiotic molecules. *Nat. Chem.* **11**, 779–788 (2019).
- Ianeselli, A., Mast, C. B. & Braun, D. Periodic melting of oligonucleotides by oscillating salt concentrations triggered by microscale water cycles inside heated rock pores. *Angew. Chem.* **131**, 13289–13294 (2019).
- Budin, I., Bruckner, R. J. & Szostak, J. W. Formation of protocell-like vesicles in a thermal diffusion column. *J. Am. Chem. Soc.* **131**, 9628–9629 (2009).
- Verney-Carron, A., Vigier, N. & Millot, R. Experimental determination of the role of diffusion on Li isotope fractionation during basaltic glass weathering. *Geochim. Cosmochim. Acta* **75**, 3452–3468 (2011).
- Allègre, C. J. et al. The fundamental role of island arc weathering in the oceanic Sr isotope budget. *Earth Planet. Sci. Lett.* **292**, 51–56 (2010).
- Dessert, C., Dupré, B., Gaillardet, J., François, L. M. & Allègre, C. J. Basalt weathering laws and the impact of basalt weathering on the global carbon cycle. *Chem. Geol.* **202**, 257–273 (2003).
- Gislason, S. R. & Oelkers, E. H. Mechanism, rates, and consequences of basaltic glass dissolution. II. An experimental study of the dissolution rates of basaltic glass as a function of pH and temperature. *Geochim. Cosmochim. Acta* **67**, 3817–3832 (2003).
- Robertson, M. P. & Joyce, G. F. Highly efficient self-replicating RNA enzymes. *Chem. Biol.* **21**, 238–245 (2014).



## ARTICLES

## NATURE CHEMISTRY

38. McCollom, T. M. & Donaldson, C. Experimental constraints on abiotic formation of tubules and other proposed biological structures in subsurface volcanic glass. *Astrobiology* **19**, 53–63 (2019).
39. de Ronde, C. E. J., Channer, D. M. D., Faure, K., Bray, C. J. & Spooner, E. T. C. Fluid chemistry of Archean seafloor hydrothermal vents: implications for the composition of circa 3.2 Ga seawater. *Geochim. Cosmochim. Acta* **61**, 4025–4042 (1997).
40. Takeyama, N. & Nakashima, K. Proportionality of intrinsic heat of transport to standard entropy of hydration for aqueous ions. *J. Solution Chem.* **17**, 305–325 (1988).
41. Petit, C. J., Hwang, M.-H. & Lin, J.-L. The Soret effect in dilute aqueous alkaline earth and nickel chloride solutions at 25 °C. *Int. J. Thermophys.* **7**, 687–697 (1986).
42. Lide, D. R. *CRC Handbook of Chemistry and Physics. A Ready-Reference Book of Chemical and Physical Data* 84th edn (CRC, 2003).
43. Potuzak, M., Nichols, A. R. L., Dingwell, D. B. & Clague, D. A. Hyperquenched volcanic glass from Loihi Seamount, Hawaii. *Earth Planet. Sci. Lett.* **270**, 54–62 (2008).
44. Nichols, A. R. L., Potuzak, M. & Dingwell, D. B. Cooling rates of basaltic hyaloclastites and pillow lava glasses from the HSDP2 drill core. *Geochim. Cosmochim. Acta* **73**, 1052–1066 (2009).
45. Dimroth, E., Cousineau, P., Leduc, M. & Sanschagrin, Y. Structure and organization of Archean subaqueous basalt flows, Rouyn–Noranda area, Quebec, Canada. *Can. J. Earth Sci.* **15**, 902–918 (1978).
46. Sigurðsson, H. *Encyclopedia of Volcanoes* 4th edn (Academic, 2007).
47. Knauth, L. P. & Lowe, D. R. High Archean climatic temperature inferred from oxygen isotope geochemistry of cherts in the 3.5 Ga Swaziland Supergroup, South Africa. *Geol. Soc. Am. Bull.* **115**, 566–580 (2003).
48. Robert, F. & Chaussidon, M. A palaeotemperature curve for the Precambrian oceans based on silicon isotopes in cherts. *Nature* **443**, 969–972 (2006).
49. Smith, B. J. Rock temperature measurements from the northwest Sahara and their implications for rock weathering. *CATENA* **4**, 41–63 (1977).
50. Keil, L., Hartmann, M., Lanzmich, S. & Braun, D. Probing of molecular replication and accumulation in shallow heat gradients through numerical simulations. *Phys. Chem. Chem. Phys.* **18**, 20153–20159 (2016).
51. Lester, D. R., Metcalfe, G. & Trefry, M. G. Is chaotic advection inherent to porous media flow? *Phys. Rev. Lett.* **111**, 174101 (2013).
52. Bygrave, F. L. The ionic environment and metabolic control. *Nature* **214**, 667–671 (1967).
53. Maurer, S. The impact of salts on single chain amphiphile membranes and implications for the location of the origin of life for an origin of life. *Life* **7**, 44 (2017).
54. Milshtey, D., Damer, B., Havig, J. & Deamer, D. Amphiphilic compounds assemble into membranous vesicles in hydrothermal hot spring water but not in seawater. *Life* **8**, 11 (2018).
55. Priftis, D. & Tirrell, M. Phase behaviour and complex coacervation of aqueous polypeptide solutions. *Soft Matter* **8**, 9396–9405 (2012).
56. Reichl, M., Herzog, M., Götz, A. & Braun, D. Why charged molecules move across a temperature gradient: the role of electric fields. *Phys. Rev. Lett.* **112**, 198101 (2014).

**Publisher's note** Springer Nature remains neutral with regard to jurisdictional claims in published maps and institutional affiliations.

© The Author(s), under exclusive licence to Springer Nature Limited 2021

## Methods

**Basaltic sample preparation.** The tholeiitic basalt was collected from 1975–1984 Krafla Fires deposits. The sample was exposed on the surface until collection and interacted with organic matter. To remove the organics, the sample was crushed with a hammer to an average grain size of 1–2 cm. The crushed tholeiite was incubated in H<sub>2</sub>O<sub>2</sub> (10 vol%) for 7 days, washed with purified water and dried for 24 h at 200 °C in a furnace. Afterwards, the basalt was ground by a vibration mill to <500 μm mesh size and the size separated by hand sieving to grain sizes between 500 and 63 μm. For the synthesis of tholeiitic glass, 40 g of the fraction smaller than 63 μm was heated in a platinum crucible at 1,500 °C until molten. The molten sample was quenched in a copper container for rapid cooling and crushed afterwards. This procedure was repeated three times to obtain a homogeneous glass. The tholeiitic glass was then crushed with a hammer, ground by a vibration mill and size separated as above.

**Basalt leaching.** Basalt samples were weighed and submerged into 150 μl of MilliQ, assumed prebiotic or hydrothermal water (Supplementary Method 1 and Supplementary Table 2). The composition of the presumed prebiotic sea water in our experiments was inspired by McCollom and Donaldson<sup>58</sup> and Brown et al.<sup>57</sup>. Following a combination of their recipes, we used 479.439 mM NaCl, 9.5 mM NH<sub>4</sub>Cl, 4.85 mM KCl, 4.8 mM CaCl<sub>2</sub>, 1.3 mM NaHCO<sub>3</sub> and 0.433 mM KBr, which resulted in a pH of 7.45. After initial vortexing, leaching took place under a controlled temperature (T100 Thermal Cycler, Bio-Rad Laboratories). After incubation, the supernatant was cooled to room temperature and diluted with MilliQ water for IC measurement. Results were corrected accordingly (Supplementary Method 3). Experiments with continuous agitation were done using a ThermoMixer C (Eppendorf).

**Heat flow cell.** The construction of the heat flow cell is described in Supplementary Methods 4 and 5. The cells were prepurged with low-viscosity fluorinated oil (3M Nove 7500 Engineered Fluid) to check for leaks and push out residual gas inclusions. The assembled cell was then mounted on an aluminium block cooled by a water bath (TXF-200 R5, Grant) and the heat flow controlled by a modified PID controller (Repeater firmware on Arduino). The throughflow was controlled using high-precision syringe pumps (neMESYS) that were connected using FEP tubings with a 1 mm inner diameter and UNF ¼-28G screw system (Techlab). Temperatures were measured using a thermistor (cold side) or a thermal camera (Seek Thermal).

**Finite element simulation.** Comsol v5.4 was used to successively solve heat conduction and water movement in an exact three-dimensional model of the experimental set-up. The solution was then used to determine the time- and location-dependent concentrations of the salts in a drift-diffusion model (see Extended Data Fig. 3, Supplementary Method 7 and Supplementary Figs. 4 and 5 for details).

**Ion chromatography.** An IC system (Dionex Aquion, ThermoFisher Scientific) with an analytical column (Dionex IonPac CS12A), guard column (Dionex IonPac CG12A) and suppressor (Dionex CDRS 600) was used to measure the salt concentration. Different methods were used for analysis, mostly method 2 (0.25 ml min<sup>-1</sup> flow, isocratic elution with 20 mM methane sulfonic acid and 15 mA suppression; see Supplementary Method 2 for further method details). Eluted ions were detected with a conductivity detector (DS6 Heated Conductivity Cell). Data were analysed with Chromeleon 7.2.10 (ThermoFisher Scientific).

**pH measurement.** Measurement of the pH values for the different outflows was done using a Thermo Scientific Orio 9826BN Micro pH Electrode (Thermo Fisher Scientific). The gradient observed was weak, with values close to neutrality and a slightly more neutral bottom: ΔpH = pH<sub>bottom</sub> - pH<sub>top</sub> = 0.57 ± 0.16 (inlet, 6.64 ± 0.23; top outlet, 6.20 ± 0.35; middle outlet, 6.58 ± 0.21; bottom outlet, 6.77 ± 0.39).

**RNA synthesis.** All the RNA was produced by in vitro transcription, except 5'-Cy5 tagged substrate A and substrate BA, which were ordered from IDT and used without further purification. Templates for in vitro transcription were created by fill-in PCR using GoTaq (Promega). Briefly, two partially complementary single-stranded DNA oligonucleotides were annealed and extended, which resulted in double-stranded DNA (dsDNA) templates that contained a 5'-terminal T7 promoter and the downstream transcription templates of interest. Following fill-in PCR, all dsDNA products were purified using the Monarch DNA Cleanup Kit (NEB). Most RNAs were synthesized by run-off transcription using the MEGAShortsript T7 Transcription Kit (Thermo Scientific) according to the manufacturer's instructions. The transcription reaction proceeded for 3.5 h at 37 °C, after which 0.1 volumes of TURBO DNase (Thermo Scientific) were added and the reaction incubated for a further 30 min at 37 °C. The transcription products were purified using a Monarch RNA Cleanup Kit (NEB), and then gel purified using 15–20 % denaturing PAGE. RNAs were extracted from gel slices by diffusion, and then precipitated

using ethanol and isopropanol. The resulting RNA pellet was suspended in double-distilled H<sub>2</sub>O. The concentration was determined by absorbance at 260 nm using specific extinction coefficients calculated from the RNA sequence using OligoCalc (<http://biotools.nubic.northwestern.edu/OligoCalc.html>). For very short RNA fragments (self-replicator substrate B, 14 nucleotides), an alternative transcription protocol was used to improve the yields. Briefly, a partially complementary dsDNA template that contained the T7 promoter was created by incubating an equimolar mixture of both strands at 85 °C, and then cooling on ice. The transcription reaction mixture comprised 500 nM dsDNA template, 50 mM Tris pH 7.8, 25 mM MgCl<sub>2</sub>, 3.75 mM each nucleotide triphosphate, 10 mM dithiothreitol, 2 mM spermidine, 5 U ml<sup>-1</sup> *Escherichia coli* inorganic pyrophosphatase (NEB) and 1,500 units of T7 polymerase (purified from a recombinant source at the Core Facility of the Max Planck Institute for Biochemistry). The transcription reaction proceeded for 3.5 h at 37 °C. Downstream purification was performed as previously described.

**Ribozyme activity assay.** R3C self-replicator reactions were performed in Tris buffer (25 mM, pH 8.5) with 0.00625–8 mM MgCl<sub>2</sub>, 0.5 μM ribozyme E<sub>R</sub>, 1 μM substrate A (100% Cy5 tagged) and 1 μM substrate B. The NaCl concentration was 0×, 10× or 1,000× the MgCl<sub>2</sub> concentration. Ribozyme concatamer ligation reactions were performed similarly in Tris buffer (25 mM, pH 8.5) with 0.00625–8 mM MgCl<sub>2</sub>, 0.5 μM ribozyme E<sub>L</sub> and 1 μM substrate BA (10% Cy5 tagged). The NaCl concentration was 0×, 10× or 1,000× the MgCl<sub>2</sub> concentration. The reaction temperature in the bulk solution conditions was 35 °C. The reaction was quenched by adding an aliquot to four volumes of RNA gel loading buffer (formamide, EDTA (10 mM, pH 8.0) and bromophenol blue (0.025% w/v)). The reaction products were separated by denaturing PAGE on 15–20% acrylamide gels run in 1× TBE buffer, then visualized by Cy5-tag fluorescence (Typhoon FLA-5000, GE Healthcare Life Sciences, excitation wavelength = 635 nm and emission wavelength = 670 nm). Band intensities were determined using ImageQuant.

**Simulation of large systems of interconnected thermogravitational traps.** The examples given in the main text (in particular Fig. 5d,e) were limited to a special case in which several traps followed each other in a defined manner. A constant influx of fresh water was assumed and thus a large accumulation of magnesium salts with a simultaneous depletion of sodium salts was achieved. The question therefore arises whether this special case is representative of large systems of interconnected thermogravitational traps. To address this question, we extended the simulation of a single thermogravitational molecular trap (discussed in Fig. 3 and in the Supplementary Information) to a large system of interconnected traps. Some results of this approach are shown in Extended Data Fig. 6. For extensive details of the simulation, see Supplementary Method 12 and Supplementary Figs. 13–19.

## Data availability

The data supporting the findings of this study are available within the paper and its Supplementary Information. Raw data in the form of images (gels) or data series (Excel files) are also provided in the Supplementary Information. Source data are provided with this paper.

## Code availability

The full details of the finite element simulation from Fig. 3 are documented in the mph files in the Supplementary Information. The extrapolation from Fig. 5d,e and Supplementary Figs. 14–19 was done using a Labview program, which is also provided in the Supplementary Source file.

## References

- Brown, J., Bearman, G. & Wright, J. *Seawater: Its Composition, Properties and Behaviour* 2nd edn (Butterworth-Heinemann, 1995).

## Acknowledgements

Funded by the Deutsche Forschungsgemeinschaft (DFG, German Research Foundation)—Project-ID 364653263—TRR 235 (CRC235), Project P08 (C.B.M. and H.M.), P09 (D.B. and B.S.) and P03 (B.S.). Funding by the Volkswagen Initiative 'Life?—A Fresh Scientific Approach to the Basic Principles of Life' (C.B.M., D.B., H.M., K.L., T.M., D.B.D. and A.Z.C.), from the Simons Foundation (327125 to D.B.) and from Germany's Excellence Strategy EXC-2094-390783311 is gratefully acknowledged. We thank Quantitative Biology Munich for funding (A.K.). This project has received funding from the European Research Council (ERC) under the European Union's Horizon 2020 research and innovation programme (grant agreement no. 802000, RiboLife) (H.M.). H.M. is grateful for funding by the MaxSynBio consortium, which is jointly funded by the Federal Ministry of Education and Research of Germany and the Max Planck Society. D.B.D. acknowledges the support of ERC ADV 2018 Grant 834225 (EAVESDROP) and D.B. is grateful for financial support from ERC-2017-ADG from the European Research Council. The work is supported by the Center for Nanoscience Munich (CeNS). We thank E. Song for fruitful discussions.

## ARTICLES

## NATURE CHEMISTRY

**Author contributions**

T.M., K.L., A.S., P.A., L.B., A.Z.Ç., E.S., C.S. and C.B.M. performed the experiments. T.M., K.L., A.S., L.B., A.Z.Ç., E.S., A.K., C.S., B.S., D.B.D., D.B., H.M. and C.B.M. conceived and designed the experiments. T.M., K.L., P.A., L.B., A.Z.Ç., E.S., A.K., C.S., B.S., H.M. and C.B.M. analysed the data. T.M., K.L., A.S., P.A., L.B., A.Z.Ç., A.K., B.S., D.B., H.M. and C.B.M. wrote the paper. All the authors discussed the results and commented on the manuscript.

**Competing interests**

The authors declare no competing interests.

**Additional information**

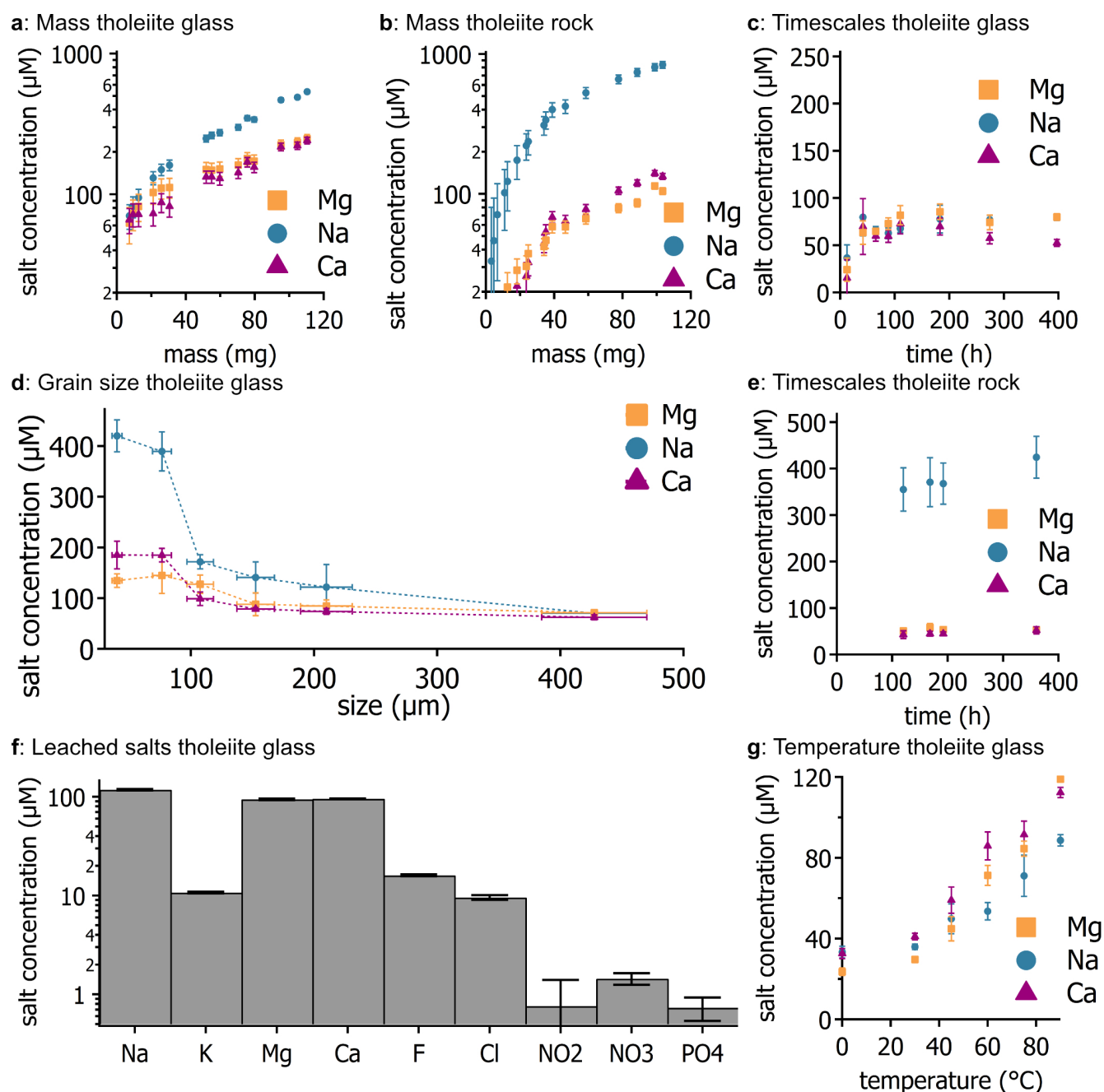
**Extended data** is available for this paper at <https://doi.org/10.1038/s41557-021-00772-5>.

**Supplementary information** The online version contains supplementary material available at <https://doi.org/10.1038/s41557-021-00772-5>.

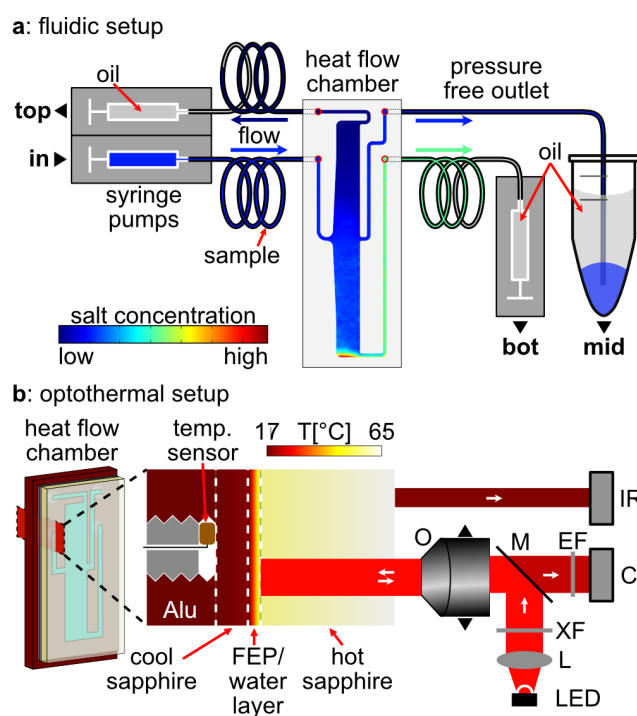
**Correspondence and requests for materials** should be addressed to H.M. or C.B.M.

**Peer review information** *Nature Chemistry* thanks Katarzyna Adamala, Rowena Ball and Philip Bevilacqua for their contribution to the peer review of this work.

**Reprints and permissions information** is available at [www.nature.com/reprints](http://www.nature.com/reprints).

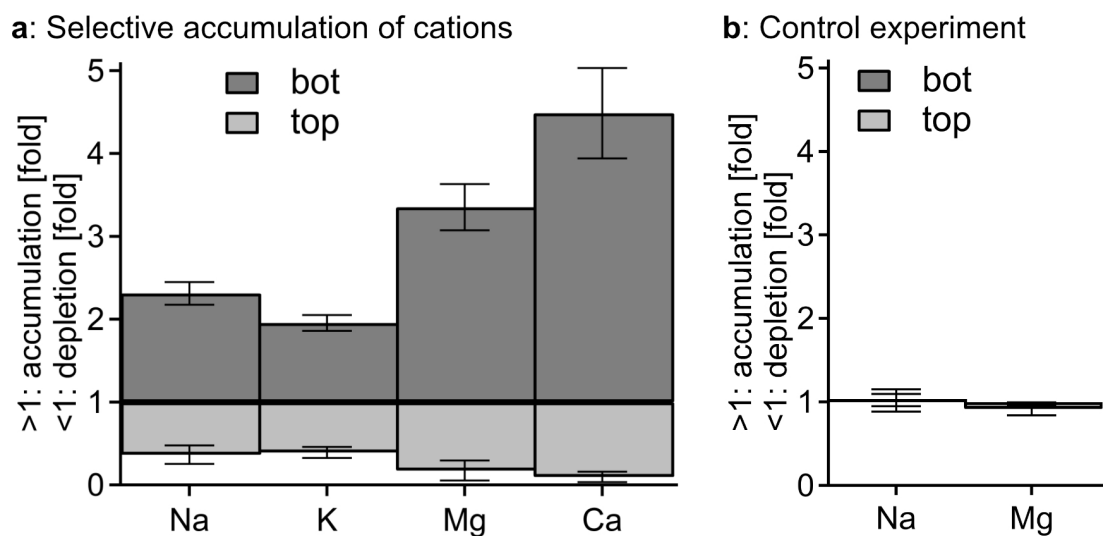


**Extended Data Fig. 1 | Leaching of salts from basaltic rock and glass.** Except where stated otherwise, 30 mg of sample were leached at 60 °C in 150  $\mu\text{l}$  ultrapure water without agitation. **(a)** Tholeiite glass samples with grain size of 90–125  $\mu\text{m}$  and a weight of up to 120 mg were leached at 60 °C in 150  $\mu\text{l}$  pure water for 110 h. Magnesium and calcium concentrations remain at similarly low levels (200  $\mu\text{M}$ ), while sodium concentration exceeds by up to a factor of three. Standard deviations are taken from **g**, grain size 90–125  $\mu\text{m}$ . **(b)** Tholeiite rock samples of 90–125  $\mu\text{m}$  size were leached for 36 h under the same conditions as in **a**. Error bars are taken from **e**. **(c)** Characteristic equilibration timescales for tholeiite glass, as shown for magnesium in the main text, Fig. 2. Timescales are around 30 hours. The grain size used here is 355–500  $\mu\text{m}$ . For comparison with **e**, the leached concentrations are converted to 90–125  $\mu\text{m}$  grains using the grain size dependence from **g**. **(d)** Grain size dependence of leached salt concentrations for tholeiite glass, incubated at 60 °C for 95 h. **(e)** Characteristic equilibration timescales for basaltic rock of grain size 90–125  $\mu\text{m}$  under the same conditions as in **d**. **(f)** Complete picture of leached ions from tholeiite glass (grain size 125–180  $\mu\text{m}$ , 110 h, 60 °C, pure water). In the first place, sodium (120  $\mu\text{M}$ ) is leached with magnesium and calcium (both 90  $\mu\text{M}$ ) following at lower concentrations. Fluoride, chloride and potassium are detectable at low concentrations (all 10–20  $\mu\text{M}$ ). Other trace elements such as phosphate, nitrite and nitrate are present but below 2  $\mu\text{M}$ . **(g)** Basalt glass samples of 355–500  $\mu\text{m}$  grain size were leached for 48 h at varying temperature under otherwise identical conditions as in **a**. The leached salt concentrations increase with temperature but stay at low levels.



**Extended Data Fig. 2 | Detailed description of fluidic setup.** (a) Fluidic setup. Microfluidic access to the heat flow cell is implemented by backside connection of FEP tubing through the four access holes on the backside aluminium and sapphire pieces (see Supplementary Fig. 2). Slow geothermal convection is mimicked by a slow through flow, controlled by three high precision syringe pumps with a constant volume rate. One pump (in) provides positive pressure and injects fresh sample into the chamber. The remaining two pumps (top, bot) provide negative pressure and remove the sample from the top or bottom output, respectively. The centered output (mid) releases the remaining pressure to an open Eppendorf tube. To minimized possible detrimental surface interactions, the complete system including chamber, tubing and syringes is pre-flushed with fluorinated oil. After the experiment, samples from bot, mid and top are recovered from the tubing and analyzed via IC. (b) Optothermal setup. Special care was taken to precisely determine the temperature inside the microfluidic layer: A temperature sensor is directly in contact with the cold sapphire from the backside and held in place via a UNF screw (grey). The surface temperature of the hot sapphire is measured with an IR camera (IR). The temperature field inside the liquid is then calculated from the known heat conductivity of the sapphire layers. Fluorescence measurements of the RNA reaction were obtained using a custom-made, motorized fluorescence microscope comprising an objective (O, TL4/2X-SAP, Thorlabs), dichroic mirror (M), excitation and emission filters (XF, EF, Cy5 Kit XF416, Laser Components), a lens (L) that collimates the light from a LED (LED, M625L3, Thorlabs) and a camera (C, Stingray 145-B, Allied Vision).



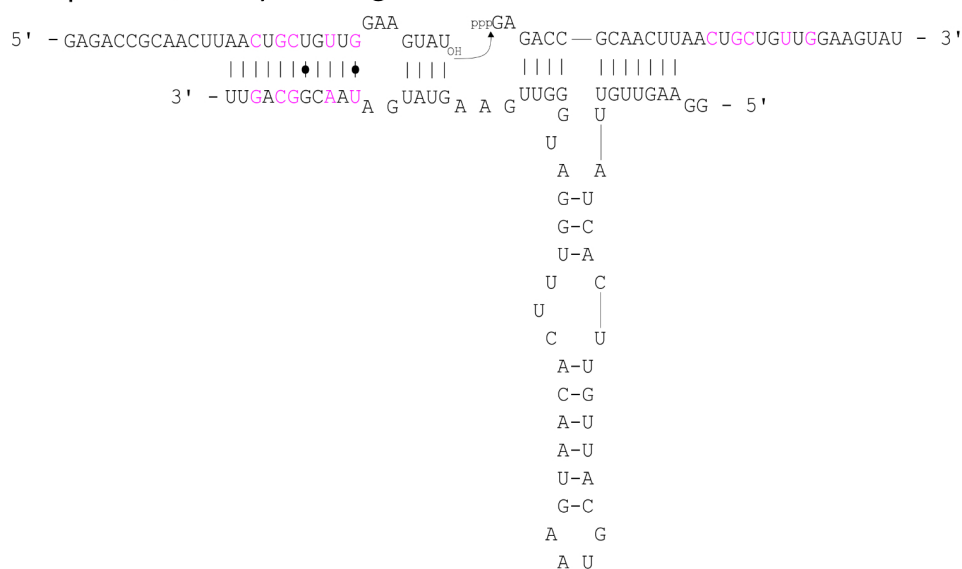


**Extended Data Fig. 4 | Trapping experiments with other salt species and control.** Errors bars represent the standard deviation calculated from data provided in Supplementary Table 3. **(a)** Selective accumulation of sodium, potassium, magnesium and calcium. In an experiment similar to Fig. 3, main text, samples of 1.5 mM of all salts were pushed through the microfluidic chamber at 11.8 nl/s applying a temperature gradient of 40 K to analyze selective accumulation. As shown, sodium (2.3-fold) and potassium (2-fold) are less accumulated at the bottom than magnesium (3.4-fold) and calcium (4.5-fold). Together with a top outlet that is mainly depleted in the latter but also has reduced concentration of Na and K, this opens the door to many different salty habitats. **(b)** Control experiments with no applied temperature gradient show (as expected) no shift of salt concentrations.

## a: initial ribozyme design

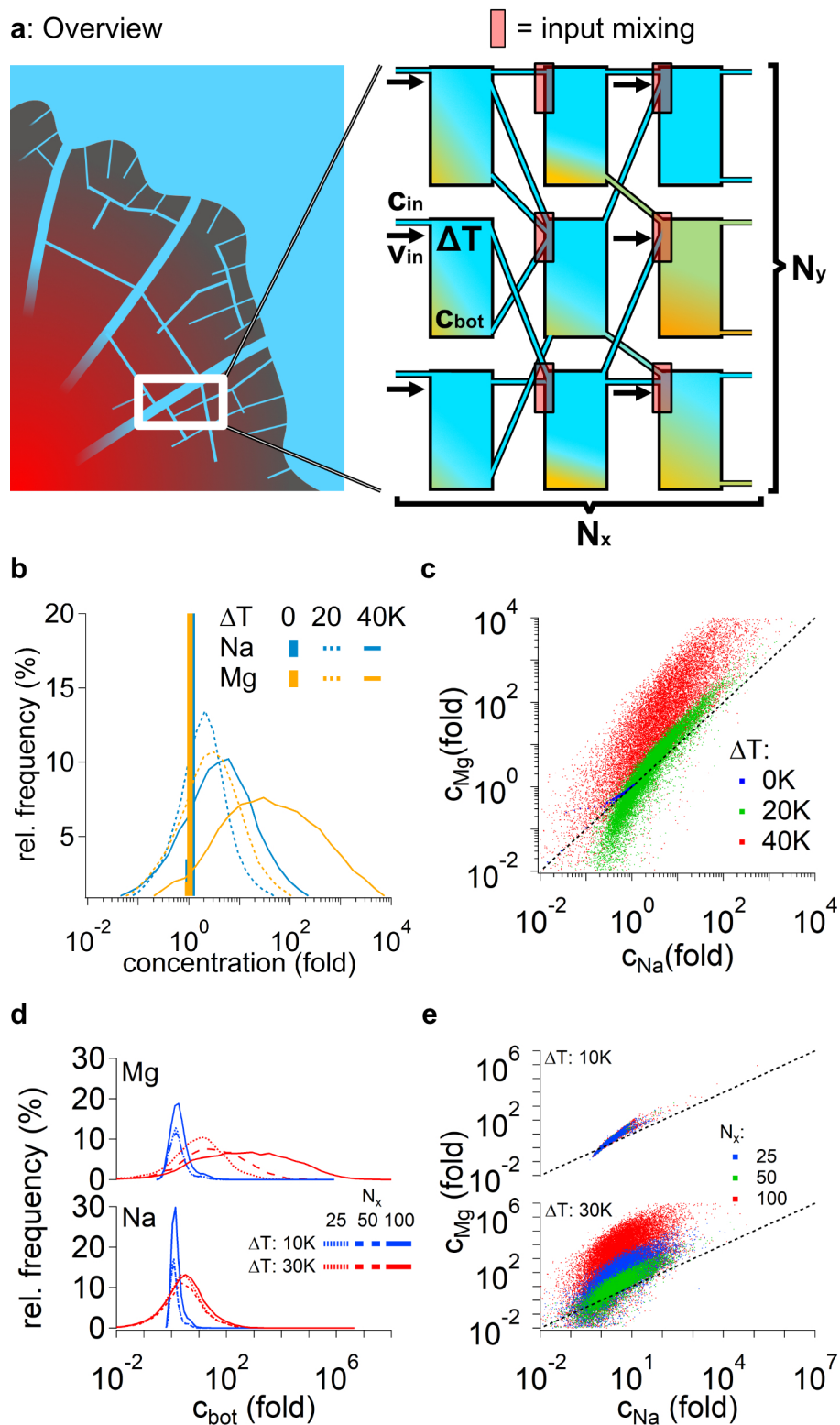


## b: optimized ribozyme design



**Extended Data Fig. 5 | Secondary structure diagrams of ribozymes.** Diagrams showing the initial (**a**) and final (**b**) concatemer ligation ribozyme designs. In the initial design **a**, regions of the substrate originating from R3C substrate A are shown in red, whilst regions originating from substrate B are shown in blue. In **b**, mutations made to reduce homodimer formation and promote substrate binding are highlighted in pink.





Extended Data Fig. 6 | See next page for caption.

**Extended Data Fig. 6 | Interconnected molecular traps mimicking branching rock fissures.** (a) Illustration of the system of interconnected molecular traps mimicking branching rock fissures in a realistic geological scenario. For a detailed description, see Supplementary Method 12 and Supplementary Figs. 13–19. (b) Statistics of the accumulated concentrations at the chamber bottom for different temperature differences. Histogram of resulting ion concentrations. With increasing temperature difference, magnesium ions (orange) are increasingly better accumulated, up to 4 orders of magnitude better than sodium ions (blue) at  $\Delta T=40$  K. (c) Correlation plot for magnesium and sodium concentrations. At higher temperature differences, magnesium is accumulated with increasing selectivity compared to sodium. (d) Scaling of the width of the chamber system. Histogram of the frequency of chambers with a given concentration of magnesium (top) and sodium ions (bottom) at the chamber bottom for different temperature gradients  $\Delta T=10$  K (blue) and 30 K (red) and system widths  $N_x = 25, 50, 100$  chambers. (e) Correlation plots of magnesium and sodium ion concentration at the chamber bottom at  $\Delta T=10$  K (top) and 30 K (bottom).

## Supplementary information

Supplementary Methods.....	3
Supplementary Method 1: Composition of sea waters .....	3
Supplementary Method 2: Ion chromatography .....	3
Supplementary Method 3: Data analysis for leaching experiments .....	3
Supplementary Method 4: Preparation of heat flow cells .....	4
Supplementary Method 5: Protocol for through flow salt separation in heat flow cells .....	5
Supplementary Method 6: pH measurement .....	5
Supplementary Method 7: Finite element simulation details .....	6
Chamber design. ....	6
Modelling of through flow salt separation. ....	7
Supplementary Method 8: Ribozyme design .....	7
Supplementary Method 9: RNA ligases in a heat flow cell .....	8
Supplementary Method 10: Ribozyme sensitivity on salt concentration and comparison with operation in heat flow cell.....	9
Supplementary Method 11: Optimal temperature of RNA ligase operation.....	10
Supplementary Method 12: Simulation of large systems of interconnected thermogravitational traps .....	10
Grid simulation.....	10
Variation of temperature difference. ....	11
Fluctuating vs. constant temperature difference. ....	12
Size of system.....	12
Study of behavior of other ions. ....	13
Variation of flow rates. ....	13
Supplementary Figures.....	15
Supplementary Figure 1: Leaching of salts from basaltic rock and glass .....	15
Supplementary Figure 2: Structure of heat-flow cells.....	17
Supplementary Figure 3: Detailed setup description.....	18
Supplementary Figure 4: Thermal design of the heat flow cell using finite element simulations.....	19
Supplementary Figure 5: Solutions of heat conduction, Navier-Stokes flow and coupled drift diffusion of the diluted salt species.....	20
Supplementary Figure 6: Additional trapping experiments – other salt species and control .....	21

Supplementary Figure 7: Secondary structure diagrams of ribozymes .....	22
Supplementary Figure 8: Fluorescence curves for the non-equilibrium experiments .....	23
Supplementary Figure 9: Salt screening of R3C replicator .....	24
Supplementary Figure 10: Screening of dry-down experiments .....	25
Supplementary Figure 11: Salt screening of RCL and R3C.....	26
Supplementary Figure 12: Testing different temperature conditions for RCL .....	27
Supplementary Figure 13: Illustration of the system of interconnected molecular traps mimicking branching rock fissures in a realistic geological scenario. ....	29
Supplementary Figure 14: Statistics of the accumulated concentrations at the chamber bottom for different temperature differences. ....	29
Supplementary Figure 15. Comparison of the behavior of the chamber system under constant or fluctuating temperature differences. ....	30
Supplementary Figure 16: Scaling of the width of the chamber system. ....	30
Supplementary Figure 17: Scaling of the height of the chamber system. ....	31
Supplementary Figure 18: Behavior of ions with similar Soret coefficients. ....	31
Supplementary Figure 19: Effect of different maximum flow rates through the system....	32
Supplementary Tables.....	33
Supplementary Table 1: Major and trace element composition of used geomaterials .....	33
Supplementary Table 2: Overview of different leaching experiments .....	35
Supplementary Table 3: Overview of different experimental conditions of heat flow cells	36
Supplementary Table 4: Thermophoretic and diffusive mobilities for salt species.....	37
Supplementary Table 5: RNA ribozyme and substrate sequences .....	37
Supplementary Table 6: DNA primer sequences and purposes.....	37
References for supplement .....	38
Supplementary Data Files of Gels .....	39
Supplementary Figure 9 Source images .....	39
Supplementary Figure 10 Source images .....	43
Supplementary Figure 11 Source images .....	44
Supplementary Figure 12 Source images .....	48

## Supplementary Methods

### Supplementary Method 1: Composition of sea waters

To probe the effect of different aqueous solvent compositions on leaching efficiency, we tested ultrapure water (MilliQ), presumed prebiotic sea water and hydrothermal sea water. The composition of the presumed prebiotic sea water in our experiments was inspired by McCollom<sup>1</sup> and Brown<sup>2</sup>. Following a combination of their recipes, we used: 479.439 mM NaCl, 9.5 mM NH<sub>4</sub>Cl, 4.85 mM KCl, 4.8 mM CaCl<sub>2</sub>, 1.3 mM NaHCO<sub>3</sub> and 0.433 mM KBr, resulting in a pH of 7.45. For the leaching experiments, MgCl<sub>2</sub> was omitted as its presence while analysing the amount of leached magnesium would make subsequent analysis of the latter via ion chromatography impossible. This was also done for low magnesium concentrations, no impact on the outcome of the leaching process was observed. The hydrothermal prebiotic sea water was mixed as described by de Ronde *et al.*<sup>3</sup>, preparing a solution of 633.98 mM NaCl, 42.59 mM CaCl<sub>2</sub>, 19.071 mM KOH, 5 mM NaOH and 2.61 mM KBr, giving us a pH of 11.366.

### Supplementary Method 2: Ion chromatography

An ion chromatography system (Dionex Aquion, ThermoFisher Scientific, USA) with an analytical column (Dionex IonPac CS12A), guard column (Dionex IonPac CG12A) and suppressor (Dionex CDRS 600) was used to measure salt concentrations. Three different methods are used throughout the analysis: method 1: 0.30 ml/min flow, isocratic elution with 25 mM MSA (Methanesulphonic acid), 22 mA suppression, method 2: 0.25 ml/min flow, isocratic elution with 20 mM MSA, 15 mA suppression, method 3: 0.25 ml/min flow, isocratic elution with 15 mM MSA, 11 mA suppression. For all methods, the following parameters were kept constant: cell temperature of 35 °C and column temperature of 30 °C. Eluted ions were detected with a conductivity detector (DS6 Heated Conductivity Cell). Data was analysed with Chromeleon 7.2.10 (ThermoFisher Scientific, USA). Integration was performed by automatic peak integration, except for experiments with prebiotic sea water and hydrothermal sea water where manual integration was used. For the thermal chamber experiment, integrals measured for the different outlets were compared to the inlet sample, recovered from the inlet tubing.

### Supplementary Method 3: Data analysis for leaching experiments

In order to compare the leached concentrations, the initial masses of the individual samples were normalized to one standard mass (30 mg). Supplementary Figure 1a and b show that for masses below 45 mg, this normalization can be done linearly in good approximation:

$$c_{norm}^l = c_{measure}^l * \frac{m^{ref}}{m} \quad (1)$$

where  $c_{norm}^l$  is the normalized concentration, shown in the plots,  $c_{measure}^l$  the measured leached concentration,  $m$  the mass of the sample and  $m^{ref}$  the reference mass (30 mg).

For the time evolution of tholeiite glass (Supplementary Figure 1d), the results were mapped to a different grain size: while the measurement was done at 355-500  $\mu\text{m}$  (indicated by the index (2) in the equation), the data was plotted for a grain size of 90-125  $\mu\text{m}$  (with index (1) in the equations) to make comparison with other leaching results. The converted leached concentration  $c_{(1)}^l$  was calculated for each salt species separately by:

$$c_{(1)}^l = c_{(2)}^l * \frac{c_{(1)}^{ref}}{c_{(2)}^{ref}} \quad (2)$$

with  $c_{(2)}^l$  being the measured leached concentration for 355-500  $\mu\text{m}$  and  $c_{(1)}^{ref}$  and  $c_{(2)}^{ref}$  the reference leached concentrations for the respective salt species from Supplementary Figure 1g for the different grain sizes. The error for the converted leached concentration  $\Delta c_{(1)}^l$  (for grain size 90-125  $\mu\text{m}$ ) was calculated by Gaussian error propagation as follows:

$$\Delta c_{(1)}^l = \sqrt{(\Delta c_{(2)}^l)^2 * \left(\frac{c_{(1)}^{ref}}{c_{(2)}^{ref}}\right)^2 + (\Delta c_{(1)}^{ref})^2 * \left(\frac{c_{(2)}^l}{c_{(2)}^{ref}}\right)^2 + (\Delta c_{(2)}^{ref})^2 * \left(\frac{c_{(2)}^l * c_{(1)}^{ref}}{(c_{(2)}^{ref})^2}\right)^2} \quad (3)$$

In this case,  $\Delta c_{(2)}^l$  are the standard deviations for the different timepoints of the measured leached concentrations,  $\Delta c_{(1)}^{ref}$  and  $\Delta c_{(2)}^{ref}$  are the standard deviations of the data point 90-125  $\mu\text{m}$  and 355-500  $\mu\text{m}$ , respectively (in Supplementary Figure 1g).

#### Supplementary Method 4: Preparation of heat flow cells

Bold numbers refer to the corresponding digits shown in Supplementary Figure 2a: The 170  $\mu\text{m}$  thick FEP-foil (**6**, Holscot, Netherlands) was cut into the selected shape using an industrial plotter (CE6000-40 Plus, Graphtec, Germany) and sandwiched between two sapphires (**5+9**, Kyburz, Switzerland) with thicknesses of 500  $\mu\text{m}$  (**5**, cooled sapphire, with 4 laser-cut holes of 1 mm diameter) and 2000  $\mu\text{m}$  (**9**, heated sapphire, no holes), respectively. The sapphire-FEP-sapphire block was then placed on an aluminum base (**3**) with an intermediary layer of heat conducting foil (**4**, EYGS091203DP, graphite, 25 $\mu\text{m}$ , 1600 W/mK, Panasonic, Japan) and held there by a steel frame (**10**) mounted with six torque-controlled steel screws for homogeneous force distribution. A second heat conducting foil (**11**, EYGS0811ZLGH, graphite, 200 $\mu\text{m}$ , 400 W/mK, Panasonic, Japan) is applied to thermally connect the heated sapphire (**9**) to the electric heating element (**12**), which is also fixed by torque-controlled steel screws. The heater body has milled holes to allow optical access to the system e.g. by fluorescence microscopy. The height of the microfluidic chamber was measured with a confocal micrometer (CL-3000 series with CL-P015, Keyence, Japan) at three positions (top, middle, bottom) to ensure homogeneous thickness along the chamber. The chambers were pre-flushed with low-viscosity fluorinated oil (3M™ Novec™ 7500 Engineered Fluid) to check for tightness and to

force out residual gas inclusions. The assembled chamber was then mounted onto an aluminium block cooled by a heat bath (Grant R5 and TXF200, Grant industries, UK) (1), again with a 200  $\mu\text{m}$  thick heat conducting foil (2, EYGS0811ZLGH, see above). The heating elements were connected to a 400 W, 24 V power supply and solid state relays controlled by Arduino boards with a customized version of the open-source firmware "Repetier", originally developed for 3D printing. A photo of the partly assembled components is shown in Supplementary Figure 2b.

### Supplementary Method 5: Protocol for through flow salt separation in heat flow cells

The in- and outlets of the heat flow cell were connected via tubing to syringes that are placed on high-precision syringe pumps (Low Pressure Syringe Pump neMESYS 290N with Quadruple Syringe Holder Low-Pressure, cetoni, Germany). For the microfluidic connections, we used the following (Techlab, Germany): connectors (Verbinder zöllig, UP P-702-01), end caps (Tefzel cap for 1/4-28 Nut, UP P-755), screws (Nut, Delrin, flangeless, VBM 100.823, VBM 100.824, VBM 100.825, VBM 100.826, VBM 100.827, VBM 100.828), ferrules (Ferrule VBM 100.632) and tubings (Tubing Teflon (FEP), KAP 100.969). The flow speeds of the syringe pumps (controlled via neMESYS UserInterface, cetoni, Germany) were selected as such that 5% of the inflow was removed from the top and bottom outlet, leaving 90% coming out of the middle outlet. The syringes used (Göhler-HPLC Syringes, Germany) are chemically resistant heavy-duty syringes with PTFE seals: 2606714, 2606814, 2606914, 2606015, 2606035, 2606055 and 2606075 (ILS, Germany). The cryostat (Grant TXF200-R5, UK) was set to  $-30^{\circ}\text{C}$  and the heating elements to  $95^{\circ}\text{C}$ , resulting in a temperature difference from  $20^{\circ}\text{C}$  to  $60^{\circ}\text{C}$  within the microfluidic chamber. The temperatures were measured on the surface of the sapphires with a heat imaging camera (ShotPRO Wärmebildkamera, EAN: 0859356006217, Seek Thermal, USA) on the heated side and a temperature sensor (GTH 1170, Greisinger, Germany and B&B Thermo-Technik 06001301-10, Germany) on the cold side.

Before starting experiments, all tubings and the thermal chamber were re-flushed with fluorinated oil. Samples were then loaded into the inlet tubing. Experiments were started and left running for 2-3 days. To stop experiments, the applied temperatures were set to room temperature to defrost the trap and check for possible problems of the experiment. The samples were recovered from the tubings and collected for measurement by ion chromatography. Due to volume constraints, the samples had to be diluted with MilliQ water 2 to 4 fold before injection.

### Supplementary Method 6: pH measurement

Measurement of the pH values for the different outflows was done using a Thermo Scientific™ Orion™ 9826BN Micro pH Electrode (Thermo Fisher Scientific, USA). The gradient observed was weak, with values close to neutrality and a slightly more neutral bottom:  $\Delta\text{pH} =$

$pH_{bottom} - pH_{top} = 0.57 \pm 0.16$  (inlet:  $6.64 \pm 0.23$ , top outlet:  $6.20 \pm 0.35$ , middle outlet:  $6.58 \pm 0.21$ , bottom outlet:  $6.77 \pm 0.39$ ).

### Supplementary Method 7: Finite element simulation details

*Chamber design.* In order to investigate the effect of thermal non-equilibria, i.e. temperature gradients due to heat flows on a system in a reproducible and modellable way, a temperature distribution along the x/y-axis as uniform as possible is necessary (see Supplementary Figure 4a). Along the z-axis, i.e. in the direction of the heat flow vertically through the thin water layer, the temperature drop should be as linear as possible. In principle, all results shown here can also be applied to more complex geometries and temperature curves<sup>4</sup> but it is then more difficult to obtain reproducible and modellable data. In order to achieve these goals, the experimental setup was rebuilt from scratch using three-dimensional finite element simulations. Special attention was paid to the heater shape, which should allow both an optical observation of the sample in the heat flow cell and uniform heating. This was achieved by the combination of a 2 mm thick sapphire on the hot chamber side, which compensates for thermal unevenness due to the viewing windows in the heater, while causing only a moderate temperature drop of about 14%, when compared to the total temperature difference between the cooled aluminum back and the heating element (see Figure 1). The model was created using 3D CAD software and imported into the finite element software (COMSOL 5.4). Thermal conductivities were taken from the COMSOL internal database or from the product data sheets of the materials used and are at room temperature  $k_{H_2O} \sim 0.62 \frac{W}{mK}$  for water,  $k_{Steel} \sim 44.5 \frac{W}{mK}$  for the steel frames,  $k_{Alu} \sim 237 \frac{W}{mK}$  for the aluminium elements,  $k_{Sapphire} \sim 35 \frac{W}{mK}$  for the sapphire elements and  $k_{FEP} = 0.2 \frac{W}{mK}$  for the FEP foils.

Since the space around the heat flow cells is fully covered, an approximately insulating thermal boundary condition for the heat flow through the outer surfaces of the full model was assumed (see Supplementary Figure 4a), i.e.  $Q|_{extSurface} = 0$ . The heat conduction was then calculated according to the equation

$$\rho c_p \left( \frac{\partial T}{\partial t} + \mathbf{u} \cdot \nabla T \right) + \nabla \cdot (k \nabla T) = Q \quad (4)$$

and solved for the entire structure, where  $\rho$  is the density,  $c_p$  the specific heat capacity and  $k$  the thermal conductivity of the respective material,  $T$  the temperature,  $Q$  the heat flow and  $\mathbf{u}$  the velocity vector of the solution in the chamber. In the stationary case, which in our experiment is reached after a few minutes, and assuming a very slow fluid velocity  $\mathbf{u}$  ( $\sim 35 \mu m/s$ , see Supplementary Figure 5), equation 1 simplifies to

$$\nabla T \cdot (k \nabla T) = Q \quad (5)$$

whose solution is shown in Supplementary Figure 4. The temperature distribution is homogeneous with maximum deviations of about 2 K on the hot side of the solution ( $z = 170 \mu m$ ), and less than 0.5 K on the cold side of the solution ( $z = 0$ ). Since optical access should be possible at the lower end of the chamber ( $y = 0$  to  $1.5 mm$ ), the temperature on



the hot side is only about 50 °C instead of 60 °C elsewhere ( $y = 1.5 - 50\text{mm}$ ). This is a small disturbance and only marginally affects the concentration of the solutes.

*Modelling of through flow salt separation.* Since the lateral temperature distribution was known from the above results, the thermal situation within the fluid chamber could be derived by measuring the temperatures on the outer sides of the cold and hot sapphire, respectively. The measurement of the outside temperature of the hot sapphire was performed with an IR camera, the outside temperature of the cold sapphire was measured by using a thermistor (S, see Supplementary Figure 4a) pressed against the sapphire from below. The resulting temperature distribution within the fluid could now be coupled to the Navier-Stokes equation via the temperature dependent density  $\rho(T)$  and viscosity  $\eta(T)$ :

$$\rho(T)(\mathbf{u} \cdot \nabla)\mathbf{u} = \nabla \cdot \left[ -p + \eta(\nabla\mathbf{u} + (\nabla\mathbf{u})^+) - \frac{2}{3}\eta(\nabla \cdot \mathbf{u}) \right] - \mathbf{e}_y \cdot g\rho(T) \quad (6)$$

Where  $\mathbf{u}$  is the velocity vector of the fluid,  $p$  is the local pressure,  $\mathbf{e}_y$  is the unit vector in  $y$ -direction and  $g$  is the gravitational acceleration. After setting a non-slip boundary condition at all surfaces except at the in- and outlets, where the respective volume flow rate used in the experiment was assumed, a complete numerical solution for  $\mathbf{u}$  could be found (see Supplementary Figure 5a-c).

To determine the selective concentration of different salt species, the numerical model was further extended by a drift-diffusion component. This includes thermophoresis, i.e. the movement of the dissolved salt ions along the temperature difference, normal diffusion, which counteracts local concentration gradients and the coupling to the velocity field of the solution  $\mathbf{u}$ :

$$\nabla \cdot (-D_i \nabla c_i + (\mathbf{u} + S_{T,i} D_i \nabla T) \cdot c_i) = 0 \quad (7)$$

Here  $D_i$  is the normal diffusion coefficient,  $c_i$  the local concentration and  $S_{T,i}$  the Soret coefficient of the respective salt species. The latter is defined by the ratio of thermophoretic to diffusive mobility  $S_{T,i} = D_{T,i}/D_i$ . The coupling to equation 2 and 3 is done by the temperature  $T$  and the velocity field  $\mathbf{u}$ . The values for  $S_{T,i}$  and  $D_i$  were taken from the literature (see Supplementary Table 4). Electrostatic interactions of the ions are already included in the Soret coefficients, since they were also found experimentally, in this case using a ratio cell according to Turner<sup>5</sup>. Due to the only moderate local concentration differences (factor 10 over 50 mm), no electrostatic interactions were therefore considered. One exemplary solution for equation 4 is shown in Supplementary Figure 5d, other results are given in the main text, Figure 3.

### Supplementary Method 8: Ribozyme design

The optimised self-replicating R3C ribozyme developed by Robertson and Joyce<sup>6</sup> was used as a model system for these experiments. The ribozyme ( $E_R$ ) ligates two fragments (A and B) to form a copy of itself. A modified ribozyme substrate capable of concatemer ligation was

produced from substrate fragments A and B. First, three 5' bases of substrate A were deleted, then substrate B was appended at the new 5' end of fragment A. The catalytic stem loop in A was then removed, yielding a 31 nt fragment. This initial design is shown in Supplementary Figure 7a. To reduce substrate homodimer formation and promote ribozyme-substrate binding, five point mutations were introduced to substrate strand BA (G16C, U18G, G19C, G22U, U24G), whilst five point mutations and a deletion were made in the substrate binding arm of the ribozyme E (G55U, C57A, C60G, A61C, C63G, 66del), yielding substrate BA and ribozyme E<sub>L</sub>, shown in Supplementary Figure 7b.

All RNA and DNA sequences were purchased from IVT (eurofins Genomics, Germany) or IDT (Integrated DNA Technologies, USA), as stated in Supplementary Tables 5 and 6.

### Supplementary Method 9: RNA ligases in a heat flow cell

To demonstrate that the various ribozymes were able to function in the selectively concentrating heat flow environment, we ran ligation reactions whilst monitoring distribution of RNA within the cell. To do this, we measured the local RNA concentrations via fluorescence of the substrate 5' Cy5 tag (100% of replicator substrate A, 10% of ladder substrate BA) at both the top and bottom positions of the cell, and compared these to initial values. The temperatures of the hot and cold sides were set at 60°C and 20°C, as previously described. The sides of the cell were set 170 µm apart, and no flow through the chamber was applied. RNA concentrations for the replicator reaction were fixed at 0.5 µM ribozyme E<sub>R</sub>, 1 µM substrate A (100% Cy5 tagged) and 1 µM substrate B, and for the ladder reaction at 0.5 µM ribozyme E<sub>L</sub> and 1 µM substrate BA (10% Cy5 tagged). All reactions were performed in Tris-HCl buffer (25 mM, pH 8.5) with varying MgCl<sub>2</sub> (0.00625-8 mM). In these experiments it was assumed that upstream flow cells have already improved salt conditions to the point that the NaCl concentration is negligible (Figure 4). Supplementary Figure 8 shows that the RNA is concentrated by factors of 10 and 13 for the replicator and ladder systems, respectively. The somewhat higher concentration of the ladder ribozyme system is due to the longer overall length of the ligated products: In general, longer nucleic acid strands have a larger Soret coefficient and are therefore more efficiently concentrated in a thermal trap<sup>7,8</sup>. Following incubation, aliquots of the reactions were quenched in 4 volumes of loading buffer, and the products separated using 15-20% urea PAGE. In order to determine the ligation yield  $L_{R3C}$  of the replicase, the intensity of the fluorescence signal  $I_p$  of the gel bands of a product  $p$  was corrected with respect to their local environment  $I_{bg,p}, I_{bg,S}$  and compared with the total unhydrolyzed amount of substrate  $I_S$  and product:

$$L_{R3C} \equiv \frac{I_p - I_{bg,p}}{(I_S - I_{bg,S}) + (I_p - I_{bg,p})}$$

Analogously, in the case of the RCL system, the ligation yield  $L_{RCL}$  is defined as the quotient of the sum of the amounts of all products  $I_{p,n}$ , which consist of  $n$  substrate pieces, over the total amount of unhydrolyzed RNA:

$$L_{RCL} \equiv \frac{\sum_{i=1}^{\infty} (I_{p,n} - I_{bg,p,n})}{I_s - I_{bg,s} + \sum_{i=1}^{\infty} (I_{p,n} - I_{bg,p,n})}$$

Quantifying hydrolysis by comparing total intensity at  $t = 0\text{h}$  and  $t = 2\text{h}$  is non-trivial due to variations in gel loading, sample recovery from the heat flow cell and hydrolytic cleavage of the Cy5 tag from the RNA. In order to quantify hydrolysis in the simple replicator system, we therefore considered all gel bands below the unligated substrate band as partially hydrolysed material (Supplementary Figure 9e). We calculated the amount of hydrolyzed material ( $H_{R3C}$ ) as the ratio of the summed intensity of these bands ( $I_H$ ) to the summed intensity of the whole lane ( $I_p + I_s + I_H$ ):

$$H_{R3C} = \frac{I_H - I_{bg,H}}{(I_s - I_{bg,s}) + (I_p - I_{bg,p}) + (I_H - I_{bg,H})}$$

For the ladder ligase system, any degradation of the extended products leads to a set of degradation product bands that overlays the ligation products. In addition, the smallest degradation products may run off the gel due to the lower acrylamide percentage used in these experiments. We have therefore not used this method to quantify degradation in this system.

#### Supplementary Method 10: Ribozyme sensitivity on salt concentration and comparison with operation in heat flow cell

As already noted in the main text, we investigated the operating range for both ribozymes (R3C ladder, R3C replicator) for a wide range of concentrations of  $\text{MgCl}_2$  and  $\text{NaCl}$ . As shown in Supplementary Figure 9, ribozymes can be already limited in their function at a  $[\text{Mg}]:[\text{Na}]$  ratio of 1:10.

*Ladder ribozyme (RCL).* Under thermal equilibrium conditions, the ladder ribozyme is functional without  $\text{NaCl}$  above a  $\text{MgCl}_2$  concentration of 1 mM, whereas a product is only detectable at 4 mM  $\text{MgCl}_2$  when 10 times the amount of  $\text{NaCl}$  is present (Supplementary Figure 9a vs. 9c). Reaction conditions were constant temperature of 35 °C for 2 h. The solution contained 0.5  $\mu\text{M}$  enzyme, 10 mM Tris, 1  $\mu\text{M}$  unlabelled substrate and 0.1  $\mu\text{M}$  Cy5 labelled substrate to allow the PAA gel analysis shown in Figure 5. For comparison, Supplementary Figure 9c also included samples that were previously incubated under non-equilibrium conditions in the heat flow cell (20-60 °C, 2 h, 170  $\mu\text{m}$  chamber thickness), in which product can be obtained at 0.25 mM  $\text{MgCl}_2$ , enabled by the co-concentrated magnesium salt. At a 1000-fold  $\text{NaCl}$  excess compared to the respective  $\text{MgCl}_2$  concentration, any ribozyme function is completely inhibited.

*Replicator ribozyme (R3C).* The replicator ribozyme is more robust at low concentrations of  $\text{NaCl}$ : without added  $\text{NaCl}$  and under the thermal equilibrium conditions specified above,

function is detectable from 0.5 mM  $\text{MgCl}_2$ , as well as in the presence of 10 times the amount of NaCl (also see Figure 4b in main text). Under thermal non-equilibrium conditions (settings: see above) the replicator enzyme without NaCl is active at 0.25 mM  $\text{MgCl}_2$ . As before, a 1000-fold excess of NaCl over the respective  $\text{MgCl}_2$  concentration completely inhibits the function of the ribozyme. This shows that even small amounts of NaCl can have a negative effect on ribozyme function.

### **Supplementary Method 11: Optimal temperature of RNA ligase operation**

To allow an optimal comparison between thermal equilibrium (free solution) and non-equilibrium conditions (heat flow cell), the RNA ligase was first exposed to different thermal conditions. In free solution, consisting of 0.5  $\mu\text{M}$  ribozyme  $E_L$ , 1  $\mu\text{M}$  substrate, 0.1  $\mu\text{M}$  Cy5-labeled substrate, 25 mM Tris pH 8.5 and 1 mM  $\text{MgCl}_2$ , different constant temperatures between 5 and 55 °C in 10 K steps were applied. For all experiments, the reaction time was set to 2 hours. The results depicted in Supplementary Figure 12 show that the ribozyme used can catalyse the ligation of the substrate strands at low temperatures, but is most efficient at about 35°C. Higher temperatures lead to significantly lower product yields and degradation by hydrolysis. In the experiments shown in the main text we have therefore used the optimal temperature of 35°C for the equilibrium experiments and a still realistic temperature range of 20°C to 60°C for the non-equilibrium experiments in the heat flow cell. Since the charged RNA strands will be located rather on the cold side of the heat flow cell due to the thermophoresis, we expect a correspondingly lower hydrolysis compared to the conditions in free solution.

### **Supplementary Method 12: Simulation of large systems of interconnected thermogravitational traps**

The examples given in the main text (in particular Figure 5d-e) were limited to a special case in which several traps follow each other in a defined manner. A constant influx of fresh water was assumed and thus a large accumulation of magnesium salts with simultaneous depletion of sodium salts was achieved. The question therefore arises whether this special case is representative of large systems of interconnected thermogravitational traps, or whether it is merely a stroke of luck. In the latter case, the use of the discussed system for prebiotic scenarios would be limited.

*Grid simulation.* To address this question, we extended the simulation of a single thermogravitational molecular trap (discussed in main text Figure 3 and in the SI) to a large system of interconnected traps. Since this requires the consideration of thousands of traps to obtain the necessary statistics and the calculation of such large systems by finite element methods is not reasonable due to the long calculation time, we resorted to a two-step procedure:

1. We modified the geometry shown in main text Figure 3 by removing the exit at mid-chamber height so that there is now one entrance (top) and two exits (top, bottom).

We then calculated the properties of a single thermal trap for a total of 600 different parameter sets:

- a. Temperature difference between the chamber surfaces (0 K, 10 K, 30 K, 50 K, 70 K).
  - b. Influx into the chamber (1 nl/s, 5 nl/s, 10 nl/s, 20 nl/s, 50 nl/s, 100 nl/s).
  - c. Proportion of the flow which is going out through the lower outlet, which also determines the flow through the upper outlet (1 %, 5 %, 10 %, 20 %, 50 %).
  - d. Different salt species (Na, Ca, Mg, K) with their values of Soret and diffusion coefficients as shown in Supplementary Table 4.
2. We then created virtual systems of interconnected chambers (see Supplementary Figure 13) using a homemade LabVIEW program, which are arranged in a matrix pattern with a width of  $N_x$  chambers and a height of  $N_y$  chambers. Each of these chambers has an upper inlet where the previously determined concentrations  $c_{in}(salt, channel)$  of all salt species from the different incoming channels are taken. Considering the corresponding inflow velocities  $v_{in}(channel)$ , this yields new effective concentrations for each species as well as a summed inflow velocity at the upper inlet. Here, perfect mixing of all channels present at the inlet was assumed, which is the worst-case scenario in our case. The flow through the chamber then splits randomly between the upper and lower outputs, which is expected to approximately reflect random geometric properties of the chamber. In this case, the exits themselves can each be connected to up to three other chambers in the next column between which the flow splits randomly as well. For each split, mass conservation of the salt species and the flow medium is ensured.

Overall, this results in a system of chambers in which the fluid flows from left to right, switching between the different rows from one column to the next. Each column corresponds to  $N_y$  independent traps. For the different temperature gradients  $\Delta T$  of the traps, the accumulation of all salt species in a chamber relative to the input concentration is determined from the set of solutions precalculated using finite element methods. This then yields the non-equilibrium steady state concentrations at the top and bottom of the trap, which determines the corresponding flux densities of the outputs. Since the randomly generated trap parameters (e.g. temperature difference  $\Delta T$ , flow rate down/up) are not necessarily equal to the previously calculated parameter sets, but may lie in between, we determined the solution of intermediate parameter sets by 4-dimensional linear interpolation. Thus, a large number of systems of interconnected thermogravitational chambers could be calculated very quickly. It was always ensured that the computational parameters used in the system simulation (temperature difference, flow rate, outflow fractions and salt species) were not outside the parameter range covered by the finite element simulation (e.g., temperature difference  $>70$  K, etc.).

*Variation of temperature difference.* First, we consider the statistics of a total of 100 systems, each with a size of  $N_x = 50$  and  $N_y = 5$ , an initial flow rate of 1 nl/s (rate of inflow at the chambers of the first column), a normalized inlet concentration ( $c_{in,x=1} = 1$ ) and a fixed temperature difference  $\Delta T$  between 0 K, 20 K and 40 K (Supplementary Figure 14), i.e.  $25e3$  chambers. In Supplementary Figure 14a, the relative frequency of chambers with a given accumulated concentration of magnesium or sodium salts at the bottom of the chamber is

shown as a histogram. If no temperature difference is present, concentration is 1 in all chambers as expected ( $\Delta T = 0 K$ ). With larger temperature differences, an increasing proportion of chambers show high salt accumulations. Magnesium ions are accumulated more strongly (up to  $1e4$ -fold) in contrast to sodium ions, as expected. A correlation plot (Supplementary Figure 14b) shows the selective ion enrichment per trap, where the distance of an accumulation state ( $c_{Mg}, c_{Na}$ ) to the black dashed line ( $c_{Mg} = 1, c_{Na} = 1$ ) indicates the respective selectivity. Despite the random mixing of the traps by the connecting channels, selection in favor of magnesium ions is achieved with up to 3 orders of magnitude at  $\Delta T = 40K$ .

*Fluctuating vs. constant temperature difference.* Next, we considered 100 systems of  $N_x = 50$  by  $N_y = 5$  chambers with the same boundary conditions for initial influx as above, but now with fluctuating temperature differences between different chambers. We compared this with chambers that are exposed to the corresponding average temperature difference, e.g. 0-20 K (fluctuating) and 10 K (constant mean), see Supplementary Figure 15. Subfigure **a** again shows the relative frequency of chambers with defined accumulated ion concentrations at the chamber bottom ( $c_{bot}$ ) for magnesium (orange) and sodium (blue). A system with identical temperature differences for all chambers (solid line) is compared to one with randomly selected temperature differences between a defined range (dashed line) for each individual chamber. In addition, the case without temperature difference (black) is shown. The differences between the constant and changing temperature gradients are particularly apparent for magnesium, for which concentrations of up to a factor of 100 can be achieved despite mixing of highly enriched fluxes with the outputs of low-accumulation chambers (with lower temperature differences). Subfigure **b**) shows that for the case of temperature differences varying from chamber to chamber, there is greater selectivity (up to a factor of 100, lower part of figure) compared to temperature differences of the same average magnitude that are constant for all chambers (up to a factor of 10, upper part of figure). Selectivity is defined here as the deviation from the equilibrium concentration line  $c_{Na} = c_{Mg}$  (black, dashed). This behavior is expected since the accumulation due to thermal trapping increases non-linearly with the temperature gradient.

All results presented here are valid for the non-equilibrium steady state, where a persistent physical non-equilibrium (here the heat flux) leads to certain, temporally constant, concentration ratios in the accumulation chambers. The case of temporally fluctuating temperature differences can only be inadequately predicted by numerical simulations for such large systems due to the computational effort required. For small temperature fluctuations on a time scale faster than the relaxation time of the accumulation dynamics, a behavior similar to that of a chamber with a constant temperature difference corresponding to the mean value of the fluctuations is expected. If the temperature fluctuation takes place on a larger time scale, the entire chamber system will adjust to the new situation after each change in the temperature difference and should thus be like the results shown in Supplementary Figure 15.

*Size of system.* An interesting further question is how the selectivity and behavior of the chamber system scales with the size of the overall system while keeping the chamber properties constant. In our simplified example, the chambers were arranged in rows and

columns, with one column always connected to the next by randomly arranged channels. If we now increase the number of columns per system ( $N_x$ ), this means that the solution must flow through more chambers until it exits the system again. In Supplementary Figure 16a, a histogram for the concentration at the chamber bottom is shown for 100 systems of size  $N_y = 5$  with different values for  $N_x = 25, 50, 100$  (subplots for sodium and magnesium ions at a temperature difference of  $\Delta T = 10 K$  (blue) and  $\Delta T = 30 K$  (red), with maximum flow speeds used as above (1 nl/s)). For both cases, the ability of the system to accumulate ions increases with  $N_x$ , but the increase is more pronounced for larger  $\Delta T$ . Supplementary Figure 16b shows that this applies even more clearly for the selectivity, since for some chambers, magnesium ions are accumulated much stronger than sodium ions.

If we now scale the height  $N_y$  of the systems instead of the width  $N_x$ , we obtain a behavior as shown in Supplementary Figure 17 for the same boundary conditions when simulating 100 systems. In subfigure a, the histograms of the ion concentrations (magnesium: top, sodium: bottom) at the chamber bottom are shown for temperature gradients of  $\Delta T = 10 K$  (blue) and  $\Delta T = 30 K$  (red) and system heights  $N_y = 5, 10, 15$  chambers. It is clear that there are no amplifying effects when increasing the size of the system. This is reasonable as more rows only increases the throughput of the system, but does not change the number of chambers the solution must pass on average when flowing from left to right ( $x = 0$  to  $x = N_x$ ). Supplementary Figure 17b shows the corresponding correlation plots analogous to Supplementary Figure 16, which show no increased selectivity by increasing  $N_y$ , as expected.

*Study of behavior of other ions.* So far, we have focused on sodium and magnesium ions, since they have a major influence on the function of RNA enzymes. If we also consider other ions, such as potassium or calcium, it becomes clear that these show an almost identical behavior as sodium and magnesium, respectively, due to the very similar Soret coefficients. Supplementary Figure 18a again shows the histograms of the ion concentrations at the chamber bottom for  $\Delta T = 10 K$  (top) and 30 K (bottom) for sodium (blue), magnesium (orange), calcium (purple) and potassium (green). We then simulated a matrix of  $N_x=50$  times  $N_y=5$  heat flow cells 100 times. Calcium is accumulated to a similar extent as magnesium, and potassium to a similar extent as sodium. In Supplementary Figure 18b, the correlation plots between sodium and potassium (top) show that these two ions can be separated only slightly, i.e., up to an order of magnitude at 30K temperature gradient. In the case of magnesium and calcium, even less selective behavior is observed.

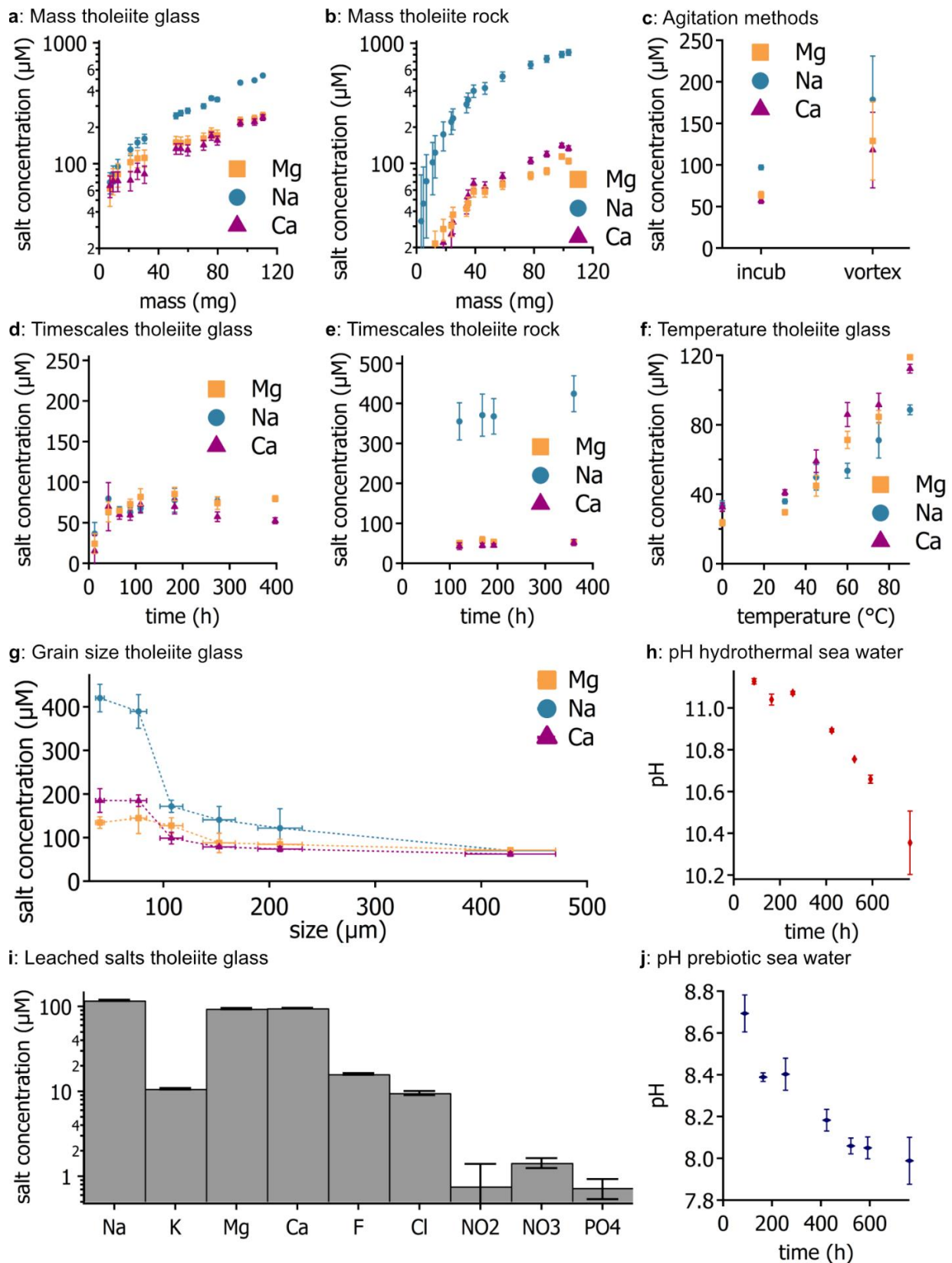
*Variation of flow rates.* So far, all systems were simulated with an initial maximum flow rate per trap of 1 nl/s. This means that the chambers in the first column were filled with randomly selected rates between 0 and 1nl/s. All other flow rates result from the arrangement of the connecting channels and the proportion of liquid flowing out of the lower chamber outlet. It is therefore still interesting to know how the system performs for different maximum flow rates. The statistics of 50 systems of size  $N_x = 50$  times  $N_y = 5$  is shown in Supplementary Figure 19 for a temperature difference  $\Delta T = 30 K$  and maximum flow rates of  $v_{flow,max} = 1$  nl/s, 10 nl/s and 50 nl/s. In subfigure a, the histogram of ion concentrations for sodium (top, blue) and magnesium (bottom, orange) at the chamber bottom is shown. An increased flow rate lead to more disturbances in the system and thus the accumulation of ions can no longer take place as effectively. In subfigure b, the correlation plot between the ion concentrations

of magnesium and sodium at the chamber bottom is shown. Here, too, it is clear that the selectivity, i.e. the deviation of the phase space points from the equiconcentration line  $c_{Na} = c_{Mg}$  (black, dashed), decreases with increasing flow rate. However, this is only a drawback to a certain extent, since if the system is increased in size, the flow rate would also decrease if applying the same pressure difference. This would then lead to a twofold amplifying effect of ion concentration and selection, once as shown in Supplementary Figure 16 and once as shown Supplementary Figure 19.

It can thus be summarized that the results shown in the main text Figure 5d-e are on average also valid for more complex systems and thus represent a realistic scenario for natural selection and optimization of salt conditions for prebiotic chemistry.

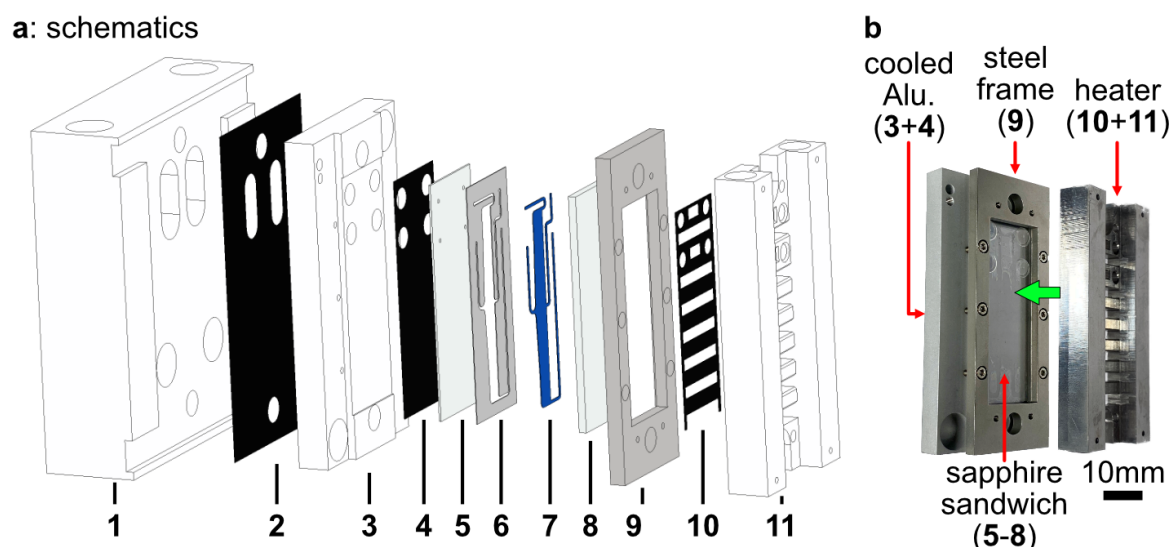


## Supplementary Figures

**Supplementary Figure 1: Leaching of salts from basaltic rock and glass**

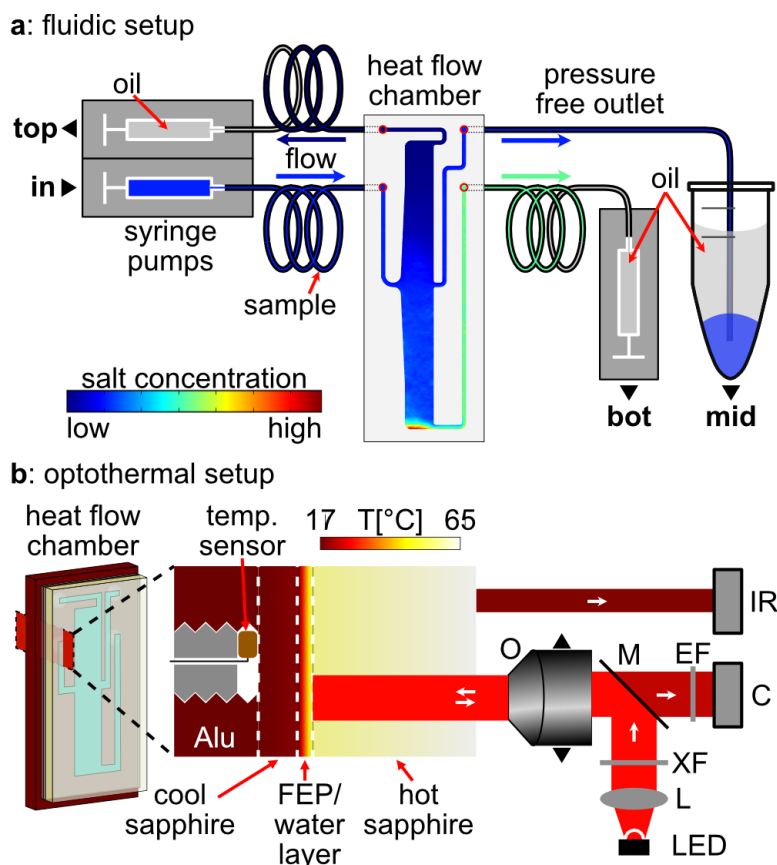
Except where stated otherwise, 30 mg of sample were leached at 60 °C in 150 µl ultrapure water without agitation. Error bars are calculated by using the standard deviations from

multiple measurements (numbers of measurements are shown in Supplementary Table 2) except for the mass dependence where no triplicates were possible. There, error bars from similar measurement conditions were used, as introduced below where applies. **(a)** Tholeiite glass samples with grain size of 90-125  $\mu\text{m}$  and a weight of up to 120 mg were leached at 60 °C in 150  $\mu\text{l}$  pure water for 110 h. Magnesium and calcium concentrations remain at similarly low levels (200  $\mu\text{M}$ ), while sodium concentration exceeds by up to a factor of three. Standard deviations are taken from g, grain size 90-125  $\mu\text{m}$ . **(b)** Tholeiite rock samples of 90-125  $\mu\text{m}$  size were leached for 36 h under the same conditions as in a. The sodium concentrations are up to 10 times higher than those of magnesium and calcium ions, both being at 100  $\mu\text{M}$ . Error bars are taken from e. **(c)** Agitation methods on tholeiite glass, 90-125  $\mu\text{m}$  for 16 h at 60 °C. While continuous agitation (= vortexing) increases leached concentrations compared to prebiotically more plausible incubation, the difference remains low. **(d)** Characteristic equilibration timescales for tholeiite glass, as shown for magnesium in the main text, Figure 2. Timescales are around 30 hours. The grain size used here is 355-500  $\mu\text{m}$ . For comparison with e, the leached concentrations are converted to 90-125  $\mu\text{m}$  grains using the grain size dependence from g (see Eq. 6). Error bars are calculated via Gaussian error propagation as shown in Equation 7. **(e)** Characteristic equilibration timescales for basaltic rock of grain size 90-125  $\mu\text{m}$  under the same conditions as in d. **(f)** Basalt glass samples of 355-500  $\mu\text{m}$  grain size were leached for 48 h at varying temperature under otherwise identical conditions as in a. The leached salt concentrations increase with temperature but stay at low levels. **(g)** Grain size dependence of leached salt concentrations for tholeiite glass, incubated at 60 °C for 95 h. **(h)** pH values over time for tholeiite glass samples (355-500  $\mu\text{m}$ ) in hydrothermal sea water, 60 °C. A slow shift towards less basic pH values can be observed. **(i)** Complete picture of leached ions from tholeiite glass (grain size 125-180  $\mu\text{m}$ , 110 h, 60 °C, pure water). In the first place, sodium (120  $\mu\text{M}$ ) is leached with magnesium and calcium (both 90  $\mu\text{M}$ ) following at lower concentrations. Fluoride, chloride and potassium are detectable at low concentrations (all 10-20  $\mu\text{M}$ ). Other trace elements such as phosphate, nitrite and nitrate are present but below 2  $\mu\text{M}$ . **(j)** pH evolution of basaltic glass samples in prebiotic sea water (other conditions identical to h). The trend towards lower pH values remains the same as for hydrothermal sea water.



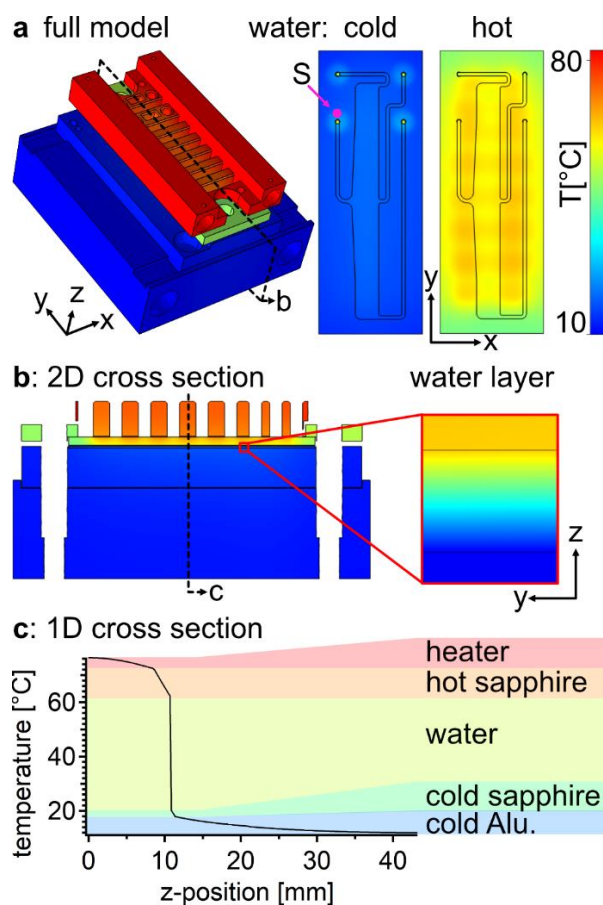
### Supplementary Figure 2: Structure of heat-flow cells

(a) All layers of the thermal microfluidics shown as described in the text. Cryostat cooled aluminium block (1), heat conducting graphite foils (2,4,11), aluminium base (3) that holds the sapphire sandwich, that consists out of a bottom sapphire with holes (5), FEP sheet with cut microfluidics (6) containing the liquid sample (7), and top sapphire (9). The top sapphire is heated by an aluminium element (12) with mounted Ohmic heaters and fixed on a steel frame (10) that ensures tightness of the complete system. (b) Photo of partially assembled system. Numbers correspond to digits shown in a.



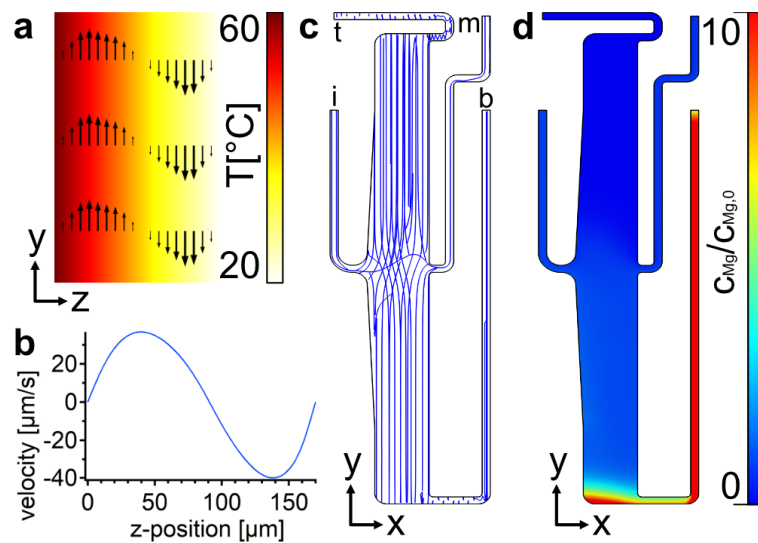
### Supplementary Figure 3: Detailed setup description

(a) Fluidic setup. Microfluidic access to the heat flow cell is implemented by backside connection of FEP tubing through the four access holes on the backside aluminium and sapphire pieces (see Supplementary Figure 2). Slow geothermal convection is mimicked by a slow through flow, controlled by three high precision syringe pumps with a constant volume rate. One pump (**in**) provides positive pressure and injects fresh sample into the chamber. The remaining two pumps (**top**, **bot**) provide negative pressure and remove the sample from the top or bottom output, respectively. The centered output (**mid**) releases the remaining pressure to an open Eppendorf tube. To minimize possible detrimental surface interactions, the complete system including chamber, tubing and syringes is pre-flushed with fluorinated oil. After the experiment, samples from **bot**, **mid** and **top** are recovered from the tubing and analyzed via IC. (b) Optothermal setup. Special care was taken to precisely determine the temperature inside the microfluidic layer: A temperature sensor is directly in contact with the cold sapphire from the backside and held in place via a UNF screw (grey). The surface temperature of the hot sapphire is measured with an IR camera (**IR**). The temperature field inside the liquid is then calculated from the known heat conductivity of the sapphire layers. Fluorescence measurements of the RNA reaction were obtained using a custom-made, motorized fluorescence microscope comprising an objective (**O**, TL4/2X-SAP, Thorlabs), dichroic mirror (**M**), excitation and emission filters (**XF**, **EF**, Cy5 Kit XF416, Laser Components), a lens (**L**) that collimates the light from a LED (**LED**, M625L3, Thorlabs) and a camera (**C**, Stingray 145-B, Allied Vision).



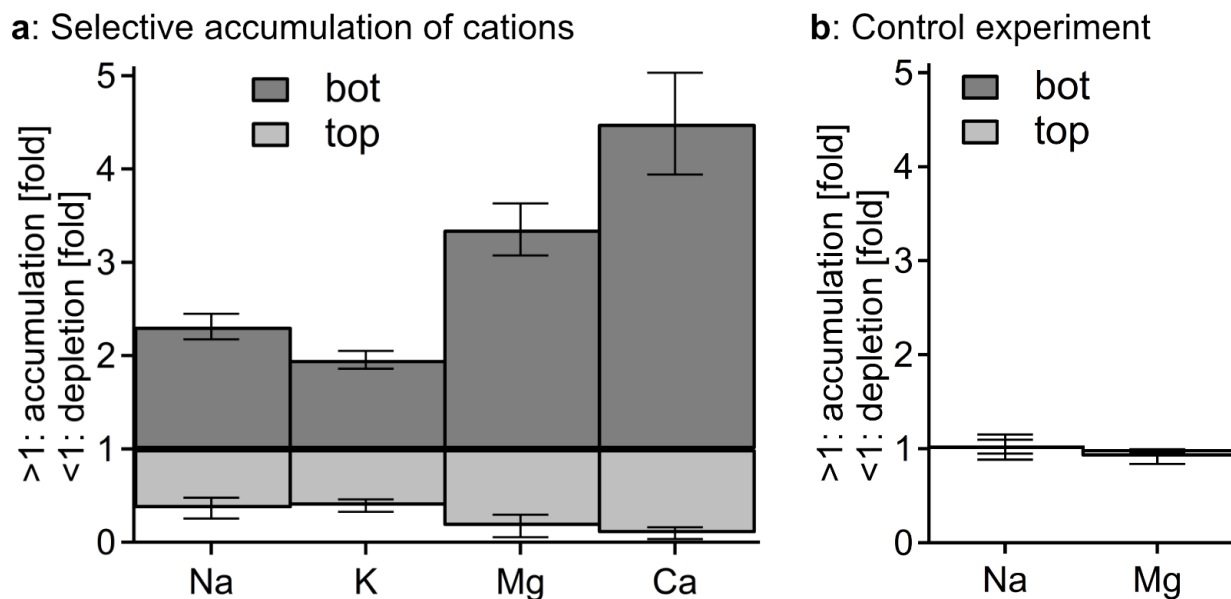
#### Supplementary Figure 4: Thermal design of the heat flow cell using finite element simulations

(a) The full three-dimensional model including all elements shown in Supplementary Figure 2. The temperature was measured on the cold aluminum base and on the heating element by thermistors and kept constant under PID control. The temperatures on the hot and cold sapphire are measured with an IR camera and a thermistor (S), respectively, and compared to the calculated 2D temperature distribution. Thus, the temperature distribution on the cold or hot side within the microfluidic chamber can be derived. (b) The two-dimensional average of a depicts the calculated temperature distribution on the z-y surface in the center of the chamber, showing the uniform temperature distribution along the y-axis. (c) One-dimensional average of b. Most of the temperature difference is effective in the microfluidic chamber filled with aqueous solution.



**Supplementary Figure 5: Solutions of heat conduction, Navier-Stokes flow and coupled drift diffusion of the diluted salt species**

(a) The temperature field of 20 to 60 °C is obtained by previous simulations and measurements (see Supplementary Figure 4) and modulates the local density of the fluid. (b) This results in a convective flow within the microfluidic chamber, also called microconvection, which has a maximum flow velocity of 37 μm/s and -40 μm/s respectively. (c) We also take into account a large-scale geothermal drift by applying a slow flow (here: 10 nl/s) through the chamber from the inlet (i). The flow lines indicate a small thrust in the x-direction as soon as the fluid passes the z-position of the inlet. Outlet positions are indicated by t (top), m (mid) and b (bottom). (d) Using the previous solution of thermal field and fluid velocity, a solution for the combined drift-diffusion problems, including thermophoresis and ordinary diffusion, can be obtained.



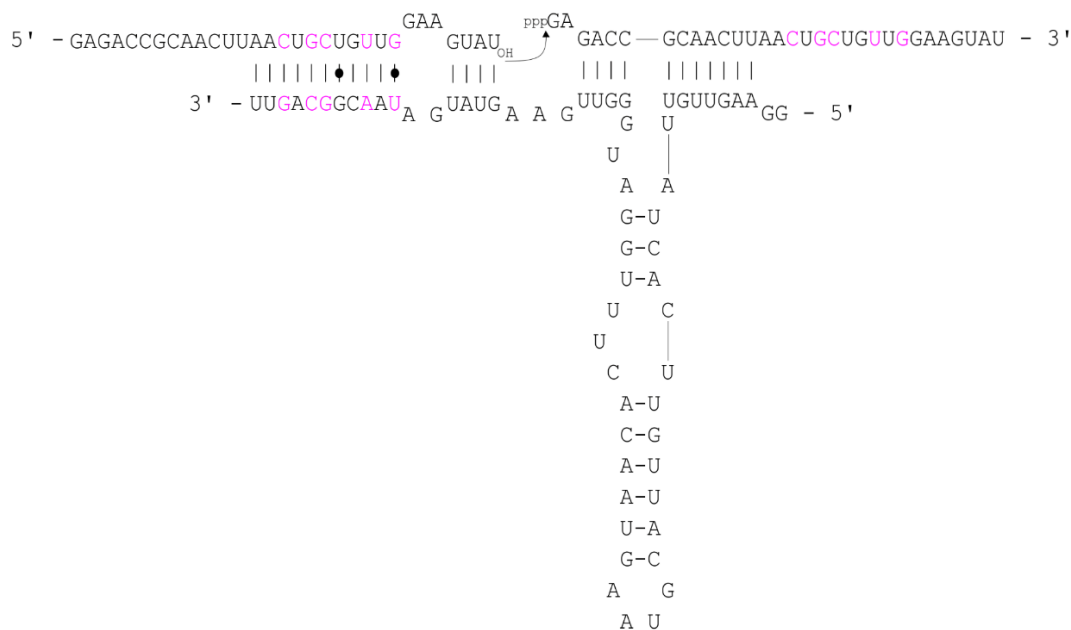
**Supplementary Figure 6: Additional trapping experiments – other salt species and control**

Errors bars represent the standard deviation calculated from data provided in Supplementary Table 3. **(a)** Selective accumulation of sodium, potassium, magnesium and calcium. In an experiment similar to Figure 3, main text, samples of 1.5 mM of all salts were pushed through the microfluidic chamber at 11.8 nl/s applying a temperature gradient of 40 K to analyze selective accumulation. As shown, sodium (2.3-fold) and potassium (2-fold) are less accumulated at the bottom than magnesium (3.4-fold) and calcium (4.5-fold). Together with a top outlet that is mainly depleted in the latter but also has reduced concentration of Na and K, this opens the door to many different salty habitats. **(b)** Control experiments with no applied temperature gradient show (as expected) no shift of salt concentrations.

## a: initial ribozyme design

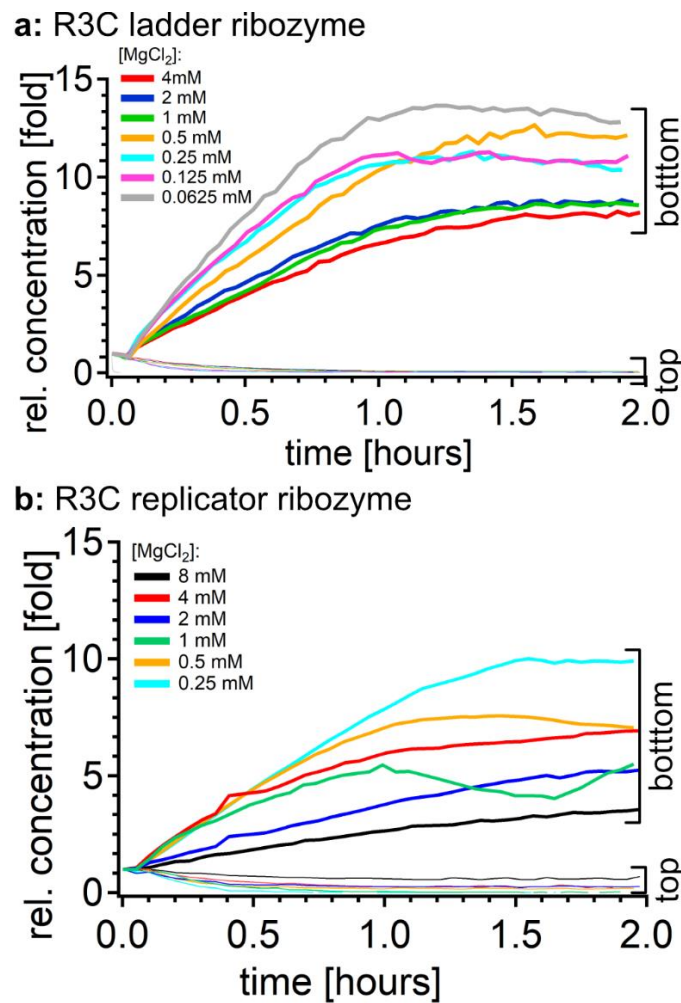


## b: optimized ribozyme design

**Supplementary Figure 7: Secondary structure diagrams of ribozymes**

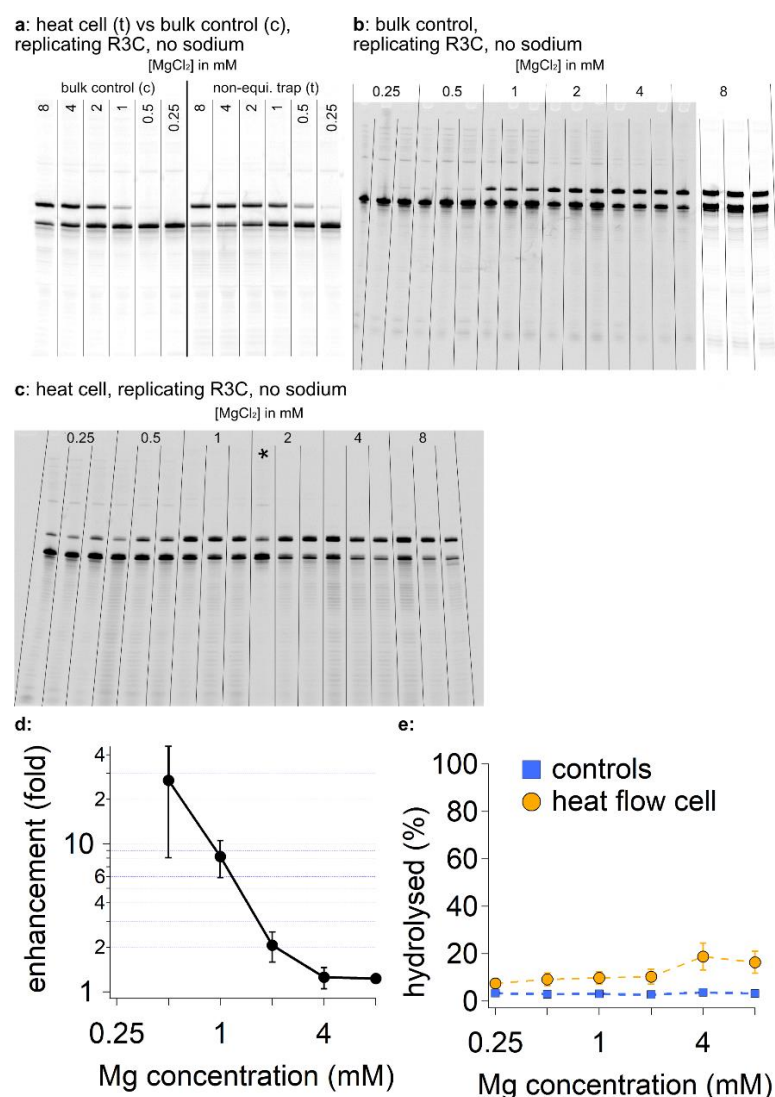
Diagrams showing the initial (a) and final (b) concatemer ligation ribozyme designs. In the initial design a, regions of the substrate originating from R3C substrate A are shown in red, whilst regions originating from substrate B are shown in blue. In b, mutations made to reduce homodimer formation and promote substrate binding are highlighted in pink.





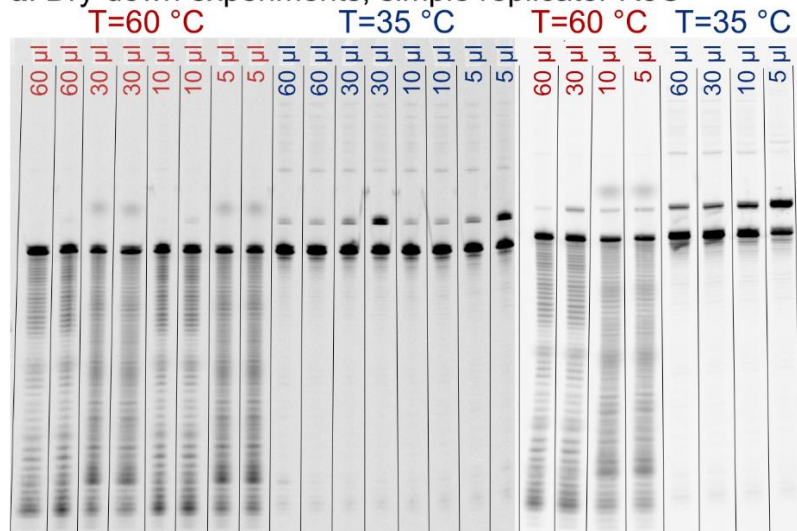
### Supplementary Figure 8: Fluorescence curves for the non-equilibrium experiments

Experiments of two hours in the heat flow cell for the two R3C ribozymes (ladder and replicating). Thermophoresis and convection driven by the temperature difference (20-60 °C) lead to a concentration of RNA (ribozyme, substrate and product) at the lower end of the chamber ("bottom"), while RNA is depleted at the upper end of the chamber ("top"). (a) For the ladder ribozyme, depending on the salt concentration, up to 13 times the fluorescence is measured compared to the start of the experiment. The data shown represent an average value over the thickness of the heat flow cell over a height of 0.5 mm. At the upper end of the chamber no RNA is detectable after 45 min. (b) The replicator ribozyme is concentrated up to 10-fold at the lower end of the chamber. Concentration and depletion are weaker compared to ladder ribozyme because the product of the replicator ribozyme is limited in length to 66 bases which reduces length dependent thermophoresis.



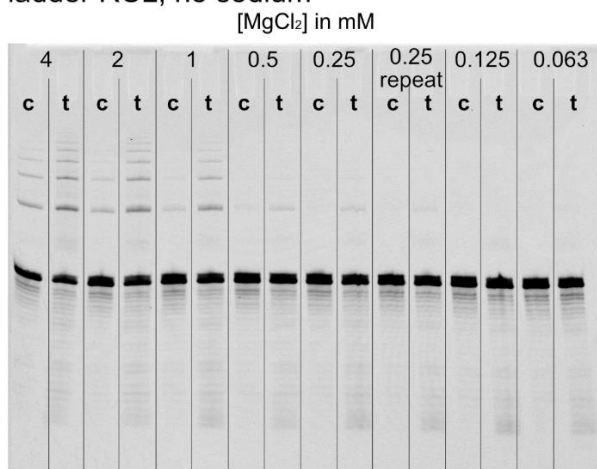
### Supplementary Figure 9: Salt screening of R3C replicator

The bulk control samples were incubated for 2 hours at 35 °C, the heat cell experiments were carried out in a 170 μm heat cell with a temperature difference of 40 K between 20 °C and 60 °C without any drift flow, as shown in the main text, Figure 4. 10 % of substrate strands were labeled with Cy5. **(a)** Without NaCl, the replicating ribozyme starts to operate at 0.25 - 0.5 mM MgCl<sub>2</sub> in the heat cell and at 1 mM MgCl<sub>2</sub> for the bulk control. These findings are confirmed by further replicates shown in **(b)** (for the bulk control) and **(c)** (for the heat cell). **(d)** Enhancement of R3C function in the heat flow cell (ΔT: +) compared to the bulk control at 35 °C (ΔT: -) corresponding to the plots shown in Figure 4b. Error bars were calculated using the standard error propagation of the standard deviations shown in Figure 4b. **(e)** Quantification of hydrolysed RNA from **(b)** and **(c)** as described in Supplementary Method 9. Panel d shows a composite gel (0.25 mM to 5 mM MgCl<sub>2</sub> and 8 mM MgCl<sub>2</sub>). Source images are shown at the end of the Supplementary Information.

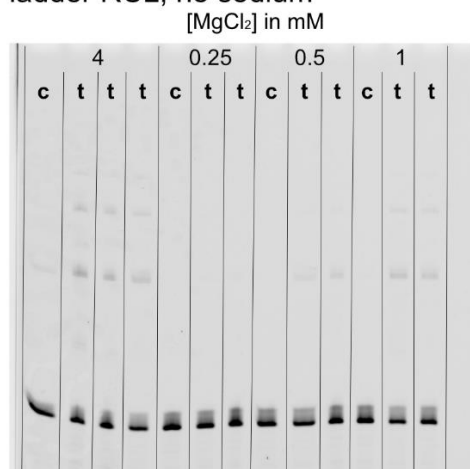
**a: Dry-down experiments, simple replicator R3C****Supplementary Figure 10: Screening of dry-down experiments**

Comparison in triplicates of R3C activity when incubated for 2h at 35°C and 60°C in open vessel (10% labeled with Cy5). Evaluated in main text Figure 4d/e. At higher temperature, hydrolysis plays a much larger role than at low temperatures, as expected. Despite identical reaction conditions, fluctuations in e.g. local humidity give slightly different results due to the different degree of dehydration. The picture is a composite of two gel images (first 16 lanes and last 8 lanes). Source images are shown at the end of the Supplementary Information.

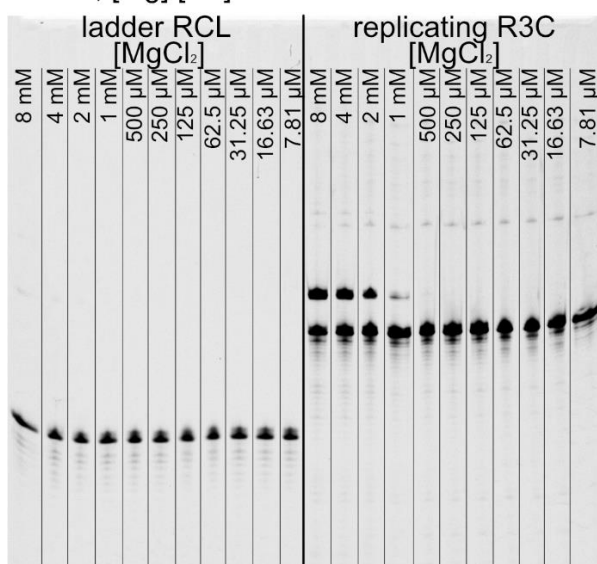
**a:** heat cell (t) vs bulk control (c),  
ladder RCL, no sodium



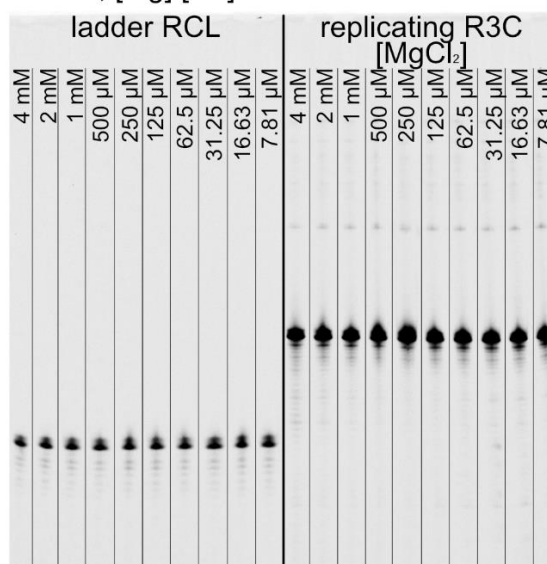
**b:** heat cell (t) vs bulk control (c),  
ladder RCL, no sodium



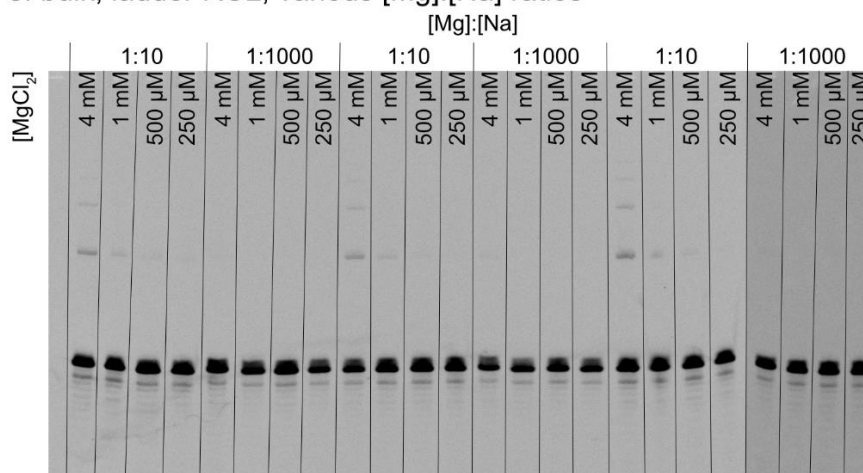
**c:** bulk, [Mg]:[Na] ratio 1:10



**d:** bulk, [Mg]:[Na] ratio 1:1000



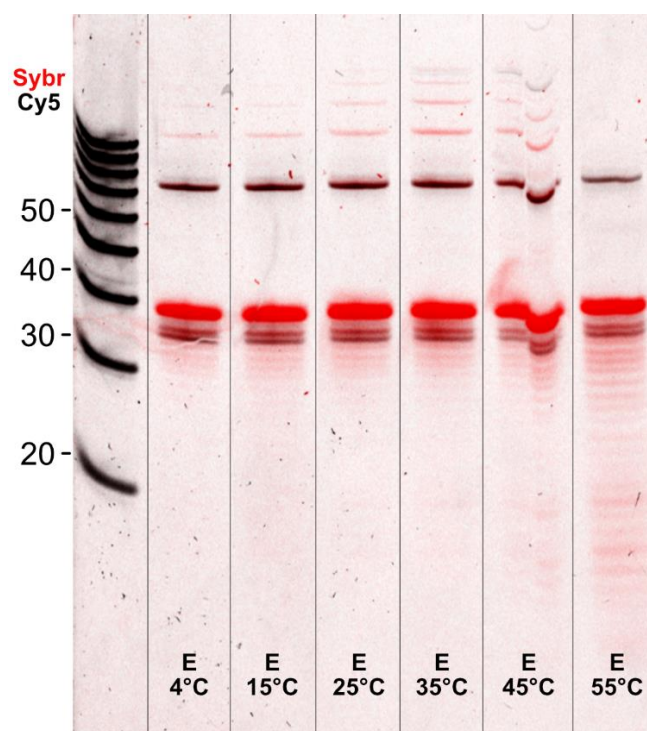
**e:** bulk, ladder RCL, various [Mg]:[Na] ratios



### Supplementary Figure 11: Salt screening of RCL and R3C

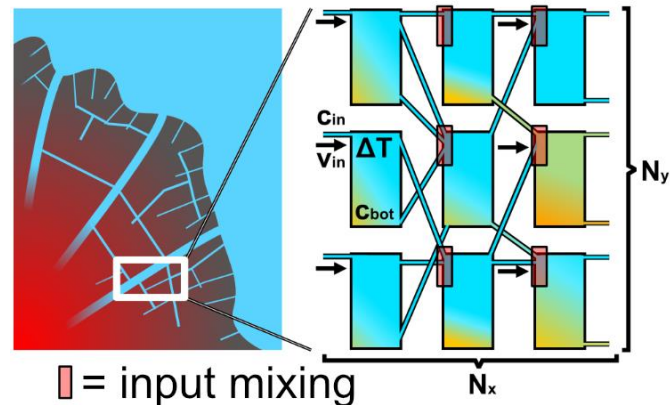
Incubation time 2 hours at 35 °C, 10 % of substrate strands were labeled with Cy5. (a) Without NaCl, the ladder ribozyme starts to operate under equilibrium conditions from 1 mM MgCl<sub>2</sub>,

indicated by letter c. For comparison, samples incubated for 2 h under non-equilibrium conditions, are indicated by letter t. These latter experiments were carried out in a 170  $\mu\text{m}$  heat cell with a temperature difference of 40 K between 20  $^{\circ}\text{C}$  and 60  $^{\circ}\text{C}$  without any drift flow, as shown in the main text, Figure 4. (b) shown further replicates of these experiments. (c) Titration of the  $\text{MgCl}_2$  and  $\text{NaCl}$  concentration at a constant  $[\text{Mg}]:[\text{Na}]$  ratio of 1:10 with  $\text{MgCl}_2$  concentrations specified in each lane. The ladder ribozyme starts to produce product from 4 mM  $\text{MgCl}_2$  upwards. The replicating R3C ribozyme starts to function at a  $\text{MgCl}_2$  concentration of 1 mM and above. (d) At  $[\text{Mg}]:[\text{Na}]$  ratios of 1:1000, both enzymes are completely inhibited within the  $\text{MgCl}_2$  range between 4 mM and 7.8  $\mu\text{M}$ . (e) shows further experiments with these  $[\text{Mg}]:[\text{Na}]$  ratios for varying  $\text{MgCl}_2$  concentrations. Panel e shows a composite of two gel images (first 20 lanes and last 4 lanes). Source images are shown at the end of the Supplementary Information.

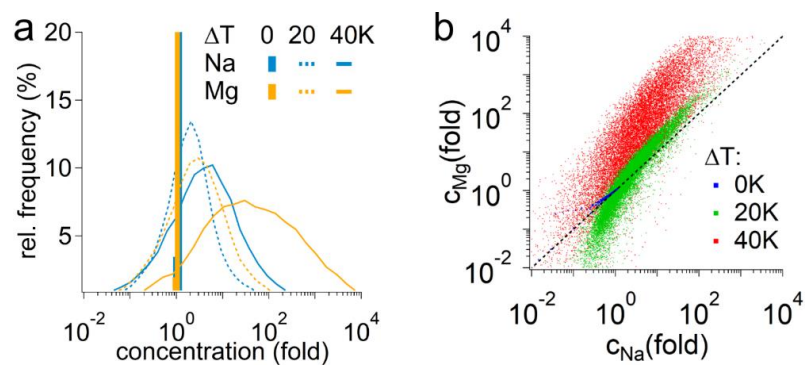


#### Supplementary Figure 12: Testing different temperature conditions for RCL

Ten percent of the substrate were labelled with a 5' Cy5 tag (black), additionally gel staining was performed using SybrGold (red) which emphasizes longer strands due to intercalation. Equilibrium conditions (E) with a constant temperature (indicated) were applied over a time of 2 h. Results indicate that the ribozyme works even at low temperatures and reaches its operation optimum at 35  $^{\circ}\text{C}$  which was therefore used in the experiments presented in the main text. Higher temperatures lead to pronounced hydrolysis.

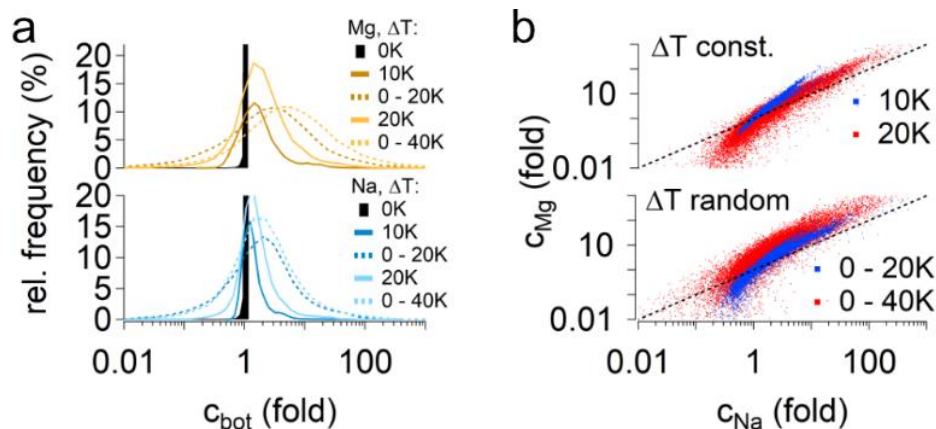


**Supplementary Figure 13: Illustration of the system of interconnected molecular traps mimicking branching rock fissures in a realistic geological scenario.**



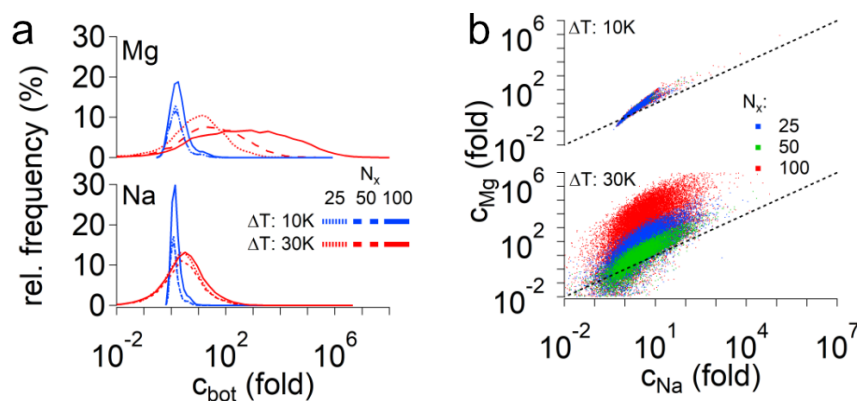
**Supplementary Figure 14: Statistics of the accumulated concentrations at the chamber bottom for different temperature differences.**

**(a)** Histogram of the resulting ion concentrations. With increasing temperature difference, magnesium ions (orange) are increasingly better accumulated, up to 4 orders of magnitude better than sodium ions (blue) at  $\Delta T = 40K$ . **(b)** Correlation plot for magnesium and sodium concentrations. At higher temperature differences, magnesium is accumulated with increasing selectivity compared to sodium.



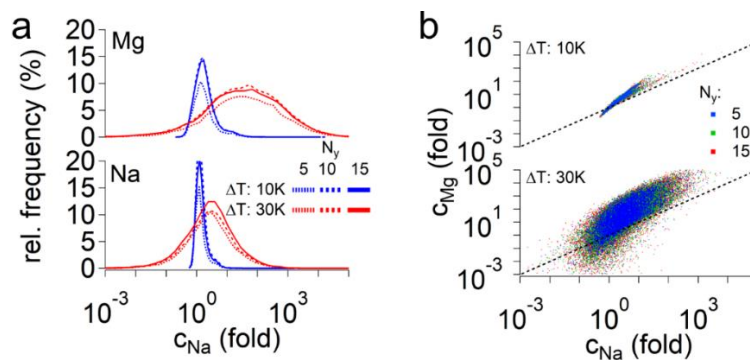
**Supplementary Figure 15. Comparison of the behavior of the chamber system under constant or fluctuating temperature differences.**

(a) Histogram of non-equilibrium steady state concentrations at the chamber bottom for magnesium (orange) and sodium (blue) for constant temperature differences (solid line) and per-chamber randomly chosen temperature differences (dashed line). (b) Correlation plots between accumulated sodium (x-axis) and magnesium concentrations (y-axis) for constant temperature differences (top) and corresponding temperature fluctuations (bottom).



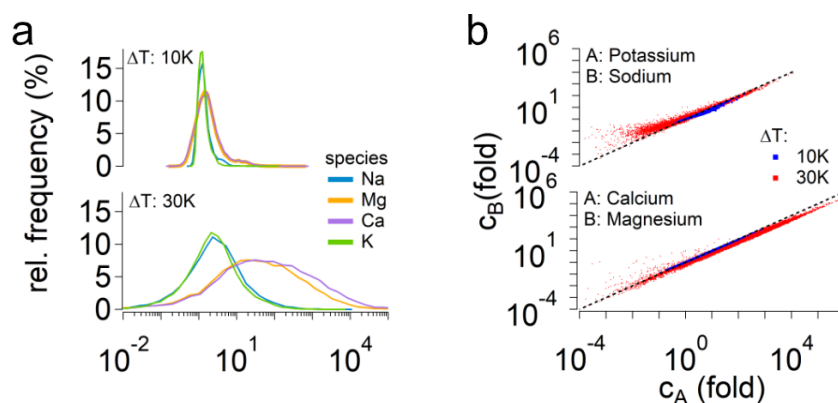
**Supplementary Figure 16: Scaling of the width of the chamber system.**

(a) Histogram of the frequency of chambers with a given concentration of magnesium (top) and sodium ions (bottom) at the chamber bottom for different temperature gradients  $\Delta T = 10 K$  (blue) and  $30 K$  (red) and system widths  $N_x = 25, 50, 100$  chambers. (b) Correlation plots of magnesium and sodium ion concentration at the chamber bottom at  $\Delta T = 10 K$  (top) and  $30 K$  (bottom).



**Supplementary Figure 17: Scaling of the height of the chamber system.**

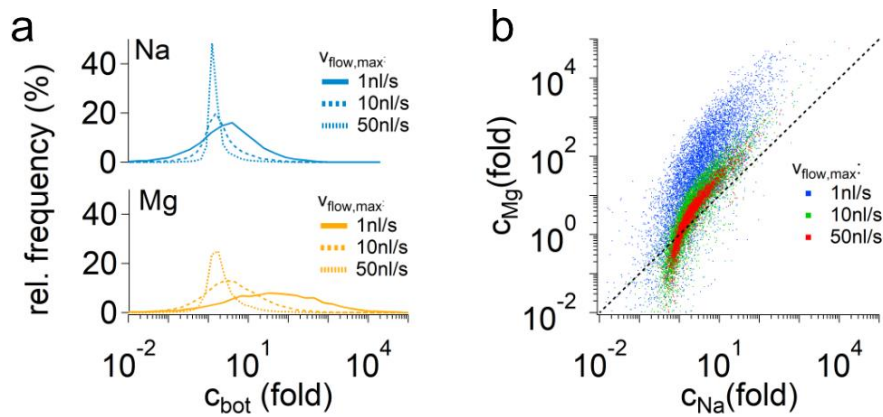
(a) Histogram of the occurrence of chambers with a given concentration of magnesium (top) and sodium ions (bottom) at the chamber bottom for different temperature gradients  $\Delta T = 10\text{ K}$  (blue) and  $30\text{ K}$  (red) and system heights  $N_y = 5, 10, 15$  chambers. (b) Correlation plots of magnesium and sodium ion concentrations at the chamber bottom at  $\Delta T = 10\text{ K}$  (top) and  $30\text{ K}$  (bottom).



**Supplementary Figure 18: Behavior of ions with similar Soret coefficients.**

(a) Histogram of the frequency of ion concentrations at the chamber bottom for sodium (blue), magnesium (orange), calcium (purple) and potassium (green) for temperature differences of  $10\text{ K}$  (top) and  $30\text{ K}$  (bottom). The data represents 100 simulations of a matrix of flowcells with the size of  $N_x = 50 \times N_y = 5$  respectively. (b) Correlation plots between potassium and sodium (top) and calcium and magnesium (bottom) at  $10\text{ K}$  (blue) and  $30\text{ K}$  (red) temperature difference.





**Supplementary Figure 19: Effect of different maximum flow rates through the system.**

(a) Histograms of sodium (top, blue) and magnesium (bottom, orange) ion concentrations at the chamber bottom at a temperature difference of 30 K for different flow rates of 1-50 nl/s. (b) Correlation plot of magnesium and sodium ion concentrations at the chamber bottom for different maximum flow rates.

## Supplementary Tables

Element	Unit	Krafla01 syn glass	Krafla2019 washed	Krafla2019 unwashed (natural sample)
SiO <sub>2</sub>	(%)	49.15	48.85	48.94
Al <sub>2</sub> O <sub>3</sub>	(%)	13.1	13.46	13.52
Fe <sub>2</sub> O <sub>3</sub>	(%)	16.24	15.91	15.99
MnO	(%)	0.24	0.23	0.23
MgO	(%)	5.81	5.62	5.54
CaO	(%)	10.22	10.29	10.16
Na <sub>2</sub> O	(%)	2.23	2.2	2.19
K <sub>2</sub> O	(%)	0.34	0.32	0.32
TiO <sub>2</sub>	(%)	2.07	2.02	2.04
P <sub>2</sub> O <sub>5</sub>	(%)	0.19	0.19	0.19
SO <sub>3</sub>	(%)	0.009	0.088	0.111
Cr <sub>2</sub> O <sub>3</sub>	(%)	0.0187	0.0234	0.0198
NiO	(%)	0.0077	0.008	0.0066
LOI	(%)	-0.83	-0.97	-0.75
sum	(%)	98.79	98.23	98.52
Ba	(ppm)	49	44	50
Co	(ppm)	84	54	58
Cr	(ppm)	125	140	123
Cs	(ppm)	0	0	0
Cu	(ppm)	121	116	114
Ga	(ppm)	18	18	18
Nb	(ppm)	13	12	12
Ni	(ppm)	60	59	53
Pb	(ppm)	2	1	4
Rb	(ppm)	9	9	8
Sc	(ppm)	41	40	41
Sr	(ppm)	154	153	153
Th	(ppm)	3	0	1
U	(ppm)	0	0	0
V	(ppm)	465	437	441
W	(ppm)	363	105	178
Y	(ppm)	34	33	34
Zn	(ppm)	134	126	126
Zr	(ppm)	131	122	121

**Supplementary Table 1: Major and trace element composition of used geomaterials**

Major and trace element composition of synthetic glass and tholeiitic basalt (washed and unwashed) from Krafla, Iceland, analysed by X-ray fluorescence spectroscopy. The analyses were carried out at the University of Mainz using a Malvern Panalytical Axios FAST X-ray fluorescence spectrometer. The major element analyses were carried out on fused glass discs whereas the trace element analyses were carried out on compacted powder pellets. Typical

accuracy of the analyses of the standard references was  $\sim 1\%$  relative (RMS) for major elements and  $\sim 4\%$  relative (RMS) for trace elements.

Experiment	Figure	Material	# of samples	Time	Temperature	Mass	Grain size	Agitation	Solution
Different grain sizes tholeiite glass	MF 2d SF 1g	Tholeiite glass	28	95 h	60 °C	31.38 +- 4.14 mg	<63 $\mu\text{m}$ (5) 63-90 $\mu\text{m}$ (5) 90-125 $\mu\text{m}$ (3) 125-180 $\mu\text{m}$ (4) 180-250 $\mu\text{m}$ (5) 355-500 $\mu\text{m}$ (6)	No	MilliQ water
Different masses tholeiite glass	MF 2b SF 1a	Tholeiite glass	19	110 h	60 °C	7.26 - 116.07 mg	90-125 $\mu\text{m}$	No	MilliQ water
Different masses tholeiite rock	MF 2c SF 1b	Tholeiite rock	18	36 h	60 °C	3.18 mg - 133.65 mg	90-125 $\mu\text{m}$	No	MilliQ water
Time evolution tholeiite glass	MF 2e SF 1d	Tholeiite glass	30	12.2 h (3) 41.6 h (3) 65 h (3) 88.2 h (4) 110.2 h (5) 182.7 h (6) 274 h (3) 397.2 h (3)	60 °C	30.02 +- 0.84 mg	355-500 $\mu\text{m}$	No	MilliQ water
Time evolution tholeiite rock	SF 1e	Tholeiite rock	29	120 h (6) 168 h (6) 192 h (9) 360 h (8)	60 °C	30.27 +- 0.86 mg	355-500 $\mu\text{m}$	No	MilliQ water
Different temperatures tholeiite glass	SF 1f	Tholeiite glass	36	16 vs 48 h	0 °C (6) 30 °C (6) 45 °C (6) 60 °C (6) 75 °C (5) 90 °C (6)	30.27 +- 0.74 mg	355-500 $\mu\text{m}$	No	MilliQ water
Time evolution tholeiite glass in prebiotic sea water	MF 2e SF 1j	Tholeiite glass	26	88 h (5) 163.5 h (5) 255 h (3) 423.5 h (3) 522 h (3) 591 h (3) 762 h (4)	60 °C	29.13 +- 1.36 mg	355-500 $\mu\text{m}$	No	Prebiotic sea water
Time evolution tholeiite glass in hydrothermal water	Discussion in main text SF 1h	Tholeiite glass	20	88 h (3) 163.5 h (3) 255 h (3) 423.5 h (3) 522 h (2) 591 h (2) 762 h (2)	60 °C	29.24 +- 1.43 mg	355-500 $\mu\text{m}$	No	Hydrothermal water
			6	197.5 h	60 °C	100.57 +- 1.09 mg			
Agitation methods	SF 1c	Tholeiite glass	8	16 h	60 °C	37.20 +- 4.59 mg	90-125 $\mu\text{m}$	Yes (5) vs No (3)	MilliQ water
Complete analysis of	SF 1i	Tholeiite glass	5	110 h	60 °C	32.29 +- 0.60 mg	125-180 $\mu\text{m}$	No	MilliQ water

leached ions									
-----------------	--	--	--	--	--	--	--	--	--

**Supplementary Table 2: Overview of different leaching experiments**

The plots depicting leached concentrations and pH values are shown in the main part, Figure 2, and in the Supplementary Figure 1. For each experiment, the number of measurements is given and explicitly stated how they are distributed among different parameters within one experiment (in brackets where applicable). All measurements (except for mass evolutions) are normalized to 30 mg according to Equation 5. Prebiotic sea water and hydrothermal sea water were prepared as described in section Supplementary Method 1.

Experiment	Shown in Figure	$T_{\text{hot}}, T_{\text{cold}}$ $\Delta T$	Initial sample composition	Flow speeds (nl/s)	
Selective accumulation of Na vs Mg ions.	Figure 3, main text	20.2 °C, 61 °C, 40.8 K	1.5 mM MgCl <sub>2</sub> , 1.5 mM NaCl	5.9 nl/s	
		20.2 °C, 59 °C, 38.8 K		11.8 nl/s	
		20.2 °C, 58 °C, 37.8 K		23.6 nl/s	
		20.2 °C, 61 °C, 40.8 K		5.9 nl/s	
		20.2 °C, 59 °C, 38.8 K		11.8 nl/s	
		20.2 °C, 60 °C, 39.8 K		23.6 nl/s	
		20.2 °C, 61 °C, 40.8 K		5.9 nl/s	
		20.2 °C, 59 °C, 38.8 K		11.8 nl/s	
		20.2 °C, 60 °C, 39.8 K		23.6 nl/s	
	Supplementary Figure 6b	25 °C => 0 K	1.5 mM MgCl <sub>2</sub> , 1.5 mM NaCl	11.8 nl/s	
		27 °C => 0 K			
26 °C => 0 K					
Sequential salt separation of Na vs. Mg ions after reconstitution and refeeding.	Figure 5b+c, main text	Same as above 20.2 °C, 59 °C, 38.8 K	1.5 mM MgCl <sub>2</sub> , 1.5 mM NaCl	11.8 nl/s	
		Same as above 20.2 °C, 59 °C, 38.8 K			
		Same as above 20.2 °C, 59 °C, 38.8 K			
			20.2 °C, 57 °C, 36.8 K	5.25 mM MgCl <sub>2</sub> , 3.45 mM NaCl	11.8 nl/s
			20.2 °C, 61 °C, 40.8 K		
			20.2 °C, 59 °C, 38.8 K		
			20.2 °C, 58 °C, 37.8 K	18.67 mM MgCl <sub>2</sub> , 9.04 mM NaCl	
			20.2 °C, 60 °C, 39.8 K		
20.2 °C, 59 °C, 38.8 K					
Selective accumulation of Na, K, Mg and Ca ions.	Supplementary Figure 6a	20.2 °C, 58 °C, 37.8 K	1.5 mM NaCl, 1.5 mM KCl, 1.5 mM MgCl <sub>2</sub> , 1.5 mM CaCl <sub>2</sub>	11.8 nl/s	
		20.2 °C, 59 °C, 38.8 K			
		20.2 °C, 61 °C, 40.8 K			

**Supplementary Table 3: Overview of different experimental conditions of heat flow cells**

The experimental results of the salt-separation experiments are shown in Figures 3 and 5 and in Supplementary Figure 6.

Ion	Diffusive mobility D ( $\mu\text{m}^2/\text{s}$ )	Soret coefficient $S_T \left(\frac{1}{K}\right) = \frac{D_T}{D}$
Na <sup>+</sup>	1334	$4.69 \cdot 10^{-3}$
Ca <sup>2+</sup>	792	$1.33 \cdot 10^{-2}$
Mg <sup>2+</sup>	706	$1.22 \cdot 10^{-2}$
K <sup>+</sup>	1957	$3.51 \cdot 10^{-3}$

**Supplementary Table 4: Thermophoretic and diffusive mobilities for salt species**

The values for thermophoretic ( $D_T$ ) and diffusive ( $D$ ) mobilities used in the finite element simulations were taken from literature<sup>9-11</sup>.

Nucleic Acid	Source	5' modification	Sequence (5' to 3')
E <sub>R</sub> Ribozyme	IVT	-	GGAAGUUGUUAUCACUUGUUACGUAA GUAACACUUUGGAUGGGUUGAAGUAU GAGACCGCAACUUA
A Substrate	IDT	Cy5	GGAAGUUGUUAUCACUUGUUACGUAA GUAACACUUUGGAUGGGUUGAAGUAU
B Substrate	IVT	PPP	GAGACCGCAACUUA
E <sub>L</sub> Ribozyme	IVT	-	GGAAGUUGUUAUCACUUGUUACGUAA GUAACACUUUGGAUGGGUUGAAGUAU GAUAACGGCAGUU
BA Substrate	IVT	PPP	GAGACCGCAACUUAACUGCUGUUGGAA GUAU
Cy5 BA	IDT	Cy5	GAGACCGCAACUUAACUGCUGUUGGAA GUAU

**Supplementary Table 5: RNA ribozyme and substrate sequences**

Differences between the ladder ribozyme and the replicator ribozyme are marked in green.

Nucleic Acid	Source	Sequence (5' to 3')	Purpose
T7 Promoter + Clamp	IDT	GATCGATCTCGCCCGCGAAATTAATACGACTCA <u>CTATA</u>	Forward primer for fill-in PCR reaction
T7 Promoter	IDT	<u>GAAATTAATACGACTCACTATA</u>	Forward primer for partially dsDNA
E <sub>R</sub> Ribozyme Template	IDT	TAAGTTGCGGTCTCATACTTCAACCCATCCAAA GTGTTACTTACGTAACAAGTGATAACAACCTCC TATAGTGAGTCGTATTAATTTTC	Reverse primer for fill-in PCR
B Substrate Template	IDT	TAAGTTGCGGTCTCTATAGTGAGTCGTATTAAT TTC	Reverse primer for partially dsDNA
E <sub>L</sub> Ribozyme Template	IDT	ATACTTCCAACAGCAGTTAAGTTGCGGTCTCTA TAGTGAGTCGTATTAATTTTC	Reverse primer for fill-in PCR
BA Substrate Template	IDT	AACTGCCGTTATCATACTTCAACCCATCCAAAGT GTTACTTACGTAACAAGTGATAACAACCTCCTAT AGTGAGTCGTATTAATTTTC	Reverse primer for fill-in PCR

**Supplementary Table 6: DNA primer sequences and purposes**

Appearances of the T7 promoter sequence are underlined, their reverse complements are marked in red.

**References for supplement**

1. McCollom, T. M. & Donaldson, C. Experimental Constraints on Abiotic Formation of Tubules and Other Proposed Biological Structures in Subsurface Volcanic Glass. *Astrobiology* **19**, 53–63; 10.1089/ast.2017.1811 (2019).
2. Brown, J., Bearman, G. & Wright, J. *Seawater. Its composition, properties and behaviour*. 2nd ed. (Butterworth-Heinemann, Oxford, 1995).
3. Ronde, C. E.J. de, Channer, D. M.d., Faure, K., Bray, C. J. & Spooner, E. T.C. Fluid chemistry of Archean seafloor hydrothermal vents: Implications for the composition of circa 3.2 Ga seawater. *Geochimica et Cosmochimica Acta* **61**, 4025–4042; 10.1016/S0016-7037(97)00205-6 (1997).
4. Keil, L., Hartmann, M., Lanzmich, S. & Braun, D. Probing of molecular replication and accumulation in shallow heat gradients through numerical simulations. *Physical chemistry chemical physics : PCCP* **18**, 20153–20159; 10.1039/c6cp00577b (2016).
5. Thermal diffusion in solutions of electrolytes. *Proc. R. Soc. Lond. A* **255**, 307–330; 10.1098/rspa.1960.0070 (1960).
6. Robertson, M. P. & Joyce, G. F. Highly efficient self-replicating RNA enzymes. *Chemistry & biology* **21**, 238–245; 10.1016/j.chembiol.2013.12.004 (2014).
7. Reichl, M., Herzog, M., Götz, A. & Braun, D. Why charged molecules move across a temperature gradient: the role of electric fields. *Physical review letters* **112**, 198101; 10.1103/PhysRevLett.112.198101 (2014).
8. Mast, C. B., Schink, S., Gerland, U. & Braun, D. Escalation of polymerization in a thermal gradient. *Proceedings of the National Academy of Sciences of the United States of America* **110**, 8030–8035; 10.1073/pnas.1303222110 (2013).
9. Takeyama, N. & Nakashima, K. Proportionality of intrinsic heat of transport to standard entropy of hydration for aqueous ions. *J Solution Chem* **17**, 305–325; 10.1007/BF00650412 (1988).
10. Petit, C. J., Hwang, M.-H. & Lin, J.-L. The Soret effect in dilute aqueous alkaline earth and nickel chloride solutions at 25C. *Int J Thermophys* **7**, 687–697; 10.1007/BF00502400 (1986).
11. Lide, D. R. ed. *CRC handbook of chemistry and physics. A ready-reference book of chemical and physical data* (CRC Press, Boca Raton, 2003).





# Appendix B

## Formation mechanism of thermally controlled pH gradients

Published in *Communications Physics* in January 2023.

**Matreux, T.\***, Altaner, B.\*, Raith, J.\*, Braun, D., Mast, C. B. & Gerland, U.

Formation mechanism of thermally controlled pH gradients

*Communications Physics*

**6**, 14

2023

<https://doi.org/10.1038/s42005-023-01126-y>

According to Springer Nature, the ownership of copyright in original research articles remains with the author, who retains the non-exclusive rights to reproduce the contribution in whole or in part in any printed volume (book or thesis) of which they are the author(s).

# communications physics

ARTICLE

<https://doi.org/10.1038/s42005-023-01126-y>

OPEN

## Formation mechanism of thermally controlled pH gradients

Thomas Matreux<sup>1,3</sup>, Bernhard Altaner<sup>2,3</sup>, Johannes Raith<sup>2,3</sup>, Dieter Braun<sup>1</sup>, Christof B. Mast<sup>1</sup>✉ & Ulrich Gerland<sup>2</sup>✉

Spatial proton gradients create energy in biological systems and are likely a driving force for prebiotic systems. Due to the fast diffusion of protons, they are however difficult to create as steady state, unless driven by other non-equilibria such as thermal gradients. Here, we quantitatively predict the heat-flux driven formation of pH gradients for the case of a simple acid-base reaction system. To this end, we (i) establish a theoretical framework that describes the spatial interplay of chemical reactions with thermal convection, thermophoresis, and electrostatic forces by a separation of timescales, and (ii) report quantitative measurements in a purpose-built microfluidic device. We show experimentally that the slope of such pH gradients undergoes pronounced amplitude changes in a concentration-dependent manner and can even be inverted. The predictions of the theoretical framework fully reflect these features and establish an understanding of how naturally occurring non-equilibrium environmental conditions can drive pH gradients.

<sup>1</sup>Systems Biophysics, Ludwig Maximilian University Munich, 80799 Munich, Germany. <sup>2</sup>Physics of Complex Biosystems, Technical University of Munich, 85748 Garching, Germany. <sup>3</sup>These authors contributed equally: Thomas Matreux, Bernhard Altaner, Johannes Raith. ✉email: [christof.mast@physik.uni-muenchen.de](mailto:christof.mast@physik.uni-muenchen.de); [gerland@tum.de](mailto:gerland@tum.de)

Cells from all kingdoms of life use pH gradients to drive the synthesis of ATP via ATP synthase<sup>1</sup>. This is often seen as an indication that pH gradients were also a driving force during the emergence of life. This hypothesis is substantiated by phylogenetic analysis<sup>2</sup> and geochemical considerations<sup>3,4</sup>. In non-equilibrium settings, such as heat flows through rock fissures or hydrothermal systems, pH gradients can provide a prebiotic proton-motive force to drive early metabolisms<sup>5</sup>. Prebiotic systems may also benefit from pH gradients to localize pH-selective chemical reactions such as nucleotide adsorption<sup>6</sup> to certain spatial zones, or to spatially couple the effects of ribozymes that operate at different pH<sup>7</sup>. However, the physicochemical mechanisms that can produce pH gradients in plausible non-equilibrium settings are so far insufficiently understood.

Experimentally, a controlled non-equilibrium setting to study the formation of chemical gradients is created by heat flows across microfluidic chambers<sup>8,9</sup>. Such experiments mimic ubiquitous natural settings, e.g. in porous rocks near hydrothermal vents<sup>10</sup> (Fig. 1b). A previous study demonstrated that heat flow across narrow (100  $\mu\text{m}$ -scale) pores can induce pH gradients of 2 units along the pore length (mm-scale)<sup>11</sup>. The gradients were generated by a complex interplay of convection, thermophoresis, electrostatic interactions, and acid-base reactions.

Here, we focus on the physical parameters of this interplay to understand the control of both the amplitude and the direction of the pH gradient (Fig. 1c). We performed an experimental case study (Fig. 1a) of a prebiotically relevant<sup>12,13</sup> acid-base system consisting of formic acid (HCOOH) and sodium hydroxide (NaOH) diluted in an aqueous solution. The mixture was kept within a microfluidic chamber and subjected to a lateral heat flow. Based on a separation of timescales, we then developed a heuristic theoretical description for this reaction-transport system, which incorporates the electrostatic coupling between the reacting species, as well as their transport due to drift and diffusion processes. This description captures the parameter dependence of the experimentally observed behavior, including a concentration-

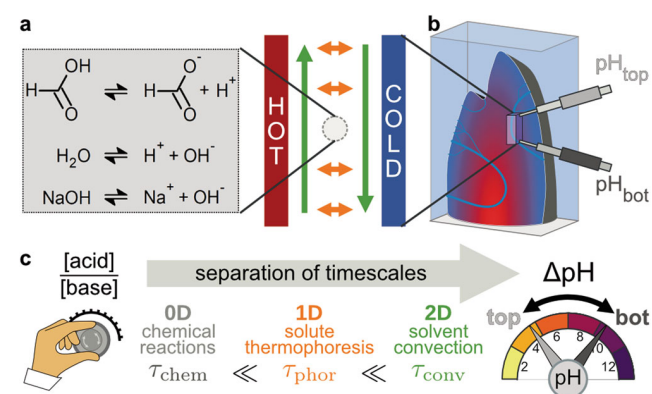


**Fig. 1 Heat flows create pH gradients in acid-base mixtures.** **a** Dominant dynamic processes in a heat flux chamber: Chemical reactions (gray) remain locally equilibrated ( $\tau_{\text{chem}} \lesssim 10^{-3}$  s). Thermophoretic horizontal accumulation ( $\tau_{\text{phor}} \sim 10^2$  s, orange arrows) is faster than vertical Rayleigh-Bénard convection ( $\tau_{\text{conv}} \sim 10^4$  s, green arrows), given the high aspect ratio (height/width) of the heat flux chamber that mimics, e.g., a rock fissure. Thermophoresis and convection combined drive a selective accumulation of molecules. Their net accumulation is proportional to their effective Soret coefficient  $S_{\text{H}}^{\text{eff},0}$ , derived in the main text. **b** Heat flows across rock fissures provide a non-equilibrium environment that drives proton gradients. By analyzing local outflows with standard pH-meters, we measure the pH values quasi in situ. **c** By tuning the concentrations of acids and bases, both amplitude and direction of the created pH gradient can be controlled.

dependent steepening and inversion of the pH gradient. The model can be generalized to systems with more reacting species subject to electrostatic coupling, as long as the effective timescales of the local reactions and the global transport are sufficiently separated. The quantitative understanding enables the prediction and the control of thermally induced pH gradients.

## Results

**Experimental setup and procedure.** For this study, we developed a continuous flow microfluidic device with openings that allowed us to probe the local pH at three different outflow positions and using standard pH meters (Fig. 2a; see Methods for a detailed description). This setup avoids complications imposed by a fluorescent pH reporter needed to monitor pH in a closed device<sup>11</sup>.

The microfluidic structure containing the fluid was cut out of fluorinated ethylene propylene (FEP) foil and subsequently sandwiched between two sapphire windows (chamber dimensions: width  $w = 170 \mu\text{m}$ , height  $h = 50 \mu\text{m}$ ). This design guaranteed that the liquid sample only has contact to FEP and sapphire, providing an inert environment even for aggressive chemistry. Sapphire was chosen for its transparency (for optical control) and high heat conductivity (to ensure a homogeneous temperature distribution). One of the sapphire windows was

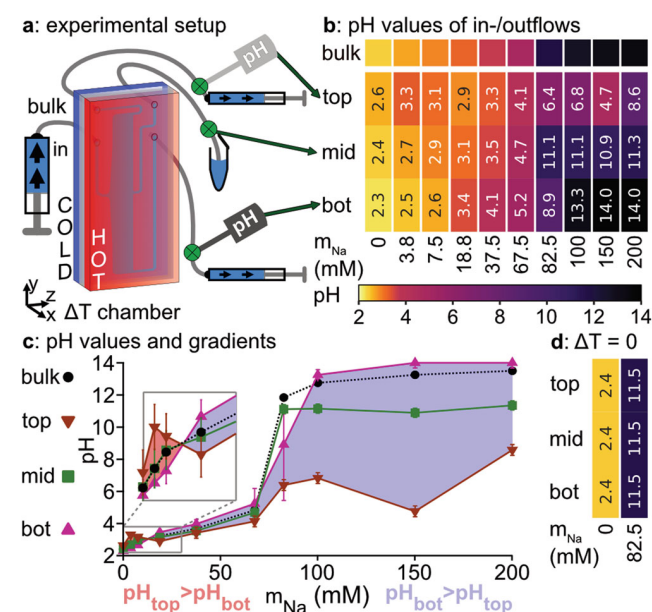


**Fig. 2 Experimental setup and results.** **a** Experimental setup. The thin thermal reaction chamber is continuously supplied with a premixed solution containing varying concentrations of formic acid and sodium hydroxide. The outflow is split into three parts (top 12%, middle 76% and bottom 12%) and the pH value of each fraction is measured (green circles). For experimental details see Methods. **b** These pH values are depicted for 75 mM formic acid and varying concentrations of NaOH ( $m_{\text{Na}}$ ) for the inlet (bulk) and the different outlets. While the bottom fraction qualitatively follows the bulk, especially the top fraction displays a complex, concentration-dependent behavior both for its value and for the resulting pH gradient ( $\Delta\text{pH}_{\text{vert}}$  between top and bottom of the heat flux cell (measurements for other formic acid concentrations shown in Supplementary Fig. 2)). **c** When plotting the pH values of the different fractions (black circle: bulk, brown inverted triangle: top, green square: middle, pink triangle: bottom), a positive gradient ( $\text{pH}_{\text{top}} > \text{pH}_{\text{bot}}$ , red) for low concentrations of NaOH is observed which is inverted (blue) at higher concentrations of NaOH and increases massively when  $m_{\text{Na}} > m_{\text{HCOOH}}$ . Error bars are shown as discussed in Methods. **d** In the absence of a temperature gradient, no pH gradient forms ( $m_{\text{HCOOH}} = 75 \text{ mM}$ ).

cooled by an aluminum heat exchanger connected to a cryostat, while the other window was kept at high temperatures by Ohmic heating, resulting in a constant heat flux through the chamber. The device had one inlet at the left side and three outlets at the right side, at different vertical positions ('top', 'middle', 'bottom') where the pH value was measured.

The inlet was used to push a mixture of pure water, acid and base (with initial pH value denoted as  $\text{pH}_0$ ) at a flow rate of 3.28 nl/s into the chamber. Using syringe pumps at each of the outlets, the flux splitting between the three outlets was adjusted to outflow fractions of 12% (top), 76% (middle), and 12% (bottom). These values reflect a trade-off that kept the thermogravitational accumulation within the chamber relatively unperturbed, the total time required for the experiment manageable and the spatial regions from which the top and bottom samples are collected relatively localized (see Methods for a detailed discussion).

**Experimental pH gradients.** Using this setup, we performed experiments with solutions containing different amounts of formic acid ( $m_{\text{form}}$ ) and NaOH ( $m_{\text{Na}}$ ). The heat flow through the chamber was set by keeping the temperatures at the front and back at  $60 \pm 2^\circ\text{C}$  and  $21 \pm 1^\circ\text{C}$ , respectively. The pH values of the different fractions obtained with 75 mM formic acid and varying amounts of NaOH are shown in Fig. 2b, c (for other formic acid concentrations see Supplementary Fig. 2).

While the pH in the bottom of the cell qualitatively follows the pH behavior in the equilibrated bulk solution (see Supplementary Fig. 1), the pH in the middle and top fractions displays a markedly different behavior as a function of the NaOH concentration. The pH dependence in the bottom fraction of the cell and the bulk solution is consistent with well-known acid-base characteristics, with a change from acidic to alkaline at equimolar concentrations of NaOH and formic acid. However, the pH behavior in the top fraction is surprisingly complex, leading to a previously not observed<sup>11</sup> inversion of the pH difference ( $\Delta\text{pH}_{\text{vert}}$ ) (see Fig. 3) between the top and bottom fraction at low NaOH concentrations ( $\sim 10$  mM). Above equimolarity, the pH difference sharply increases. Despite NaOH being a strong base, even at NaOH concentrations much larger than formic acid concentrations, the pH value of the top fraction is actively pushed into the acidic regime by the heat flux.

**Theoretical approach.** The complex experimental behavior of the emergent pH gradient arises from the combined effects of diffusion, convection, thermophoresis, electrostatic interactions, and acid-base reactions. The interplay of these effects can be studied by numerically solving the underlying reaction-transport equations, but a full characterization of the system is challenging, due to the large parameter space and the multiple different timescales of the dynamics<sup>11</sup>.

Due to thermal expansion of the solvent and gravity acting in vertical direction, an approximately rotationally symmetric circular buoyant convection flow is established in the chamber: solutes closer to the hot side will be driven upwards while molecules on the cold side will be transported downwards. Additionally, dissolved molecules are driven along the horizontal temperature gradient by thermophoresis. While the magnitude of the ensuing velocities of both processes are comparable, a small aspect ratio  $w/h$  causes the horizontal equilibration to occur on a faster timescale than the vertical accumulation, see Fig. 1a and Methods. Seminal work by P. Debye showed that an expansion in the aspect ratio yields approximate solutions, where concentration gradients along the horizontal dimension shape those along the vertical dimension of the setup<sup>14</sup>. Electrostatic interactions were taken into account for electrolytes by Guthrie and coworkers<sup>15</sup>. From a theoretical perspective, the task at hand therefore is to

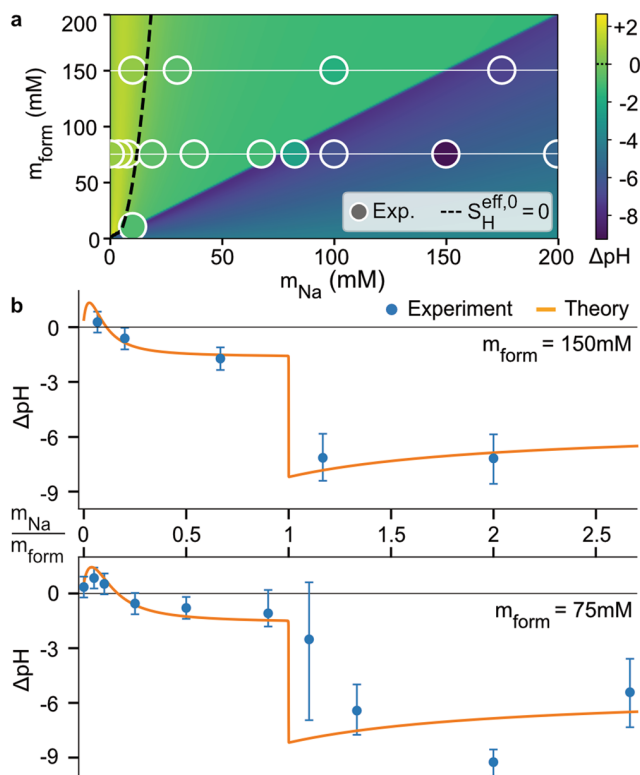
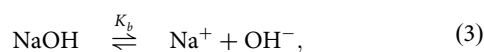
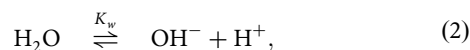


**Fig. 3 Comparison of analytically predicted and experimentally measured pH gradients.** **a** Heat maps of theoretically calculated pH differences are compared to measurements (circles) for varying concentrations of formic acid ( $m_{\text{form}}$ ) and sodium hydroxide (NaOH,  $m_{\text{Na}}$ ). Our model predicts a complex phase diagram with a positive (yellow), a weakly negative (green) and a strongly negative (blue) pH gradient. The inversion is shown by a black dashed line and corresponds to  $S_{\text{H}}^{\text{eff},0} = 0$ , see Eq. (9). The experimental results are in very good agreement with the analytical model. **b** Theoretical (orange line) and experimental (blue circles) pH differences for 150 mM and 75 mM formic acid (white lines in **a**), showing again the good agreement between theory and experiment. The error bars include experimental standard deviations from replicate measurements as well as uncertainties accounting for concentration fluctuations from thermal gradient effects in the outflow channels (for more details see Methods).

explicitly integrate chemical reactions to the theoretical description, and to study their effect on the system behavior. Until now, only the case of a chemical reaction of a single species without electrostatic interactions has been considered<sup>16</sup>.

In this work, we derive an expression for vertical concentrations gradients, in particular, the proton gradient, as a function of the initial chemical concentrations. In the following, we will rely on a timescale separation between the (zero-dimensional) chemical reaction dynamics, the (one-dimensional, horizontal  $x$ -axis) effects of thermophoresis and the (two-dimensional,  $x$ - $y$  axis) effects of buoyant convection, see Fig. 1.

**Chemical dynamics.** Our system is determined by the system of the  $\mathcal{R} = 3$  chemical reactions



where we assume that the concentration of  $\text{H}_2\text{O}$  is approximately constant. The equilibrium concentrations  $c_i^0$  of the  $\mathcal{N} = 6$  dynamical chemical species  $X_i$  are determined by the equilibrium constants for the acid, base, and water, respectively:

$$\begin{aligned} K_a &= \frac{c_{\text{COOH}^-}^0 c_{\text{H}^+}^0}{c_{\text{HCOOH}}^0}, & K_b &= \frac{c_{\text{Na}^+}^0 c_{\text{OH}^-}^0}{c_{\text{NaOH}}^0}, \\ K_w &= c_{\text{OH}^-}^0 c_{\text{H}^+}^0. \end{aligned} \quad (4)$$

In general, closed chemical systems always conserve certain chemical sub-species, so-called moieties<sup>17</sup>. We define the moiety concentrations

$$\begin{aligned} m_{\text{form}} &= c_{\text{COOH}^-} + c_{\text{HCOOH}}, & m_{\text{Na}} &= c_{\text{NaOH}} + c_{\text{Na}^+}, \\ m_c &= c_{\text{Na}^+} + c_{\text{H}^+} - c_{\text{COOH}^-} - c_{\text{OH}^-}. \end{aligned} \quad (5)$$

Here,  $m_{\text{form}}$  and  $m_{\text{Na}}$  are the total concentration of formate and sodium-containing molecules in the system, which are experimentally controllable parameters. Similarly,  $m_c$  is the net charge concentration. Notice that the moieties are not uniquely defined, and any linear combination of a moiety yields another conserved quantity. However, we can always define them in a way that includes the charge moiety and experimentally controllable parameters. Specifying the moiety concentrations  $m_{\text{Na}}$  and  $m_{\text{form}}$  and using, due to charge neutrality,  $m_c = 0$ , together with Eqs. (4) uniquely determines the values of the equilibrium concentrations  $c_i^0$  of all chemical species. Even though the full system is not at equilibrium, given that chemical reactions occur on the fastest timescale  $\tau_{\text{chem}} < 10^{-3}$  s, the relations between the homogeneous equilibrium concentrations Eqs. (4), will hold approximately as local relations also in a spatially extended system.

**Horizontal currents.** Next, we consider the horizontal currents that form due to thermophoresis in an effective one-dimensional system. This is motivated since the timescale of the horizontal dynamics is given by  $\tau_{\text{phor}} \gg \tau_{\text{chem}}$  (see Methods). The horizontal flux  $J_i(x)$  of molecule species  $X_i$  with horizontal concentration profile  $c_i(x)$  is given by

$$J_i = -D_i \frac{\partial c_i}{\partial x} - \left( S_i D_i \frac{\partial T}{\partial x} - z_i D_i \frac{FE}{RT} \right) c_i, \quad (6)$$

where  $D_i$ ,  $S_i$ , and  $z_i$  are the diffusion constant, Soret coefficient, and valence of  $X_i$ ,  $T(x)$  is a linear temperature profile,  $F$  the Faraday constant, and  $E$  the electrical field. In a steady state, the divergence of these currents is balanced by a source term given by the chemical reactions. Due to moiety conservation in local chemical reactions, the associated moiety currents are divergence-free. Since in a one-dimensional closed system any divergence-free current must vanish, it follows that the (horizontal) moiety currents  $I$  vanish identically. The vanishing electric current,  $I_c = J_{\text{Na}^+} + J_{\text{H}^+} - J_{\text{COOH}^-} - J_{\text{OH}^-} = 0$ , allows us to solve for the electrical field

$$\frac{FE}{RT} = \frac{\sum_i z_i D_i \left( \frac{\partial c_i}{\partial x} + S_i c_i \frac{\partial T}{\partial x} \right)}{\sum_i z_i^2 c_i D_i}. \quad (7)$$

Inserting this expression into (6) allows us to express the currents  $\mathbf{J} = (J_{\text{H}}, J_{\text{OH}}, J_{\text{HCOOH}}, J_{\text{COOH}}, J_{\text{Na}}, J_{\text{NaOH}})$  as linear functions of the horizontal concentration gradients  $\partial_x \mathbf{c} = \left( \frac{\partial c_{\text{H}}}{\partial x}, \frac{\partial c_{\text{OH}}}{\partial x}, \frac{\partial c_{\text{HCOOH}}}{\partial x}, \frac{\partial c_{\text{COOH}}}{\partial x}, \frac{\partial c_{\text{Na}}}{\partial x}, \frac{\partial c_{\text{NaOH}}}{\partial x} \right)$  as  $\mathbf{J} = \mathbf{D} \partial_x \mathbf{c} + \mathbf{b}$ . The matrix  $\mathbf{D}$  is a (cross-)diffusion matrix with components

$$\begin{aligned} \mathbf{D}_{ij} &= \delta_{ij} D_i + D_j z_j c_j \frac{z_i D_i}{\sum_k z_k^2 c_k D_k} \quad \text{and} \quad \mathbf{b}_j = -D_j c_j \frac{\partial T}{\partial x} S_j^{\text{ES}}, \quad \text{where} \\ S_j^{\text{ES}} &= S_j - z_j \frac{\sum_k z_k D_k S_k c_k}{\sum_k z_k^2 c_k D_k} \end{aligned}$$

is the Seebeck coefficient, see also refs. 15,18.

The remaining two horizontal moiety currents  $\mathbf{I} = (I_{\text{Na}}, I_{\text{form}}) = \mathbf{L} \mathbf{J}$  are given by a  $2 \times \mathcal{N}$  matrix  $\mathbf{L}$  as a linear combination of  $\mathbf{J}$ . Similarly to the charge current  $I_c$ , they are divergence-free and thus vanish, and we can write  $\mathbf{I} = 0$  as a linear equation for the horizontal concentration gradients  $\partial_x \mathbf{c}$

$$(\mathbf{LD}) \partial_x \mathbf{c} = \mathbf{Lb}. \quad (8)$$

In order to uniquely solve for the concentration gradients, additional constraints are needed. One of these constraints is given by the condition of approximate local electroneutrality in the bulk,  $m_c(x) = 0, \forall x$ , which can be systematically derived<sup>19,20</sup>. Differentiating this condition with respect to the horizontal position yields  $\sum_i z_i \partial_x c_i = 0$ , which we can write with a  $1 \times \mathcal{N}$  matrix  $\mathbf{Z}$  with entries  $z_i$  as:

$$\mathbf{Z} \partial_x \mathbf{c} = \mathbf{0}. \quad (9)$$

Finally, since chemical reactions are fast as compared to the transport processes, we can assume that their concentrations  $c_i(x)$  obey Eqs. (4) as *local equilibrium* relations. Taking the horizontal derivatives yields

$$\mathbf{Q} \partial_x \mathbf{c} = \mathbf{0}, \quad (10)$$

where  $\mathbf{Q}$  is the  $3 \times \mathcal{N}$  (Jacobian) matrix of the mass-action ratios.

Equations (8), (9) and (10) constitute  $\mathcal{N} = 6$  linearly independent equations for the  $\mathcal{N} = 6$  concentrations gradients. They can be inverted with a computer algebra system to give the concentrations gradients  $\partial_x \mathbf{c}$  as non-linear and convoluted expressions of the concentrations. In particular, we obtain a solution for the proton gradient, which we can formally write as

$$\frac{\partial c_{\text{H}}}{\partial x} = -S_{\text{H}}^{\text{eff}} [\{c_i(x)\}] \frac{\partial T}{\partial x} c_{\text{H}}. \quad (11)$$

with the concentration-dependent effective Soret coefficient for the hydrogen ion  $S_{\text{H}}^{\text{eff}}$ , whose sign and magnitude determine the horizontal proton gradient (see also Supplementary Note 1 for a complete solution). We consequently expand  $c_i(x) = c_i^0 + \gamma_i(x)$  around the (homogeneous) bulk equilibrium concentrations, i.e.  $S_{\text{H}}^{\text{eff}} = S_{\text{H}}^{\text{eff},0}(\{c_i^0\}) + \mathcal{O}(\{\gamma_i(x)\})$ . For small temperature gradients and small widths of the heat flux chamber, we assume  $\gamma_i \ll c_i^0$  and neglect the inhomogeneous part. Since the  $c_i^0$  are uniquely determined by the moieties, i.e. the controlled molar concentrations of sodium hydroxide,  $m_{\text{Na}}$ , and formic acid,  $m_{\text{form}}$ , the homogenous effective Soret coefficient  $S_{\text{H}}^{\text{eff},0}(m_{\text{Na}}, m_{\text{form}})$  can be calculated from tunable experimental conditions.

The scheme outlined above will work for *arbitrary* chemical reactions networks and is thus general. On first glance, it might be surprising that we obtain exactly  $\mathcal{N}$  independent linear equations for the  $\mathcal{N}$  gradients of dynamical species. However, this fact can be traced to the algebraic structure of the stoichiometric matrix<sup>17</sup>. In particular, situations can arise where not all of Eqs. (4) leading to Eq. (10) are independent. However, the number of independent equations defining the moieties, Eqs. (5), and thus Eqs. (8) are algebraically related, such that we can always find  $\mathcal{N}$  linear equations for the gradients of  $\mathcal{N}$  dynamical species, regardless of the number  $\mathcal{R}$  of reactions involved (see Methods or ref. 17).

**Vertical pH gradient.** Integrating equation (11) along the horizontal axis yields a horizontal pH difference  $(\Delta \text{pH})_{\text{hor}} \approx \frac{\Delta T}{\ln(10)} S_{\text{H}}^{\text{eff},0}$ . Given such horizontal gradients, a theory for calculating the resulting

vertical concentration gradient in a Clusius column has been formulated by Debye<sup>14</sup>, and adapted later to a situation including electrical fields<sup>15</sup>. This approach works, since the corresponding convective timescale  $\tau_{\text{conv}}$  is much larger than the thermophoretic timescale,  $\tau_{\text{conv}} \gg \tau_{\text{phor}}$  (Methods). It then turns out that the relation between horizontal and vertical gradients is given by a linear factor  $\alpha_{\text{th}} = 358.5$ , whose value depends only on material parameters of the solution, the geometric aspect ratio of the chamber, and the applied temperature gradient (see Methods). As such, the effective Soret coefficient  $S_{\text{H}}^{\text{eff}}$  for the horizontal dynamics can be used to estimate the vertical pH difference  $(\Delta\text{pH})_{\text{vert}}$  measured experimentally,

$$(\Delta\text{pH})_{\text{vert}} \approx \alpha_{\text{th}} \cdot S_{\text{H}}^{\text{eff},0}(m_{\text{Na}}, m_{\text{form}}) \quad (12)$$

Hence, weaker and more plausible temperature gradients in nature can be balanced by equally more plausible larger aspect ratios. As consequence, there is no lower threshold of temperature difference required for the formation of proton gradients, since shallow gradients can be compensated with higher aspect ratio<sup>21</sup>.

**Comparison with experiments.** The heat map from our theoretical model can roughly be divided into three regions: positive (yellow), weakly negative (green) and strongly negative (blue). As depicted in Fig. 3a, our measurements (shown in circles) fully recapitulate this behavior, both for the amplitude of the pH gradient and its inversion.

To avoid distortion from the flow extraction for pH measurement, we chose a slow flow ( $\tau_{\text{flow}} = 13,000$  s). This timescale is the time that a volume element on average remains in the heat flux chamber before it is extracted horizontally by the measurement cross-flow ( $z$ -axis in Fig. 2a). The slow extraction can however also slightly change the  $m_{\text{Na}}/m_{\text{form}}$  ratio in the effluent channel by thermophoretic accumulation, for which we estimate a systematic error of 2%. This effect has the greatest impact in the vicinity of  $m_{\text{Na}} = m_{\text{form}}$ , since the local pH then depends sensitively on the concentration ratio. This is reflected in the large error in pH determination at  $m_{\text{Na}}/m_{\text{form}} = 1.1$  in Fig. 3b (see Methods).

## Discussion

The experimental measurements are in good agreement with our analytical results. The characteristic, concentration-dependent features of an early inversion and massive increase at equimolar concentrations are reproduced without fitting parameters. The used solutes, formic acid and sodium hydroxide, are an example of a prebiotically plausible acid-base reaction system<sup>22–25</sup>. Possible roles of formic acid in prebiotically relevant synthesis reactions have been investigated<sup>23,26–28</sup> together with the link to formamide-based reactions<sup>29,30</sup>.

Our analytical approach provides a more generally applicable theory for the interplay of chemical reactions, electrostatic interactions, and transport processes driven by external gradients. In the present case of thermally driven pH gradients, it allows a deeper understanding, and, compared to the previous computational analysis by Keil et al.<sup>11</sup>, it permits the treatment of strong acids and bases and much steeper pH gradients. This theoretical advance is complemented by our experimental method to measure local pH values in the heat flux cell using standard pH meters. These can cover a far broader pH spectrum and strong acids/bases compared to fluorescence methods. Together, this enables us to control and predict proton gradients and opens the door to applications involving synthesis reactions and the formation of tunable chemical gradients.

While the local equilibrium assumption is an excellent approximation in the present experimental context, it would be desirable to relax this assumption, in order to be able to apply the

presented theoretical framework also to systems with slower chemical reactions. The behavior of such systems depends explicitly on the Damköhler number, a parameter that measures the relative timescales associated with the transport and reaction kinetics<sup>31</sup>. The inverse Damköhler number may serve as a useful expansion parameter to systematically extend the presented theoretical framework.

An intuitive explanation of the sign change of the pH gradient can be given by using the Soret coefficients listed in Supplementary Table 1 and considering all prevalent electrostatically coupled species. For this, we take into account that ions ( $\text{H}^+$ ,  $\text{OH}^-$ ,  $\text{COOH}^-$ ,  $\text{Na}^+$ ) show much stronger thermophoresis than uncharged substances, which can thus be neglected in this qualitative discussion. Therefore, at vanishing concentrations of NaOH ( $m_{\text{Na}}$ ), the only relevant ion pair for thermophoresis is  $\text{COOH}^-$  and  $\text{H}^+$ . Its enrichment in the lower part of the chamber increases the proton concentration and correspondingly lowers the pH value. With higher NaOH concentrations, ion pairs such as  $\text{Na}^+$  and  $\text{OH}^-$  become more dominant and by accumulation therefore also more prevalent at the chamber bottom. This results in an increasing local pH value, first compensating the accumulated protons, and finally inverting the pH gradient.

Along this line of reasoning, the respective influence of the contributions of thermophoresis, thermal convection, chemical reactions, and electrostatics can also be understood. While thermophoresis by itself is only a weak effect, it is exponentially amplified by thermal convection<sup>14</sup>. Neglecting electrostatic interaction in an ion-bearing system would lead to their accumulation according to their Soret coefficient (see Supplementary Table 1). Consequently, a less complex pH difference profile is achieved with higher pH differences at low concentrations of NaOH due to a larger proton transport that otherwise is counteracted by electrostatic forces (Supplementary Fig. 5c). The temperature dependence of the reaction rate constants has only a minor impact on the formation of the pH gradient and can therefore be neglected in the following considerations (see Supplementary Fig. 5b/c). In contrast, a system devoid of chemical reactions is dominated by thermogravitational accumulation. This leads to a well-defined concentration ratio of the solutes and accordingly to a constant pH difference between the upper and lower part of the chamber irrespective of the absolute NaOH concentration (see Supplementary Fig. 5a). In absence of a thermal gradient, no accumulation and no pH gradient occur (Fig. 2d). Therefore, only the consideration of all these effects together provides a comprehensive understanding of this highly coupled system.

Since heat fluxes are ubiquitous on Early Earth, requirements for proton gradients to occur are significantly less demanding than complex chemical non-equilibria e.g. originating from confluent outflows from reservoirs with different pH<sup>32</sup>. Cooperative coupling to other gradients such as ion gradients<sup>33</sup> will show interesting effects and help to solve enigmas such as prebiotically required separation of long RNA strands. Recent work by Mariani et al. has evaluated strand separation minimizing hydrolysis by pH oscillations<sup>34</sup>. This effect was recently used in a system of air-water interfaces to boost the replication of DNA<sup>35</sup>.

## Methods

**Preparation of heat flow chambers and microfluidic setup.** The FEP-foil (Holscot, Netherlands) with a thickness of 170  $\mu\text{m}$  (width) is cut by an industrial plotter device (CE6000-40 Plus, Graphtec, Germany) and sandwiched between two sapphires (Kyburz, Switzerland) with a thickness of 500  $\mu\text{m}$  (cooled sapphire) and 2000  $\mu\text{m}$  (heated sapphire), respectively. The back sapphire has 4 laser-cut holes with a diameter of 1 mm. The sapphire-FEP-sapphire block is then placed on an aluminum base covered by a heat conducting foil (EYGS091203DP, Graphite, 25  $\mu\text{m}$ , 1600 W/mK, Panasonic, Japan) and held in place by a steel frame, mounted by six torque-controlled steel screws for a homogeneous force distribution. A second heat conducting foil (EYGS0811ZLGH, Graphite, 200  $\mu\text{m}$ , 400 W/mK,

Panasonic, Japan) connects the heated sapphire with the electrical heater element, and is also fixed by torque-controlled steel screws. The height of the microfluidic chamber is measured using a confocal micrometer (CL-3000 series with CL-P015, Keyence, Japan) at three positions (top, mid, bottom) to ensure homogeneous width along the chamber. Chambers are pre-flushed using low-viscosity, fluorinated oil (Novec™ 7500 Engineered Fluid, 3M, USA) to check for tightness and push out residual gas inclusions. The assembled chamber is then mounted to a cooled aluminum block. The Ohmic heaters are connected to a 400 W, 24 V power supply that is controlled via Arduino boards with a customized version of the open-source firmware “Repetier”, originally made for 3D printing. All elements were optimized using finite-element simulation to provide a homogeneous temperature profile while minimizing the thickness of the sapphire windows and hence maximizing the thermal gradient.

The in- and outlets of the thermal chamber are connected via tubings to syringes placed on high-precision syringe pumps (Low Pressure Syringe Pump neMESYS 290N with Quadruple Syringe Holder Low-Pressure, cetoni, Germany). For the microfluidic connections, (all from techlab, Germany): connectors (Verbinder zöllig, UP P-702-01), end caps (Tefzel Cap for 1/4-28 Nut, UP P-755), screws (Nut, Delrin, flangeless, VBM 100.823-100.828), ferrules (Ferrule VBM 100.632) and tubings (Tubing Teflon (FEP), KAP 100.969) are used. The flow speeds of the syringe pumps (controlled via neMESYS UserInterface, cetoni, Germany) are chosen such that 12% of the inflow are sucked out at the top and at the bottom outlet, leaving 76% coming out of the middle outlet. The syringes used (all from Göhler-HPLC Syringes, Germany) are: Chemically Resistant Heavy Duty Syringes with PTFE seals: 2606814 and 2606035 (ILS, Germany).

**Sample preparation and experimental procedure.** The samples are prepared mixing formic acid (Carl Roth GmbH, Germany) and sodium hydroxide (Sigma-Aldrich, USA) with MilliQ-water to reach the given concentration. The pH (for initial pH values as compared to theoretical predictions, see Supplementary Fig. 1) is measured using an Orion™ 9826BN Micro pH Electrode and a 8220BNWP Micro pH Electrode (both Thermo Fisher Scientific, USA), also used for pH measurements after the experiment. For strongly alkaline pH values (>13), measurement is done using pH paper and a larger error was assumed.

The cryostat (TXF-200 R5, Grant, UK) is set to  $-30^{\circ}\text{C}$  and the heaters to  $95^{\circ}\text{C}$  which results in a temperature difference from  $\sim 20^{\circ}\text{C}$  to  $60^{\circ}\text{C}$  within the microfluidic chamber. Temperatures are measured on the sapphires with a heat imaging camera (ShotPRO Wärmebildkamera, EAN: 0859356006217, Seek Thermal, USA) and a temperature sensor (GTH 1170, Greisinger, Germany and B&B Thermo-Technik 06001301-10, Germany), giving an average cold temperature of  $21^{\circ}\text{C} \pm 1^{\circ}\text{C}$  and an average hot temperature of  $60^{\circ}\text{C} \pm 2^{\circ}\text{C}$ . Averaging over the temperature differences throughout all experiments gives a value of  $38.9^{\circ}\text{C} \pm 1.4^{\circ}\text{C}$  (as the higher cold temperatures usually go together with higher warm temperatures). Before starting the experiment, the tubings and thermal chamber are re-flushed with fluorinated oil. The samples are then loaded into the inlet tubing. The experiment is started and left running for 6–7 days. To stop the experiment, the applied temperatures are set to room temperature. The samples are recovered from the tubings and collected for pH measurement.

**Experimental uncertainties.** The experimental error splits into two main contributions: one standard error from replicate measurements and one to account for concentration fluctuations caused by effects from the thermal gradient in the outflow channels. As described in the main text, our experimental setup was designed to determine the pH value as realistically as possible inside the heat flux cell. For this purpose, the pH values were measured with a standard laboratory pH meter and no pH-dependent dyes were used, which are not designed for use in these extreme temperature conditions and are not compatible with measurements in the entire pH range. However, since measurements using a pH meter are not possible directly inside the cell due to the small dimensions of the microfluidic system, we slowly and continuously extract the cell volume at the top, middle and bottom of the cell respectively to obtain the necessary measurement volume. By doing so and balancing the outflows with respect to each other, the cell volume is split into three fixed volume portions, of which the contents are extracted through the respective outlet. At the same time, we allow the appropriate amount of stock solution to flow through the input channel so that the cell is completely filled with fluid at all times.

The aim of these considerations was to keep the effects of this slow drift flow on the actual experiment as small as possible and thus to obtain an unbiased picture of the pH distribution inside the cell. The corresponding timescale  $\tau_{\text{flow}}$  indicates how long a volume element introduced into the cell by the drift flow remains in the cell on average until extraction. If it is greater than the relaxation time of the accumulation process occurring in the heat flow cell, i.e. if the drift flow is sufficiently small, it can be assumed that the accumulation remains essentially undisturbed. If the drift flux is correspondingly too fast, the accumulation will be disturbed. For the extraction at the lower outlet, the following problem appears: In order to avoid a diffusive loss of accumulated material, we placed the exit hole for the lower output channel not at the bottom of the cell but rather sufficiently high (as shown in the main text, Fig. 2). However, this requires the to-be extracted material to overcome a thermogravitational process, since the vertical part of the exit channel has a convection flow and thermophoresis similar to the main chamber. Thus, if the drift velocity through this channel is too low, the material to

be extracted will remain at the bottom of the heat flow cell and cannot be recovered. The situation here is thus exactly the inverse of the above consideration, so that a trade-off must be found between undisturbed extraction and the lowest possible retention of the material to be extracted in the exit channel.

These considerations made us choose an inflow speed of 3.28 nl/s, resulting in a measurement extraction timescale  $\tau_{\text{flow}}$  of  $\sim 13,000$  s. In order to avoid a too high retention of the material, we chose an outflow speed of 0.39 nl/s, thus giving a separation into 12% at top and bottom, leaving the remaining 76% flowing out through the middle. The value for top and bottom fractions was still kept relatively low in order to average over as little material as possible and thus to keep as close as possible to the situation present inside the heat flow cell.

To account for this systematic uncertainty, we introduced an additional error in the composition of the bottom fraction. Taking the experimental standard deviation ( $\delta^{\text{exp}}$ ), we calculated the point on the graph for both maximal and minimal value and added/subtracted an error  $m_{\text{Na}}/m_{\text{form}} = 0.02$  (called  $\delta^{\text{distortion}}$ ). Since the determination of the composition is concentration-dependent, we measured the bottom outflows using ion chromatography and got an average concentration of 3.8 fold the inflow concentration. The errors can be merged by addition since they are independent. The resulting ratio can then be transformed back to the corresponding pH value, resulting in a complete uncertainty, potentially non-symmetrical. The procedure is shown in more details in Supplementary Fig. 3.

We expect this additional distortion to have weak effects on the measurement everywhere except for the equimolar region. The non-linearity near the equivalence line between sodium hydroxide and formic acid makes the measured pH values vulnerable to slight differences in concentration. Around this equimolar point, nearly all molecules are present in their charged state ( $\text{Na}^+$  for  $m_{\text{Na}}$  and  $\text{HCOO}^-$  for  $m_{\text{form}}$ ). Consequently, the distortion is introduced by different retentions of these ions in the outflow channels and thus dependent on their thermodiffusive properties.

**Chemical reaction networks.** We closely follow the works of Rao and Esposito<sup>17</sup>. Assume we have  $\mathcal{N}$  species  $X_i$  in the system, subject to  $\mathcal{R}$  reactions. The  $\rho$ -th reaction is written as

$$\sum_i \nu_{\rho+}^i X_i \xrightleftharpoons[k^{\rho-}]{k^{\rho+}} \sum_i \nu_{\rho-}^i X_i \quad (13)$$

where  $\nu_{\rho\pm}^i$  are the stoichiometric coefficients of species  $X_i$  in the forward (+) and backward (−) direction of reaction  $\rho$  with  $k^{\rho\pm}$  the bare forward and backward reaction rates. The dynamical evolution of the concentration  $c_i$  of species  $X_i$  in a well-mixed (zero-dimensional) system follows

$$\frac{\partial c_i}{\partial t} = \omega_i = \sum_{\rho} \nu_{\rho}^i \left( k^{\rho+} \prod_i c_i^{\nu_{\rho+}^i} - k^{\rho-} \prod_i c_i^{\nu_{\rho-}^i} \right) = \sum_{\rho} \nu_{\rho}^i r_{\rho} \quad (14)$$

with the reaction current  $r_{\rho}$  and the total reaction rate of species  $X_i$  denoted  $\omega_i$ . It vanishes if the species are in chemical equilibrium, described by an equilibrium constant  $K^{\rho}$

$$K^{\rho} = \log_{10} \left( \frac{k^{\rho+}}{k^{\rho-}} \right) = \log_{10} \left( \prod_i (c_i^{\text{eq}})^{\nu_{\rho}^i} \right) \quad (15)$$

where  $c_i^{\text{eq}}$  denote (molar) concentrations in chemical equilibrium. Summarizing the stoichiometric coefficients of all (forward and backward reactions) in a matrix with elements  $\nu_{\pm} = \{\nu_{\rho\pm}^i\}$ , the stoichiometric matrix reads  $\nu := \nu_- - \nu_+$  and has dimensions  $\mathcal{N} \times \mathcal{R}$ .

**Stoichiometric algebra: conservation laws and reaction cycles.** Consider an  $\mathcal{N} \times \mathcal{R}$  matrix  $\nu$ . Denote the the dimensions of its right ( $\nu \mathbf{v} = 0$ ) and left ( $\nu^T \mathbf{w} = 0$ ) null-spaces by  $\mathcal{Z}$  and  $\mathcal{C}$ , respectively. The rank-nullity theorem ensures that

$$\mathcal{Z} = \mathcal{R} - \text{rank}(\nu), \quad \mathcal{C} = \mathcal{N} - \text{rank}(\nu), \quad (16)$$

where  $\text{rank}(\nu)$  is the rank of  $\nu$ . Assume we have a row vector  $\mathbf{n}$  of size  $\mathcal{N}$  consisting of integer values  $n_i$  representing the number of instances of each species  $X_i$  present in the (well-mixed) system. In addition, we have a reaction vector  $\mathbf{q}$  of length  $\mathcal{R}$  with integer entries  $q_{\rho}$ . The mapping  $\nu \mathbf{q}$  yields the change in the number of species ( $n_i$ ) after carrying out the  $\rho$ -th reaction in forward direction  $q_{\rho}$  times. Hence, a non-zero right null-vector of  $\nu$  can be interpreted as carrying out multiple reactions after which the vector  $\mathbf{n}$  remains unchanged. This constitutes a reaction cycle. The number of independent reaction cycles is given by the dimensions of the right nullspace of  $\nu$ . Each independent reaction cycle  $\tilde{\rho}$  however diminishes the number of independent equilibrium constants by linearly relating them, as

$$\sum_{\rho} \tilde{q}_{\rho} K^{\rho} = \sum_{\rho} \tilde{q}_{\rho} \left( \sum_i \nu_i^{\rho} \log_{10} (c_i^{\text{eq}}) \right) = \sum_i \log_{10} (c_i^{\text{eq}}) \sum_{\rho} \nu_i^{\rho} \tilde{q}_{\rho} = 0. \quad (17)$$

Complementary, a mapping  $\nu^T \mathbf{n}^T$  yields a reaction vector  $\mathbf{q}$  which entries  $q_{\rho}$  give how often the  $\rho$ -th reaction needs to be carried out to change the numbers of species  $X_i$  denoted in  $\mathbf{n}$ . A non-zero right nullvector  $\mathbf{l}^{(j)} = (l_i^{(j)})$  of  $\nu^T$  hence defines a linear combination of species that remain unchanged by carrying out any reaction. Therefore, these linear combination define conserved quantities, which we

call moieties. The number of these is given by the right nullspace of  $v^T$ . Moeity concentrations  $m^{(i)} = \sum_i l_i^{(i)} c_i$  are kept constant by the reaction dynamics because  $l^{(i)}$  is a right null-eigenvector and hence

$$\frac{\partial}{\partial t} m^{(i)} = \sum_i l_i^{(i)} \frac{\partial c_i}{\partial t} = \sum_i l_i^{(i)} \omega_i = \sum_{i,\rho} l_i^{(i)} \nu_{i,\rho}^{(\rho)} r_\rho = \sum_{i,\rho} \underbrace{\nu_{i,\rho}^{(\rho)} l_i^{(i)}}_{=0} r_\rho = 0. \quad (18)$$

By the rank-nullity theorem there are always  $\mathcal{R} - \mathcal{Z} = \mathcal{N} - C$  independent equilibrium constants, which give rise to constraints of the form of Eqs. (10). In addition, there are always  $C - 1$  moieties that are linearly independent from the charge moiety and thus give rise to the constraints shown in Eqs. (8). Finally, one can always use differential electroneutrality that gives rise to the single constraint as shown in Eqs. (9). As such, in general we have

$$(\mathcal{N} - C) + (C - 1) + 1 = \mathcal{N} \quad (19)$$

independent linear equations for the  $\mathcal{N}$  dynamical species. This fact ensures the existence and uniqueness of a solution for general chemical networks.

**Chemostated system.** In chemostated systems, some of the species are not considered as “dynamic” species but assumed to be set constant. In our system, water is considered a chemostated species and the corresponding equilibrium constant  $K_w$  includes this fixed concentration. Algebraically, the above statements still hold. Due to the Rank-Nullity-Theorem each chemostated species either breaks a conservation law or creates a linear dependence between species, reducing the number of independent equilibrium constants by one. Hence, no matter the number of species chemostated, the equations fixing the dynamical species will always match their respective number. For more details see ref. 17.

### Thermogravitational accumulation

**Thermophoresis.** Colloidal particles travel along an external temperature gradient (thermophoresis). In the overdamped limit, this drift is written as

$$J_{DT} = -DS_T c \nabla T, \quad (20)$$

with  $T$  a temperature field,  $D$  the diffusion coefficient of the colloidal particle and  $S_T$  its Soret coefficient, describing the coupling-strength of the particle to the temperature field. The phenomenology of thermophoretic movement can be described thermodynamically<sup>36</sup>.

**2-D description of thermal traps with thermophoresis and convection.** A mathematical approach modeling thermal traps was given by Debye<sup>14,15</sup>. The temporal evolution of the concentration  $c$  of a species in a trap is given by the continuity equation

$$\frac{\partial c}{\partial t} = -\nabla J \quad (21)$$

with the flux

$$J = -D \nabla c + (\mathbf{u} - DS_T \nabla T) c. \quad (22)$$

In the bulk of the thermal trap the convective flow field  $\mathbf{u}$  mainly consists of its vertical component  $u_y$ , with

$$u_y(x) = \frac{\beta g \rho \Delta T}{12\mu} \left( x - \frac{x^3}{b^2} \right) \quad (23)$$

with  $\beta, \rho, \mu$  the material specific values for the coefficient of thermal expansion, the density and the viscosity,  $g$  the gravitational acceleration and  $\Delta T$  the temperature difference across the short side of the trap with width  $w$ . The convective flow is symmetric with respect to the midpoint of the trap. The flow is directed downwards at the cold side and upwards at the hot side of the thermal trap. The average vertical velocity in one half side of the trap can then be calculated to be

$$\bar{u}_y = \frac{1}{b} \int_0^b u_y(x) dx = \frac{\beta g \rho \Delta T}{12\mu} \int_0^b \left( x - \frac{x^3}{b^2} \right) dx = \frac{\beta g \rho \Delta T}{12\mu} \frac{1}{16} w^2 \quad (24)$$

The steady state vertical concentration profile is then found to be

$$c(y) = G \exp\left(-\frac{y}{l}\right) \quad \text{with} \quad \frac{1}{l} = \frac{4}{15} \frac{\Delta T S_T \bar{u}_y}{D + \frac{128}{315} \frac{(u_y b)}{D}}. \quad (25)$$

A logarithmic concentration difference between bottom and top then writes as

$$\Delta \log_{10}(c) = \frac{h}{l} \log_{10}(e), \quad (26)$$

with  $h$  the height of the trap.

**Electroneutrality.** In order for the bulk electroneutrality assumption to hold to good approximation, electrostatic interactions need to be the strongest forces in the system. In our case they therefore need to be compared with the charge separation processes diffusion and thermophoresis. To estimate the deviation from electroneutrality in one dimension we assume the following situation: a positively charged species is homogeneously distributed around  $x = 0$  and a negatively charged

compound is linearly distributed with concentration difference  $\Delta c$  at  $x = \pm \Delta x$ . The electric field is then—according to Poissons equation—given by

$$-\nabla E = \frac{1}{\epsilon} \rho = \frac{1}{\epsilon} F(c_+ - c_-) \quad (27)$$

Putting in the concentration profile depicted above we can approximate

$$c_- \approx c_+ + \frac{x}{\Delta x} \Delta c \Rightarrow \frac{dE}{dx} \approx \frac{F}{\epsilon} \Delta c \frac{x}{\Delta x} \Rightarrow E \approx \frac{F}{\epsilon} \Delta c \frac{x^2}{\Delta x} \quad (28)$$

the contribution to the fluxes are (disregarding diffusive fluxes)

$$J_{DT,i} = -D_i S_{T,i} \frac{\partial T}{\partial x} c_i \quad \text{and} \quad J_{el,i} = z_i \frac{D_i F}{RT} E c_i \quad (29)$$

with the steady state condition

$$J_{-DT} = J_{-el} \iff D_i S_{T,i} \frac{dT}{dx} c_i = \frac{D_i F}{RT} E c_i \iff S_{T,i} \frac{\partial T}{\partial x} = \frac{F}{RT} \frac{F x^2}{\epsilon \Delta x} \quad (30)$$

regarding the situation at  $x = \Delta x$  we get for the deviation from electroneutrality  $\Delta c$

$$\Delta c = \frac{S_{T,i} R T \epsilon \Delta T}{F^2 \Delta x w} \approx 10^{-10} [\text{mol}/\text{m}^3]. \quad (31)$$

We used  $F = 96485.338 \text{ C/mol}$ ,  $R = 8.314 \text{ J/(mol} \cdot \text{K)}$ ,  $\epsilon = \epsilon_r \epsilon_0 = 80 \cdot 8.854 \cdot 10^{-12} \text{ F/m}$ <sup>37</sup>. This result shows that by comparing the magnitude of the constants related to the electrostatic flux to those involved in the thermomodiffusive flow, the electroneutrality condition is rendered valid. Even though our system is not homogeneous, one can use electroneutrality to calculate the electric field, as explained in more detail by Feldberg<sup>20</sup>.

**Zerth-order approximation in the 1-D case.** Solving the linear Equations (8), (9) and (10) expresses the gradients as nonlinear functions of the concentrations.

$$\frac{\partial c_i}{\partial x} = -S_{T,i}^{\text{eff}}(\{c_k\}) \frac{\partial T}{\partial x} c_i. \quad (32)$$

With  $S_{T,i}^{\text{eff}}(\{c_i\})$  may in general have some arbitrary non-linear dependence on the steady-state concentrations of (in principle) all species  $\{c_i\}$ . We define  $\gamma = c_i - c_i^0$  the deviation of the steady-state concentration from the initial concentration  $c_i^0 = c_i(t=0)$ . The initial concentration is reached, after the constituents have chemically equilibrated. We expand  $S_{T,i}^{\text{eff}}(\{c_i\})$  around  $\gamma = 0$

$$S_{T,i}^{\text{eff}}(\{c_i\}) = S_{T,i}^{\text{eff}}(\{c_i^0\}) + \sum_{n=1}^{\infty} \frac{(S_{T,i}^{\text{eff}}(\{c_i^0\}))^{(n)}}{n!} \gamma^n = S_{T,i}^{\text{eff},0} + \mathcal{O}[\gamma] \quad (33)$$

For  $\gamma \ll 1$  we can make the approximation

$$S_{T,i}^{\text{eff}}(\{c_i\}) \approx S_{T,i}^{\text{eff}}(\{c_i^0\}) = S_{T,i}^{\text{eff},0}(m_{\text{Na}}, m_{\text{form}}). \quad (34)$$

The steady-state solution is then an exponential (with linear temperature gradient  $\frac{\partial T}{\partial x} = \frac{\Delta T}{w}$ ,  $w$  the width,  $\Delta T$  the temperature difference)

$$c^*(x) = g_0^* \exp\left(-S_{T,i}^{\text{eff},0} \frac{\Delta T}{w} x\right) \quad (35)$$

with the constant  $g_0^*$  remains to be fixed (e.g. by global conservation of species). Since we are only interested in pH differences,  $g_0^*$  does not play a role for calculating  $\Delta \text{pH}$ .

**Homogenous concentrations  $c_i^0$ .** The homogenous concentrations to be used to calculate  $S_{T,i}^{\text{eff},0}(m_{\text{Na}}, m_{\text{form}})$  are given by the steady state conditions of the well mixed chemical reaction network. Explicitly, the equations for the concentrations are:

$$\begin{aligned} K_a &= \frac{c_{\text{H}^+}^0 c_{\text{COOH}^-}^0}{c_{\text{HCOOH}}^0} \\ K_w &= c_{\text{H}^+}^0 c_{\text{OH}^-}^0 \\ m_{\text{form}} &= c_{\text{HCOOH}}^0 + c_{\text{A}^-}^0 \\ 0 &= c_{\text{H}^+}^0 - c_{\text{COOH}^-}^0 + c_{\text{Na}^+}^0 - c_{\text{OH}^-}^0 \\ K_b &= \frac{c_{\text{Na}^+}^0 c_{\text{OH}^-}^0}{c_{\text{NaOH}}^0} \\ m_{\text{Na}} &= c_{\text{Na}^+}^0 + c_{\text{NaOH}}^0 \end{aligned} \quad (36)$$

with  $K_a = 10^{-3.745}$ ,  $K_b = 10^{-0.56}$ ,  $K_w = 10^{-14}$ . We can always solve these equations such that we can express the concentrations  $c_i^0$  as functions of the moieties  $m$ . Experimentally, the molar moiety concentrations  $m_{\text{form}}$  (the amount of bare formic acid) and  $m_{\text{Na}}$  can be controlled.

**Separation of timescales.** The crucial assumption for the development of a hierarchical theory is the separation of timescales associated to the different dynamic processes. In the following we will give reasoning on why these assumptions are reasonable. For an overview over the timescales involved, see Supplementary Fig. 4.



**Reaction timescale**  $\tau_{\text{chem}}$ . For the protonation and deprotonation of simple acid-base reactions, it is known that timescales are nearly instantaneous<sup>38</sup>. As an example, this has been studied for the deprotonation of formic acid where it was confirmed that timescales are  $<10^{-3}$  s<sup>39</sup>.

**Thermophoretic timescale**  $\tau_{\text{phor}}$ . Since the steady state temperature profile across the thermal trap is linear, the velocity associated with the thermophoretic movement is

$$u_{\text{phor}} = DS_T \frac{\Delta T}{w} \approx 39 \cdot 10^{-6} \text{ m/s}, \quad (37)$$

with  $\Delta T = 39\text{K}$  and  $w = 0.17\text{mm}$ . Thus, the time-scale of the phoretic motion in horizontal direction is given as

$$\tau_{\text{phor}} \approx w/u_{\text{phor}}$$

The Soret and diffusion coefficient for the hydrogen ion and the associated phoretic timescales are given in Supplementary Table 1).

**Convective timescale**  $\tau_{\text{conv}}$ . The average velocity of the convective flow is

$$u_{\text{conv}} = \bar{u}_y = \frac{1}{16} \frac{\beta g \rho \Delta T}{12 \mu} w^2 \approx 5.0 \cdot 10^{-6} \text{ m/s}$$

where we used the values  $\beta = 69 \cdot 10^{-6} \text{ 1/K}$ ,  $g = 9.81 \text{ m/s}^2$ ,  $\rho = 10^3 \text{ kg/m}^3$  and  $\mu = 0.80 \text{ mPa} \cdot \text{s}$ <sup>37</sup>. Thus, for a chamber height  $h = 50 \text{ mm}$  we obtain a time-scale

$$\tau_{\text{conv}} = h/u_{\text{conv}} \approx 10000\text{s}, \quad (38)$$

which is much larger than the typical phoretic time scales.

**Measurement (flow) timescale**  $\tau_{\text{flow}}$ . The timescale of the measurement process  $\tau_{\text{flow}}$  is defined by the volume of the thermal chamber and the flow rate applied. The volume  $V$  is calculated using the height  $h$  (50 mm), the width  $w$  (170  $\mu\text{m}$ ) and the broadness  $d$  (5 mm), giving  $V = 42.5 \mu\text{l}$ . Relating to the flow rate used throughout the experiments (3.28  $\frac{\text{ml}}{\text{s}}$ ), we get a timescale

$$\tau_{\text{flow}} = \frac{\text{vol}_{\text{thermalchamber}}}{\text{flow rate}} \approx 13000 \text{ s}, \quad (39)$$

which is somewhat larger than the convective time-scale. Hence, we assume that the concentration dynamics in the convective setting are only slightly disturbed in the experiment.

### Interpretation in 2D and 3D

**Interpretation in 2D via the Debye factor.** While in a purely one-dimensional case, the above expression can directly be used to calculate accumulation profiles of species, in two dimensions, convective transport has to be taken into account. We are able to make qualitative predictions about this situation since the processes happen on different timescales as shown in the section ‘‘Separation of timescales’’. The initial configuration of the system is homogeneous and chemically equilibrated. As shown above, the two main transport processes, thermophoresis and convection, have similar velocities, however their timescales differ as the length-scale for each process is different by orders of magnitude ( $w/h \sim 3.4 \cdot 10^{-4}$ ). Hence, the concentration field is first equilibrated in the horizontal direction with the exception of the upper and lower end of the trap. Stopping the process and taking a snapshot would reveal a horizontal concentration gradient, while in vertical direction, the species would be largely distributed homogeneously. The convective flow field is zero in the middle of the trap and flows up or downwards on the hot or cold side, respectively. Consequently, species located at either side of the trap are transported upwards or downwards. The horizontal gradient established by thermophoresis within its timescale is an approximation on the magnitude of the expected vertical flow, as it imposes different levels of concentration on either side of the thermal trap. From the slope of the gradient we can therefore estimate what fraction of the total species will be transported either upwards or downwards. This net transport over time accumulates species in the vertical direction until a steady-state of the vertical transport is reached as diffusive and convective currents are balancing each other. Therefore, through the different equilibration timescales of thermophoresis and convection we can make statements about the vertical gradient by looking at the horizontal gradient. The latter in turn is proportional to  $S_{\text{H}}^{\text{eff},0} \frac{\Delta T}{w}$ . Hence, by calculating  $S_{\text{H}}^{\text{eff},0}$  for a given chemical reaction network we are able to make predictions about the outcome of thermal trap experiments in the full dimension.

As introduced in the main text, the effective Soret coefficient relates to the horizontal pH gradient by  $(\Delta \text{pH})_{\text{hor}} \approx \frac{\Delta T}{\ln(10)} S_{\text{H}}^{\text{eff},0}$ . For the amplitude of the full 2D gradient, we use the scaling  $(\Delta \text{pH})_{\text{vert}} \approx \alpha_{\text{th}} \cdot S_{\text{H}}^{\text{eff},0} (m_{\text{Na}}, m_{\text{form}})$ . Following the results by Debye<sup>14</sup>, we approximate the vertical concentration profile by an exponential function

$$c(y) = G \exp\left(-\frac{y}{l}\right) \quad \text{with} \quad \frac{1}{l} = \frac{4}{15} \frac{\Delta T S \bar{u}_y}{D + \frac{128}{315} \left(\frac{\bar{u}_y}{D}\right)^2}.$$

A logarithmic concentration difference between bottom and top then gives

$\Delta \log_{10}(c) = \frac{h}{l} \log_{10}(e)$  so we can write the factor  $\alpha_{\text{th}}$

$$\alpha_{\text{th}} \approx \frac{\Delta T}{\ln(10)} \cdot \frac{4}{15} \frac{h \bar{u}_y}{D + \frac{128}{315} \left(\frac{\bar{u}_y}{D}\right)^2}, \quad \text{where} \quad \bar{u}_y = \frac{\beta g \rho \Delta T}{12 \eta} \frac{1}{16} w^2 \quad (40)$$

With thermal expansion coefficient  $\beta = 207 \cdot 10^{-6} \text{ 1/K}$ , gravitational constant  $g = 9.81 \text{ m/s}^2$ , density of water  $\rho = 995.67 \text{ kg/m}^3$  (at 30  $^{\circ}\text{C}$ ), viscosity  $\eta = 797 \cdot 10^{-6} \text{ mPa} \cdot \text{s}$ , temperature difference  $\Delta T = 39 \text{ K}$ , height of trap  $h = 0.05 \text{ m}$ , width of trap  $w = 170 \cdot 10^{-6} \text{ m}$ . Influences of formic acid and sodium hydroxide on density and viscosity can be neglected. As diffusion coefficient, we take  $D_{\text{H}}$  from Supplementary Table 1. We take the values for 30  $^{\circ}\text{C}$  as most material is accumulated towards the colder side. This gives us an  $\alpha_{\text{th}}$  of 358.5, used in the main text, Fig. 3.

**Extrapolation to 3D and flow distortions.** In the experimental part however, we measure the pH gradient in a 3D setting, continuously extracting the fluid through 3 outlets which we want to compare to the theoretical predictions. As discussed above, there are multiple uncertainties linked to the experimental setup. In addition and as mentioned before, the measured pH values on the top and bottom outflows are averaged over 12 % of the length of the thermal trap. Depending on the specific arrangement of each concentration profile this averaging procedure alters the concentration ratios of each dissolved compound at the outflows.

### Impact of chemical reactions, electrostatics and temperature dependent reaction rates.

For a better understanding of the individual contributions from chemical reactions, electrostatics and the temperature dependence of reaction rates, we simulated the chemical system in a 1 dimensional finite-element simulation (Comsol 5.4, see Supplementary Data 1). For a detailed study, we had to restrict ourselves to the 1D case since simulations for the 2D or 3D case are not converging when including electrostatic interactions between solutes according to our best knowledge.

For this, we combined the modules ‘‘heat transfer in solids’’, ‘‘general form PDE’’ and ‘‘electrostatics’’. In the stationary state and under assumption of insulation, the heat transfer is calculated from

$$\rho \cdot C_p \cdot \mathbf{u} \cdot \nabla T + \nabla \cdot (-\mathbf{k} \cdot \nabla T) = Q \quad (41)$$

with the density  $\rho$ , the specific heat capacity  $C_p$ , the velocity of the fluid  $\mathbf{u}$ , the temperature  $T$ , the thermal conductivity  $k_{\text{H}_2\text{O}} = 0.62 \frac{\text{W}}{\text{mK}}$  of water and the heat flux  $Q$ . Assuming a very slow fluid velocity, the first term can be neglected.

The result is then coupled to a general PDE and electrostatics. The former gives the following equation:

$$e_a \partial_i^2 c + d_a \partial_i c + \nabla \Gamma = f \quad (42)$$

with the mass coefficients  $e_a$ , the concentration vector  $\mathbf{c} = [c_{\text{H}}, c_{\text{A}}, \dots]$ , the damping coefficients  $d_a$ , the flux  $\Gamma$  and the source term  $f$ . In our case, the matrix  $e_a$  is zero. The flux writes as follows:

$$\Gamma = -D_i \cdot c_i - S_{T,i} \cdot D_i \cdot c_i \cdot \Delta T - \frac{z_i \cdot D_i \cdot F_{\text{const}}}{R_{\text{const}} \cdot T} \cdot \Delta V \cdot c_i \quad (43)$$

with temperature  $T$ , electric potential  $V$ , gas constant  $R_{\text{const}}$  and Faraday constant  $F_{\text{const}}$ . For each species  $i$ , the concentration ( $c_i$ ), the charge ( $z_i$ ) the diffusion coefficient ( $D_i$ ), and the Soret coefficient ( $S_{T,i}$ ) are used, for the latter see Supplementary Table 1. The source term includes all reactions, for example in the case of formic acid (AH):

$$f_{\text{AH}} = -k_{\text{on}} \cdot c_{\text{AH}} + k_{\text{off}} \cdot c_{\text{H}} \cdot c_{\text{A}} \quad (44)$$

For the temperature dependence of the dissociation constants of water ( $K_{\text{w}}$ ) and formic acid ( $K_{\text{A}}$ ), we used the values from<sup>40</sup> for formic acid and<sup>41</sup> for water.

For the electrostatics, the equations write as follows:

$$\nabla \cdot \mathbf{D} = \rho_V \quad \text{and} \quad \mathbf{E} = -\nabla V \quad (45)$$

with the electric displacement  $\mathbf{D} = \epsilon_0 \epsilon_r \mathbf{E}$  (including the permittivities), the electric field  $\mathbf{E}$ , the relative permittivity  $\epsilon_r$ , the vacuum permittivity  $\epsilon_0$ , the electric potential  $V$  and the space charge density  $\rho_V$  which writes as follows:

$$\rho_V = F_{\text{const}} \cdot \sum_i c_i \cdot z_i \quad (46)$$

To better understand the individual contributions of electrostatics, temperature dependence etc, we turned them off one by one (Supplementary Fig. 5).

### Data availability

All the data that support the plots and the other findings of this study are available from the corresponding authors upon reasonable request. The full details of the finite-element simulation from the Methods section and Supplementary Fig. 5 are documented in the mph file in Supplementary Data 1.

Received: 28 July 2022; Accepted: 30 December 2022;

Published online: 19 January 2023

## References

- Lodish, H. F. et al. *Molecular Cell Biology* Vol 4 (WH Freeman, 2006).
- Weiss, M. C. et al. The physiology and habitat of the last universal common ancestor. *Nat. Microbiol.* **1**, 1–8 (2016).
- Martin, W., Baross, J., Kelley, D. & Russell, M. J. Hydrothermal vents and the origin of life. *Nat. Rev. Microbiol.* **6**, 805–814 (2008).
- Lane, N. & Martin, W. F. The origin of membrane bioenergetics. *Cell* **151**, 1406–1416 (2012).
- Lane, N. Proton gradients at the origin of life. *BioEssays* **39**, 1600217 (2017).
- Lawless, J. et al. pH profile of the adsorption of nucleotides onto montmorillonite. *Orig. Life Evol. Biosph.* **15**, 77–88 (1984).
- Le Vay, K., Salibi, E., Song, E. Y. & Mutschler, H. Nucleic acid catalysis under potential prebiotic conditions. *Chem. Asian J.* **15**, 214–230 (2020).
- Budin, I., Bruckner, R. J. & Szostak, J. W. Formation of protocell-like vesicles in a thermal diffusion column. *J. Am. Chem. Soc.* **131**, 9628–9629 (2009).
- Kreysing, M., Keil, L., Lanzmich, S. & Braun, D. Heat flux across an open pore enables the continuous replication and selection of oligonucleotides towards increasing length. *Nat. Chem.* **7**, 203–208 (2015).
- Kelley, D. S. et al. An off-axis hydrothermal vent field near the mid-atlantic ridge at 30° n. *Nature* **412**, 145–149 (2001).
- Keil, L. M., Möller, F. M., Kieß, M., Kudella, P. W. & Mast, C. B. Proton gradients and pH oscillations emerge from heat flow at the microscale. *Nat. Commun.* **8**, 1–9 (2017).
- Becker, S. et al. Unified prebiotically plausible synthesis of pyrimidine and purine rna ribonucleotides. *Science* **366**, 76–82 (2019).
- Kruse, F. M., Teichert, J. S. & Trapp, O. Prebiotic nucleoside synthesis: the selectivity of simplicity. *Chem. Eur. J.* **26**, 14776–14790 (2020).
- Debye, P. Zur theorie des clusiuschen trennungsverfahrens. *Ann. Phys.* **428**, 284–294 (1939).
- Guthrie, G., Wilson, J. N. & Schomaker, V. Theory of the thermal diffusion of electrolytes in a clusius Column. *J. Chem. Phys.* **17**, 310–313 (1949).
- Mast, C. B., Schink, S., Gerland, U. & Braun, D. Escalation of polymerization in a thermal gradient. *Proc. Natl Acad. Sci. USA* **110**, 8030–8035 (2013).
- Rao, R. & Esposito, M. Nonequilibrium thermodynamics of chemical reaction networks: wisdom from stochastic thermodynamics. *Phys. Rev. X* **6**, 041064 (2016).
- Reichl, M., Herzog, M., Götz, A. & Braun, D. Why charged molecules move across a temperature gradient: The role of electric fields. *Phys. Rev. Lett.* **112**, 198101 (2014).
- MacGillivray, A. D. Nernst-planck equations and the electroneutrality and donnan equilibrium assumptions. *J. Chem. Phys.* **48**, 2903–2907 (1968).
- Feldberg, S. W. On the dilemma of the use of the electroneutrality constraint in electrochemical calculations. *Electrochem. Commun.* **2**, 453–456 (2000).
- Keil, L., Hartmann, M., Lanzmich, S. & Braun, D. Probing of molecular replication and accumulation in shallow heat gradients through numerical simulations. *Phys. Chem. Chem. Phys.* **18**, 20153–20159 (2016).
- Gore, V. Formation of sugars in mixtures of tartaric acid and aldehydes in tropical sunlight. *J. Phys. Chem.* **37**, 745–749 (1933).
- Orgel, L. E. Prebiotic chemistry and the origin of the rna world. *Crit. Rev. Biochem. Mol. Biol.* **39**, 99–123 (2004).
- Miller, S. L. Production of some organic compounds under possible primitive earth conditions. *J. Am. Chem. Soc.* **77**, 2351–2361 (1955).
- Choughuley, A., Subbaraman, A., Kazi, Z. & Chada, M. A possible prebiotic synthesis of thymine: uracil-formaldehyde-formic acid reaction. *BioSystems* **9**, 73–80 (1977).
- Pine, S. H. & Sanchez, B. L. The formic acid-formaldehyde methylation of amines. *J. Org. Chem.* **36**, 829–832 (1971).
- Cody, G. D. et al. Primordial carbonylated iron-sulfur compounds and the synthesis of pyruvate. *Science* **289**, 1337–1339 (2000).
- Becker, S. et al. Origin of life: a high-yielding, strictly regioselective prebiotic purine nucleoside formation pathway. *Science* **352**, 833–836 (2016).
- Saladino, R., Crestini, C., Costanzo, G., Negri, R. & Di Mauro, E. A possible prebiotic synthesis of purine, adenine, cytosine, and 4(3h)-pyrimidinone from formamide: Implications for the origin of life. *Bioorg. Med. Chem.* **9**, 1249–1253 (2001).
- Saladino, R., Crestini, C., Pino, S., Costanzo, G. & Di Mauro, E. Formamide and the origin of life. *Phys. Life Rev.* **9**, 84–104 (2012).
- Göppel, T., Palyulin, V. V. & Gerland, U. The efficiency of driving chemical reactions by a physical non-equilibrium is kinetically controlled. *Phys. Chem. Chem. Phys.* **18**, 20135–20143 (2016).
- Möller, F. M., Kriegel, F., Kieß, M., Sojo, V. & Braun, D. Steep pH gradients and directed colloid transport in a microfluidic alkaline hydrothermal pore. *Angew. Chem. Int. Ed.* **56**, 2340–2344 (2017).
- Matreux, T. et al. Heat flows in rock cracks naturally optimize salt compositions for ribozymes. *Nat. Chem.* **13**, 1038–1045 (2021).
- Mariani, A., Bonfio, C., Johnson, C. M. & Sutherland, J. D. ph-driven rna strand separation under prebiotically plausible conditions. *Biochemistry* **57**, 6382–6386 (2018).
- Ianeselli, A. et al. Water cycles in a hadean co2 atmosphere drive the evolution of long DNA. *Nat. Phys.* **18**, 1–7 (2022).
- Burelbach, J., Frenkel, D., Pagonabarraga, I. & Eiser, E. A unified description of colloidal thermophoresis. *Eur. Phys. J. E* **41**, 1–12 (2018).
- Lide, D. R. & Baysinger, G. Crc handbook of chemistry and physics: a ready-reference book of chemical and physical data. *Choice Rev. Online* **41**, 41–4368–41–4368 (2004).
- Donten, M. L., VandeVondele, J. & Hamm, P. Speed limits for acid–base chemistry in aqueous solutions. *Chimia* **66**, 182–186 (2012).
- Jolly, G. S., McKenney, D. J., Singleton, D. L., Paraskevopoulos, G. & Bossard, A. R. Rates of hydroxyl radical reactions. part 14. rate constant and mechanism for the reaction of hydroxyl radical with formic acid. *J. Phys. Chem.* **90**, 6557–6562 (1986).
- HwaáKim, M., ShikáKim, C. & WooáLee, H. et al. Temperature dependence of dissociation constants for formic acid and 2, 6-dinitrophenol in aqueous solutions up to 175° c. *J. Chem. Soc., Faraday trans.* **92**, 4951–4956 (1996).
- Bandura, A. V. & Lvov, S. N. The ionization constant of water over wide ranges of temperature and density. *J. Phys. Chem. Ref. Data* **35**, 15–30 (2006).

## Acknowledgements

This work was funded by the Deutsche Forschungsgemeinschaft (DFG, German Research Foundation)—Project-ID 364653263—TRR 235 (T.M., J.R., D.B., C.B.M., U.G.) and under Germany's Excellence Strategy—EXC-2094—390783311 (D.B., U.G.). Funding by the Volkswagen Initiative 'Life?—A Fresh Scientific Approach to the Basic Principles of Life' (T.M., C.B.M., D.B.) is gratefully acknowledged. This work was further supported by the Center for Nanoscience Munich (CeNS). We thank A. Schmid and P. Aikkila for experimental support.

## Author contributions

T.M., B.A., J.R. and C.B.M. performed the research. T.M., B.A., J.R., D.B., C.B.M. and U.G. designed the research, T.M., B.A., J.R., D.B., C.B.M. and U.G. analyzed the data and wrote the Letter.

## Funding

Open Access funding enabled and organized by Projekt DEAL.

## Competing interests

The authors declare no competing interests.

## Additional information


**Supplementary information** The online version contains supplementary material available at <https://doi.org/10.1038/s42005-023-01126-y>.

**Correspondence** and requests for materials should be addressed to Christof B. Mast or Ulrich Gerland.

**Peer review information** *Communications Physics* thanks Ludovic Jullien and the other, anonymous, reviewers for their contribution to the peer review of this work. Peer reviewer reports are available.

**Reprints and permission information** is available at <http://www.nature.com/reprints>

**Publisher's note** Springer Nature remains neutral with regard to jurisdictional claims in published maps and institutional affiliations.

 **Open Access** This article is licensed under a Creative Commons Attribution 4.0 International License, which permits use, sharing, adaptation, distribution and reproduction in any medium or format, as long as you give appropriate credit to the original author(s) and the source, provide a link to the Creative Commons license, and indicate if changes were made. The images or other third party material in this article are included in the article's Creative Commons license, unless indicated otherwise in a credit line to the material. If material is not included in the article's Creative Commons license and your intended use is not permitted by statutory regulation or exceeds the permitted use, you will need to obtain permission directly from the copyright holder. To view a copy of this license, visit <http://creativecommons.org/licenses/by/4.0/>.

© The Author(s) 2023

## Contents

<b>Supplementary Notes</b>	<b>3</b>
Supplementary Note 1: Complete algebraic solution for the horizontal $H^+$ gradients . . . . .	3
<b>Supplementary Figures</b>	<b>5</b>
Supplementary Figure 1: Initial pH values . . . . .	5
Supplementary Figure 2: List of additional measurements . . . . .	6
Supplementary Figure 3: Determination of experimental error . . . . .	7
Supplementary Figure 4: Overview of the different timescales involved	8
Supplementary Figure 5: Overview of the effects of the different contributions to pH gradients . . . . .	9
<b>Supplementary Tables</b>	<b>10</b>
Supplementary Table 1: Soret and diffusion coefficients . . . . .	10
<b>Supplementary References</b>	<b>11</b>

## Supplementary Notes

### Supplementary Note 1: Complete algebraic solution for the horizontal $H^+$ gradients

Solving for the expression of the proton gradient as a function of the other concentrations with a symbolic computation software like Mathematica yields

$$\frac{\partial c_{\text{H}}}{\partial x} = -S_{\text{H}}^{\text{eff}}[\{c_i(x)\}] \frac{\partial T}{\partial x} c_{\text{H}} . \quad (1)$$

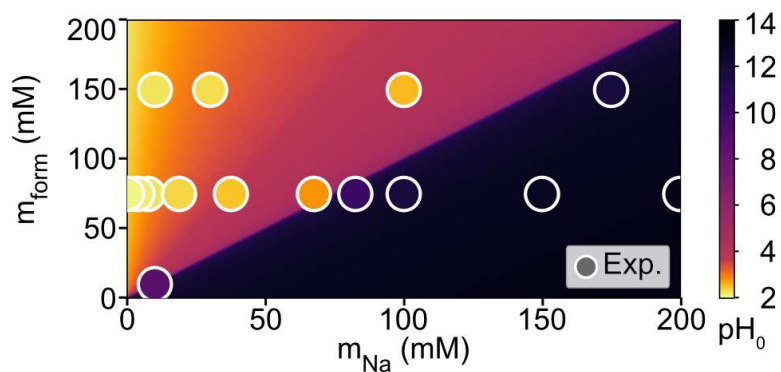
with the effective Soret coefficient:

$$\begin{aligned}
S_H^{\text{eff}}[\{c_i(x)\}] = & - \left[ -c_{\text{COOH}}^2 D_{\text{COOH}} (c_{\text{Na}} D_{\text{Na}} (c_{\text{HCOOH}} D_{\text{HCOOH}} S_{\text{HCOOH}} \right. \\
& + c_{\text{NaOH}} D_{\text{NaOH}} (S_{\text{COOH}} + S_{\text{Na}} - S_{\text{NaOH}}) \\
& + c_{\text{OH}} D_{\text{OH}} (S_{\text{COOH}} - S_{\text{OH}})) \\
& + c_{\text{NaOH}} D_{\text{NaOH}} (c_{\text{HCOOH}} D_{\text{HCOOH}} S_{\text{HCOOH}} \\
& + c_{\text{OH}} D_{\text{OH}} (S_{\text{COOH}} - S_{\text{OH}})) \\
& + c_{\text{H}} D_{\text{H}} (S_{\text{COOH}} + S_{\text{H}}) (c_{\text{Na}} D_{\text{Na}} + c_{\text{NaOH}} D_{\text{NaOH}}) \\
& + c_{\text{COOH}} (c_{\text{HCOOH}} D_{\text{HCOOH}} (c_{\text{Na}} (c_{\text{NaOH}} D_{\text{COOH}} D_{\text{NaOH}} S_{\text{NaOH}} \\
& - D_{\text{Na}} S_{\text{HCOOH}} (c_{\text{H}} D_{\text{H}} + c_{\text{NaOH}} D_{\text{NaOH}} + c_{\text{OH}} D_{\text{OH}})) \\
& - c_{\text{NaOH}} D_{\text{NaOH}} S_{\text{HCOOH}} (c_{\text{H}} D_{\text{H}} + c_{\text{OH}} D_{\text{OH}}) \\
& + c_{\text{Na}}^2 D_{\text{COOH}} D_{\text{Na}} (S_{\text{COOH}} - S_{\text{HCOOH}} + S_{\text{Na}})) \\
& + c_{\text{Na}} D_{\text{COOH}} (c_{\text{H}} D_{\text{H}} (c_{\text{Na}} D_{\text{Na}} (S_{\text{Na}} - S_{\text{H}}) + c_{\text{NaOH}} D_{\text{NaOH}} S_{\text{NaOH}}) \\
& + c_{\text{Na}} D_{\text{Na}} (c_{\text{NaOH}} D_{\text{NaOH}} S_{\text{NaOH}} + c_{\text{OH}} D_{\text{OH}} (S_{\text{Na}} + S_{\text{OH}})) \\
& + c_{\text{NaOH}} c_{\text{OH}} D_{\text{NaOH}} D_{\text{OH}} S_{\text{NaOH}})) \\
& + c_{\text{HCOOH}} c_{\text{Na}} D_{\text{HCOOH}} (c_{\text{H}} D_{\text{H}} (c_{\text{Na}} D_{\text{Na}} (S_{\text{Na}} - S_{\text{H}}) \\
& + c_{\text{NaOH}} D_{\text{NaOH}} S_{\text{NaOH}}) + c_{\text{Na}} D_{\text{Na}} (c_{\text{NaOH}} D_{\text{NaOH}} S_{\text{NaOH}} \\
& + c_{\text{OH}} D_{\text{OH}} (S_{\text{Na}} + S_{\text{OH}})) + c_{\text{NaOH}} c_{\text{OH}} D_{\text{NaOH}} D_{\text{OH}} S_{\text{NaOH}}) \left. \right] \\
& / \left[ (c_{\text{COOH}} + c_{\text{H}} + c_{\text{Na}} + c_{\text{OH}}) (c_{\text{COOH}} D_{\text{COOH}} \right. \\
& (c_{\text{HCOOH}} D_{\text{HCOOH}} (c_{\text{Na}} D_{\text{Na}} + c_{\text{NaOH}} D_{\text{NaOH}}) \\
& + c_{\text{H}} D_{\text{H}} (c_{\text{Na}} D_{\text{Na}} + c_{\text{NaOH}} D_{\text{NaOH}}) \\
& + c_{\text{OH}} D_{\text{OH}} (c_{\text{Na}} D_{\text{Na}} + c_{\text{NaOH}} D_{\text{NaOH}}) + c_{\text{Na}} c_{\text{NaOH}} D_{\text{Na}} D_{\text{NaOH}}) \\
& + c_{\text{HCOOH}} D_{\text{HCOOH}} (c_{\text{H}} D_{\text{H}} (c_{\text{Na}} D_{\text{Na}} + c_{\text{NaOH}} D_{\text{NaOH}}) \\
& + c_{\text{Na}} D_{\text{Na}} (c_{\text{NaOH}} D_{\text{NaOH}} + c_{\text{OH}} D_{\text{OH}}) + c_{\text{NaOH}} c_{\text{OH}} D_{\text{NaOH}} D_{\text{OH}})) \left. \right] \quad (2)
\end{aligned}$$

The according numerical values are found in Supplementary Table 1.

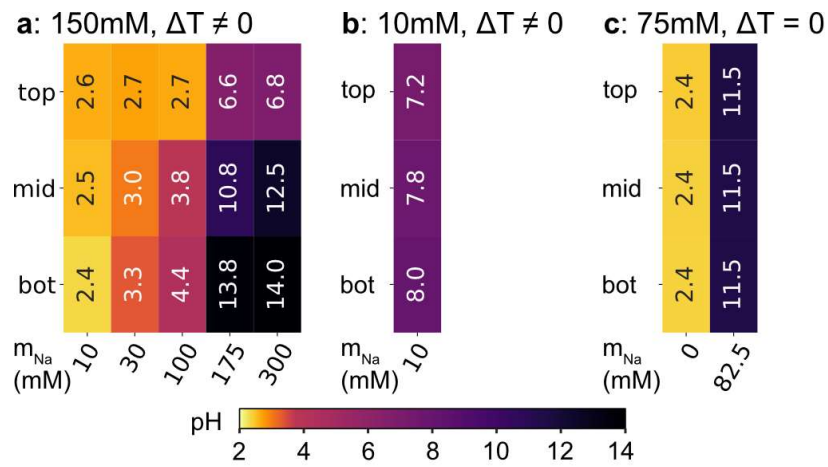
## Supplementary Figures

Supplementary Figure 1: Initial pH values



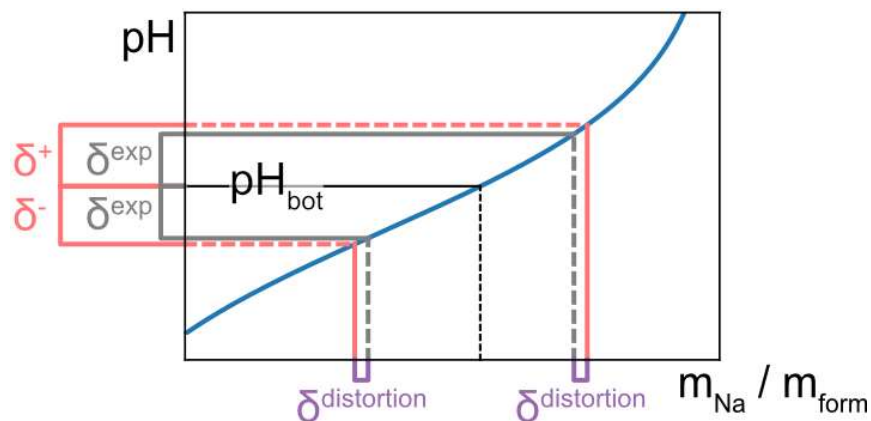
The pH values of the premixed solutions are compared to the initial state of the theoretical model. The experimental values (in circles) show a very good agreement with the analytical assumptions.

Supplementary Figure 2: List of additional measurements



List of measurements with **a:** 150 mM and **b:** 10 mM of formic acid and varying amounts of sodium hydroxide ( $m_{Na}$ ). For each combination, the pH of the different outflow fractions are shown. The values for 75 mM formic acid are shown in the main text, Fig. 2b. **c** presents the control measurements with  $\Delta T = 0$  K, showing no pH gradient as expected.

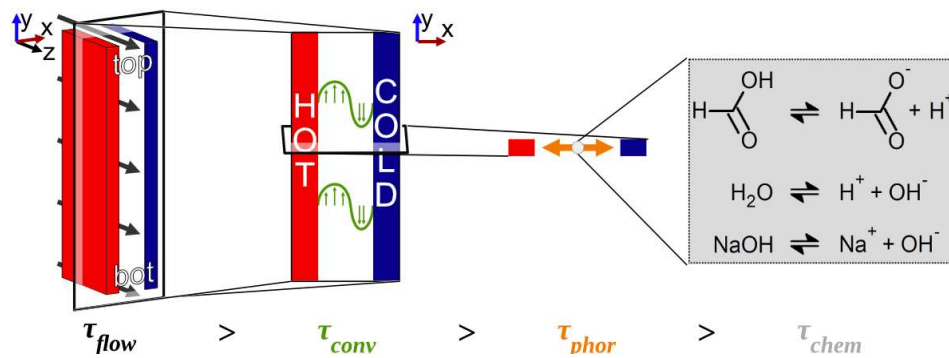
Supplementary Figure 3: Determination of experimental error



The pH error calculated from experimental replicates is converted to an error in  $m_{\text{Na}}/m_{\text{form}}$  around the measured value. On both sides, an uncertainty accounting for concentration fluctuations from thermal gradient effects in the outflow channels  $\delta^{\text{distortion}} = 0.02 m_{\text{Na}}/m_{\text{form}}$  is added. By transforming the resulting minimum and maximum back to pH value, we get the full experimental errors  $\delta^+$  and  $\delta^-$ , used for example in Fig. 3. Fully drawn lines indicate value in their initial dimensions (i.e. measured values), dashed lines indicate calculate values.

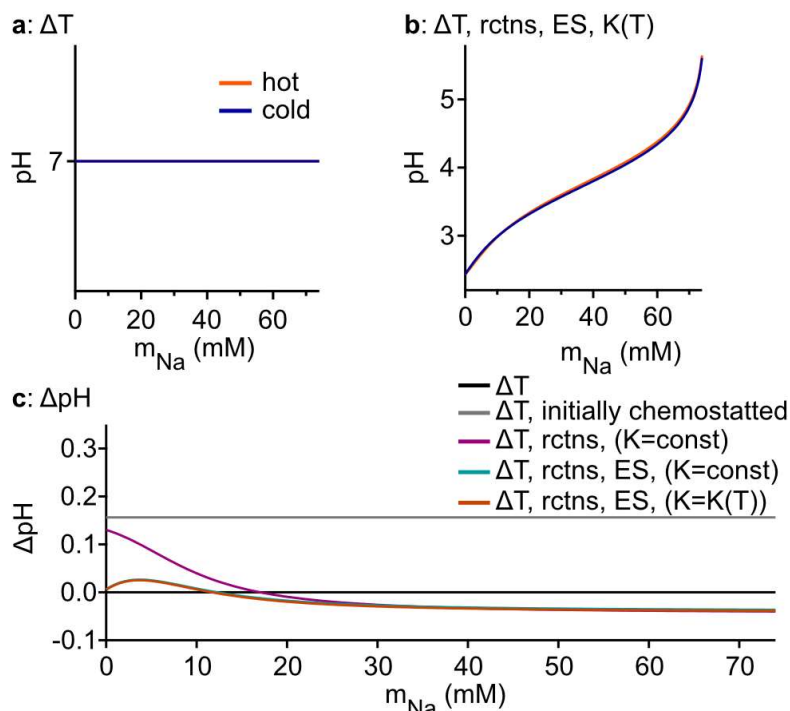


Supplementary Figure 4: Overview of the different timescales involved



$\tau_{flow}$  corresponds to the drift through the system for measuring the different fractions,  $\tau_{conv}$  and  $\tau_{phor}$  are the convective and thermophoretic timescales respective, corresponding to equilibration in horizontal and vertical direction.  $\tau_{chem}$  is the fastest timescale, corresponding to local chemical equilibrium. As shown above (and in main Fig. 3a), each of these corresponds to a number of dimensions involved, from 3 to 0 dimensions.

**Supplementary Figure 5: Overview of the effects of the different contributions to pH gradients**



**a-b:** Exemplary cases without any contributions and with the full one dimensional simulation. The hot side corresponds to the top part of the full heat flux chamber, the cold side to the bottom part. In both cases, we used point probes (0.1 % on each side). **a:** In the case without any chemical reactions, the pH does not vary for different concentrations of NaOH. **b:** In a full 1D simulation including chemical reactions, electrostatics and the temperature dependence of  $K_a$  and  $K_w$ , the complex behaviour of the experiment is reproduced. **c:** The pH gradient for all different stages of contributions shows the importance of all parts: in the non-reacting case (black, " $\Delta T$ "), no pH gradient appears. When adding an initial chemostating step (before entry into the heat flux cell), a constant pH gradient for all concentrations of NaOH appears (grey, " $\Delta T$ , initially chemostatted"). Turning on reactions inside the heat flux cell (purple, " $\Delta T$ , rctns, ( $K=\text{const}$ )") yields a more complex behaviour and includes an inversion; however, it lacks the first minimum and shows more extreme pH gradients since overcrowding is not prohibited by electrostatic repulsion. When adding electrostatic interactions (turquoise, " $\Delta T$ , rctns, ES, ( $K=\text{const}$ )"), the theoretically predicted profile appears which is only slightly changed by including the temperature dependence of dissociation constants (red, " $\Delta T$ , rctns, ES, ( $K=K(T)$ )").

## Supplementary Tables

**Supplementary Table 1: Soret and diffusion coefficients**

Species $j$	Charge	$S_{T,j}$ [1/K]	$D_j$ [ $10^{-9} m^2/s$ ]	$\tau_{\text{phor}}$ [s]
OH <sup>-</sup>	-1	0.02327 [1]	5.273 [2]	6.04
H <sup>+</sup>	+1	0.01809 [1]	9.311[2]	4.4
COOH <sup>-</sup>	-1	0.0055 [3]	1.454 [2]	92.7
Na <sup>+</sup>	+1	0.00468[1]	1.334[2]	119
HCOOH	0	0.00055 <sup>1</sup>	1.49[4]	904
NaOH	0	0.0004 <sup>1</sup>	1.49 <sup>1</sup>	1243

Numerical Values of Soret and diffusion coefficients and calculated phoretic timescales.

<sup>1</sup>Estimated from comparison of charged/uncharged molecules in [5].

## Supplementary References

- [1] Takeyama, N., Nakashima, K.: Proportionality of intrinsic heat of transport to standard entropy of hydration for aqueous ions. *J. Solution Chem.* **17**(4), 305–325 (1988). <https://doi.org/10.1007/BF00650412>
- [2] Lide, D.R., Baysinger, G.: *Crc handbook of chemistry and physics: a ready-reference book of chemical and physical data*. *Choice Rev. Online* **41**(08), 41–4368414368 (2004)
- [3] Domonkos, L., Liszi, J.: Thermal diffusion of weak electrolytes III. The soret coefficients of normal carboxylic acids. *Zeitschrift fur Phys. Chemie* **214**(1), 55–64 (2000). <https://doi.org/10.1524/zpch.2000.214.1.055>
- [4] Winkelmann, J.: Diffusion coefficient of formic acid in water at infinite dilution, 1946–1946 (2018)
- [5] Keil, L.M.R., Möller, F.M., Kieß, M., Kudella, P.W., Mast, C.B.: Proton gradients and pH oscillations emerge from heat flow at the microscale. *Nat. Commun.* **8**(1), 1–9 (2017). <https://doi.org/10.1038/s41467-017-02065-3>

# Appendix C

## Heat flows enrich prebiotic building blocks and enhance their reactivity

Published in *Nature* in April 2024.

**Matreux, T.\***, Aikkila, P.\*, Scheu, B., Braun, D. & Mast, C. B.  
Heat flows enrich prebiotic building blocks and enhance their reactivity

*Nature*

**628**, 110–116

2024

<https://doi.org/10.1038/s41586-024-07193-7>

According to Springer Nature, the ownership of copyright in original research articles remains with the author, who retains the non-exclusive rights to reproduce the contribution in whole or in part in any printed volume (book or thesis) of which they are the author(s).

As the Supplementary Information contains numerous pages of tables of raw data, they are omitted here and can be found online.

## Article

# Heat flows enrich prebiotic building blocks and enhance their reactivity

<https://doi.org/10.1038/s41586-024-07193-7>

Thomas Matreux<sup>1,3</sup>, Paula Aikkila<sup>1,3</sup>, Bettina Scheu<sup>2</sup>, Dieter Braun<sup>1</sup> & Christof B. Mast<sup>1✉</sup>

Received: 13 September 2022

Accepted: 9 February 2024

Published online: 3 April 2024

Open access

 Check for updates

The emergence of biopolymer building blocks is a crucial step during the origins of life<sup>1–6</sup>. However, all known formation pathways rely on rare pure feedstocks and demand successive purification and mixing steps to suppress unwanted side reactions and enable high product yields. Here we show that heat flows through thin, crack-like geo-compartments could have provided a widely available yet selective mechanism that separates more than 50 prebiotically relevant building blocks from complex mixtures of amino acids, nucleobases, nucleotides, polyphosphates and 2-aminoazoles. Using measured thermophoretic properties<sup>7,8</sup>, we numerically model and experimentally prove the advantageous effect of geological networks of interconnected cracks<sup>9,10</sup> that purify the previously mixed compounds, boosting their concentration ratios by up to three orders of magnitude. The importance for prebiotic chemistry is shown by the dimerization of glycine<sup>11,12</sup>, in which the selective purification of trimetaphosphate (TMP)<sup>13,14</sup> increased reaction yields by five orders of magnitude. The observed effect is robust under various crack sizes, pH values, solvents and temperatures. Our results demonstrate how geologically driven non-equilibria could have explored highly parallelized reaction conditions to foster prebiotic chemistry.

The formation of the first biopolymers and their building blocks on the early Earth was a key moment during the origins of life. Possible reaction pathways for the formation of nucleotides, amino acids and lipids have been studied with great success<sup>1–6</sup>. To uncover the details of such pathways and to map them reproducibly, laboratory experiments usually start with well-defined concentrations of previously purified reactants<sup>15–18</sup> (Fig. 1a). Often, a well-defined sequence of manual steps is required, such as the addition of further reactants or the selective purification of intermediates to increase the yield of the final products. Although high starting concentrations can be helpful, the number of side products substantially increases for complex reaction pathways. Therefore, without some form of intermediary purification<sup>19–21</sup>, the reaction will result in vanishingly small concentrations of the desired product or even be completely inhibited.

Although such further steps seem artificial and challenging to perform in a prebiotic context, some plausible, substance-specific purification processes have been found, including the crystallization of nucleotide precursors<sup>22,23</sup> or the precipitation of aminonitriles<sup>24</sup>. Other selective approaches use reaction-specific interconversions<sup>25</sup>, ultraviolet (UV) light<sup>26</sup>, sequestration<sup>27</sup> or adsorption and enrichment of RNA<sup>28</sup> or RNA building blocks<sup>29</sup> on surfaces. Coacervates locally optimize conditions for prebiotic chemistry through phase separation<sup>30,31</sup>. However, these mechanisms only work for specific prebiotic compounds and may require mutually exclusive environmental conditions. A natural mechanism that spatially separates and simultaneously purifies a wide range of prebiotic compounds and implements numerous connected reaction environments remains elusive.

In this work, we show that heat flows through thin rock cracks provide an answer to this problem. These cracks, for example, generated by thermal stress, form large networks and were presumably ubiquitous on the early Earth<sup>9,10</sup>. Specifically, water-filled fractures and thin, connected pathways are found in a variety of geological settings, from mafic to ultramafic rocks in volcanic complexes to geothermal or hydrothermal systems and sedimentary layers, for example, in shallow submarine or lacustrine environments<sup>10,32,33</sup>. Our results show the simultaneous but spatially separated, heat-flux-driven purification of more than 50 prebiotically relevant organic compounds. Although the overall system is fed by slow geothermal fluxes, each rock fracture hosts local solvent convection (Fig. 1b, black arrows) and thermophoretic drift of solutes along the temperature gradient (Fig. 1b, white arrows). The interplay of both effects increases the concentrations differently for the various solutes, shifting their concentration ratios by several orders of magnitude. This specificity results from the sensitive dependence of thermophoresis on charge, size and solvent interaction<sup>8,34–37</sup>. Heat flows are readily available in the early Earth lithosphere, cooling down from accretion and being fed by radioactive decay. Such large-scale thermal gradients are superimposed by local thermal gradients, for example, in volcanically active or geothermal environments, and as a thermoaureole linked to magmatic intrusions<sup>32</sup>. Also, heat is a waste product of various chemical and petrological processes. This mechanism thus offers a wide range of ubiquitously available reaction conditions for prebiotic chemistry within geological compartments.

Heat fluxes were shown to locally enrich nucleotides<sup>7,38</sup>, help copy oligomers in a length-dependent manner<sup>39</sup>, generate local pH differences<sup>40,41</sup> and optimize salt conditions for ribozymes<sup>42</sup>. However, it is

<sup>1</sup>Systems Biophysics, Ludwig-Maximilians-Universität München, Munich, Germany. <sup>2</sup>Department of Earth and Environmental Sciences, Ludwig-Maximilians-Universität München, Munich, Germany. <sup>3</sup>These authors contributed equally: Thomas Matreux, Paula Aikkila. ✉e-mail: [christof.mast@physik.uni-muenchen.de](mailto:christof.mast@physik.uni-muenchen.de)

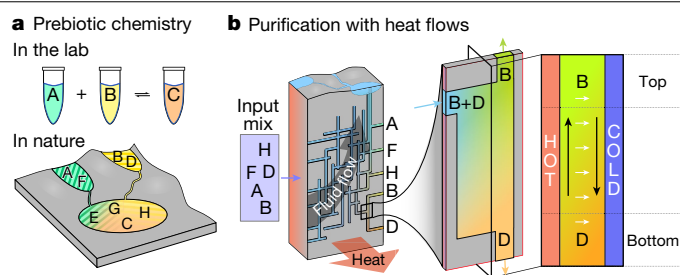


**Fig. 1 | Purifying the prebiotic clutter.** **a**, Prebiotic chemistry reactions often require precisely timed mixing of well-defined starting materials with intermediate purification steps for high product yields. In nature, starting solutions are complex mixtures that react to produce many undesirable side products. **b**, Ubiquitous heat flows through thin rock fractures, fed by geothermal fluid flow (grey arrow), form a geo-microfluidic system that separates even highly similar prebiotic chemicals from each other through substance-sensing thermophoresis (white arrows) and fluid convection (black arrows). Owing to the geological scale, many different solution compositions are reached simultaneously.

unclear how heat fluxes affect complex mixtures of small, prebiotically relevant organics and whether these can be selectively enriched and separated spatially in geologically plausible systems.

To answer this question, we used geologically inspired microfluidic heat flow chambers as a first step to experimentally study the thermophoretic accumulation of complex mixtures in a single rock fracture. In the second step, we numerically investigated the effects on large fracture networks and experimentally verified the results in proof-of-principle minimal network systems.

Numerical modelling of such networks requires the mostly unknown thermophoretic properties of the molecules involved, which are not accessible at low concentrations using available methods. For instance, high-sensitivity methods rely on fluorenescent labels, which substantially alter the diffusive and thermophoretic properties of the target molecule<sup>43</sup>. Holographic techniques require high concentrations that lead to pH shifts and only allow the measurement of one component at a time<sup>44</sup>. We have, therefore, developed a method to simultaneously measure the thermophoretic properties of up to 20 compounds from their mixtures, limited only by high-performance liquid chromatography (HPLC) sensitivity.

Our experimental and numerical results show that even weak heat fluxes separate and locally enrich 2-aminoazoles, amino acids, nucleobases and nucleotides in their various phosphorylation states. The effect distinguishes substances of equal mass and works in a wide pH range and for different solvents. We demonstrate the benefit for prebiotic chemistry with the TMP-driven dimerization of glycine, which is enhanced by selective purification of the reactants in a single heat flow chamber and numerically model the reaction in networks of connected cracks to explain the large-scale effects in natural environments.

We mimicked a single thin rock fracture with a heat flow chamber, defined by a 170- $\mu\text{m}$ -thin fluorinated ethylene propylene (FEP)-defined microfluidic structure between a heated (40 °C) and a cooled sapphire (25 °C) (Fig. 2a and Extended Data Fig. 1; Methods) and filled it with a mixture of prebiotic compounds  $i$  (initial concentration  $c_0 = 20\text{--}50\ \mu\text{M}$  each). By the interplay of fluid convection and solute thermophoretic drift  $v_{Ti} = -\nabla T \times S_{Ti} \times D_i$ , an exponential concentration profile built up within the heat flow chamber<sup>45,46</sup>, with  $S_{Ti}$  denoting the Soret coefficient as a measure of the thermophoretic strength and  $D_i$  the diffusive mobility of the solute. After 18 h, we stopped the experiment, froze the chamber and divided its contents into four parts of equal volume. The concentration ratio of the respective substances in each section relative to the chamber-averaged concentration  $c_0$  of this substance was then

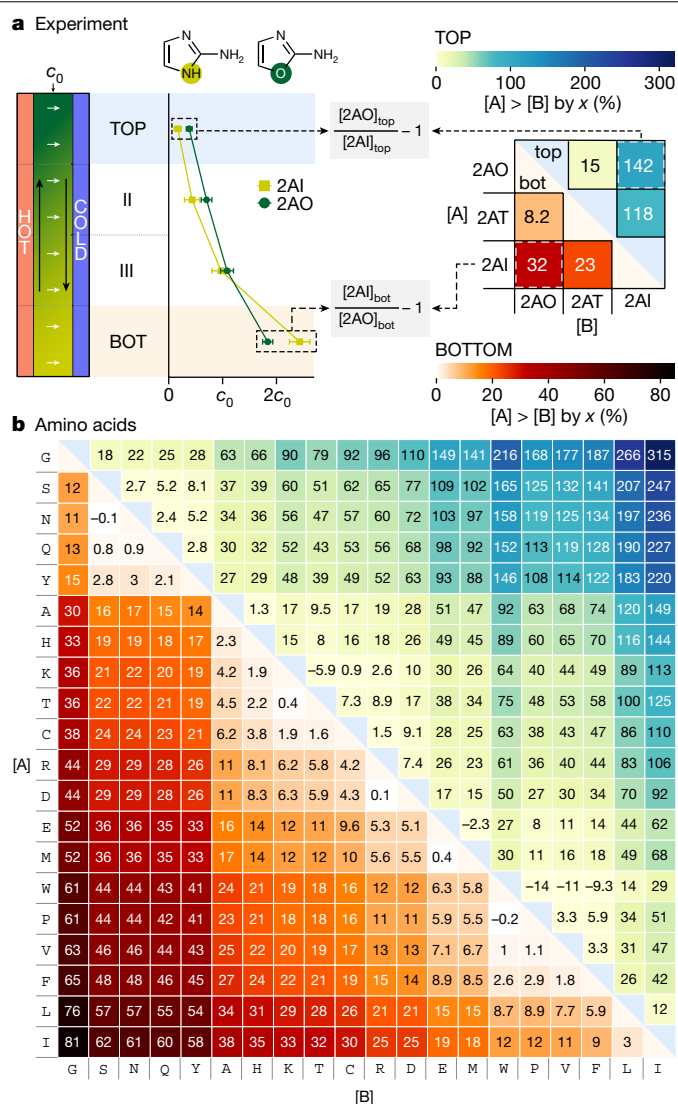


**Fig. 2 | Thermophoretic enrichment of prebiotic organics in a single heat flow chamber.** **a**, Illustration of the selective enrichment of prebiotic components for a mixture of 2AI, 2AT and 2AO in a thermal gradient (25–40 °C). Heat maps show the concentration ratios of all possible substance pairs in the bottom (orange shaded) and top (blue shaded) sections of the chamber. For example (dashed boxes), in the top section, 2AO is (142 ± 52)% more concentrated than 2AI, whereas in the bottom section, 2AI is (32 ± 3.6)% enriched over 2AO (errors = s.d., three repeats). **b**, Enrichment in a mixture of all proteogenic amino acids (30  $\mu\text{M}$  each) reveals a strong enrichment of aliphatic amino acids isoleucine (I), valine (V) and leucine (L) in the bottom section (orange shade) against glycine (G) (up to (81 ± 25)% and serine (S), asparagine (N) and glutamine (Q) (up to (62 ± 17)%). Consistently, the aliphatic amino acids are strongly depleted in the top section (blue shade), resulting in up to (315 ± 138)% higher local glycine concentration. See Extended Data Figs. 2–4 for measurements at other initial pH values, temperature gradients, salt concentrations and error maps.

determined by HPLC. In this way, measurements of different mixtures of nucleobases or amino acids could be compared despite different initial concentrations of the individual components. The mean enrichment  $[A_j]/[B_j] - 1$  between compounds A and B in the top ( $j = \text{top}$ ) and bottom ( $j = \text{bot}$ ) chamber parts was determined from triplicate experiments (Figs. 2–3, Extended Data Figs. 2–5 and raw data in Supplementary Tables 5–65; Methods).

The degree of enrichment and spatial separation of different substances in a single heat flow chamber is visualized by comparing their

## Article

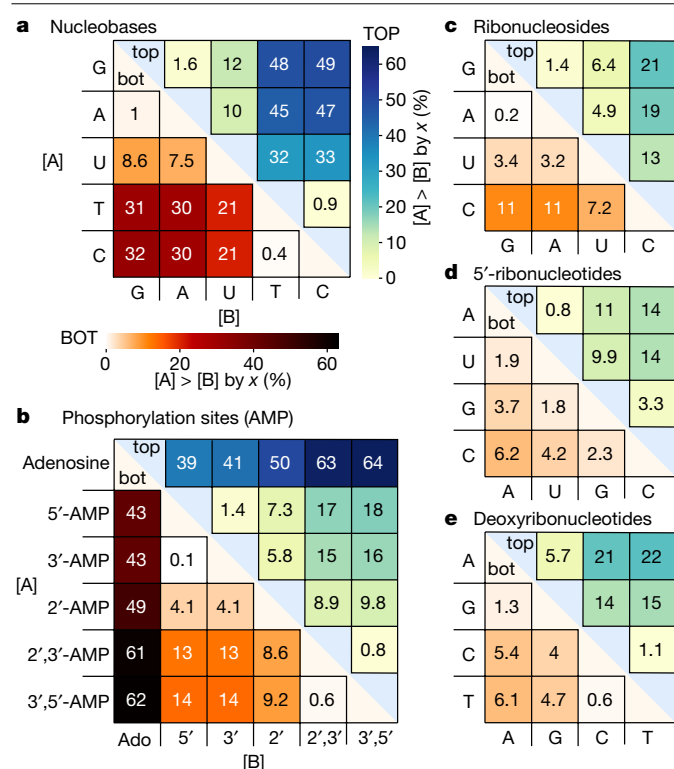


**Fig. 3 | Enrichment of nucleobases, nucleosides and nucleotides.** **a**, In mixtures of nucleobases A, U, T, C and G with an initial concentration of 30  $\mu\text{M}$ , C and T are enriched up to  $(32 \pm 13)\%$  (error = s.d., three repeats) against G, A and U in the bottom section. Enrichments in the top section are inverted but at lower absolute concentrations because of thermophoretic depletion (11.5 to 31  $\mu\text{M}$ , corresponding to 0.5–0.9-fold  $c_0$ ). **b**, Enrichment strongly depends on the phosphorylation state. In the bottom section, cyclic 2',3'-AMP and 3',5'-AMP are enriched up to  $(62 \pm 0.3)\%$  relative to adenosine and  $(14 \pm 0.6)\%$  relative to the linearly phosphorylated 5'-AMP, 3'-AMP or 2'-AMP. The enrichment is inverted in the top section. **c–e**, Enrichment patterns similar to those of nucleobases, but with reduced strength, are also found for nucleosides (**c**) and nucleotides (**d,e**). Extended Data Fig. 5 and Supplementary Figs. 1–3 show more conditions and error tables.

concentrations in the uppermost (blue shaded) and lowermost (orange shaded) sections in Figs. 2 and 3. In a mixture of 2-aminoazoles, simple RNA precursors and catalysts, we found that, in the bottom section, 2-aminoimidazole (2AI) is enriched over 2-aminoxazole (2AO) by  $[\text{2AI}]_{\text{bot}}/[\text{2AO}]_{\text{bot}} - 1 = (32 \pm 3.6)\%$ . In the diluted top section, 2AO is enriched by  $[\text{2AO}]_{\text{top}}/[\text{2AI}]_{\text{top}} - 1 = (142 \pm 52)\%$  over 2AI (Fig. 2a and Extended Data Fig. 2 for errors). The absolute concentrations of species in the bottom section range from 64 to 173  $\mu\text{M}$ , whereas we measured between 6 and 20  $\mu\text{M}$  in the top section. Owing to the almost complete depletion (about 0.17-fold  $c_0$ ) of the thermophoretically stronger species, the remaining, weaker accumulating species are highly enriched here.

Amino acids, the building blocks of peptides and proteins, are a critical class of prebiotically plausible and relevant substances<sup>6,47</sup>. To determine their thermophoretic separation, we analogously investigated a mixture of all 20 proteinogenic amino acids at physiological pH (Fig. 2b). Although thermophoretically similar amino acids such as aspartic acid (D) and arginine (R) are not strongly separated from each other ( $[\text{D}]_{\text{bot}}/[\text{R}]_{\text{bot}} - 1 = (0.1 \pm 2.8)\%$ ), we found a massive separation of isoleucine (I) against glycine (G) by  $[\text{I}]_{\text{bot}}/[\text{G}]_{\text{bot}} - 1 = (81 \pm 25)\%$  in the bottom fraction. Sorting the amino acids according to their mutual enrichment, we found that glycine, as the smallest amino acid, concentrates most weakly in the bottom fraction, whereas the aliphatic

amino acids leucine (L), valine (V) and I accumulate most strongly. The situation is inverted in the top fraction, as the amino acids with the weakest thermophoretic strength have the highest concentration here ( $[\text{G}]_{\text{top}}/[\text{I}]_{\text{top}} - 1 = (315 \pm 138)\%$ ). Even mass-identical amino acids I and L are separated up to  $[\text{L}]_{\text{top}}/[\text{I}]_{\text{top}} - 1 = (12 \pm 0.3)\%$ . The enrichment values and their errors for amino acids at other pH values and different ionic strengths show similar separation patterns (Extended Data Figs. 3 and 4). In a mixture of 17 proteogenic and nine non-proteogenic amino acids, we found no clear bias towards either (Extended Data Fig. 2). We also found no thermophoretic separation between amino acids<sup>48</sup> and nucleosides of different chirality (Extended Data Fig. 5s–u).

In a mixture of all canonical nucleobases in water, thymine (T) and cytosine (C) are enriched by up to  $(32 \pm 13)\%$  over adenine (A) and guanine (G) in the bottom section of the chamber (Fig. 3a and Extended Data Fig. 5a for errors). The observed pattern is mainly identical in 10% formamide<sup>16</sup> solution, in 100 mM phosphate buffer<sup>15,17,18,22</sup> and for various crack diameters and pH values (Extended Data Fig. 5b,c,e–m). In 10% methanol<sup>21,24,29</sup> solution, accumulation and enrichment are almost entirely suppressed (Extended Data Fig. 5d).

Adenosine nucleotides (AMPs) are concentrated between  $(43 \pm 1)\%$  and  $(62 \pm 0.3)\%$  more than the adenosine nucleoside (Ado) in the bottom section, owing to the extra phosphate group that increases the charge and, thus, the thermophoretic strength<sup>35</sup> (Fig. 3b). Cyclic AMPs are accumulated up to  $(14 \pm 0.6)\%$  more than linear AMPs. Despite identical mass, 2'-AMP is enriched by  $(4.1 \pm 0.3)\%$  over 3'-AMP and 5'-AMP. Similar results are found for cytidine and its nucleotides (Extended Data Fig. 5q).

Mixtures of RNA or DNA nucleosides and nucleotides in all phosphorylation states show a similar enrichment pattern as for bases, albeit with lower magnitude (Fig. 3c–e and Extended Data Fig. 5n–p). The reduced thermophoretic separation is reasonable because the ribose and phosphate groups added to the different bases are identical for all nucleosides and nucleotides, thus decreasing the relative structural difference between species.

Because thermogravitational accumulation approaches exponential concentration profiles in the steady state<sup>45,46</sup>, the volume-averaged enrichments measured are lower than the actual values present at the bottom. For instance, separation in the lowest one-twelfth is substantially higher compared with the lowest quarter, at the cost of an increased error (Extended Data Fig. 2b). At the lowest end of the exponential profile, 2AI is enriched up to 406% over 2AO (Extended Data Fig. 2c,  $S_{Ti}$  from Extended Data Table 1), in contrast to  $(32 \pm 3.6)\%$  in the lowest quarter (Fig. 2a). See Extended Data Fig. 2e for how this translates to separation at lower temperature gradients.

### Enrichment in geological networks

The above measurements were performed in a single heat flow chamber, however, geological systems of interconnected fractures are highly variable in size and can span from millimetres to tens or even hundreds of metres. To approach such complex systems, we first performed a proof-of-principle experiment (Fig. 4a–c). We applied a flow of 1 nl  $\text{s}^{-1}$  of mixed compounds to the first heat flux chamber 1 (violet shade, Fig. 4a), which branches into chambers 2 and 3 (brown and blue shades, Fig. 4a). To determine the spatial enrichment, we ran a mixture of amino acids through the chambers ( $\Delta T = 16 \text{ K}$ ) for 60 h, froze them and divided them into the colour-graded areas shown in Fig. 4a for analysis through HPLC. Figure 4b shows the position and concentration of exemplarily selected amino acids phenylalanine (F), I and asparagine (N) with the corresponding colour assignment (Extended Data Fig. 6 and Supplementary Fig. 4 for various amino acids). The scatter plots, including I and N, show the separation of concentration ratios per chamber. The range of enrichments in a three-chamber network ( $[\text{N}]/[\text{I}] = 23$ -fold and  $[\text{I}]/[\text{N}] = 4.2$ -fold) is higher than achievable in a single chamber (Fig. 4b, left and Supplementary Fig. 5). This shows that the enrichment effect



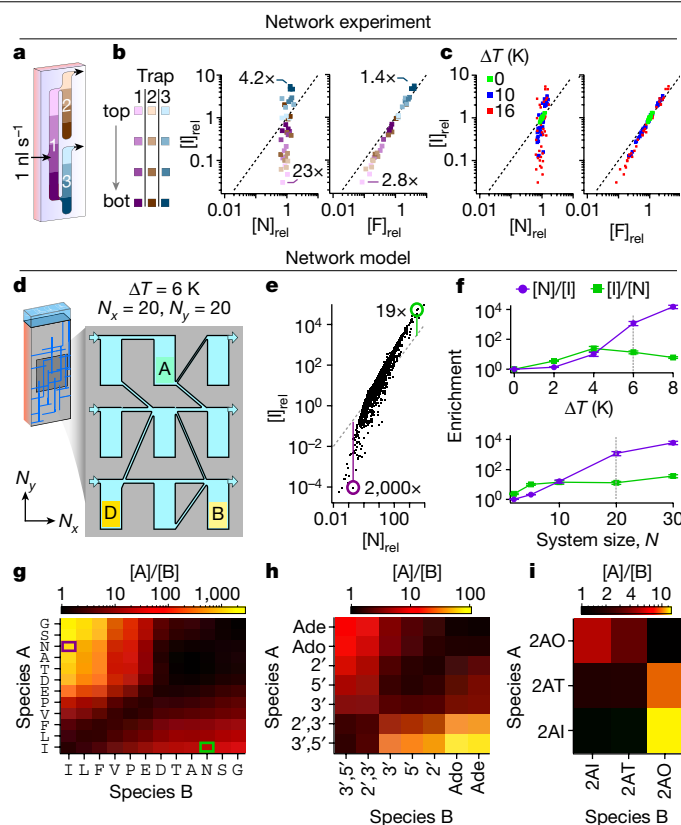


**Fig. 4 | Experimental and modelled purification of prebiotic organics in a network of connected rock cracks.** **a**, Experimental setup of a small network of three interconnected chambers with a volume inflow of  $1 \text{ nl s}^{-1}$  of an amino acid mixture and  $\Delta T = 16 \text{ K}$ . **b**, After 60 h, the chamber contents from three repeats were frozen and divided into individual parts according to the colour gradations in **a** and measured by HPLC. Exemplary separations of amino acids I versus N and I versus F are shown. Concentration ratios in chamber 2 (brown shade) versus 3 (blue shade) range from  $[I]/[N] = 23\text{-fold}$  (brown) to  $[N]/[I] = 4.2\text{-fold}$  (blue). For thermophoretically similar amino acids F and I, these range from  $[I]/[F] = 2.8\text{-fold}$  (brown) to  $[F]/[I] = 1.4\text{-fold}$  (blue). The dashed black line indicates equal concentration. **c**, Data from **b** in red compared with an otherwise identical run at  $\Delta T = 10 \text{ K}$  (blue) and  $0 \text{ K}$  (control, green) show stronger enrichment at higher temperatures and no effect without heat flux.

**d**, Larger systems ( $N_x \times N_y = 20 \times 20$ ,  $\Delta T = 6 \text{ K}$ ) of connected heat flow chambers with a volume inflow of  $1 \text{ nl s}^{-1}$  per input channel are modelled numerically. **e**, Concentration ratios between amino acids I and N in the chamber system show a similar but amplified pattern as in **b**. **f**, Maximum enrichments  $[N]/[I]$  (purple) and  $[I]/[N]$  (green) scale with the temperature difference and the size of the system. The dashed lines show the conditions in **e** and **g**. Error bars represent the s.d. from several simulations (Methods). **g–i**, Maximum enrichments in the system shown in **d** for all possible combinations of substances for a mixture of amino acids (**g**), adenine (nucleobase/nucleoside/nucleotides) (**h**) and 2-aminoazoles (**i**). Highlighted boxes indicate maximum enrichments for the pair I and N shown in **e**. See Extended Data Fig. 6 for error values.

is compatible with throughflows and is boosted substantially by the interaction of three chambers in a network. Maximum enrichments for thermophoretically different amino acids, such as I versus N, are much greater than those for thermophoretically similar amino acids, such as I versus F (Fig. 4b, right and more examples in Extended Data Fig. 6). As expected, the enhancement becomes stronger for larger temperature differences (Fig. 4c, blue  $\Delta T = 10 \text{ K}$ , red  $\Delta T = 16 \text{ K}$ ) and disappears without a heat flux (green,  $\Delta T = 0 \text{ K}$ ).

These results encouraged us to model the behaviour of larger systems in silico. We numerically assembled a network of  $N_x = 20$  by  $N_y = 20$  connected heat flow chambers with a size of  $50 \times 200 \text{ mm}$ , fed by a geothermal fluid flow (Fig. 4d). To understand the behaviour of each species inside the complete system, we first determined the thermophoretic properties of all solutes (Supplementary Code and Data and Extended Data Table 1; Methods). For 3',5'-AMP, one of the few compounds used in this work with known thermophoretic properties, our result  $S_{T,3',5'\text{-AMP}} = (0.0051 \pm 0.0009) \text{ K}^{-1}$  (at  $40 \text{ }^\circ\text{C}$ ) agrees with the literature values  $S_{T,3',5'\text{-AMP,ref}} = 0.005 \text{ K}^{-1}$  (at  $30 \text{ }^\circ\text{C}$ ) within the error margin<sup>7</sup>.

On the basis of these results, we calculated the average concentrations for mixtures of prebiotic compounds in the lower parts of all network chambers for 30 separate networks and a temperature difference

of  $6 \text{ K}$  (Fig. 4e–i). The flow rate for the inlet channels, which mimic the slow geothermal flow, was set to  $1 \text{ nl s}^{-1}$  as assumed realistic in geological systems<sup>49</sup> and used in the experiments in Fig. 4a–c. The flow rates for the individual chambers of the network mostly varied between  $0.1$  and  $10 \text{ nl s}^{-1}$  as a result of the randomly assigned throughputs of the connecting channels (Supplementary Fig. 10).

Similar to the experimental results shown in Fig. 4b,c, species with high Soret coefficients are strongly concentrated in upstream chambers and depleted downstream. There, species with small Soret coefficients are dominant and, therefore, highly enriched (Extended Data Fig. 9). Accordingly, the maximum ratio of concentrations of the amino acids I versus N is 19-fold at higher absolute concentrations, whereas the ratio of N versus I in another chamber is 2,000-fold at reduced absolute concentrations (Fig. 4e). Each point in Fig. 4e represents the average concentrations in the lower part of the respective heat flow chamber of the network, showing a similar but amplified pattern compared with the experiments. Extended Data Fig. 7 shows further examples of amino acid combinations analogous to Fig. 4e, demonstrating enrichments at notable absolute concentrations.

In natural systems, temperature differences across chamber cross-sections are eventually below the assumed  $\Delta T = 6 \text{ K}$ . For this

## Article

reason, we varied the temperature difference in Fig. 4f and found a near-exponential dependence for the enrichment of N versus I. The reverse enrichment, that is, I versus N, saturates at  $(25 \pm 9)$ -fold and even declines at higher temperature differences (Fig. 4f, top), owing to the throughflow-limited thermophoretic accumulation of solutes at the chamber bottom at higher temperature gradients. By contrast, in the upper chamber region, species with strong thermophoresis can deplete almost completely, leading to high enrichments of species with smaller Soret coefficients with increasing temperature gradients (Supplementary Fig. 11). The errors were determined from three repeated simulations, considering the errors of the Soret coefficients (Extended Data Table 1; Methods). Notably, even a slight temperature difference of only 2 K drives an up to  $(3.5 \pm 0.2)$ -fold enrichment of I versus N (Supplementary Discussion 1). The enrichment is further boosted with increasing network size, in particular for the thermophoretic weaker species (N versus I, Fig. 4f, bottom).

Figure 4g shows the maximum enrichment of amino acids under the same model parameters as in Fig. 4e. The network amplifies the respective values compared with Fig. 2b; for example, G is enriched up to  $(2,726 \pm 713)$ -fold compared with I; in other chambers, I is enriched  $(38 \pm 14)$ -fold. Amino acids with similar Soret coefficients, such as I and V, are enriched up to a maximum of  $[I]/[V] = (1.6 \pm 0.1)$ -fold. Similar effects were observed between nucleobases and nucleotides of different phosphorylation states and 2-aminoazoles (Fig. 4h–i and Extended Data Fig. 6).

Starting with a 1:1 solution of two substances with sufficiently different thermophoresis, such as I and N, heat fluxes in networks can thus provide niches with at least 95% purity of the stronger accumulated substance. For the thermophoretically weaker compound, even 99.9% purity is feasible.

### Habitat for prebiotic reactions

How does prebiotic chemistry benefit from the heat-flow-driven purification outlined above? We address this question using the example of a TMP-driven reaction. As a highly water-soluble phosphate species, TMP is particularly interesting for prebiotic chemistry, enabling various prebiotic reactions even in water or pasteurized environments<sup>13,19</sup>. However, TMP is considered scarce on the prebiotic Earth because of energy-intensive synthesis pathways, making its selective enrichment critical<sup>14</sup>.

As an example of a TMP-driven reaction, we examine the dimerization of glycine in water<sup>11,12</sup> (Fig. 5a). We filled a heat flux chamber with a mixture of 1 mM (Fig. 5b, pink) or 10 mM glycine (Fig. 5b, purple) and 1 mM TMP. After 16 h runtime with a temperature difference of  $\Delta T = 14$  K, the product yields were increased from an undetectable level ( $\Delta T = 0$  K, Fig. 5b, black,  $T = 85^\circ\text{C}$ ) to  $(3.6 \pm 0.6)\%$ , enabled by the selective enrichment of TMP over the thermophoretically weaker glycine (Extended Data Table 1).

Encouraged by these results, we sought to model the dimerization of glycine in a network of heat flow chambers. We first determined the reaction rates of the reaction model (equations (9)–(13)), studying the dimerization of glycine experimentally in bulk under TMP titration at  $90^\circ\text{C}$  and with initial pH 10.5 over up to 120 h (Fig. 5c; Methods). The model network consists of  $20 \times 20$  connected heat flow chambers, fed with a mixture of TMP and glycine ( $1 \mu\text{M}$  each) at a flow rate of  $1 \text{ nl s}^{-1}$  per inlet (Fig. 5d).

In the absence of heat flows, the concentrations of the product GlyGly are vanishingly small at around 10 fM (Fig. 5e, solid lines). The situation changes substantially on applying a temperature difference of 10 K to each chamber. The heat-flow-driven enrichment increases the maximum reactant concentrations by four orders of magnitude (blue and black dashed lines, Fig. 5e) and enhances the maximal product yields  $2c_{\text{GlyGly}}/(2c_{\text{GlyGly}} + c_{\text{Gly}})$  by up to five orders of magnitude, reaching around 10% at  $\Delta T = 10$  K (Fig. 5f). These results

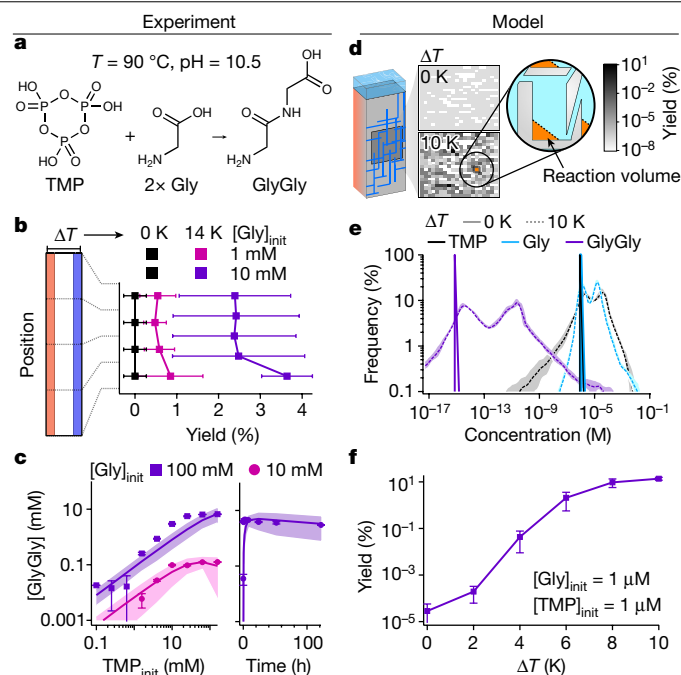


**Fig. 5 | Experimental and modelled enhancement of reaction yields by heat-flow-driven, selective purification of reactants.** **a**, TMP-associated dimerization of glycine<sup>11</sup>. **b**, Even in a single heat flux chamber ( $\Delta T = 14$  K), the product yield of Gly dimerization increases to up to  $(3.6 \pm 0.6)\%$  after 16 h from undetectable yields in the controls ( $\Delta T = 0$  K) for  $[\text{Gly}]_{\text{init}} = 1 \text{ mM}$  and  $10 \text{ mM}$  and  $[\text{TMP}]_{\text{init}} = 1 \text{ mM}$  (errors = s.d., three repeats). **c**, The reaction rates from equations (9)–(13) were determined experimentally by simultaneously fitting to the product concentrations for bulk glycine dimerization after 16 h with 10 mM and 100 mM initial Gly concentrations over three orders of magnitude of TMP concentrations (left) and to a time series up to 120 h for  $[\text{Gly}]_{\text{init}}$  and  $[\text{TMP}]_{\text{init}} = 100 \text{ mM}$  (right). **d**, Gly dimerization was modelled numerically in networks of connected cracks by using reaction rates obtained in **c**. The 2D maps show product concentrations of GlyGly from TMP-induced dimerization after 120 h without ( $\Delta T = 0$  K) and with ( $\Delta T = 10$  K) applied heat flux with an inflow rate of  $1 \text{ nl s}^{-1}$  per input channel. Each pixel corresponds to the bottom concentration of GlyGly in a separate crack (reaction volume, orange). **e**, Statistics of all reactant concentrations in 100 distinct systems of  $N_x = 20$  by  $N_y = 20$  connected cracks. Without heat flow ( $\Delta T = 0$  K, solid line), TMP (black) and Gly (blue) concentrations remain unchanged at  $1 \mu\text{M}$ , leading to vanishingly low product concentration (GlyGly, purple). With heat flow ( $\Delta T = 10$  K), reactant concentrations are increased more than four orders of magnitude, so that—in 0.1% of all chambers—at least  $10 \mu\text{M}$  of product can be formed. Shaded area denotes the s.d. by several runs (Methods). **f**, The reaction yields of TMP-driven glycine dimerization increase exponentially with the applied temperature gradient.

show that otherwise challenging prebiotic reactions are massively boosted by the heat-flow-driven selective accumulation and local enrichment.

### Conclusion

In summary, we have studied experimentally and numerically the selective and localized enrichment of more than 50 prebiotically relevant substances by heat fluxes. The scenario mimics the situation in extended geological networks of rock cracks and shows how geothermal heat flows could have driven the sensitive separation of highly similar molecules. At moderate temperature differences, distinct amino acids are separated from each other by up to three orders of magnitude, components of nucleotides by up to two orders of magnitude and the different 2-aminoazoles by a factor of 10. In the upstream part of the

network, species with strong thermophoresis are accumulated and depleted further downstream. Here residual chemicals with weak thermophoresis are enriched at moderate thermophoretic accumulations (Extended Data Figs. 6, 7 and 9). The resulting concentration ratios could be conveyed to higher absolute concentrations by non-selective up-concentration modes such as local drying or accumulation at gas–water interfaces. As long as the thermophoretic strength of two substances differs sufficiently, they can be spatially separated, enriched and mixed with other concentrated chemicals in the geo-microfluidic system.

The mechanism works over a wide range of pH (3–11) and solvent conditions (Extended Data Figs. 3–5). The strength of the enrichment scales exponentially with the temperature difference. Smaller heat fluxes could have been compensated by naturally occurring larger, metre-scaled networks. The process is very stable to local and temporal fluctuations in the heat flux and operates in a variety of irregular chamber geometries (Supplementary Discussion 1 and Supplementary Fig. 12). All investigated compounds exhibit considerable thermophoretic accumulation that scales exponentially with their Soret coefficients, the latter spanning a wide range between  $1.4 \times 10^{-3}$  and  $7.5 \times 10^{-3} \text{ K}^{-1}$ .

We demonstrate the advantages for prebiotic chemistry by placing an otherwise challenging reaction, glycine dimerization, in a network of interconnected cracks. Such reactions typically suffer from the low relative abundance of their driving agents, in our case, TMP. We show experimentally that the thermal non-equilibrium markedly enhances reaction yields in a single chamber and numerically demonstrate how this effect is amplified by the network, boosting yields by up to five orders of magnitude. The universal availability of heat fluxes on the early Earth, either from the geological setting or as a waste product of one of many exothermic reactions, makes this mechanism conceivable in various environments.

Systems of interconnected thin fractures and cracks or comparable permeable pathways are thought to be ubiquitous in volcanic and geothermal environments. Connected to the surface, such systems can potentially feed spatially separated ponds or pools, whose role in the origin of life has been extensively studied. Ultimately, a large number of sequential reaction conditions required by numerous prebiotic reaction pathways could have been implemented without external intervention. Given the wide availability of heat flows and fractures in rocks, the observed applicability to even small prebiotic compounds and the overall robustness of the process, thermophoretic enrichment of organics could have provided a steady driving force for a natural origins-of-life laboratory.

## Online content

Any methods, additional references, Nature Portfolio reporting summaries, source data, extended data, supplementary information, acknowledgements, peer review information; details of author contributions and competing interests; and statements of data and code availability are available at <https://doi.org/10.1038/s41586-024-07193-7>.

- Muchowska, K. B., Varma, S. J. & Moran, J. Synthesis and breakdown of universal metabolic precursors promoted by iron. *Nature* **569**, 104–107 (2019).
- Trapp, O., Teichert, J. & Kruse, F. Direct prebiotic pathway to DNA nucleosides. *Angew. Chem. Int. Ed. Engl.* **58**, 9944–9947 (2019).
- Becker, S. et al. Unified prebiotically plausible synthesis of pyrimidine and purine RNA ribonucleotides. *Science* **366**, 76–82 (2019).
- Preiner, M. et al. A hydrogen-dependent geochemical analogue of primordial carbon and energy metabolism. *Nat. Ecol. Evol.* **4**, 534–542 (2020).
- Jash, B., Tremmel, P., Jovanovic, D. & Richert, C. Single nucleotide translation without ribosomes. *Nat. Chem.* **13**, 751–757 (2021).
- Patel, B. H., Percivalle, C., Ritson, D. J., Duffy, C. D. & Sutherland, J. D. Common origins of RNA, protein and lipid precursors in a cyanosulfidic protometabolism. *Nat. Chem.* **7**, 301–307 (2015).
- Wang, Z., Kriegs, H. & Wiegand, S. Thermal diffusion of nucleotides. *J. Phys. Chem. B* **116**, 7463–7469 (2012).
- Sehnm, A. L., Niether, D., Wiegand, S. & Figueiredo Neto, A. M. Thermodiffusion of monovalent organic salts in water. *J. Phys. Chem. B* **122**, 4093–4100 (2018).
- van Otterloo, J., Cas, R. A. F. & Scutter, C. R. The fracture behaviour of volcanic glass and relevance to quench fragmentation during formation of hyaloclastite and phreatomagmatism. *Earth-Sci. Rev.* **151**, 79–116 (2015).
- Colombier, M. et al. In situ granulation by thermal stress during subaqueous volcanic eruptions. *Geology* **47**, 179–182 (2019).
- Boigenzahn, H. & Yin, J. Glycine to oligoglycine via sequential trimetaphosphate activation steps in drying environments. *Orig. Life Evol. Biosph.* **52**, 249–261 (2022).
- Chung, N. M., Lohmann, R., Orgel, L. E. & Rabinowitz, J. The mechanism of the trimetaphosphate-induced peptide synthesis. *Tetrahedron* **27**, 1205–1210 (1971).
- Gan, D., Ying, J. & Zhao, Y. Prebiotic chemistry: the role of trimetaphosphate in prebiotic chemical evolution. *Front. Chem.* **10**, 941228 (2022).
- Pham Minh, D., Ramarason, J., Nzihou, A. & Sharrock, P. One-step synthesis of sodium trimetaphosphate ( $\text{Na}_3\text{P}_3\text{O}_9$ ) from sodium chloride and orthophosphoric acid. *Ind. Eng. Chem. Res.* **51**, 3851–3854 (2012).
- Powner, M. W., Gerland, B. & Sutherland, J. D. Synthesis of activated pyrimidine ribonucleotides in prebiotically plausible conditions. *Nature* **459**, 239–242 (2009).
- Schoffstall, A. M., Barto, R. J. & Ramos, D. L. Nucleoside and deoxynucleoside phosphorylation in formamide solutions. *Orig. Life* **12**, 143–151 (1982).
- Islam, S., Bucar, D. K. & Powner, M. W. Prebiotic selection and assembly of proteinogenic amino acids and natural nucleotides from complex mixtures. *Nat. Chem.* **9**, 584–589 (2017).
- Fahrenbach, A. C. et al. Common and potentially prebiotic origin for precursors of nucleotide synthesis and activation. *J. Am. Chem. Soc.* **139**, 8780–8783 (2017).
- Gibard, C., Bhowmik, S., Karki, M., Kim, E. K. & Krishnamurthy, R. Phosphorylation, oligomerization and self-assembly in water under potential prebiotic conditions. *Nat. Chem.* **10**, 212–217 (2018).
- Schuster, P. Taming combinatorial explosion. *Proc. Natl Acad. Sci. USA* **97**, 7678–7680 (2000).
- Islam, S. & Powner, M. W. Prebiotic systems chemistry: complexity overcoming clutter. *Chem* **2**, 470–501 (2017).
- Anastasi, C., Crowe, M. A., Powner, M. W. & Sutherland, J. D. Direct assembly of nucleoside precursors from two- and three-carbon units. *Angew. Chem.* **118**, 6322–6325 (2006).
- Morasch, M. et al. Heated gas bubbles enrich, crystallize, dry, phosphorylate and encapsulate prebiotic molecules. *Nat. Chem.* **11**, 779–788 (2019).
- Ashe, K. et al. Selective prebiotic synthesis of phosphoroaminonitriles and aminothioamides in neutral water. *Commun. Chem.* **2**, 23 (2019).
- Powner, M. W. & Sutherland, J. D. Phosphate-mediated interconversion of ribo- and arabino-configured prebiotic nucleotide intermediates. *Angew. Chem. Int. Ed.* **49**, 4641–4643 (2010).
- Todd, Z. R., Szabla, R., Szostak, J. W. & Sasselov, D. D. UV photostability of three 2-aminoazoles with key roles in prebiotic chemistry on the early earth. *Chem. Commun.* **55**, 10388–10391 (2019).
- Springsteen, G. & Joyce, G. F. Selective derivatization and sequestration of ribose from a prebiotic mix. *J. Am. Chem. Soc.* **126**, 9578–9583 (2004).
- Mizuuchi, R. et al. Mineral surfaces select for longer RNA molecules. *Chem. Commun.* **55**, 2090–2093 (2019).
- Sanchez, R., Ferris, J. & Orgel, L. E. Conditions for purine synthesis: did prebiotic synthesis occur at low temperatures? *Science* **153**, 72–73 (1966).
- Le Vay, K., Song, E. Y., Ghosh, B., Tang, T.-Y. D. & Mutschler, H. Enhanced ribozyme-catalyzed recombination and oligonucleotide assembly in peptide-RNA condensates. *Angew. Chem. Int. Ed.* **133**, 26300–26308 (2021).
- Smokers, I. B. A., van Haren, M. H. I., Lu, T. & Spruijt, E. Complex coacervation and compartmentalized conversion of prebiotically relevant metabolites. *ChemSystemsChem* **4**, e202200004 (2022).
- Pirajno, F. *Hydrothermal Processes and Mineral Systems* (Springer, 2010).
- Montanaro, C. et al. Hydrothermal activity and subsoil complexity: implication for degassing processes at Solfatara crater, Campi Flegrei caldera. *Bull. Volcanol.* **79**, 83 (2017).
- Petit, C. J., Hwang, M.-H. & Lin, J. Thermal diffusion of dilute aqueous  $\text{NH}_4\text{Cl}$ ,  $\text{Me}_3\text{NCl}$ ,  $\text{Et}_4\text{NCl}$ ,  $n\text{-Pr}_4\text{NCl}$ , and  $n\text{-Bu}_4\text{NCl}$  solutions at 25°C. *J. Solut. Chem.* **17**, 1–13 (1988).
- Reichl, M., Herzog, M., Götz, A. & Braun, D. Why charged molecules move across a temperature gradient: the role of electric fields. *Phys. Rev. Lett.* **112**, 198101 (2014).
- Dhont, J. K., Wiegand, S., Duhr, S. & Braun, D. Thermodiffusion of charged colloids: single-particle diffusion. *Langmuir* **23**, 1674–1683 (2007).
- Burelbach, J., Frenkel, D., Pagonabarraga, I. & Eiser, E. A unified description of colloidal thermophoresis. *Eur. Phys. J. E* **41**, 7 (2018).
- Dirscherl, C. F. et al. A heated rock crack captures and polymerizes primordial DNA and RNA. *Phys. Chem. Chem. Phys.* **25**, 3375–3386 (2023).
- Kreysing, M., Keil, L., Lanzmich, S. & Braun, D. Heat flux across an open pore enables the continuous replication and selection of oligonucleotides towards increasing length. *Nat. Chem.* **7**, 203–208 (2015).
- Matreux, T. et al. Formation mechanism of thermally controlled pH gradients. *Commun. Phys.* **6**, 14 (2023).
- Keil, L. M. R., Möller, F. M., Kieß, M., Kudella, P. W. & Mast, C. B. Proton gradients and pH oscillations emerge from heat flow at the microscale. *Nat. Commun.* **8**, 1897 (2017).
- Matreux, T. et al. Heat flows in rock cracks naturally optimize salt compositions for ribozymes. *Nat. Chem.* **13**, 1038–1045 (2021).
- Jerabek-Willemsen, M., Wienken, C. J., Braun, D., Baaske, P. & Duhr, S. Molecular interaction studies using microscale thermophoresis. *ASSAY Drug Dev. Technol.* **9**, 342–353 (2011).
- Wiegand, S., Ning, H. & Kriegs, H. Thermal diffusion forced Rayleigh scattering setup optimized for aqueous mixtures. *J. Phys. Chem. B* **111**, 14169–14174 (2007).
- Mast, C. B., Schink, S., Gerland, U. & Braun, D. Escalation of polymerization in a thermal gradient. *Proc. Natl Acad. Sci.* **110**, 8030–8035 (2013).

## Article

46. Debye, P. Zur Theorie des Clusiusschen Trennungsvorganges. *Ann. Phys.* **428**, 284–294 (1939).
47. Ioppolo, S. et al. A non-energetic mechanism for glycine formation in the interstellar medium. *Nat. Astron.* **5**, 197–205 (2021).
48. Klussmann, M. et al. Thermodynamic control of asymmetric amplification in amino acid catalysis. *Nature* **441**, 621–623 (2006).
49. Bai, L., Baker, D. R. & Hill, R. J. Permeability of vesicular Stromboli basaltic glass: lattice Boltzmann simulations and laboratory measurements. *J. Geophys. Res. Solid Earth* **115**, B07201 (2010).

**Publisher's note** Springer Nature remains neutral with regard to jurisdictional claims in published maps and institutional affiliations.



**Open Access** This article is licensed under a Creative Commons Attribution 4.0 International License, which permits use, sharing, adaptation, distribution and reproduction in any medium or format, as long as you give appropriate credit to the original author(s) and the source, provide a link to the Creative Commons licence, and indicate if changes were made. The images or other third party material in this article are included in the article's Creative Commons licence, unless indicated otherwise in a credit line to the material. If material is not included in the article's Creative Commons licence and your intended use is not permitted by statutory regulation or exceeds the permitted use, you will need to obtain permission directly from the copyright holder. To view a copy of this licence, visit <http://creativecommons.org/licenses/by/4.0/>.

© The Author(s) 2024

## Methods

### List of substances used

For a list of abbreviations, see Supplementary Table 1. Nucleobases A and T, nucleosides Ado, Guo and Urd, nucleotides (2'-AMP, 3'-AMP, 5'-AMP, 2',3'-AMP, 3',5'-AMP, 5'-CMP, 2',3'-CMP, 5'-GMP, 3',5'-GMP and 5'-UMP), deoxyribonucleotides (dAMP, dCMP, dGMP and dTMP), 2-aminoazoles (2AO, 2AI and 2AT), oligomers of Gly (Gly, GlyGly and GlyGlyGly) and TMP were purchased from Sigma-Aldrich (USA). Nucleobase C was purchased from Carl Roth GmbH (Germany) and nucleobases U and G and nucleosides L-Cyd and D-Cyd were purchased from Biosynth Carbosynth (UK). Nucleotides 2'-CMP, 3'-CMP, 3',5'-CMP, 2',3'-GMP, 2',3'-UMP and 3',5'-UMP were purchased from Biolog (USA). For the proteogenic amino acids, an Amino Acid Mixture was used (L4461, Promega, USA) and compared with individual amino acids (Sigma-Aldrich, USA). For experiments on non-proteogenic amino acids, a mixture of amino acids and small molecules was used (A9906, Sigma-Aldrich, USA).

### Experimental procedure: preparation of heat flow cells

Bold numbers refer to the corresponding encircled numbers in Extended Data Fig. 1. The FEP foils (**5**; Holscot, the Netherlands) defining the microfluidic structure were cut by an industrial plotter device (CE6000-40 Plus, Graphtec, Germany). The cutout was then sandwiched between two sapphires (**4** and **6**; KYBURZ Switzerland, Switzerland) with thicknesses of 500  $\mu\text{m}$  (cooled sapphire) and 2,000  $\mu\text{m}$  (heated sapphire), respectively. The sapphires were previously coated with a hydrophobic coating (ProSurf MT-5, Surfactive, France) to avoid interaction with the sample and facilitate sample extraction. The cooled sapphire (**4**) has four laser-cut holes with a diameter of 1 mm. The sapphire–FEP–sapphire block was then placed on an aluminium base (**2**), covered by a heat-conducting foil (**3**; graphite, 25  $\mu\text{m}$ , 1,600 W  $\text{mK}^{-1}$ , Panasonic, Japan) and held in place by a steel frame (**7**), which is connected to the aluminium base by six torque-controlled steel screws for homogeneous force distribution.

The height of the chamber was measured with a confocal micrometer (CL-3000 series with CL-PO15, Keyence) at three positions (bottom, middle and top) to ensure a homogeneous thickness of the chamber. The average of these three measurements is later used in the numerical model to determine the Soret coefficient for each experiment. An Ohmic heating element (**9**) was mounted on the steel frame with torque-controlled screws and connected to the heated sapphire with another heat-conducting foil (**8**; EYGS0811ZLGH, graphite, 200  $\mu\text{m}$ , 400 W  $\text{mK}^{-1}$ , Panasonic).

For the microfluidic connections, we used (Techlab, Germany): connectors (UP P-702-01), end caps (UP P-755), screws (VBM 100.823-100.828), ferrules (VBM 100.632) and tubings (Teflon (FEP), KAP 100.969). As syringes, we used (ILS, Germany, bought from Göhler-HPLC Syringes, Germany) 2606814 and 2606035. Chambers were pre-flushed using low-viscosity, fluorinated oil (3M Novec 7500 Engineered Fluid, USA) to check for tightness and push out residual gas inclusions.

For the 100 mM phosphate buffer used in Extended Data Fig. 5c, we dissolved 584 mg  $\text{NaH}_2\text{PO}_4 \cdot \text{H}_2\text{O}$  and 819 mg  $\text{Na}_2\text{HPO}_4$  in 100 ml water, resulting in a solution of pH 7. Each mixture was chosen to cover a broad range of molecules while still producing separable peaks in the HPLC measurements (see Extended Data Fig. 1 and Supplementary Fig. 14).

The sample (42.5  $\mu\text{l}$ ) was loaded into the chamber with the help of a syringe filled with fluorinated oil to avoid the inclusion of air bubbles. After loading the sample, the tubings were closed with end caps.

The chamber was then mounted to a cooled aluminium block connected to a cryostat (TXF-200 R5, Grant, UK). The heaters were connected to a 400-W, 24-V power supply controlled by means of Arduino boards with a customized version of the open-source firmware Repetier, initially designed for 3D printing. The cryostat and the heaters were set to the desired temperatures. Temperatures were measured on the

sapphires with a heat imaging camera (ShotPRO, Seek Thermal, USA), giving cold and hot temperatures per experiment.

All elements were optimized using finite element simulation to provide a homogeneous temperature profile.

To stop the experiment, heaters and the cryostat were turned off and the chamber was frozen at  $-80^\circ\text{C}$  for at least 15 min. This allowed us to open the chamber and cut the frozen interior into four fractions of equal volume. Fewer fractions would lower resolution by averaging over a larger fraction of the chamber (Extended Data Figs. 1 and 2), whereas more fractions would suffer a larger positional error from manual cutting (for a comparison of 12 versus four fractions, see Extended Data Fig. 2).

For experimental network experiments, a modified cutout was used (shown in Fig. 4). Before mixing with concentrated amino acid standard, the water used for dilution was degassed by heated stirring under vacuum. The sandwich was filled with sample solution before assembly to minimize air inclusions and dilution effects from remaining water. To start the experiment, inlets and outlets were connected to tubings (250  $\mu\text{m}$  inner diameter to reduce air inclusions, KAP100.966, Techlab, Germany) filled with sample solution and connected to syringes driven by syringe pumps (Nemesys, CETONI, Germany). As soon as the temperature gradient (16 K between  $30^\circ\text{C}$  and  $46^\circ\text{C}$  and 10 K between  $32^\circ\text{C}$  and  $42^\circ\text{C}$ ) was established, the inlet was supplied with a continuous flow of  $1\text{ nl s}^{-1}$  and the outlets with  $0.5\text{ nl s}^{-1}$  each. For the recovery of fractions of the three individual chambers, a slightly modified extraction procedure was used. Because the time required to extract 12 fractions (four fractions per chamber) is increased compared with the four fractions used above, we added dry ice around the frozen block to reduce dilution by condensation. Also, we directly pipetted the recovered fraction into 7 eq. of borate buffer for pre-column derivatization.

### pH measurements

For pH measurement and adjustment, we used a Versa Star Pro device equipped with an 8220BNWP micro pH electrode (Thermo Fisher Scientific, USA). The fundamental effect of heat-flow-driven pH gradients was shown previously<sup>41</sup>. However, given the low concentrations of solutes used in this work, the obtained pH differences remained weak (delta pH between 0 and 1 units).

### LC + MS measurements

Two different LC systems were used for the various analysis methods for all molecules of interest. Also, for glycine dimerization and detection of non-proteogenic amino acids, an orbitrap MS was used. A method was created and optimized for each set of species to ensure the best separation. In the following, these will be listed for the molecules involved.

System 1: the system consists of a Vanquish Flex (VF-S01-A), a binary pump (VF-P10-A-01), a heated column compartment (VH-C10-A) and a variable-wavelength detector (VF-D40-A; all Thermo Fisher Scientific, USA). As column, we used Symmetry C18 (3.5  $\mu\text{m}$  pore size, 2.1 mm diameter, 150 mm length, 100  $\text{\AA}$  particle size, WAT106005) (Waters, USA). As eluents: eluent A: LC- $\text{H}_2\text{O}$  (0.1% v/v formic acid); eluent B: LC-acetonitrile (0.1% v/v formic acid). For all methods, we used a flow of  $0.3\text{ ml min}^{-1}$ , a column temperature of  $30^\circ\text{C}$  (still air) and detection of the UV absorption at 260 nm with 50 Hz. All methods are followed by a washing step at 40% B for 1 min and equilibration at starting concentration for 6 min.

Detailed protocols for the respective mixtures of compounds:

- Nucleobases: isocratic elution for 3 min at 0% B, then increase to 10% B over 2 min.
- Nucleosides: isocratic elution for 3 min at 0% B, then increase to 5% B over 4 min.
- Cytidine monophosphates: isocratic elution for 5 min at 0% B, then increase to 5% B over 2 min.
- Adenosine monophosphates: start with 0% B, then increase to 5% B over 12 min.

## Article

- 5'-ribonucleotides: isocratic elution for 10 min at 0% B.
- 2',3'-cyclic ribonucleotides: start with 0% B, then increase to 4.5% B over 15 min.
- 3',5'-cyclic ribonucleotides: start with 0% B, then increase to 6.8% B over 9.5 min.
- Deoxyribonucleotides: start with 0% B, then increase to 3% B over 8 min, then increase to 5% B over 4 min and 7.5% B over 1 min.
- Dimerization of glycine (variation of TMP): pre-column derivatization as described below. Isocratic elution for 10 min at 4% B.

MS-based methods: we carried out mass analysis using a Q Exactive Plus Orbitrap HR/AM (Thermo Fisher Scientific, USA), using positive ionization with a resolution of 70k, an AQC target of  $3 \times 10^6$  and a maximum IT of 200 ms. On the HESI source, a sheath gas flow rate of 2 was set, a spray voltage of 2.9 kV, 320 °C capillary temperature, 50 °C auxiliary gas heater temperature and a S-lens RF level of 50. For analysis, the main isotope mass  $\pm 0.075 m/z$  was extracted. For LC-MS methods, we used the same settings for the LC as above.

Detailed protocols for the respective mixtures of compounds:

- Dimerization of glycine (time variation and heat flow chambers): isocratic elution for 5 min at 4% B.
- Mixture of non-proteogenic amino acids, proteogenic amino acids, dipeptides and other molecules: isocratic elution for 5 min at 4% B.

System 2: the system consists of a Vanquish Core (VC-S01-A-02), a quaternary pump (VC-P20-A-01), a heated column compartment (VC-C10-A-03), a diode array detector (VC-D11-A-01) and a fluorescence detector (VC-D50-A-01; all Thermo Fisher Scientific, USA).

Separation of 2AO, 2AI and 2-aminothiazole (2AT): following a method from the literature<sup>50</sup>, we applied isocratic elution for 5 min with 90% LC-H<sub>2</sub>O, 10 mM ammonium formate and 10% LC-acetonitrile. The flow rate of 1.5 ml min<sup>-1</sup> was applied on the column InertSustain Amide (100 Å, 5 µm, 4.6 × 150 mm, GL5020-88631) (GL Sciences, Japan), with a column temperature of 40 °C and UV detection at 225 nm.

Separation of all 20 proteogenic amino acids: for the separation of amino acids, we adapted a method from the literature<sup>51</sup>. Following that protocol, we first pre-column derivatized our sample. This was done by mixing 14 µl of 50 mM borate buffer (28341, Thermo Fisher Scientific, USA) with pH adjusted to 8.8 and 2 µl of our sample. Then, 4 µl of freshly prepared 6-aminoquinolyl-N-hydroxysuccinimidyl carbamate (AQC, S041, Synchem, USA) and 4 mg ml<sup>-1</sup> in anhydrous acetonitrile (43166, Alfa Aesar, USA) were added and mixed with a pipette. The samples were then incubated for 10 min at 55 °C and stored in the autosampler at 5 °C before injection. We used the column ACCLAIM Vanquish C18 (2.2 µm, 2.1 mm × 150 mm) (Thermo Fisher Scientific, USA). Eluent A was LC-H<sub>2</sub>O (W6-212, Fisher Scientific, USA) + 50 mM ammonium formate (17843, Honeywell, USA) + 0.8% v/v formic acid (A117-50, Fisher Scientific, USA) and eluent B was LC-acetonitrile (A955-212, Fisher Scientific, USA). We set the column temperature at 45 °C (still air) and simultaneously acquired the UV absorption signal at 260 nm and the fluorescence signal (FLD) under excitation at 266 nm and emission at 473 nm (both with 50 Hz). Elution was done with a flow of 0.65 ml min<sup>-1</sup>. Best separation was achieved using the following elution protocol: isocratic elution with 0.5% B between 0 and 0.548 min, increase to 5.2% B until 3 min, to 9.2% B until 8.077 min, to 14% B until 8.626 min, maintain at 14% B until 9.5 min, increase to 19.2% B until 11.227 min, to 19.5% B until 13.696 min, to 90% B until 14.4 min and finally lower to 0.5% B and equilibrate for 6 min. For peak identification, samples of the individual amino acids were prepared according to the same protocol. Calibrations with different concentrations of amino acid standard solutions were done using the same volume as for experimental samples and for each set of measurements. After a comparison of the results of these calibrations in UV and FLD measurements, we found that the two detection methods worked equally. Because background levels in FLD are very low, we chose to proceed with the FLD channel

except for tryptophan, which does not fluoresce, and tyrosine, which is known to produce intermediary products<sup>51</sup>. For Fig. 2 and Extended Data Fig. 3, we injected each sample twice and used the average of these two injections.

### Treatment of data

Integral values of all experiments were analysed using Python. The accumulation profiles (Fig. 2a and Extended Data Figs. 2a and 8) over the chamber height were internally normalized for each species (see equation (1)) to compare enrichments despite the different initial concentrations owing to the use of different mixtures. Inherently, this makes the system compatible with mixtures with different concentrations of species. The normalized concentration  $[A]_{j,k}$  for each individual measurement was calculated for species A for fraction  $j \in \{1, 2, 3, 4\}$  and replicate number  $k \in \{1, 2, 3\}$ .

$$[A]_{j,k} = \frac{[A]_{j,k,\text{HPLC}}}{\frac{1}{4} \sum_j [A]_{j,k,\text{HPLC}}} \quad (1)$$

with the HPLC-measured concentration  $[A]_{j,k,\text{HPLC}}$  obtained from the integral values presented in Supplementary Tables 5–65. For the detection of the dimerization of glycine, we used a quadratic function of ( $\sqrt{\text{response}}$ ) to account for the nonlinear response (Supplementary Information pages 166–167). For all other species, we used an external linear calibration (Supplementary Tables 3 and 4 and examples on pages 135–165 of the Supplementary Information). The linear calibration intrinsically emphasizes that differences in calibration or absolute concentration do not change the resulting enrichments.

To compare two species inside a pool of molecules (as shown in the heat maps in Figs. 2 and 3 and Extended Data Figs. 2–5), we calculated the concentration ratio of species A compared with species B in the top ( $j = 1$ ) and respective bottom ( $j = 4$ ) fraction for each combination of species and per individual experiment. We then calculated the average of the triplicate experiments.

$$\frac{[A]_j/[B]_j}{[A]_k/[B]_k} - 1 = \frac{1}{3} \sum_k \left( \frac{[A]_{j,k}}{[B]_{j,k}} \right) - 1 \quad (2)$$

The averaging over the triplicates is done only after the calculation of the concentration ratios. This is necessary because the temperature gradients between the replicate experiments differ slightly (1–2 K). This affects the concentrations of all species present in the respective mixture of a replicate equally (Supplementary Fig. 9), so that a calculation of the concentration ratio only after averaging the species concentrations would lead to a distortion of the enrichment value actually present in the heat flow chamber. The error maps shown in the Extended Data Figures and Supplementary Figures were determined by calculating the s.d. of the enrichments  $[A]_{j,k}/[B]_{j,k}$  of all repeats from the average value described in equation (2).

Control experiments were done in parallel to check for possible degradation of individual compounds. For this purpose, one solution each was incubated at the lower or higher temperature occurring in the heat flow chamber in bulk for the duration of the accumulation experiments, but no substantial selective degradation was observed.

For the enrichment of an individual species compared with a pool of molecules (Supplementary Table 2), we normalized the individual experiments as explained previously. Then, we calculated the average concentration  $\bar{c}_{j,k}$  of the pool of all species  $k$  (per experiment) in the top ( $j = \text{top}$ ) and respective bottom ( $j = \text{bot}$ ) fraction for species  $i \in \{1, \dots, S\}$ .

$$\bar{c}_{j,k} = \frac{1}{S} \sum_i \frac{c_{i,j,k}}{\frac{1}{4} \sum_j c_{i,j,k}} \quad (3)$$

By comparing the concentration of the species with the mean concentration of the pool  $\bar{c}_j$ , we were able to determine the enrichment of

species A in fraction  $j$  (per experiment), which we averaged over the triplicate measurements (Supplementary Table 2).

$$\overline{[A]_j/\bar{c}_j} - 1 = \frac{1}{3} \sum_k ([A]_{j,k} - \bar{c}_{j,k}) - 1 \quad (4)$$

### Determination of the thermophoretic strength (Soret coefficient) of prebiotic substances in complex mixtures

A new measurement approach was necessary to determine the thermophoretic properties of the very small and highly diluted prebiotically relevant chemicals mixed together in networks of interconnected rock fractures. Previous methods require either fluorescent labelling of the measured substance, which distorts the thermophoretic properties of small molecules, or high substance concentrations, which—in our example—would strongly change the pH value and, thus, would not be representative for the prebiotic context of diluted solutions. At the same time, only one substance can be measured at a time. To overcome these difficulties, we use the same setup that mimics the geological scenario of heat flows through thin rock fractures that has also been used in previous studies<sup>40,42</sup> (Extended Data Fig. 1). The microfluidic structure is prepared as explained earlier. The combination of thermal convection and thermophoresis allows the solutes to be separated along its height of 50 mm much more effectively than would be possible by thermophoresis alone<sup>52</sup>. This spatial separation allows the entire chamber to be frozen. The content of the chamber is then cut into four equal-sized pieces (12.5 mm height each) using a scalpel. All pieces are analysed separately by HPLC (Extended Data Fig. 1), resulting in an average concentration  $[A]_j = 1/3 \sum_k [A]_{j,k}$  of species A at position  $j$ , with  $[A]_{j,k}$  as introduced in equation (1).

We assumed diffusive mobilities of  $D_{i,AA} \approx 800 \mu\text{m}^2 \text{s}^{-1}$  for amino acids<sup>53</sup> and  $D_{i,AA} \approx 1,400 \mu\text{m}^2 \text{s}^{-1}$  for the 2-aminoazoles and nucleotide components<sup>54</sup>. This approximation is reasonable because the experiment is close enough to steady state after 18 h and, hence, the fitted thermophoretic strength  $S_{T,i}$  depends only marginally on  $D_i$  (Supplementary Fig. 8).

To determine the thermophoretic strength from these datasets, we first create a 2D model of the same height (50 mm) and thickness (0.17 mm) as in the experiment using finite element methods (COMSOL 5.4). In this model, the temperatures of the sidewalls are set according to the experiment. To determine the thermal convection of the solvent, we solve the Navier–Stokes equation

$$\rho(\mathbf{u} \cdot \nabla)\mathbf{u} = \nabla \cdot \left[ -p\mathbf{I} + \mu(\nabla\mathbf{u} + (\nabla\mathbf{u})^T) - \frac{2}{3}\mu(\nabla \cdot \mathbf{u})\mathbf{I} \right] + \rho\mathbf{g} \quad (5)$$

and the continuity equation in the steady-state case

$$\nabla \cdot (\rho\mathbf{u}) = 0 \quad (6)$$

in which  $\rho$  denotes solvent density,  $\mathbf{u}$  the solvent velocity vector,  $\mathbf{I}$  the unit vector,  $p$  the pressure,  $\mu$  the dynamic viscosity and  $\mathbf{g}$  the gravitational acceleration. The results show a laminar convection flow  $\mathbf{u}$  inside the cell, which is coupled to the solute movement as it drags it with it.

This is achieved by solving the time-dependent drift–diffusion equation

$$\frac{\delta c_{i,\text{num}}}{\delta t} = \nabla \cdot [D_i \nabla c_{i,\text{num}} - (\mathbf{u} - S_{T,i} \cdot D_i \nabla T) c_{i,\text{num}}] \quad (7)$$

with the local solute concentration  $c_{i,\text{num}}$  of species  $i$  (initial concentration  $c_{i,\text{num},0} = 1$ ), its diffusive mobility  $D_i$  and Soret coefficient  $S_{T,i} \equiv \frac{D_{T,i}}{D_i}$ , which is defined using its thermophoretic mobility  $D_{T,i} = -\frac{v_{T,i}}{\nabla T}$ , including the thermophoretic drift velocity  $v_{T,i}$ .  $D_i$  is determined approximately by literature values after making sure that it does not change the determination of  $S_{T,i}$  (Supplementary Fig. 8). To obtain  $S_{T,i}$  for each

species of the mixture, we fitted the numerical results of the averaged concentrations of all four volume fractions  $V_j$ ,  $\bar{c}_{i,j,\text{num}} = \int_{V_j} c_{i,\text{num}} dV$  to the average concentrations obtained by HPLC  $\overline{[A]_j}$ ,  $i = A$ . Although external control of COMSOL is possible to include it directly in the fitting algorithm, we chose to first solve equations (5)–(7) for a wide range of parameters and then use this dataset to linearly interpolate the experimental results, yielding the respective Soret coefficient of the solute much faster and with good precision. The parameter range covered different temperature gradients ( $\Delta T$  [K]: 0, 5, 10, 20, 25), thermophoretic mobilities ( $D_T$  [ $\times 10^{-12} \text{m}^2 \text{sK}^{-1}$ ]: 1, 2.5, 5, 10, 20, 40, 60, 80) and diffusive mobilities ( $D$  [ $\times 10^{-12} \text{m}^2 \text{s}^{-1}$ ]: 1, 700, 1, 400, 1, 100, 700) for 100 equidistant time points between 0 h and 24 h, which results in 192 different concentration profiles at each time point (see model file SimpleSim\_2022\_03\_08\_new.mph, resulting in the data file 2022\_03\_08\_2DSim.dat). Using a custom-made LabVIEW program incorporating Levenberg–Marquardt algorithms (see SingleNTD\_TrapFitter\_V1-6.llb), we varied the  $D_{T,i}$  with fixed, experimentally obtained values for  $\Delta T$ ,  $D_i$  until an optimal fit between the numerical ( $\bar{c}_{i,j,\text{num}}$ ) and experimental ( $\overline{[A]_j}$ ) concentration profiles was found for each species. This procedure was repeated for all experimental repeats (triplets), after which the obtained values for  $S_{T,i}$  were averaged and a s.d. was obtained (Extended Data Table 1). Steady-state concentration profiles shown in Extended Data Fig. 2c,d and Supplementary Fig. 6 were obtained by calculating

$$c_i(y) = \exp\left(-\frac{\frac{q_i}{120} S_{T,i} \Delta T \frac{y}{\alpha}}{1 + \frac{q_i^2}{10,080}}\right), \text{ with } q \equiv \frac{\Delta T \beta g \rho \alpha^3}{6 \eta D_i} \quad (8)$$

in which  $\beta$  denotes the volume expansion coefficient of water,  $\alpha$  the distance between the hot and the cold sides of the heat flow chamber,  $\eta$  the dynamic viscosity of water and  $y$  the space coordinate along the height of the chamber.

### Modelling of a system of connected cracks/heat flow chambers

To determine the concentration profiles in a system of interconnected heat flow chambers from the previously determined Soret coefficients, we first had to calculate the behaviour of all species in a single heat flow chamber under various boundary conditions, such as temperature difference and flow rates.

For this, we created a 3D chamber in COMSOL with a height of 200 mm, a width of 60 mm and a thickness of 0.17 mm. The chamber has an inflow channel at its top end and an outflow channel at its top and bottom ends (see supplied COMSOL file SingleNTD\_v7\_simpleGeo\_Large\_allSTs\_60mmWide200mmHighTrap.mph, yielding data file SingleNTD\_v7\_simpleGeo\_Large\_60x200mmWide.dat). We then solve equations (5)–(7) in the steady-state case, calculating first the laminar flow and then the concentration distribution of the solute. Solutions are generated for all combinations of boundary conditions, that is, for different temperature differences ( $\Delta T$  [K]: 0, 1, 2, 3, 4, 5, 6, 7, 8, 9, 10, 11, 12), diffusive mobilities ( $D_i$  [ $\times 10^{-12} \text{m}^2 \text{s}^{-1}$ ]: 800, 1, 400), Soret coefficients ( $S_{T,i}$  [ $\times 10^{-3} \text{K}^{-1}$ ]: 1, 4, 8, 12) covering the range given by Extended Data Table 1, inflow volume rates ( $Q_{\text{in}}$  [ $\times 10^{-2} \text{nl s}^{-1}$ ]: 1, 5, 10, 50, 100, 500, 1, 000) and outflow rates through the bottom outflow channels as ratios of the inflow volume rate ( $Q_{\text{out,bot}}$  [%]: 1, 5, 10, 20, 50, 100). Because the random distribution of channels in the modelled network of heat flow chambers results in channels with flow rates smaller and larger than the assumed  $1 \text{nl s}^{-1}$  (Supplementary Fig. 10), we appropriately set the range of simulated flow rates  $Q_{\text{in}}$ . The outflow rate of the upper channel is determined from the mass conservation of the incompressible aqueous solution. This parametric sweep yields a dataset of 7,332 concentration profiles.

In the second step, we use this extensive dataset to extrapolate the behaviour of interconnected heat flow chambers. For this, we set up the structure of the chamber system using a self-made LabVIEW

## Article

program that fills a 3D array (see NetworkSimulation\_v3-1.llb with the settings shown in GridSimSettings.png and the program state saved in MCA31\_2023\_07\_24.dat), representing  $Z$  systems of a 2D matrix of chambers. The program assigns one inflow and a maximum of two outflow channels to each of the chambers in a random fashion. Each chamber can only connect to chambers inside the same row or one row above or below, simulating a realistic system. The inflow and outflow rates are set up according to the mass conservation of the solvent. After setting the temperature difference  $\Delta T$  and defining all species  $i$  of a mixture by setting  $D_i$  and  $S_{T,i}$ , every chamber of the system has a fully defined set of boundary conditions that can be retrieved from the previously calculated dataset. Solutions of parameter values ( $\Delta T, D_i, S_{T,i}, Q_{in}, Q_{out,bot}$ ) that are set between calculated parameters are linearly interpolated from the above dataset. The concentration profiles of each chamber  $c_{m,n,i}$  at matrix position  $m$  and  $n$  are then renormalized column by column with the total inlet concentration  $c_{in,m,n,i} = \frac{\sum_l c_{in,m,n,i,l} \times Q_{in,l}}{Q_{in}}$ , with the concentrations  $c_{in,m,n,i,l}$  and volume rates  $Q_{in,l}$  ( $Q_{in} = \sum_l Q_{in,l}$ ) of each of the  $l_{max}$  inflow channels  $l$ . The outflow concentrations  $c_{out,m,n,i}$  of each species are calculated by the finite element simulations and assigned to the inlet concentrations  $c_{in,m,n+1}$  of the next column. The renormalized averaged concentrations  $c_{bot,m,n,i}$  of the bottommost 1.5 mm volume fractions are then plotted in Fig. 4e–i. The maximum pairwise enrichments shown in Fig. 4g–i are calculated by taking the median of the ten maximum concentration ratios of two species A and B:  $\text{median} \left( \max_{\forall m,n} \left( \frac{c_{bot,m,n,i=A}}{c_{bot,m,n,i=B}} \right) \right)$ . The median is used to avoid overestimating enrichment ratios by numerical noise and outliers.

Owing to the routing of the connecting channels according to the above rules as well as the random error of the measured Soret coefficients, the numerical modelling of the heat flow chamber network also has associated errors. To quantify these, we repeated the respective simulations (that is,  $N_x$  by  $N_y$  chambers for  $Z$  systems) at least three times and calculated the mean and corresponding s.d. from the resulting enrichment values as shown in Extended Data Fig. 6. To determine the random error for the Soret coefficients shown in Extended Data Table 1, we determined the correlation of the Soret coefficients for all species present in the respective mixtures between measurement replicates (Supplementary Fig. 9). The systematic error is mainly caused by small differences in the temperature gradient between the individual replicates and equally affects the Soret coefficients of all species contained in a mixture. By fitting this correlation linearly, this systematic error can thus be determined by the deviation of the slope of the linear fit to the slope 1. Accordingly, the s.d. of the fit yields the random error (for example, because of the integral determination of the HPLC peaks, fluctuations of the column temperature during the HPLC run etc.). In the repeat runs of the network modelling for the error determination, the Soret coefficients for the species involved were, therefore, randomly chosen according to a Gaussian distribution around the average value shown in Extended Data Table 1 with a s.d. corresponding to the random error determined above. Thus, the error from the Soret coefficients could be numerically propagated and shown in the error matrices in Extended Data Fig. 6.

### Glycine-dimerization experiments

For the experiments shown in Fig. 5, we closely followed the protocol for the dimerization of glycine<sup>11</sup>.

We prepared triplicates of 200  $\mu$ l of a solution containing 10 mM and 100 mM glycine and various concentrations of TMP, ranging more than three orders of magnitude (0.10, 0.25, 0.63, 1.6, 4.0, 10, 25, 63, 158 mM). The mixture was then adjusted to pH 10.5 using NaOH and heated at 90 °C for 16 h. Using the LC protocol described above, we then analysed the yield of dimerization by comparison against standards.

The same was done for a mixture of 100 mM glycine and 100 mM TMP with measurements at different time points between 0 and 120 h.

### Modelling of reactions for network extrapolation

To model the dimerization of glycine driven by TMP in large networks of connected heat flow chambers, we first determined all required rate constants  $k_1$ – $k_5$  of the simplified reaction scheme<sup>11,12</sup>:



Here the single glycine in equation (9) is first phosphorylated (activated) by TMP. The activated glycine can then react with another glycine in equation (11) and form the GlyGly dimer. Both the activated glycine and the glycine dimer can degrade to glycine by hydrolysis (equations (10) and (13)). For TMP, a possible hydrolysis was also taken into account (equation (12)). For the determination of  $k_1$ – $k_5$ , we measured the product concentrations for a range of initial concentrations ( $[\text{Gly}]_{\text{init}} = 10 \text{ mM}, 100 \text{ mM}$  at  $[\text{TMP}]_{\text{init}} = 100 \text{ mM}, T = 90 \text{ }^\circ\text{C}$ , initial pH 10.5) at different time points (Fig. 5c and Supplementary Table 17). We determined the rate  $k_1$  separately with a solution of only  $[\text{TMP}]_{\text{init}} = 0.2 \text{ mM}$  in water under the same temperature and pH conditions to allow a better stability of the numerical fit described below for the remaining reaction constants  $k_1$ – $k_3, k_5$  and measured the decrease in TMP concentration over time (Supplementary Fig. 13 and Supplementary Table 19).

For the determination of reaction rates, either the full reaction system (equations (9)–(13)) or only the TMP hydrolysis (equation (12)) was implemented as a differential equation system in a 0D model (COMSOL 5.4, filename: MultiDFitGlyRctnModel\_20230714\_ModelV1.mph, yielding the data file 2023\_07\_14\_MultiDFit\_modelV1.dat, analysed with FreeFitter\_V4-6.llb):

$$\frac{d[\text{Gly}]}{dt} = -k_1 \times [\text{TMP}] \times [\text{Gly}] - k_3 \times [\text{GlyAct}] \times [\text{Gly}] + k_2 \times [\text{GlyAct}] + k_5 \times 2 \times [\text{GlyGly}] \quad (14)$$

$$\frac{d[\text{GlyAct}]}{dt} = -k_2 \times [\text{GlyAct}] + k_1 \times [\text{Gly}] \times [\text{TMP}] - k_3 \times [\text{GlyAct}] \times [\text{Gly}] \quad (15)$$

$$\frac{d[\text{GlyGly}]}{dt} = +k_3 \times [\text{GlyAct}] \times [\text{Gly}] - k_5 \times [\text{GlyGly}] \quad (16)$$

$$\frac{d[\text{TMP}]}{dt} = -k_1 \times [\text{Gly}] \times [\text{TMP}] - k_4 \times [\text{TMP}] \quad (17)$$

The solution of this reaction system was then solved for the initial concentrations  $[\text{Gly}]_{\text{init}} = 100 \text{ mM}$  and 10 mM and  $[\text{TMP}]_{\text{init}} = 0.0001 \text{ M}, 0.000251189 \text{ M}, 0.000630957 \text{ M}, 0.00158489 \text{ M}, 0.00398107 \text{ M}, 0.01 \text{ M}, 0.0251189 \text{ M}, 0.0630957 \text{ M}$  and 0.158489 M (corresponding to the experiment in Fig. 5c) under variation of the rate constants (Supplementary Table 18). The solution concentrations were determined for the reaction times 0–122 h. For the separate determination of  $k_4$  mentioned above, the initial concentration  $[\text{TMP}]_{\text{init}} = 0.2 \text{ mM}$  was chosen according to the experiment (Supplementary Fig. 13). With



the extensive datasets obtained in this way, we were able to simultaneously fit all of the experimental data points to a common parameter set with a custom-made LabVIEW program using a Levenberg–Marquardt algorithm (see FreeFitter\_V4-6.11b). The rates obtained in this way are:  $k_4 = 3.5 \times 10^{-7} \text{ s}^{-1}$  ( $\pm 19\%$ ) and  $k_1 = 1.0 \times 10^{-3} \text{ Ms}^{-1}$  ( $\pm 41\%$ ),  $k_2 = 1.1 \times 10^{-4} \text{ s}^{-1}$  ( $\pm 10\%$ ),  $k_3 = 9.7 \times 10^{-5} \text{ Ms}^{-1}$  ( $\pm 21\%$ ) and  $k_5 = 1.2 \times 10^{-6} \text{ s}^{-1}$  ( $\pm 20\%$ ). Although the error bars in Fig. 5c indicate the s.d. from triple replicate experiments, we have determined the error of the modelling described above by a stochastic approach. We calculated the resulting product concentrations 500 times for the fitted set of rate parameters, choosing the rates from the fit using a weighted random number generator with a Gaussian probability distribution with the s.d. according to the previously given rate error. The shaded area contains 68.27% of all these 500 runs, equivalent to one s.d. To determine the reaction yield in the network of interconnected heat flow chambers, we proceeded as described next.

Using the rate constants thus obtained, we calculated another dataset using COMSOL as the result of the equations (14)–(17), in which we varied the initial concentrations  $[\text{Gly}]_{\text{init}}$  and  $[\text{TMP}]_{\text{init}}$  over a range of  $1 \times 10^{-10} \text{ M}$  to  $1 \text{ M}$  each, with five concentrations per decade (see Grid-ReactionGlyRctnModel\_20230717\_ModelV1.mph, resulting in data file 2023\_07\_17\_ModelV1ForGridSimFig5.dat for analysis with FreeFitter\_V4-6.11b). The product concentrations were determined over a reaction time of 120 h (divided into 20 time points). We were thus able to map the TMP and Gly concentrations obtained from network modelling described above (using the Soret coefficients from Extended Data Table 1) in each individual heat flux chamber to this reaction dataset and thus determine the amount of product obtained and the reaction yield (Fig. 5d–f). The errors given in Fig. 5e,f were calculated stochastically as described above by recalculating the network model ten times, choosing the Soret coefficients with a weighted random generator with Gaussian probability distribution at one s.d. of the previously determined random error.

The network continuously provides the reactants according to the accumulation characteristics shown in Fig. 4, taking into account the high Soret coefficient of TMP  $S_{T,\text{TMP}} \approx 7 \times 10^{-3} \text{ K}^{-1}$ . As shown in Fig. 5c, right, the maximum reaction yield is already reached after 16 h, but the relaxation time of a chamber with throughflow in the range  $Q_{\text{flow}} = 1\text{--}10 \text{ nl s}^{-1}$  is expected to be on the order of  $\text{Volume}_{\text{chamber}}/Q_{\text{flow}} \approx 10^1\text{--}10^2 \text{ h}$ . Therefore, to sufficiently account for the hydrolysis included in the model, we calculate the product yield after 120 h reaction time. The reactions are each assumed to occur in a reaction volume at the bottom of the respective chamber in which the reactants are most concentrated (Supplementary Fig. 11a).

## Data availability

All data generated or analysed during this study are included in this published article (and its Supplementary Information Files). A comprehensive, ready-to-use dataset to the supplied code is included in the Supplementary Code and Data in the form of dat files as described in Methods and can be loaded directly from the LabVIEW programs. Source data are provided with this paper.

## Code availability

The full details of the finite element simulation from Figs. 4 and 5 and its analysis tools are supplied as model and LabVIEW files in the Supplementary Code and Data and described in Methods.

50. Yi, R. et al. A continuous reaction network that produces RNA precursors. *Proc. Natl Acad. Sci. USA* **117**, 13267–13274 (2020).
51. Cohen, S. A. & Michaud, D. P. Synthesis of a fluorescent derivatizing reagent, 6-aminoquinolyl-*N*-hydroxysuccinimidyl carbamate, and its application for the analysis of hydrolysate amino acids via high-performance liquid chromatography. *Anal. Biochem.* **211**, 279–287 (1993).
52. Reineck, P., Wienken, C. J. & Braun, D. Thermophoresis of single stranded DNA. *Electrophoresis* **31**, 279–286 (2010).
53. Germann, M. W., Turner, T. & Allison, S. A. Translational diffusion constants of the amino acids: measurement by NMR and their use in modeling the transport of peptides. *J. Phys. Chem. A* **111**, 1452–1455 (2007).
54. Dworkin, M. & Keller, K. H. Solubility and diffusion coefficient of adenosine 3':5'-monophosphate. *J. Biol. Chem.* **252**, 864–865 (1977).

**Acknowledgements** We thank K. Le Vay for proofreading the manuscript, J. Langlais, M. Rappold, A. Schmid and M. Weingart for experimental support and N. Yeh Martin, S. Rout, A. Kühnlein and I. Smokers for fruitful discussions. This work was financed by the Volkswagen Foundation initiative 'Life? – A Fresh Scientific Approach to the Basic Principles of Life' (T.M., D.B. and C.B.M.) and by the Deutsche Forschungsgemeinschaft (DFG, German Research Foundation) under project ID 364653263 – TRR 235 (T.M., P.A., B.S., D.B. and C.B.M.) and under Germany's Excellence Strategy – EXC-2094 – 390783311 (T.M., D.B. and C.B.M.). Funding from the Simons Foundation (327125 to D.B.) and from the European Research Council EvoTrap #787356, ERC-2017-ADG (P.A. and D.B.) is gratefully acknowledged. This work was supported by the Center for NanoScience (CeNS) in Munich.

**Author contributions** T.M., P.A. and C.B.M. conceived and designed the experiments. T.M., P.A. and C.B.M. performed the experiments. T.M., P.A. and C.B.M. analysed the data. T.M., P.A., B.S., D.B. and C.B.M. wrote the paper. All authors discussed the results and commented on the manuscript.

**Competing interests** The authors declare no competing interests.

## Additional information

**Supplementary information** The online version contains supplementary material available at <https://doi.org/10.1038/s41586-024-07193-7>

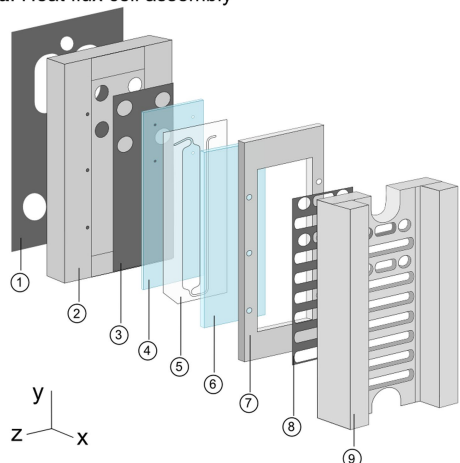
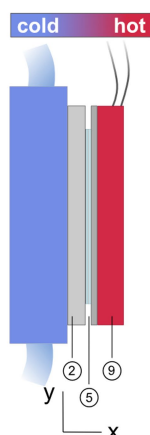
**Correspondence and requests for materials** should be addressed to Christof B. Mast.

**Peer review information** Nature thanks Sidney Becker and the other, anonymous, reviewer(s) for their contribution to the peer review of this work. Peer reviewer reports are available.

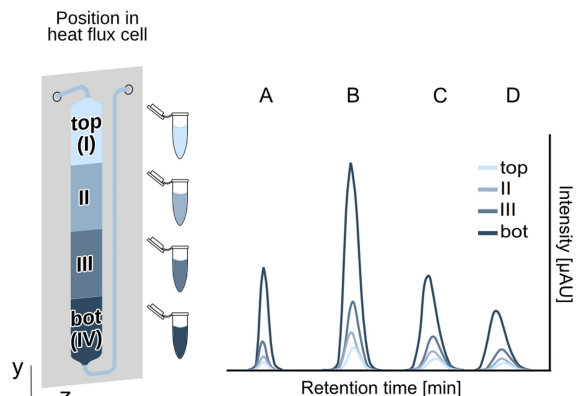
**Reprints and permissions information** is available at <http://www.nature.com/reprints>.

## Article

a: Heat flux cell assembly

b:  $\Delta T$  implementation

c: Differential analysis



**Extended Data Fig. 1 | Experiment setup and analysis.** **a**, Preparation of heat flux cells. The microfluidic structure defined by the FEP foil (5) is sandwiched between two sapphires with thicknesses of 500  $\mu\text{m}$  (4; cooled sapphire, with inlets/outlets of 1 mm diameter) and 2,000  $\mu\text{m}$  (6; heated sapphire). The sapphire–FEP–sapphire block is then placed on an aluminium base (2) covered by a heat-conducting foil on the back (1) and front (3) for optimal heat conduction to the cryostat and the sapphire, and held in place by a steel frame (7). The steel frame is connected to the aluminium base by six torque-controlled screws for a homogeneous force distribution. The height of the chamber is measured with a confocal micrometer at three positions (bottom, middle and top) to ensure a homogeneous thickness. Together with another heat-conducting foil (8), an Ohmic heating element (9) is placed on top of the heated sapphire mounted to the steel frame with torque-controlled screws. Chambers are pre-flushed using

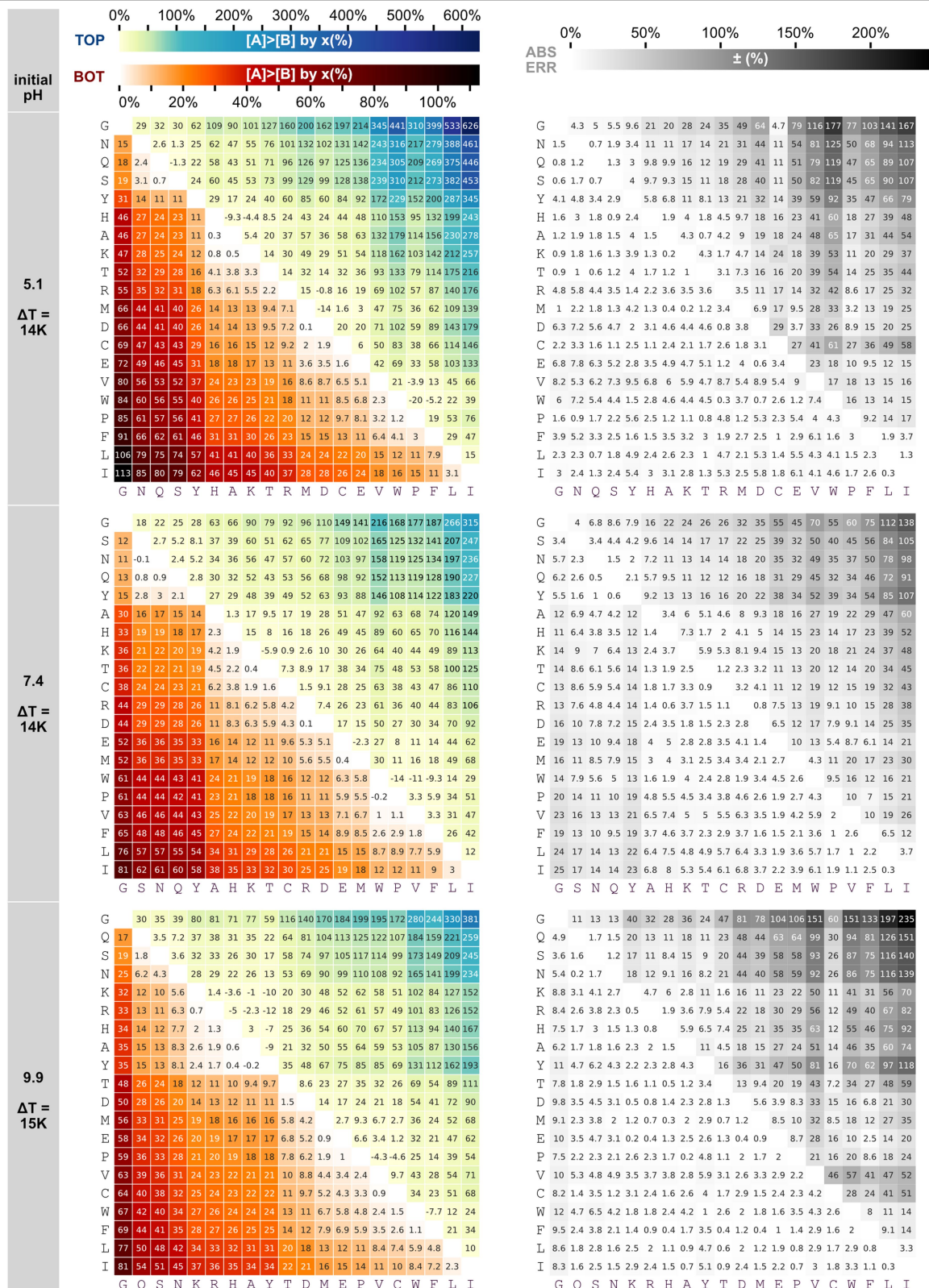
low-viscosity, fluorinated oil to check for tightness and push out residual gas inclusions. The sample is then pulled into the oil-filled chamber. After loading the sample, the tubings are closed. **b**, Application of the temperature gradient. The assembled chamber is mounted onto a cooled aluminium block connected to a cryostat. The heaters are connected to a power supply that is controlled by Arduino boards. To stop the experiment, heaters and the cryostat are turned off and the chamber is stored at  $-80\text{ }^{\circ}\text{C}$  for at least 15 min. **c**, Differential recovery of four fractions. The freezing allows us to cut the frozen interior of the heat flow cell into four fractions. Fewer fractions would lower resolution by averaging over a larger fraction of the chamber, whereas more fractions would make subsequent analysis difficult because of volume limitations and being more prone to error (Extended Data Fig. 2).



## Article

**Extended Data Fig. 2 | Enrichment of 2-aminoazoles and amino acids for different temperature gradients (errors = s.d., three repeats, same for all; see raw data tables in Supplementary Tables 5–65).** **a.** Accumulation plots for 2-aminoazoles under 5 K, 10 K and 18 K gradients. For 18 K, accumulation at the bottom is strongest (up to 2.5-fold  $c_0$ ). The strong accumulation for high thermal gradients goes together with an increased separation between species, both at the bottom, for which 2AI is most abundant, and at the top, for which the situation is reversed with up to 142% excess of 2AO versus 2AI. Corresponding errors are shown in the right column. The error maps each show the absolute enrichment error, for example, 2AI versus 2AO ( $32 \pm 3.6\%$ ), so the error range varies between  $(32 - 3.6)\% = 28.4\%$  and  $(32 + 3.6)\% = 35.6\%$ . **b.** Extraction of cysteine and isoleucine + leucine in four (25%) and 12 (8%) fractions. The 8% bottom fraction shows, as expected from theory, a higher value but has a higher error. Also, spatial errors ( $y$  axis) increase on more detailed extraction. **c.** Calculated steady state for 2-aminoazoles for  $dT = 18$  K in a closed heat flow chamber. The experimentally average zones (top 25% and bottom 25%) are

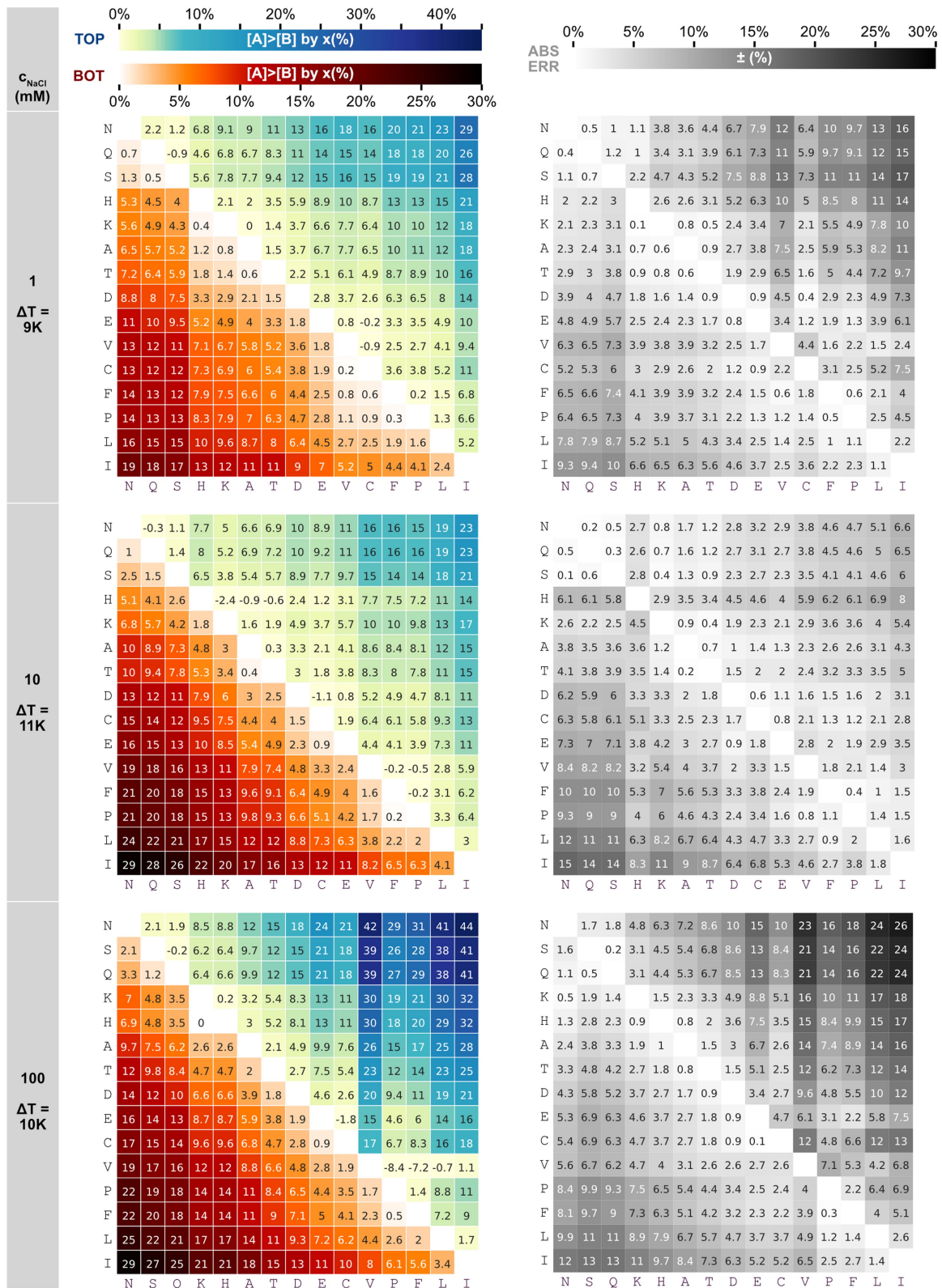
marked in grey. In the bottom fraction, the average goes over zones of different concentration ratio, including both excess and underrepresentation of species and, thus, lowering the effectively measured enrichment. This indicates that enrichments in a realistic setting can go up further. **d.** Assuming a fixed concentration at the top, we find that concentrations vary more than one order of magnitude. **e.** We use this as a measure of maximal pairwise separation between species for several temperature gradients and species (Supplementary Fig. 6), finding that, even at 5 K, separation values  $>20\%$  are possible. **f.** In a mixture of non-proteogenic and proteogenic amino acids and small organics molecules (diluted to 50  $\mu\text{M}$  and containing 0.02-fold lithium citrate, 0.01% phenol and 0.2% thiodiglycol), no clear pattern of separation is observed with non-proteogenic amino acids on both the strongly and the weakly accumulating sides. Error maps defined as in **a.** **g.** The same is the case for extraction in 8% fractions, with higher absolute values but also increased errors owing to the now higher impact of volume variations when manually cutting the frozen chamber content. Error maps defined as in **a.**



**Extended Data Fig. 3 | Enrichment between proteinogenic amino acids (30 μM each) with different initial pH values (errors = s.d., three repeats, same for all).** Analysis reveals a strong enrichment of amino acids isoleucine, leucine and phenylalanine at the bottom of the chamber for all pH values against glycine (65–113%) and serine, asparagine and glutamine (35–85%).

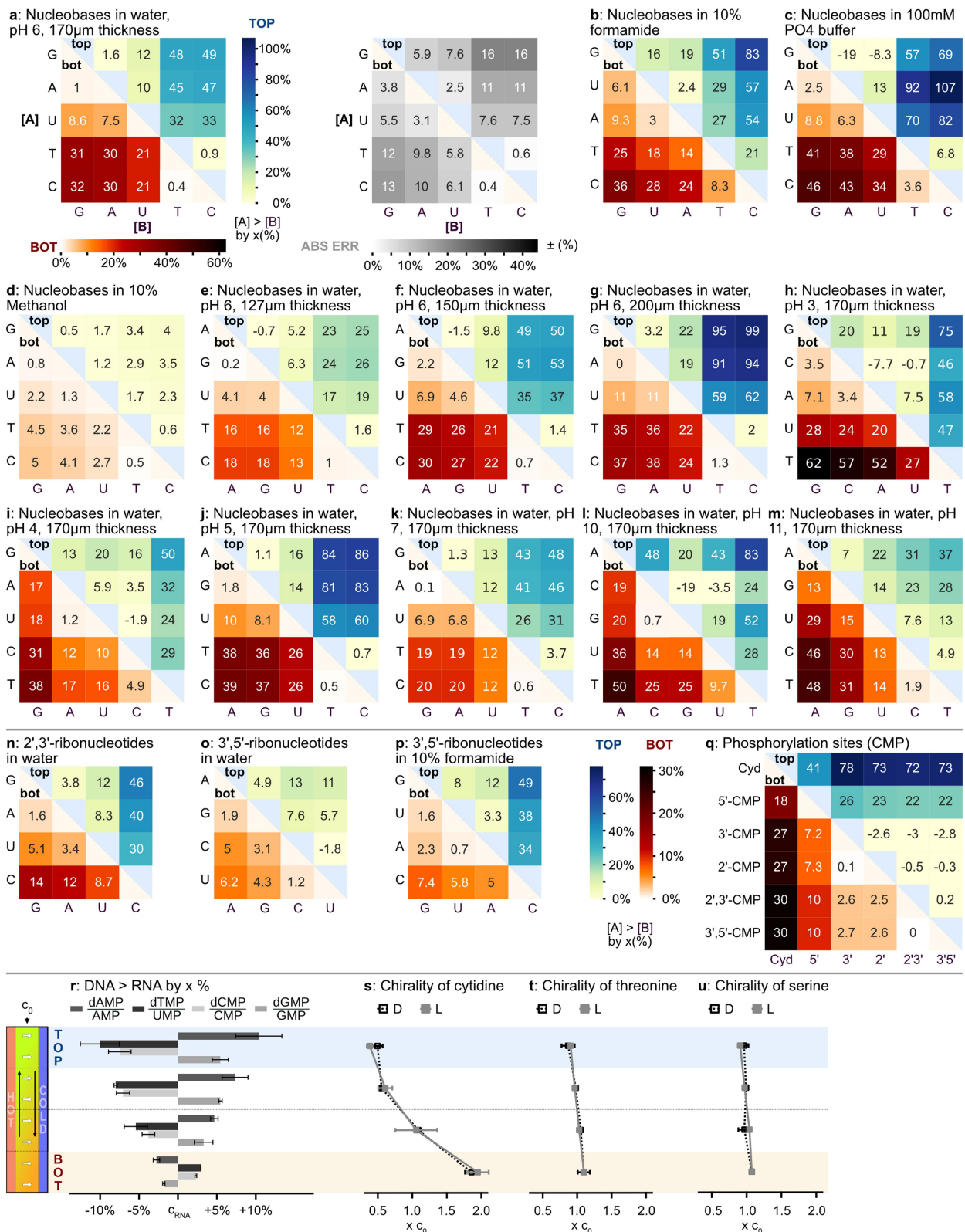
In the top fraction, the situation is inverted, with up to 300+%. The order and enrichments change with pH as thermophoresis is influenced by, for example, charged state. On the right side, the errors per value of the heat maps are shown as defined in Extended Data Fig. 2a.

Article



**Extended Data Fig. 4 | Enrichment between proteinogenic amino acids (30 μM each) with different concentrations of NaCl (errors = s.d., three repeats, same for all).** For all salt concentrations, analysis reveals a strong enrichment of amino acids isoleucine and leucine at the bottom of the chamber

against asparagine, serine and glutamine (13–29%). In the top fraction, the situation is inverted, with up to 40%. On the right side, the errors per value of the heat maps are shown as defined in Extended Data Fig. 2a.



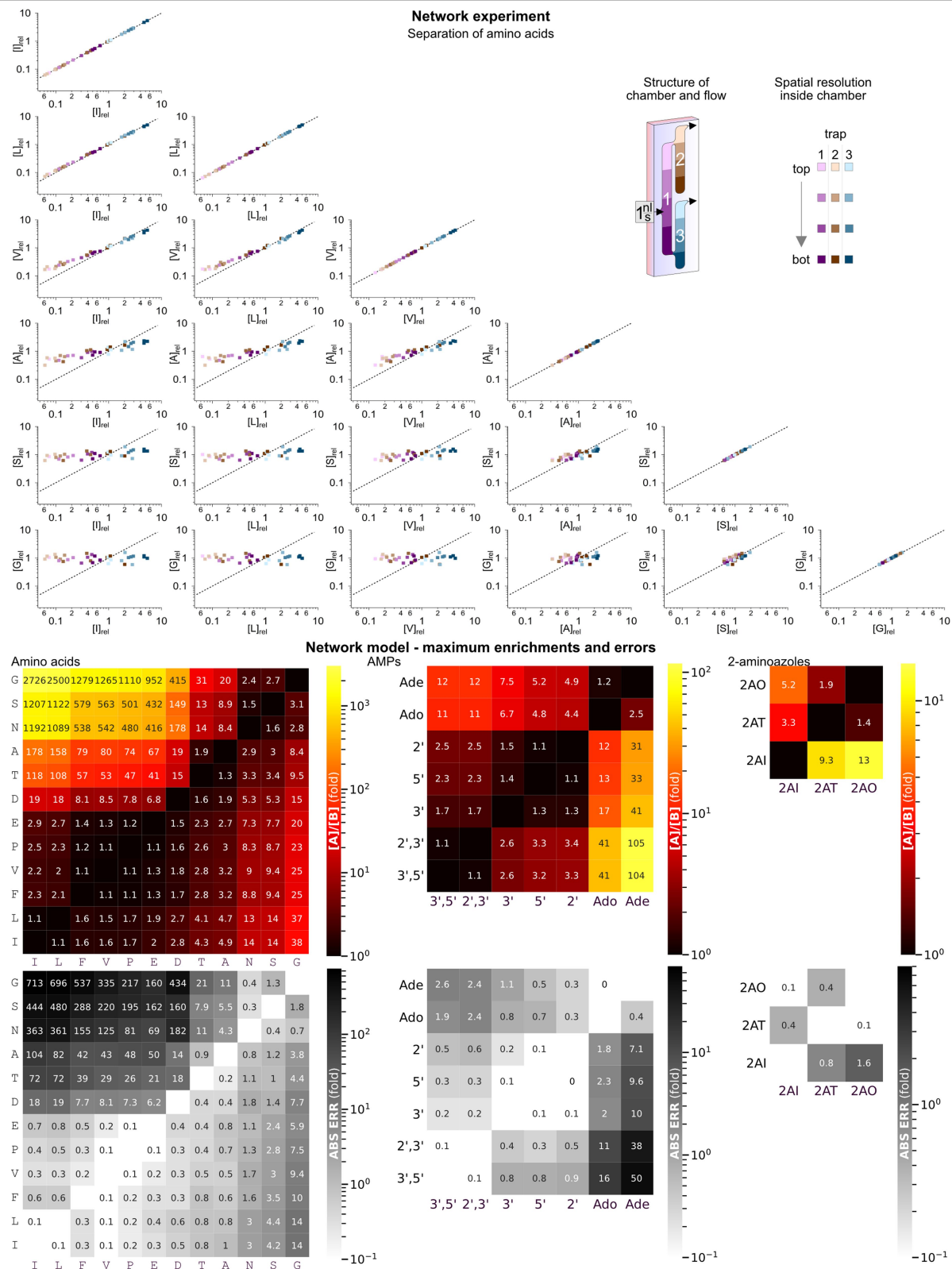
Extended Data Fig. 5 | See next page for caption.

## Article

**Extended Data Fig. 5 | Enrichment of nucleobases and nucleotides for various settings (errors = s.d., three repeats, same for all).** **a**, Plot from Fig. 3 as reference, with its corresponding error map as defined in Extended Data Fig. 2a. **b–d**, Enrichments in different solvents. Although 10% formamide and phosphate buffer do not alter accumulation and separation, for methanol, the amplitude decreases massively. **e–g**, Enrichment for different fracture thicknesses. After 18 h, accumulation is stronger for thicker cells, even though this also goes together with varied times needed to reach a steady state<sup>46</sup>. **h–m**, Enrichments for different initial pH values. The general behaviour and order of magnitude stay the same as shown in Fig. 3c. However, the most dominant species changes over pH. Error maps for **b–m** are shown in Supplementary Fig. 3. **n–p**, Enrichment of 2',3'-cyclic and 3',5'-cyclic nucleotides in water and for the latter in 10% formamide in water. For 2',3'-cyclic nucleotides, C is enriched up to 14% over the other nucleotides. For 3',5'-cyclic nucleotides, we find that

C (bottom) and G (top) are dominant in individual fractions in formamide, whereas in water, overall enrichment is weaker and dominated by A and U. **q**, Enrichment between cytidine and cytidine monophosphates (CMP, 30  $\mu$ M each). Nucleotides (5', 3', 2', 2', 3', 3', 5') are enriched against the nucleoside by at least 18%. Cyclic CMPs are enriched against linear CMPs by up to 10%. Even though having the same mass, 2'-CMP is enriched against 5'-CMP and 3'-CMP by 2.5%. Errors for **n–q** are shown in Supplementary Fig. 3. **r**, Direct comparison of DNA versus 5'-RNA nucleotides. For pyrimidine nucleotides, we observe a stronger accumulation at the bottom for DNA nucleotides (dCMP versus 5'-CMP and dTMP versus 5'-UMP). For purine nucleotides, the inverse situation is true with up to 10% DNA nucleotide excess at the top (dAMP versus 5'-AMP). **s–u**, Accumulation profiles of D-cytidine and L-cytidine, D-threonine and L-threonine and D-serine and L-serine. We do not find any substantial enrichment between the two chiralities.

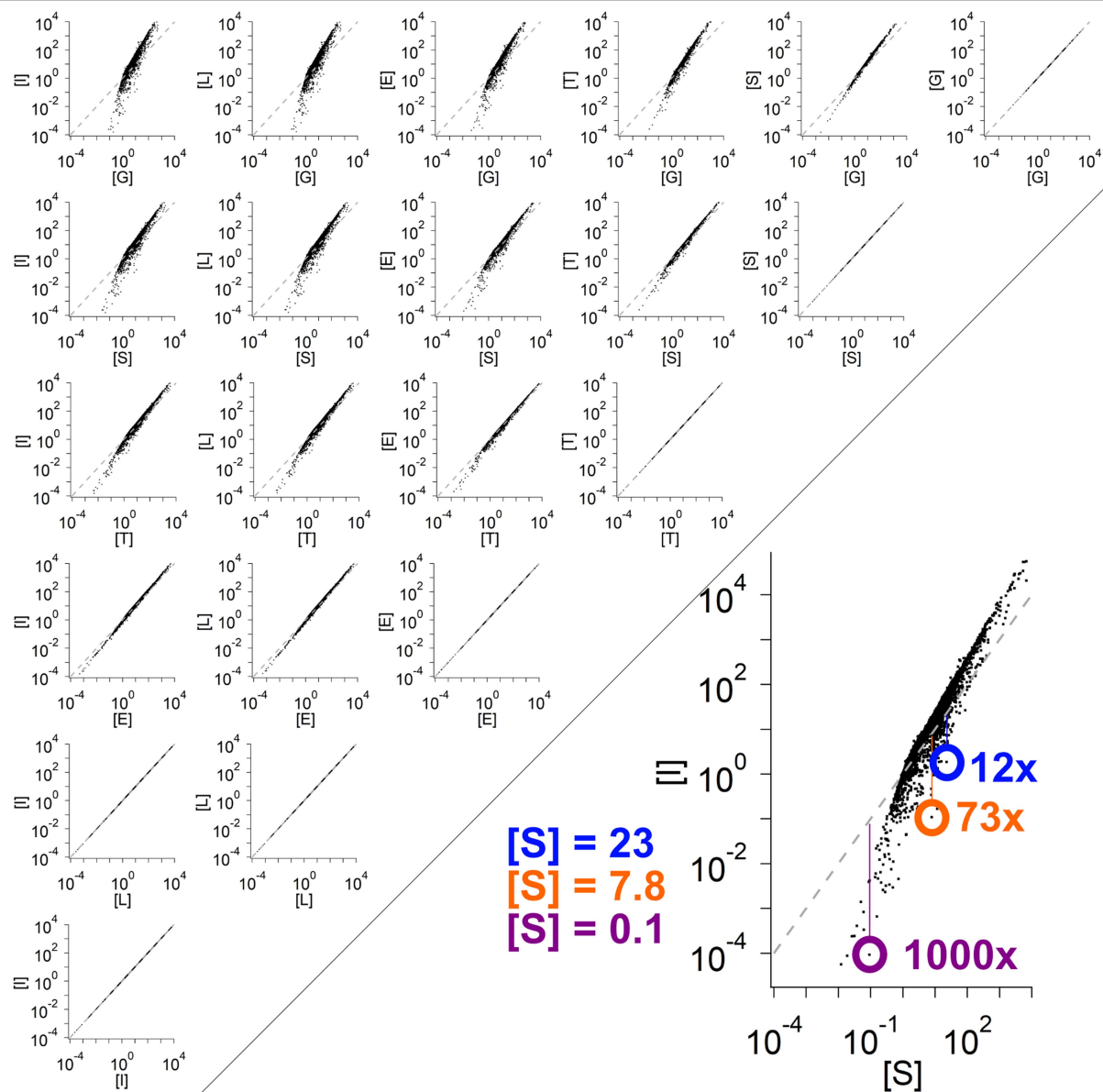




**Extended Data Fig. 6 | Experimental and modelled separation of molecules in a network of connected rock cracks.** **Top**, experimental setup of a small network of three interconnected chambers with a volume inflow of  $1 \text{ nl s}^{-1}$  of the same amino acid mixture used in Fig. 2 and  $\Delta T = 16 \text{ K}$ . After 60 h, the chamber contents from three repeats were frozen and divided into individual parts according to the colour gradations and measured by HPLC. As well as the main-text examples (I versus N and I versus F), selected pairs are shown.

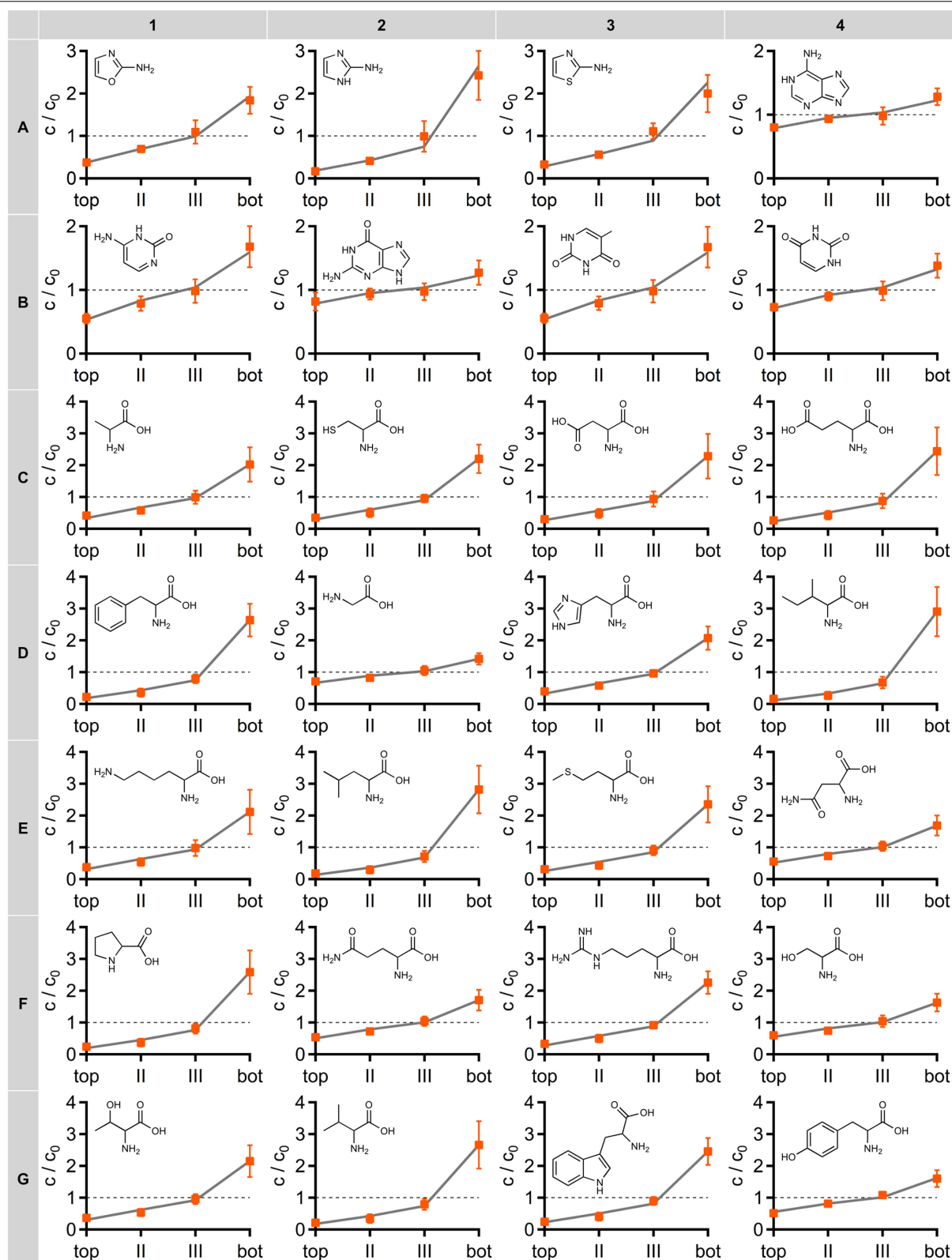
For instance, thermophoretically different amino acids glycine (G) and isoleucine (I) separate readily, whereas mass-identical L and I only show minor concentration differences in our experimental system. Further examples and a detailed overview over spatial resolution are shown in Supplementary Figs. 4 and 5. **Bottom**, maximum enrichments in the system as shown in Fig. 4d for mixtures of amino acids, adenine (nucleosides/nucleotides), and 2-aminoazoles. Error maps as defined in Extended Data Fig. 2a.

## Article



**Extended Data Fig. 7 | Pairwise enrichment of amino acids from extracts of Fig. 4g, analogous to Fig. 4e.** Each scatter plot shows the correlation of concentrations in the lower part of each heat flow chamber of 30 simulated networks of  $20 \times 20$  chambers, normalized to the inflow concentration (= 1). Amino acids with similar thermophoresis (for example, G versus S) are similarly concentrated (or depleted) and, thus, hardly enriched against each other. Amino acids with strongly different thermophoresis (see Extended Data

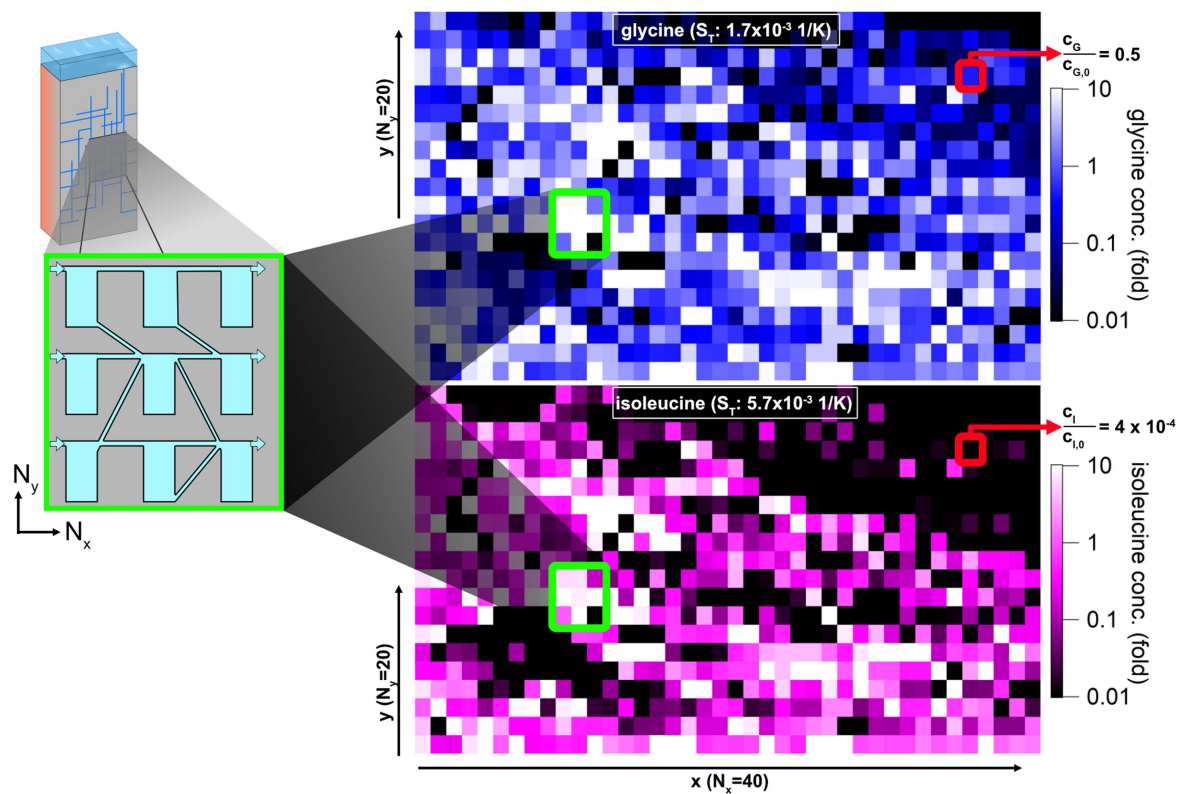
Table 1), such as I versus S, are concentrated or depleted very differently. The thermophoretically stronger species I is, thereby, more strongly depleting in the upper regions of the network than the thermophoretically weaker S, so that S occurs here, for example, with more than 1,000 times the concentration of I. The absolute concentration of S is still 0.1 times the initial concentration (purple). Even with an enrichment of 73 times S compared with I (orange), the absolute concentration of S is still at a usable 7.8 times the initial concentration.



**Extended Data Fig. 8 | Concentration profiles in heat flux cell and fit for Soret coefficients.** For aminoazoles (A1–A3), nucleobases (A4–B4) and amino acids (C1–G4), the measured concentration/initial concentration is depicted for all four fractions (errors = s.d., three repeats, same for all). Further data are shown in Supplementary Fig. 7. For fitted Soret coefficients, see Extended Data

Table 1. **A1:** 2AO; **A2:** 2AI; **A3:** 2AT; **A4:** adenine; **B1:** cytosine; **B2:** guanine; **B3:** thymine; **B4:** uracil; **C1:** alanine; **C2:** cysteine; **C3:** aspartic acid; **C4:** glutamic acid; **D1:** phenylalanine; **D2:** glycine; **D3:** histidine; **D4:** isoleucine; **E1:** lysine; **E2:** leucine; **E3:** methionine; **E4:** asparagine; **F1:** proline; **F2:** glutamine; **F3:** arginine; **F4:** serine; **G1:** threonine; **G2:** valine; **G3:** tryptophan; **G4:** tyrosine.

## Article



**Extended Data Fig. 9 | Numerical calculation of an exemplary accumulation of substances with low thermophoretic strength (for example, glycine) versus those with high thermophoretic strength (for example, isoleucine).** The 2D plots show, respectively, glycine (blue) and isoleucine (purple) bottom concentration for the same system of  $N_x = 40$  by  $N_y = 20$  randomly connected heat flow chambers (in a single system). Each pixel corresponds to one chamber. Isoleucine is more concentrated because of its high Soret coefficient, so there are many chambers with more than tenfold concentration. Owing to the resulting more efficient transport to the lower part of the system, it is only

present in low concentrations further downstream in the upper part of the system (red box, 0.0004-fold initial concentration). Glycine is less concentrated owing to the lower Soret coefficient and, thus, less transported to the lower part of the system. Downstream, it is therefore still found at higher concentrations in the upper part of the system (red box, 0.5-fold initial concentration). In summary, substances with high thermophoretic strength are purified in the front part ( $x < 20$ , upstream) of the system and substances with low thermophoretic strength in the back part ( $x \geq 20$ , downstream).

Extended Data Table 1 | Experimentally determined Soret coefficients for all species

	$S_T$ ( $10^{-3}$ 1/K)	+ - %		$S_T$ ( $10^{-3}$ 1/K)	+ - %
2AO (51 °C)	3.4	8	C (40 °C)	3.1	36
2AT	3.9	12	A	1.5	27
2AI	5.5	13	G	1.4	36
			U	1.9	30
			T	3.1	36
H (34 °C)	3.2	21	Cyd (40 °C)	2.3	51
N	2.2	17	Urd	1.9	47
S	2.2	12	Ado	1.7	46
Q	2.3	17	Guo	1.7	44
R	3.8	21	5'-CMP (40 °C)	5.3	23
G	1.7	9	5'-AMP	4.8	23
D	3.8	23	5'-UMP	5.0	23
E	4.2	26	5'-GMP	5.1	24
T	3.4	23	2',3'-CMP (40 °C)	6.5	13
A	3.1	21	2',3'-UMP	5.6	10
P	4.5	26	2',3'-AMP	5.3	17
C	3.5	23	2',3'-GMP	5.2	10
K	3.4	22	3',5'-CMP (40 °C)	5.5	21
M	4.1	23	3',5'-AMP	5.1	20
V	4.7	30	3',5'-GMP	5.3	18
I	5.7	30	3',5'-UMP	5.6	18
L	5.4	29	2'-AMP (40 °C)	3.7	21
F	4.8	26	3'-AMP	3.4	21
Y	2.1	25	2'-CMP (40 °C)	4.7	14
W	4.5	19	3'-CMP	4.6	14
			dCMP (31 °C)	5.0	12
			dAMP	4.5	14
TMP	7.5	43	dGMP	4.6	12
			dTMP	5.0	12

Temperature of the mass centre is given for each group of molecules (errors=s.d., three repeats, same for all). For the fitting routine and simulation, see Methods. The fitted experimental data are shown in Extended Data Fig. 8 and Supplementary Fig. 7.

<b>Supplementary Discussions</b> .....	5
<i>Supplementary Discussion 1: Stability of the thermogravitational accumulation against temporal fluctuations of the temperature gradient and behaviour in the limit of small temperature gradients.</i>	5
<b>Supplementary Figures</b> .....	7
<i>Supplementary Figure 1: Enrichment of nucleobases, nucleosides, 5'-nucleotides and 2',3'-cyclic nucleotides after 6 h.</i> .....	7
<i>Supplementary Figure 2: Error maps for Figure 3.</i> .....	8
<i>Supplementary Figure 3: Error maps for Extended Data Fig. 5.</i> .....	9
<i>Supplementary Figure 4: Separation of amino acids in experimental network</i> .....	10
<i>Supplementary Figure 5: Individual experiments and per-chamber depiction of network experiments</i> .....	11
<i>Supplementary Figure 6: Maximal pairwise separation for various species.</i> .....	13
<i>Supplementary Figure 7: Concentration profiles in heat flux cell and fit for Soret coefficient.</i> .....	14
<i>Supplementary Figure 8: Influence of diffusion constant on determination of Soret coefficient for different exemplary species.</i> .....	15
<i>Supplementary Figure 9: Errors in Soret coefficients for network models.</i> .....	16
<i>Supplementary Figure 10: Example distribution of flow rates for a network.</i> .....	17
<i>Supplementary Figure 11: Example of enrichment behavior in a single heat-flow chamber as used in the network simulation.</i> .....	18
<i>Supplementary Figure 12: Stability of thermogravitational accumulation against fluctuations of the applied temperature gradients.</i> .....	19
<i>Supplementary Figure 13: TMP hydrolysis under reaction conditions</i> .....	20
<i>Supplementary Figure 14: Separation of molecules in LC methods</i> .....	21
<i>Supplementary Figure 15: Reproducibility of amino acid detection in LC method described in Methods.</i> .....	22
<b>Supplementary Tables</b> .....	23
<i>Supplementary Table 1: List of abbreviations used.</i> .....	23
<i>Supplementary Table 2: Enrichment against mean concentration of set of molecules.</i> .....	25
<i>Supplementary Table 3: List of coefficients of determination, slopes and standard deviations of linear fits of LC and IC methods</i> .....	27
<i>Supplementary Table 4: List of coefficients of determination, slopes and standard deviations of linear fits of LC methods for amino acids.</i> .....	28
<i>Supplementary Table 5: Raw data Fig. 2a – 2-aminoazoles in water, 170 <math>\mu</math>m, 18 h, 18 K.</i> .....	30
<i>Supplementary Table 6: Raw data Fig. 2b and Extended Data Fig. 3 – AA in water, 170 <math>\mu</math>m, 18 h, pH 7.4.</i> .....	31
<i>Supplementary Table 7: Raw data Fig. 2b and Extended Data Fig. 3 – AA in water, 170 <math>\mu</math>m, 18 h, pH 7.4 – enrichments in top fraction</i> .....	35
<i>Supplementary Table 8: Raw data Fig. 2b and Extended Data Fig. 3 – AA in water, 170 <math>\mu</math>m, 18 h, pH 7.4 – enrichments in bottom fraction</i> .....	38

## Supplementary Discussions

*Supplementary Discussion 1: Stability of the thermogravitational accumulation against temporal fluctuations of the temperature gradient and behaviour in the limit of small temperature gradients.*

While the stability of thermogravitational accumulation to changes in chamber geometry<sup>41</sup> as well as spatial fluctuations in heat flux<sup>42</sup> has already been demonstrated, we here explore the stability of the process to temporal fluctuations in heat flux.

Using finite element simulations (Comsol 5.4), we simulate a 2-dimensional closed heat flow chamber with a height of 50 mm and a width of 0.17 mm. To show the temporal stability to heat flux fluctuations, we simulate a proxy species with a diffusion coefficient of  $D = 800 \times 10^{-12} \text{ m}^2/\text{s}$  and a Soret coefficient of  $S_T = 5.7 \times 10^{-3} \text{ 1/K}$ , which is in the range of the compounds studied in this work. The simulated differential equations correspond to those given in the method section (Determination of thermophoretic strength) but are now solved simultaneously to account for the time variance of the applied temperature difference. The cold side is kept at a constant 30 °C, while the warm side is varied as shown in Supplementary Fig. 12. The simulation is run for 14 h.

The results depicted in Supplementary Fig. 12 for constant temperature differences of  $\Delta T = 10 \text{ K}$  and  $\Delta T = 20 \text{ K}$  show, as expected, a non-linear increase of the strength of the thermogravitational accumulation with  $\Delta T$  at the point of maximum accumulation (cold, lower corner). If instead a variable temperature difference is applied, here exemplarily with a sinusoidal function of amplitude 10 K (thus varying between 0 and 20 K) and periodicity (Supplementary Fig. 12: black solid line), the average accumulation characteristic is the same as for a constant temperature difference of 12 K (Supplementary Fig. 12: orange).

The time-averaged temperature difference gives a value of 10 K. The deviation from the accumulation with a constant temperature difference of 10 K (Supplementary Fig. 12: blue) is due to the nonlinear dependence of the thermogravitational accumulation on the temperature difference. Temperature differences above 10 K therefore contribute disproportionately more to the accumulation compared to those below 10 K. Despite the very strong temporal fluctuations of the heat flux, the accumulation process under consideration shows to be extremely stable.

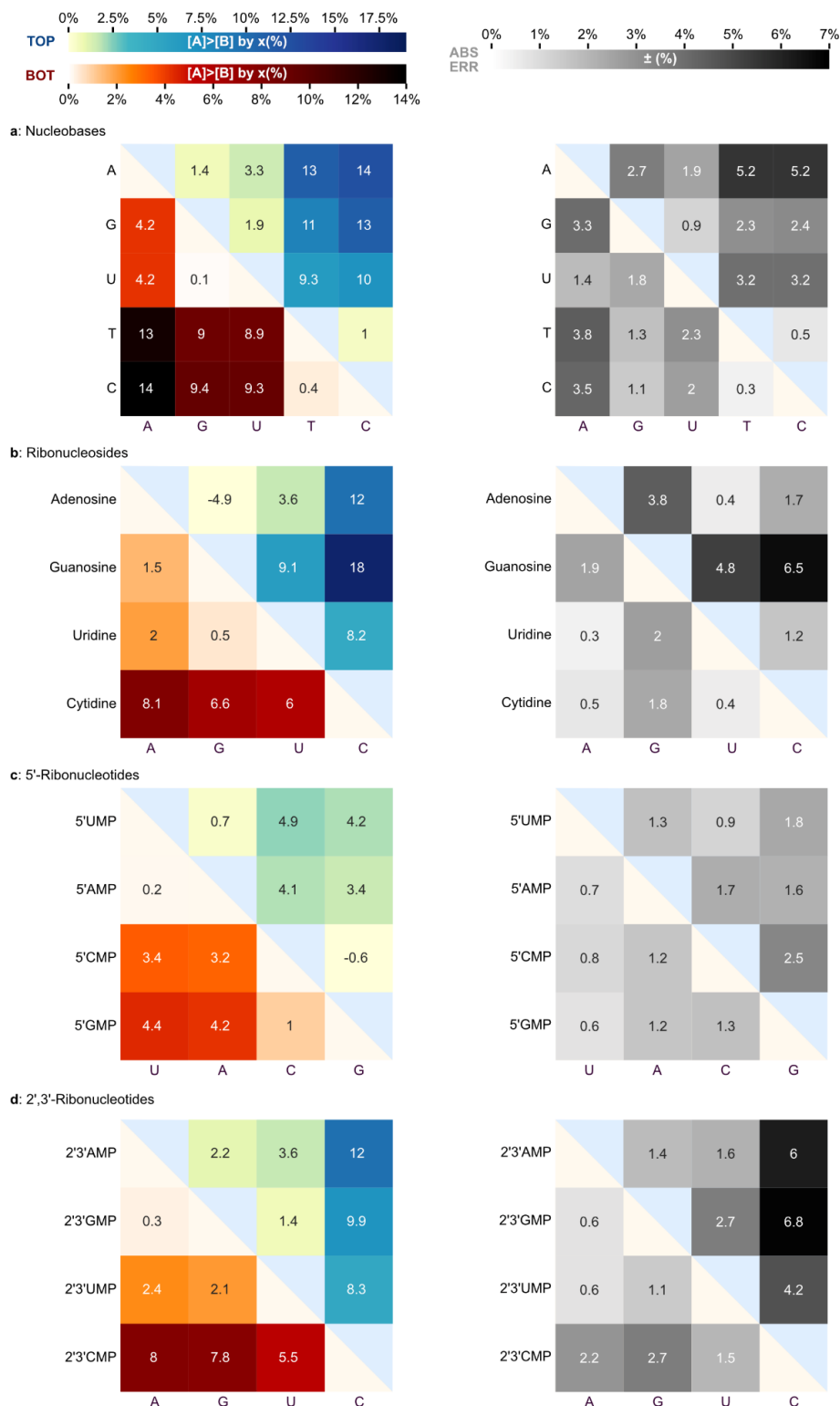
The exact determination of the temperature gradients occurring in natural systems, for example in fissures in basaltic glass, is difficult. Therefore, a discussion of the possible enrichments by heat flux driven chambers at very small temperature differences as well as the natural conditions, which also make larger temperature gradients appear realistic, is relevant. As shown in the main text in Figure 4f, even in small networks with very moderate temperature gradients of only 2 K, an enhancement of e.g. I vs N of  $(3.5 \pm 0.2)$ -fold can be achieved.

Figure 4f shows that these values can be further boosted by the size of the system, but our calculations here are limited by the measurement accuracy of the Soret coefficients involved. Due to the accumulating error of the heat flux chambers connected in series, a calculation of systems  $N > 30$  is no longer reliably possible. However, we expect here a continuation of the behavior shown in Figure 4f and thus a compensation of the smaller temperature differences discussed here.

Even larger temperature gradients are likely to be realistic within natural systems. Varying across orders of magnitude in fracture size and associated widely varying flow velocities, fast flows can serve as effective heat sources and sinks for narrower adjacent channels<sup>49,55</sup>, implementing a wide range of possible temperature differences in which the effects shown can take place. Also, it should be noted here that the temperature gradients shown here, as discussed above, need not act all the time and could also fluctuate over the local dimension (for a stability analysis over local fluctuations, see reference 42). In summary, the systems discussed here may well be considered realistic and thus may have made a relevant contribution to prebiotic chemistry.

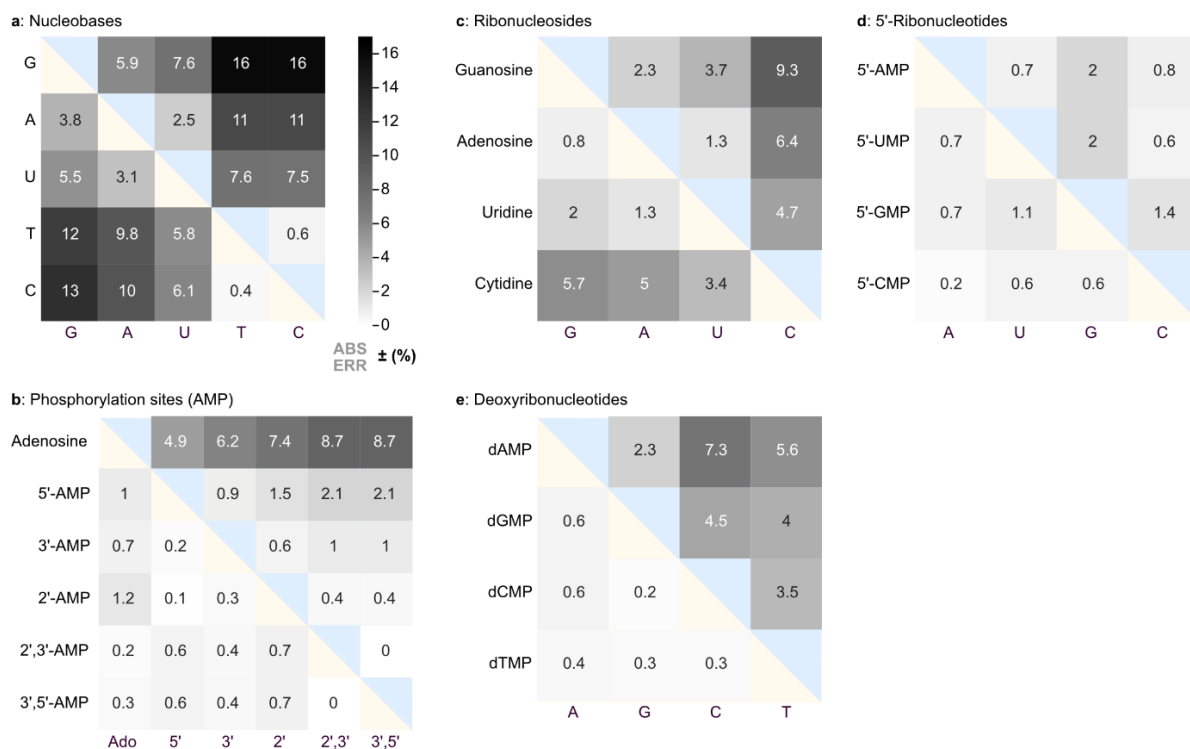


## Supplementary Figures



**Supplementary Figure 1:** Enrichment of nucleobases, nucleosides, 5'-nucleotides and 2',3'-cyclic nucleotides after 6 h.

The tendencies are the same as after 18 h (Fig. 3a/c/d, main text and Extended Data Fig. 5n) though at lowered amplitudes. Error maps show s.d. (3 repeats, for raw data see Supplementary Tables 5-65).

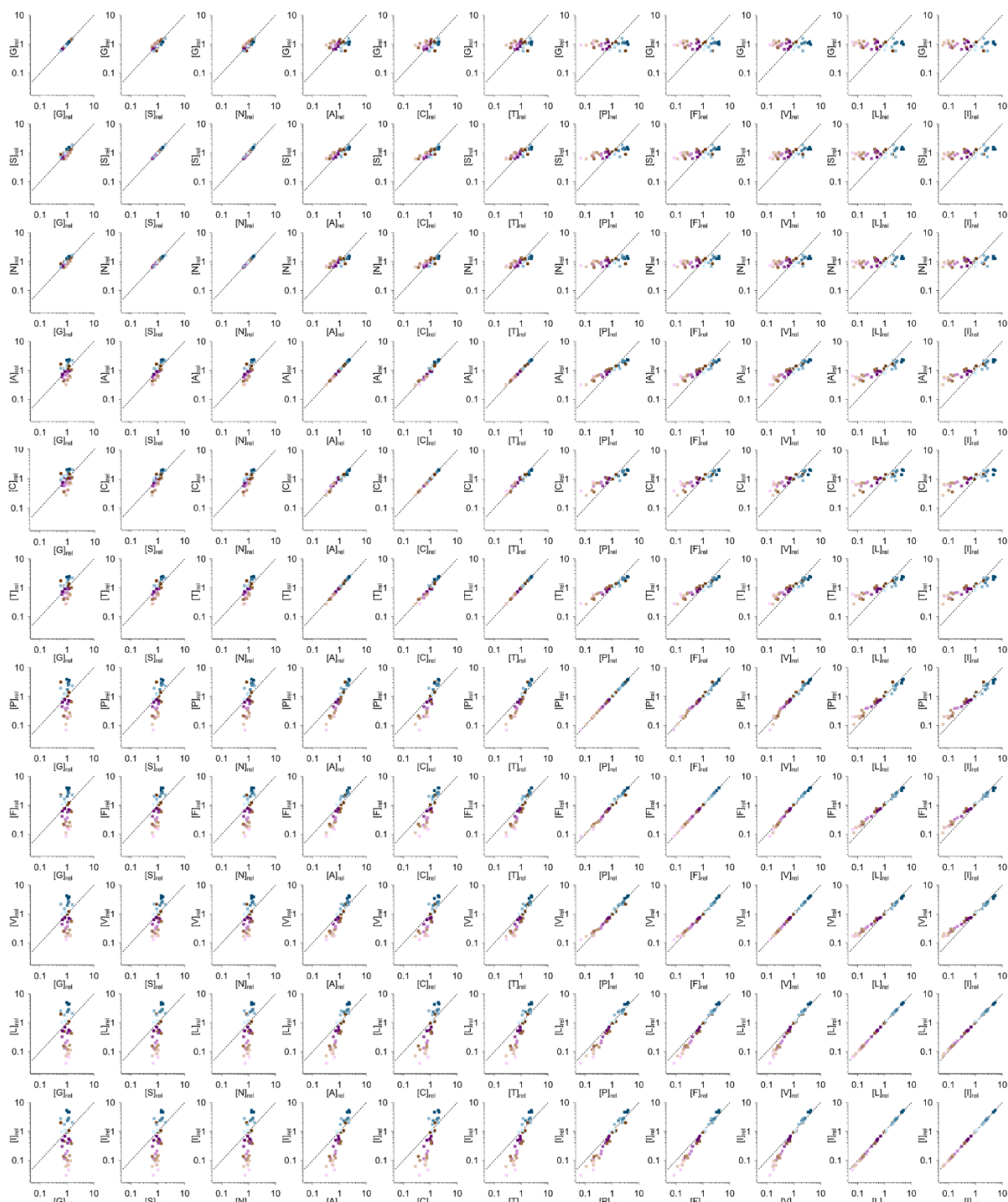


**Supplementary Figure 2: Error maps for Figure 3.**

Error maps show *s.d.* (3 repeats, for raw data see Supplementary Tables 5-65).

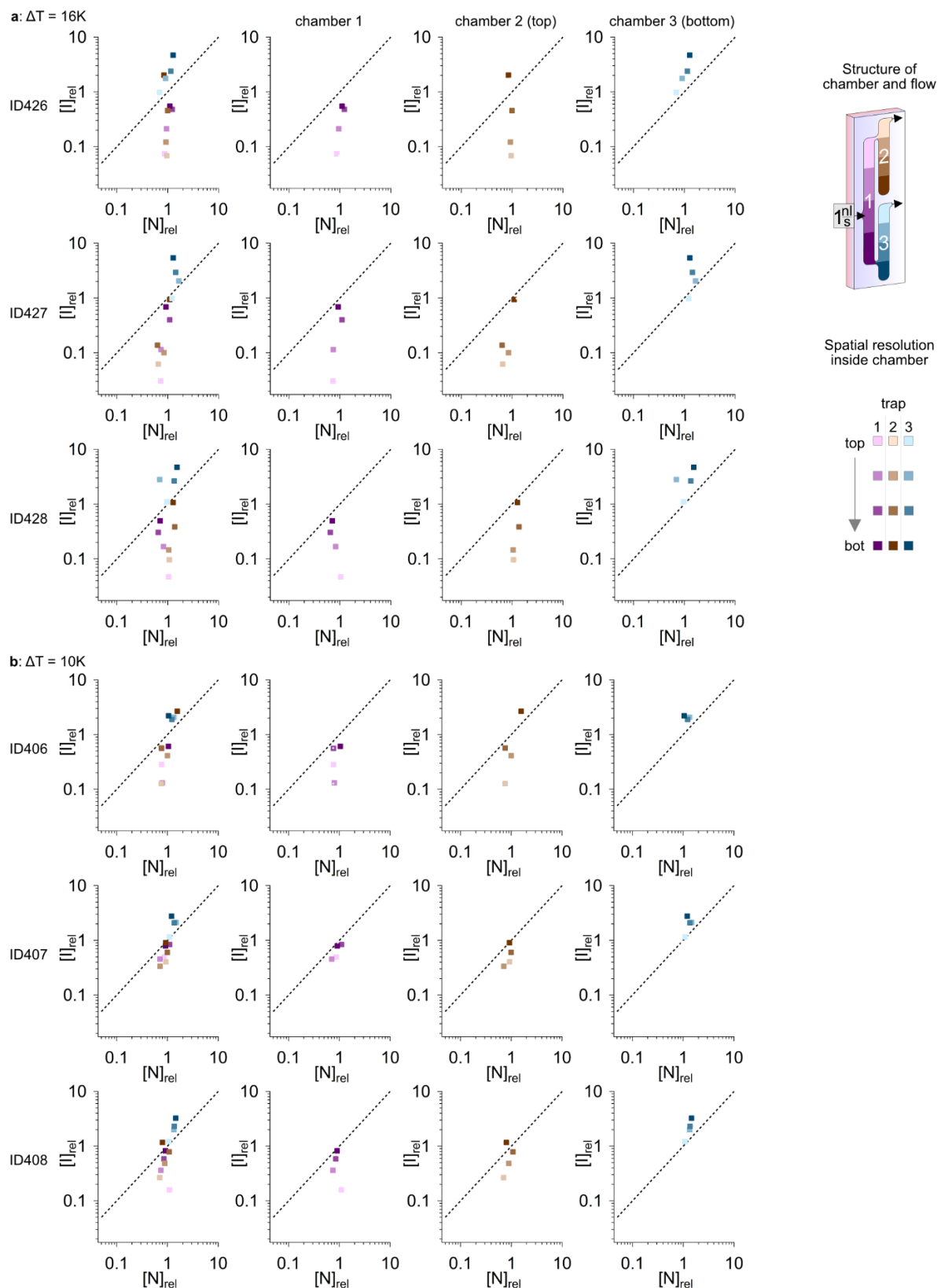


**Supplementary Figure 3: Error maps for Extended Data Fig. 5.**  
Error maps show *s.d.* (3 repeats, for raw data see Supplementary Tables 5-65).



**Supplementary Figure 4:** Separation of amino acids in experimental network

Experimental setup of a small network of three interconnected chambers with an volume-inflow of 1 nl/s of the same AA-mixture used in Figure 4 and  $\Delta T=16$  K. After 60 h, the chamber contents from 3 repeats were frozen and divided into individual parts according to the colour gradations shown in Supplementary Figure 5 and measured by HPLC. In addition to examples shown in the main text Fig. 4 and Extended Data Fig. 6, we show various combinations of pairs. For instance, thermophoretically different AAs glycine (G) and isoleucine (I) separate readily while mass-identical leucine (L) and I only show minor concentration differences in our experimental system.

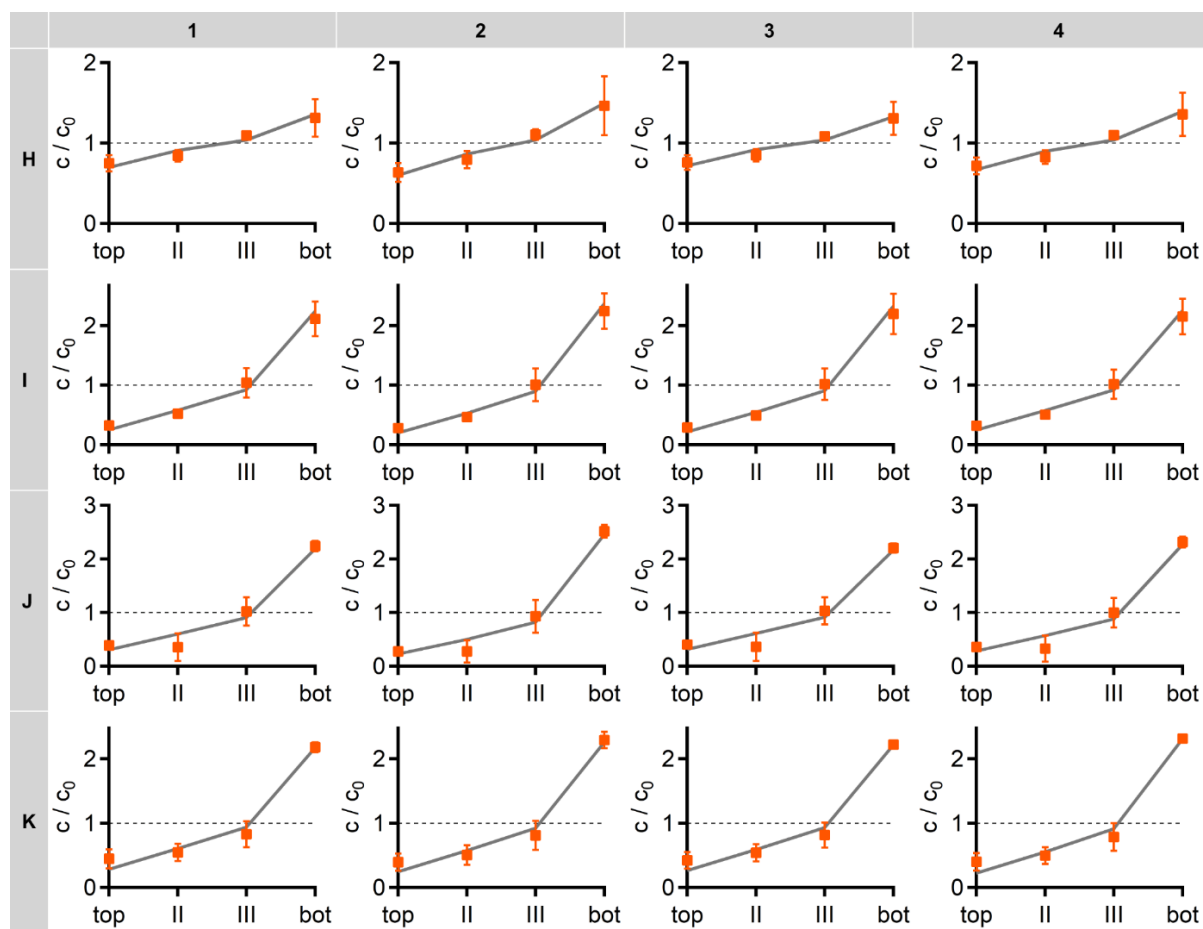


**Supplementary Figure 5:** Individual experiments and per-chamber depiction of network experiments

Experimental setup of a small network of three interconnected chambers with an volume-inflow of 1 nl/s of the same AA-mixture used in Figure 4 with a  $\Delta T$  of (a) 16K and (b) 10K. After 60 h, the chamber contents from 3 repeats at each temperature gradient were frozen and

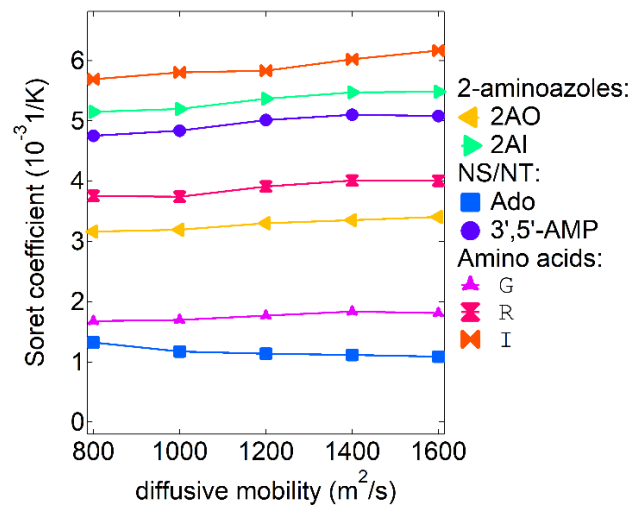
*divided into individual parts according to the colour gradations shown on the right side. For the AA pair I vs N, the concentrations per repeat and per individual chambers are shown.*





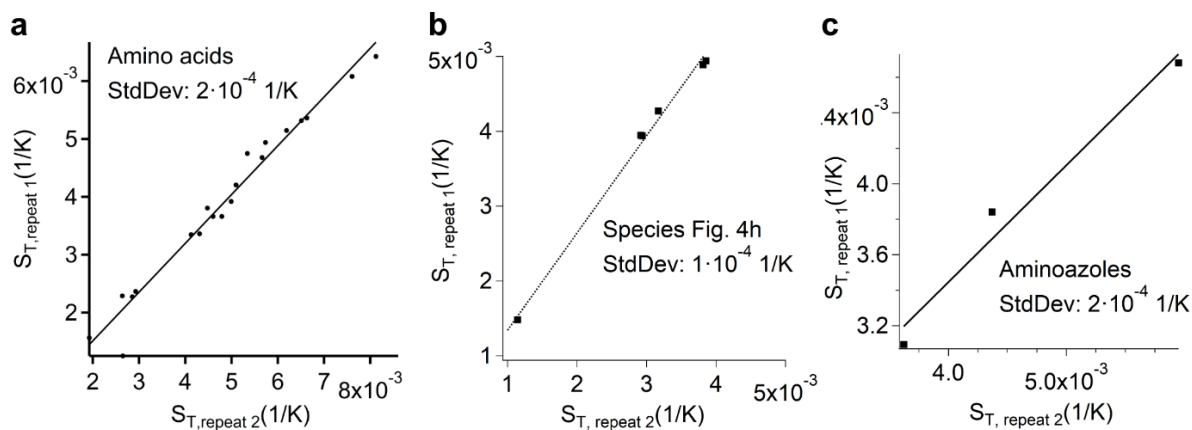
**Supplementary Figure 7:** Concentration profiles in heat flux cell and fit for Soret coefficient. In addition to data shown in Extended Data Fig. 8 (errors=s.d., 3 repeats). **H1:** Adenosine, **H2:** Cytidine, **H3:** Guanosine, **H4:** Uridine, **I1:** 5'-AMP, **I2:** 5'-CMP, **I3:** 5'-GMP, **I4:** 5'-UMP, **J1:** 2',3'-AMP, **J2:** 2',3'-CMP, **J3:** 2',3'-GMP, **J4:** 2',3'-UMP, **K1:** 3',5'-AMP, **K2:** 3',5'-CMP, **K3:** 3',5'-GMP, **K4:** 3',5'-UMP.





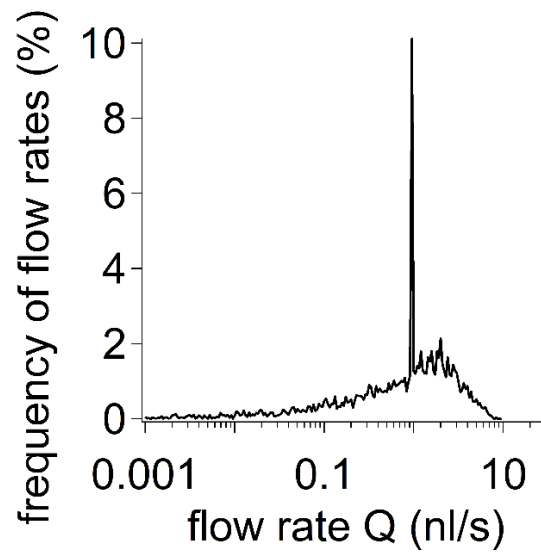
**Supplementary Figure 8:** Influence of diffusion constant on determination of Soret coefficient for different exemplary species.

For details on determination of the Soret coefficient, see Methods.



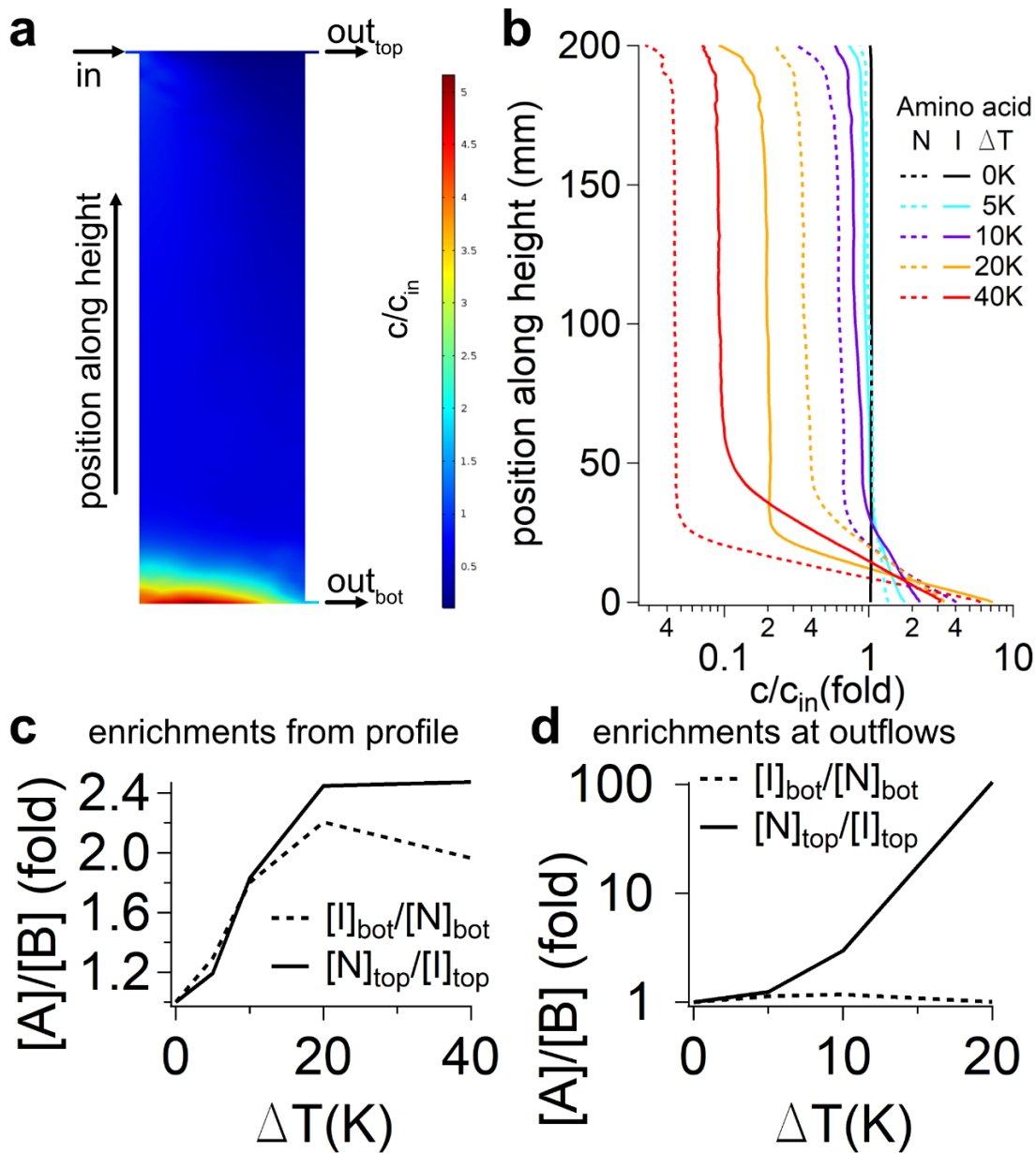
**Supplementary Figure 9:** Errors in Soret coefficients for network models.

To separate random from systematic errors, measurements of Soret coefficients for each of 2 repeats are shown in **a-c**. Systematic errors here are smaller differences in the temperature gradients between different measurements. These deviations affect the Soret coefficients of all species present in the respective mixtures equally, so they lead to a slope different from 1 in these correlation plots. The random error, e.g. by the integral determination of the peaks, then results from the standard deviation of the linear fits of these correlations (shown here as solid lines).



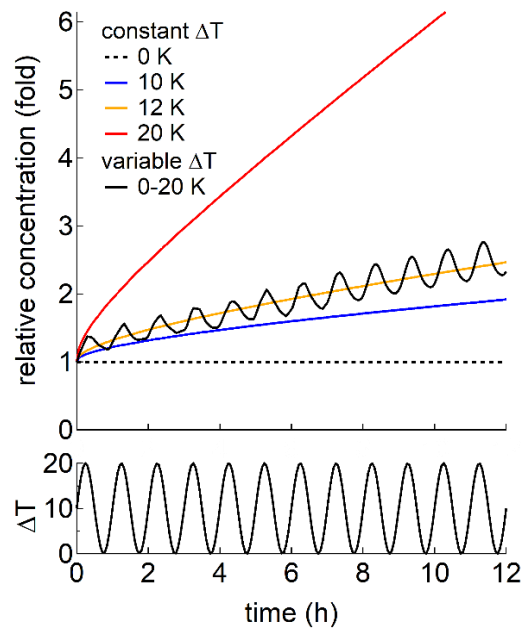
**Supplementary Figure 10:** Example distribution of flow rates for a network.

Example for system of 20 by 20 heat flux traps over 30 iterations. The input flow rate was set to 1 nl/s, which is why it is the most common. The maximum flow rates were limited to 10 nl/s, the smallest to  $1 \cdot 10^{-3}$  nl/s.



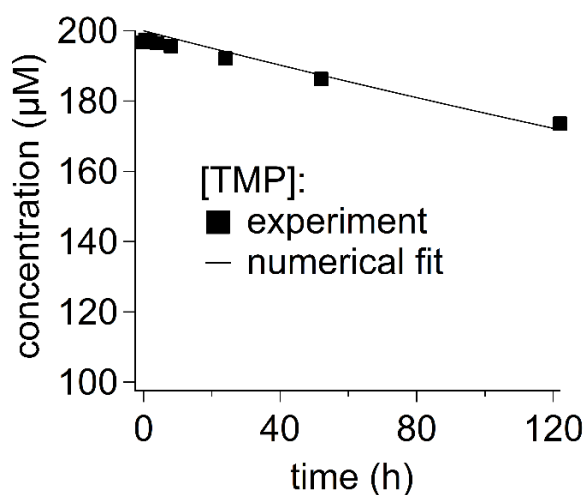
**Supplementary Figure 11:** Example of enrichment behavior in a single heat-flow chamber as used in the network simulation.

As in main text Figures 4 and 5 ( $\Delta T = 10$  K,  $v_{in} = 1 \frac{nl}{s}$ ,  $v_{out,bot} = 0.5 \frac{nl}{s}$ , height=200 mm, width=60mm, thickness=0.17mm, amino acids: I and N ). **(a)** Concentration of AA I within the complete heat flow chamber. The concentration distribution is distorted by the fluid flow toward to top and bottom outlet. **(b)** Projection of concentrations of AAs I (solid) and N (dashed) relative to the inflow concentration ( $c_{in}$ ) along the height axis of the chamber for different temperature differences  $\Delta T$ . **(c)** Increasing temperature differences lead to larger concentration ratios between AAs I and N at the top position of the chamber (at 200mm) compared to the bottom section of the chamber (at 0 mm). **(d)** Concentration ratios between the AAs I and N at the top and bottom outlet positions. The outward fluid flow toward the bottom and top change the concentration ratios to even more extreme values. This effect leads to the observed dependence on the temperature difference in a larger network and scales with the network size.



**Supplementary Figure 12:** Stability of thermogravitational accumulation against fluctuations of the applied temperature gradients.

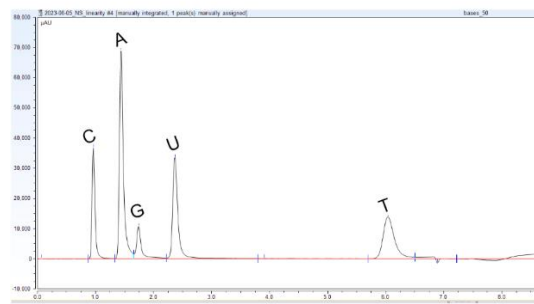
Relative concentration increase at the bottom/cold spot of the heat flow chamber is plotted versus the accumulation time. Plots that show scenarios with constant temperature difference (blue, orange, red, dashed black) show the exponential increase in accumulation efficiency. The solid black plot shows the scenario with a varying temperature difference (sine function with 10 K amplitude and 1 h periodicity).



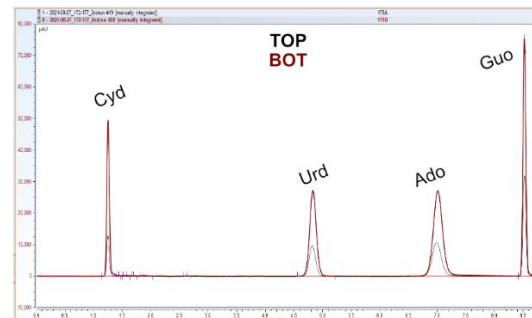
**Supplementary Figure 13:** *TMP hydrolysis under reaction conditions*

Time series at 90 °C and at an initial concentration of 200 μM and pH 10.5 (as indicated in Methods) over a period of 120 h (errors=s.d., 3 repeats). The numerical fit corresponds to the solution of Eq. 18. The reaction rate was determined to be  $k_4 = 3.5 \cdot 10^{-7}$  (1/s)(±19%).

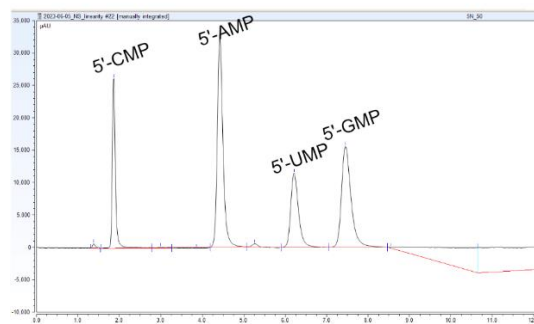
## a: Nucleobases



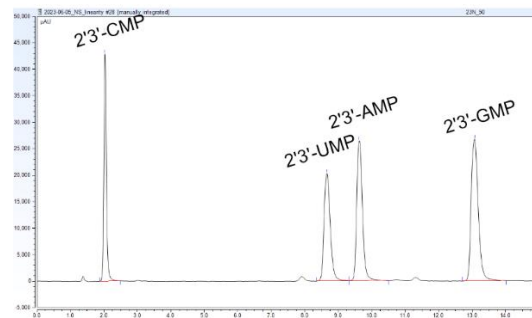
## b: Nucleosides



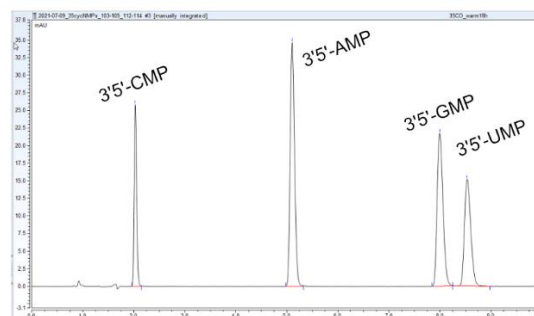
## c: 5'-Ribonucleotides



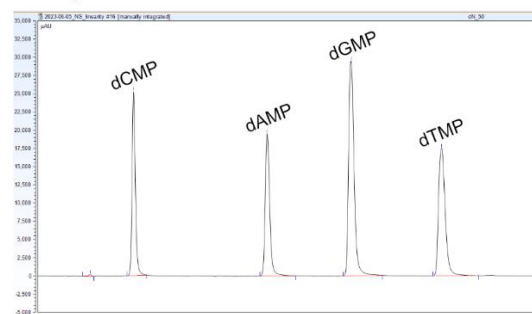
## d: 2',3',-Ribonucleotides



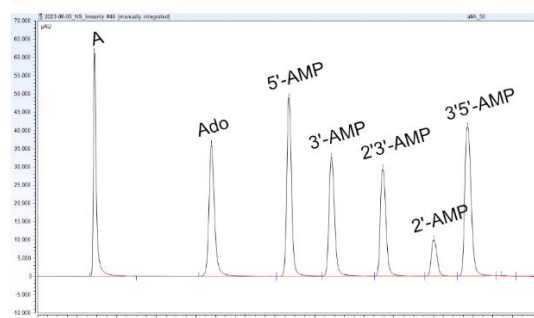
## e: 3',5',-Ribonucleotides



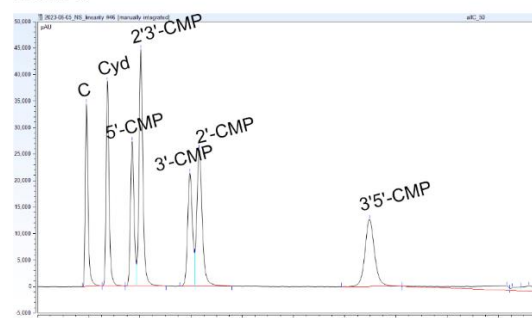
## f: Deoxyribonucleotides



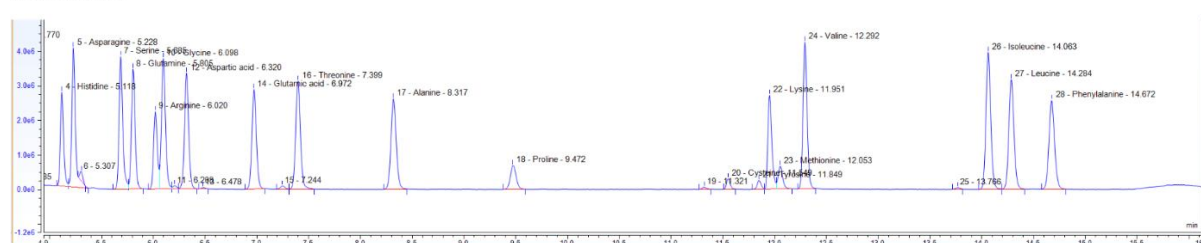
## g: AMPs



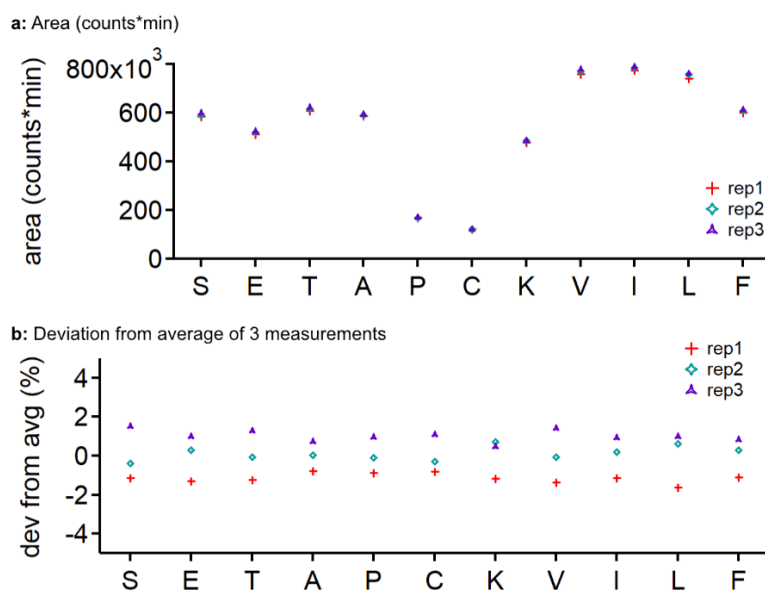
## h: CMPs



## i: Amino acids

**Supplementary Figure 14: Separation of molecules in LC methods**

In (b) we show exemplary chromatograms for the extracted top (black) and bottom (red) fractions.



**Supplementary Figure 15:** *Reproducibility of amino acid detection in LC method described in Methods.*

We separated a sample of amino acids into 3 parts and prepared each individually according to the pre-column derivatization introduced in Methods to check for potential errors. For a selection of amino acids, we show (a) the measured peak integral and (b) the deviation from the average peak integral of the 3 measurements.



## Supplementary Tables

Supplementary Table 1: List of abbreviations used.

Abbreviation	Full name
2AO	2-aminoxazole
2AI	2-aminoimidazole
2AT	2-aminothiazole
A	Adenine
C	Cytosine
G	Guanine
T	Thymine
U	Uracil
Ado	D-Adenosine
Cyd / D-Cyd	D-Cytidine (dextrorotary)
L-Cyd	L-Cytidine (levorotary)
Guo	D-Guanosine
Urd	D-Uridine
2',3'-AMP	2',3'-cyclic Adenosine monophosphate
2',3'-CMP	2',3'-cyclic Cytidine monophosphate
2',3'-GMP	2',3'-cyclic Guanosine monophosphate
2',3'-UMP	2',3'-cyclic Uridine monophosphate
2'-AMP	Adenosine 2'-monophosphate
2'-CMP	Cytidine 2'-monophosphate
3',5'-AMP	3',5'-cyclic Adenosine monophosphate
3',5'-CMP	3',5'-cyclic Cytidine monophosphate
3',5'-GMP	3',5'-cyclic Guanosine monophosphate
3',5'-UMP	3',5'-cyclic Uridine monophosphate
3'-AMP	Adenosine 3'-monophosphate
3'-CMP	Cytidine 3'-monophosphate
5'-AMP	Adenosine 5'-monophosphate
5'-CMP	Cytidine 5'-monophosphate
5'-GMP	Guanosine 5'-monophosphate
5'-UMP	Uridine 5'-monophosphate
dAMP	2'-Deoxyadenosine 5'-monophosphate
dCMP	2'-Deoxycytidine 5'-monophosphate
dGMP	2'-Deoxyguanosine 5'-monophosphate
dTMP	Thymidine 5'-monophosphate
PO <sub>4</sub>	Orthophosphate (PO <sub>4</sub> )
diPO <sub>4</sub>	Pyrophosphate (P <sub>2</sub> O <sub>7</sub> )
TMP	Trimetaphosphate (P <sub>3</sub> O <sub>9</sub> )
triPO <sub>4</sub>	Triphosphate (P <sub>3</sub> O <sub>10</sub> )
<b>Extended Data Fig. 2 and Supplementary Tables 23-28</b>	
Ans	Anserine
Arg	Arginine
Asp	Aspartic acid
Car	Carnosine
Cit	Citrulline
Cre	Creatinine

Cys	Cysteine
Cth	Cystathionine
ETA	Ethanolamine
Glu	Glutamic acid
AABA	Homoalanine
Hcy	Homocysteine
His	Histidine
Hyl	Hydroxylysine
Hyp	Hydroxyproline
Leu-Ile	Leucine + Isoleucine
Lys	Lysine
Met	Methionine
3-MH	Methylhistidine
Orn	Ornithine
Phe	Phenylalanine
Pro	Proline
Sar	Sarcosine
Ser	Serine
Tau	Taurine
Thr	Threonine
Tyr	Tyrosine
Val	Valine

**Supplementary Table 2: Enrichment against mean concentration of set of molecules.**

When not stated, conditions are: 18 h in water. Starting from a mean concentration of  $\bar{c}_0$ , at the top ( $j=top$ ), the average concentration  $\bar{c}_{top} = \frac{1}{S} \sum_i \bar{c}_{i,top}$  (see Methods, Eq. 3) of all species  $i: 1, 2, \dots, S$  decreases as the solutes are enriched by thermophoretic accumulation at the bottom. The average bottom concentration  $\bar{c}_{bot} = \frac{1}{S} \sum_i c_{i,bot}$  increases accordingly (see Methods, Eq. 3). Errors=s.d., 3 repeats.

2-aminoazoles, different temperature gradients							
Setting	fract ion $j$	$\overline{c_j/c_0}$	2AI	2AO	2AT		
5K	top	0.79	(-6.3±0.4)%	(6.9±1.2)%	(-0.5±1.6)%		
	bot	1.26	(2.8±1.2)%	(-3.1±1.5)%	(0.3±2.7)%		
10K	top	0.65	(-9.2±8.1)%	(10.9±6.2)%	(-1.7±4.1)%		
	bot	1.51	(5.5±3.8)%	(-6.8±2.5)%	(1.2±1.3)%		
18K	top	0.29	(-43±14)%	(29.5±0.9)%	(14±13)%		
	bot	2.08	(16.5±4.0)%	(-11.9±0.8)%	(-4.7±4.6)%		
Nucleobases, nucleosides, nucleotides							
Setting	fract ion $j$	$\overline{c_j/c_0}$	A	C	G	T	U
NB	top	0.69	(16.3±3.5)%	(-20.4±4.4)%	(18.1±7.2)%	(-19.7±4.6)%	(5.7±1.4)%
	bot	1.46	(-11.6±3.6)%	(14.7±4.7)%	(-12.4±5.0)%	(14.3±4.4)%	(-5.1±1.0)%
rNS	top	0.72	(5.0±0.9)%	(-11.5±3.9)%	(6.5±3.3)%		(0.1±0.4)%
	bot	1.36	(-3.3±1.4)%	(7.0±3.3)%	(-3.5±1.9)%		(-0.2±0.1)%
5'-NMP	top	0.30	(6.1±0.7)%	(-7.3±0.1)%	(-4.2±1.2)%		(5.3±0.7)%
	bot	2.18	(-2.9±0.3)%	(3.1±0.1)%	(0.8±0.6)%		(-1.0±0.5)%
dNMP	top	0.19	(11.1±3.2)%	(-7.6±3.0)%	(5.1±1.2)%	(-8.6±2.1)%	
	bot	2.73	(-3.1±0.4)%	(2.1±0.2)%	(-1.8±0.2)%	(2.8±0.1)%	
2',3'-NMP	top	0.36	(8.9±0.6)%	(-22.4±0.7)%	(13.0±0.0)%		(0.5±0.5)%
	bot	2.32	(-3.4±0.4)%	(8.5±1.0)%	(-5.0±0.7)%		(-0.1±0.1)%
3',5'-NMP	top	0.41	(6.9±1.2)%	(-5.3±0.8)%	(1.9±2.4)%		(-3.5±2.3)%
	bot	2.27	(-3.2±0.3)%	(1.7±1.8)%	(-1.4±1.1)%		(2.9±1.0)%
3',5'-NMP 10% Form.	top	0.16	(2.6±0.5)%	(-23.1±3.5)%	(14.5±2.9)%		(6.0±0.7)%
	bot	3.14	(-0.5±0.1)%	(4.5±1.0)%	(-2.7±0.6)%		(-1.2±0.3)%
Nucleobases in various pH & buffers							
Setting	fract ion $j$	$\overline{c_j/c_0}$	A	C	G	T	U
pH3	top	0.65	(8.8±0.6)%	(0.4±1.8)%	(20.6±1.4)%	(-31.0±0.3)%	(1.2±1.3)%
	bot	1.34	(-10.9±2.3)%	(-13.9±1.5)%	(-16.8±0.5)%	(34.9±0.1)%	(6.7±3.5)%
pH4	top	0.80	(3.8±0.5)%	(0.6±5.4)%	(16.9±9.7)%	(-20±12)%	(-1.8±3.8)%
	bot	1.27	(-3.3±1.1)%	(8.0±3.5)%	(-16±10)%	(13.4±8.7)%	(-2.1±1.0)%
pH5	top	0.47	(26.6±7.2)%	(-30.7±6.9)%	(25.0±4.0)%	(-30.3±6.0)%	(9.4±1.7)%
	bot	1.59	(-15.1±2.1)%	(17.9±2.3)%	(-13.6±1.7)%	(17.4±2.3)%	(-6.6±1.0)%
pH7	top	0.68	(16.3±3.7)%	(-20.3±3.4)%	(17.2±14.6)%	(-17.3±3.8)%	(4.0±3.6)%
	bot	1.29	(-8.4±3.1)%	(9.8±1.2)%	(-8.4±1.0)%	(9.1±2.0)%	(-2.2±1.1)%
pH10	top	0.48	(33.1±4.5)%	(-10.0±1.0)%	(10.7±2.9)%	(-27.1±2.5)%	(-6.7±0.4)%

pH11	bot	1.97	(-20.0±1.0)%	(-4.6±2.2)%	(-4.0±2.6)%	(19.6±0.5)%	(9.1±0.7)%
	top	0.79	(17.7±2.5)%	(-10.1±3.6)%	(10.0±2.4)%	(-14.2±2.2)%	(-3.4±0.6)%
127µm	bot	1.25	(-21.2±4.1)%	(14.7±8.7)%	(-11.3±2.4)%	(16.2±2.0)%	(1.6±2.9)%
	top	0.80	(9.3±1.8)%	(-12.5±0.7)%	(10.4±4.6)%	(-11.1±1.2)%	(3.9±1.2)%
150µm	bot	1.22	(-7.1±0.5)%	(9.2±1.2)%	(-6.9±3.4)%	(8.1±1.8)%	(-3.3±0.3)%
	top	0.65	(17.2±2.6)%	(-22.0±1.8)%	(19.0±0.4)%	(-20.9±2.8)%	(6.7±1.9)%
200µm	bot	1.49	(-11.9±2.9)%	(14.3±2.7)%	(-10.0±1.6)%	(13.5±3.6)%	(-5.9±1.8)%
	top	0.54	(27.0±9.8)%	(-32.9±8.7)%	(30.6±6.7)%	(-31.5±9.6)%	(6.8±3.9)%
10% Forma mide	bot	1.38	(-13.9±7.4)%	(17.1±8.0)%	(-14.0±4.9)%	(15.6±7.6)%	(-4.9±3.5)%
	top	0.26	(7.2±4.8)%	(-29.6±5.6)%	(27.7±2.1)%	(-15.0±4.0)%	(9.7±2.7)%
100mM PO4	bot	2.29	(-5.0±2.3)%	(17.4±6.0)%	(-13.0±4.0)%	(8.4±3.4)%	(-7.7±3.2)%
	top	0.40	(34.2±7.9)%	(-33.2±9.2)%	(9±10)%	(-29.1±6.6)%	(19.1±2.5)%
10% Methan ol	bot	1.81	(-14.3±3.7)%	(21.9±2.5)%	(-16.2±3.2)%	(17.6±0.5)%	(-9.0±1.9)%
	top	0.94	(1.4±0.7)%	(-2.0±0.7)%	(1.9±1.1)%	(-1.5±0.7)%	(0.2±0.8)%
	bot	1.10	(-1.6±1.3)%	(2.4±1.5)%	(-2.4±1.5)%	(1.9±0.8)%	(-0.3±0.8)%
	top						
Nucleobases, nucleotides after 6 hours							
<i>Setting</i>	fract ion <i>j</i>	$\overline{c_j/c_0}$	A	C	G	T	U
NB	top	0.84	(6.0±2.7)%	(-7.1±1.9)%	(4.6±0.4)%	(-6.1±1.9)%	(2.6±1.0)%
	bot	1.21	(-6.6±2.0)%	(6.3±0.9)%	(-2.8±1.1)%	(5.9±1.2)%	(-2.7±0.9)%
rNS	top	0.70	(2.3±0.7)%	(-8.7±2.0)%	(7.7±3.6)%		(-1.3±1.0)%
	bot	1.30	(-2.8±0.5)%	(5.1±0.4)%	(-1.4±1.4)%		(-0.9±0.6)%
5'- NMP	top	0.65	(1.7±0.8)%	(-2.4±1.2)%	(-1.7±1.4)%		(2.4±0.6)%
	bot	1.56	(-1.8±0.7)%	(1.4±0.7)%	(2.3±0.7)%		(-2.0±0.1)%
2',3'- NMPs	top	0.57	(4.3±1.5)%	(-6.9±3.7)%	(2.0±2.5)%		(0.6±0.4)%
	bot	1.67	(-2.6±0.6)%	(5.2±1.5)%	(-2.3±1.0)%		(-0.3±0.1)%

**Supplementary references**

References 41, 42 and 49 are also referenced in the main text.

41. Keil, L., Hartmann, M., Lanzmich, S. & Braun, D. Probing of molecular replication and accumulation in shallow heat gradients through numerical simulations. *Phys. Chem. Chem. Phys.* **18**, 20153–20159 (2016).
42. Matreux, T. *et al.* Heat flows in rock cracks naturally optimize salt compositions for ribozymes. *Nat. Chem.* **13**, 1038–1045 (2021).
49. Bai, L., Baker, D. R. & Hill, R. J. Permeability of vesicular Stromboli basaltic glass: Lattice Boltzmann simulations and laboratory measurements. *J. Geophys. Res.* **115**, B07201 (2010).
55. Viswanathan, H. S. *et al.* From Fluid Flow to Coupled Processes in Fractured Rock: Recent Advances and New Frontiers. *Reviews of Geophysics* **60**, (2022).



# Bibliography

- [1] Matreux, T., Aikkila, P., Scheu, B., Braun, D., and Mast, C. B. (April, 2024) Heat flows enrich prebiotic building blocks and enhance their reactivity. *Nature*, **628**(8006), 110–116.
- [2] Matreux, T., Schmid, A., Rappold, M., Weller, D., Caliskanoglu, A. Z., Moore, K. R., Bosak, T., Dingwell, D. B., Karaghiosoff, K., Guyot, F., Scheu, B., Braun, D., and Mast, C. B. Heat flows solubilize apatite to boost phosphate availability for prebiotic chemistry. (2024).
- [3] Matreux, T., Le Vay, K., Schmid, A., Aikkila, P., Belohlavek, L., Çalışkanoglu, A. Z., Salibi, E., Kühnlein, A., Springsklee, C., Scheu, B., Dingwell, D. B., Braun, D., Mutschler, H., and Mast, C. B. (November, 2021) Heat flows in rock cracks naturally optimize salt compositions for ribozymes. *Nature Chemistry*, **13**(11), 1038–1045.
- [4] Matreux, T., Altaner, B., Raith, J., Braun, D., Mast, C. B., and Gerland, U. (January, 2023) Formation mechanism of thermally controlled pH gradients. *Communications Physics*, **6**(1), 14.
- [5] Fry, I. (July, 2000) The emergence of life on Earth: a historical and scientific overview. *Choice Reviews Online*, **37**(11), 37–6237–37–6237.
- [6] Strecker, A. (1850) Ueber die künstliche Bildung der Milchsäure und einen neuen, dem Glycocoll homologen Körper. *Justus Liebigs Annalen der Chemie*, **75**(1), 27–45.
- [7] Strecker, A. (January, 1854) Ueber einen neuen aus Aldehyd - Ammoniak und Blausäure entstehenden Körper. *Justus Liebigs Annalen der Chemie*, **91**(3), 349–351.
- [8] Butlerov, A. (1861) Formation synthétique d'une substance sucrée. *Comptes rendus de l'Académie des Sciences*, **53**, 145–147.
- [9] Breslow, R. (January, 1959) On the mechanism of the formose reaction. *Tetrahedron Letters*, **1**(21), 22–26.
- [10] Socha, R. F., Weiss, A. H., and Sakharov, M. M. (July, 1980) Autocatalysis in the formose reaction. *Reaction Kinetics and Catalysis Letters*, **14**(2), 119–128.
- [11] Robinson, W. E., Daines, E., Van Duppen, P., De Jong, T., and Huck, W. T. S. (June, 2022) Environmental conditions drive self-organization of reaction pathways in a prebiotic reaction network. *Nature Chemistry*, **14**(6), 623–631.
- [12] Butlerov, A. (January, 1859) Ueber einige Derivate des Jodmethylens. *Justus Liebigs Annalen der Chemie*, **111**(2), 242–252.
- [13] Miller, S. L. (1953) A Production of Amino Acids Under Possible Primitive Earth Conditions. *Science*, **117**(3046), 528–529.
- [14] Miller, S. L. (August, 1957) The Formation of Organic Compounds on the Primitive Earth. *Annals of the New York Academy of Sciences*, **69**(2), 260–275.
- [15] Wachtershauser, G. (August, 1997) The origin of life and its methodological challenge. *Journal of Theoretical Biology*, **187**(4), 483–494.
- [16] Jeancolas, C., Singh, A., Jain, S., Krishna, S., and Nghe, P. (January, 2023) An interdisciplinary effort to understand chemical organizations at the origin of life. *iScience*, **26**(1), 105834.

- [17] Malaterre, C., Jeancolas, C., and Nghe, P. (July, 2022) The Origin of Life: What Is the Question?. *Astrobiology*, **22**(7), 851–862 Number: 7.
- [18] Kriebisch, C., Bantysh, O., Baranda, L., Belluati, A., Bertosin, E., Dai, K., de Roy, M., Fu, H., Galvanetto, N., Gibbs, J., et al. A roadmap towards the synthesis of Life. (2024).
- [19] Lazcano, A. (March, 2008) Towards a Definition of Life: The Impossible Quest?. *Space Science Reviews*, **135**(1-4), 5–10.
- [20] Schrödinger, E. (January, 1992) What is Life?: With Mind and Matter and Autobiographical Sketches, Cambridge University Press, 1 edition.
- [21] Dodd, M. S., Papineau, D., Grenne, T., Slack, J. F., Rittner, M., Pirajno, F., O’Neil, J., and Little, C. T. S. (March, 2017) Evidence for early life in Earth’s oldest hydrothermal vent precipitates. *Nature*, **543**(7643), 60–64.
- [22] Mojzsis, S. J., Arrhenius, G., McKeegan, K. D., Harrison, T. M., Nutman, A. P., and Friend, C. R. L. (November, 1996) Evidence for life on Earth before 3,800 million years ago. *Nature*, **384**(6604), 55–59.
- [23] Nutman, A. P., Bennett, V. C., Friend, C. R. L., Van Kranendonk, M. J., and Chivas, A. R. (September, 2016) Rapid emergence of life shown by discovery of 3,700-million-year-old microbial structures. *Nature*, **537**(7621), 535–538.
- [24] Brassler, R., Werner, S., and Mojzsis, S. (March, 2020) Impact bombardment chronology of the terrestrial planets from 4.5 Ga to 3.5 Ga. *Icarus*, **338**, 113514.
- [25] Brassler, R., Mojzsis, S., Werner, S., Matsumura, S., and Ida, S. (December, 2016) Late veneer and late accretion to the terrestrial planets. *Earth and Planetary Science Letters*, **455**, 85–93.
- [26] Genda, H., Brassler, R., and Mojzsis, S. (December, 2017) The terrestrial late veneer from core disruption of a lunar-sized impactor. *Earth and Planetary Science Letters*, **480**, 25–32.
- [27] Čuk, M. and Stewart, S. T. (November, 2012) Making the Moon from a Fast-Spinning Earth: A Giant Impact Followed by Resonant Despinning. *Science*, **338**(6110), 1047–1052.
- [28] Lock, S. J., Stewart, S. T., Petaev, M. I., Leinhardt, Z., Mace, M. T., Jacobsen, S. B., and Cuk, M. (April, 2018) The Origin of the Moon Within a Terrestrial Synestia. *Journal of Geophysical Research: Planets*, **123**(4), 910–951.
- [29] Zahnle, K., Schaefer, L., and Fegley, B. (October, 2010) Earth’s Earliest Atmospheres. *Cold Spring Harbor Perspectives in Biology*, **2**(10).
- [30] Canup, R. M. (November, 2012) Forming a Moon with an Earth-like Composition via a Giant Impact. *Science*, **338**(6110), 1052–1055.
- [31] Bottke, W. F., Vokrouhlický, D., Marchi, S., Swindle, T., Scott, E. R. D., Weirich, J. R., and Levison, H. (April, 2015) Dating the Moon-forming impact event with asteroidal meteorites. *Science*, **348**(6232), 321–323.
- [32] Kasting, J. F. and Howard, M. T. (October, 2006) Atmospheric composition and climate on the early Earth. *Philosophical Transactions of the Royal Society B-Biological Sciences*, **361**(1474), 1733–1741.
- [33] Chyba, C. F. (May, 2005) Rethinking Earth’s Early Atmosphere. *Science*, **308**(5724), 962–963.
- [34] Martin, R., Mather, T., and Pyle, D. (August, 2007) Volcanic emissions and the early Earth atmosphere. *Geochimica et Cosmochimica Acta*, **71**(15), 3673–3685.
- [35] Parker, E. T., Cleaves, H. J., Callahan, M. P., Dworkin, J. P., Glavin, D. P., Lazcano, A., and Bada, J. L. (June, 2011) Prebiotic Synthesis of Methionine and Other Sulfur-Containing Organic Compounds on the Primitive Earth: A Contemporary Reassessment Based on an Unpublished 1958 Stanley Miller Experiment. *Origins of Life and Evolution of Biospheres*, **41**(3), 201–212.



- [36] Lazcano, A. and Bada, J. L. (June, 2003) The 1953 Stanley L. Miller experiment: Fifty years of prebiotic organic chemistry. *Origins of Life and Evolution of Biospheres*, **33**(3), 235–242.
- [37] Habicht, K. S., Gade, M., Thamdrup, B., Berg, P., and Canfield, D. E. (December, 2002) Calibration of Sulfate Levels in the Archean Ocean. *Science*, **298**(5602), 2372–2374.
- [38] Fleury, B., Carrasco, N., Millan, M., Vettier, L., and Szopa, C. (December, 2017) Organic chemistry in a CO<sub>2</sub> rich early Earth atmosphere. *Earth and Planetary Science Letters*, **479**, 34–42.
- [39] Kasting, J. F. (1993) Earth’s Early Atmosphere. *Science*, **259**(5097), 920–926.
- [40] Wiechert, U. H. (December, 2002) Earth’s Early Atmosphere. *Science*, **298**(5602), 2341–2342.
- [41] Tian, F., Toon, O. B., Pavlov, A. A., and De Sterck, H. (May, 2005) A hydrogen-rich early Earth atmosphere. *Science*, **308**(5724), 1014–1017.
- [42] McCollom, T. M. and Donaldson, C. (January, 2019) Experimental Constraints on Abiotic Formation of Tubules and Other Proposed Biological Structures in Subsurface Volcanic Glass. *Astrobiology*, **19**(1), 53–63.
- [43] De Ronde, C. E., Channer, D. M., Faure, K., Bray, C. J., and Spooner, E. T. (October, 1997) Fluid chemistry of Archean seafloor hydrothermal vents: Implications for the composition of circa 3.2 Ga seawater. *Geochimica et Cosmochimica Acta*, **61**(19), 4025–4042.
- [44] Wright, J. and Colling, A. (1995) Salinity in the Oceans. In *Seawater: its Composition, Properties and Behaviour* pp. 29–38 Elsevier.
- [45] Farquhar, J., Wing, B. A., McKeegan, K. D., Harris, J. W., Cartigny, P., and Thiemens, M. H. (December, 2002) Mass-Independent Sulfur of Inclusions in Diamond and Sulfur Recycling on Early Earth. *Science*, **298**(5602), 2369–2372.
- [46] Planavsky, N. J., Rouxel, O. J., Bekker, A., Lalonde, S. V., Konhauser, K. O., Reinhard, C. T., and Lyons, T. W. (October, 2010) The evolution of the marine phosphate reservoir. *Nature*, **467**(7319), 1088–1090.
- [47] Konhauser, K. O., Lalonde, S. V., Amskold, L., and Holland, H. D. (March, 2007) Was There Really an Archean Phosphate Crisis?. *Science*, **315**(5816), 1234–1234.
- [48] Monnard, P.-A., Apel, C. L., Kanavarioti, A., and Deamer, D. W. (June, 2002) Influence of Ionic Inorganic Solutes on Self-Assembly and Polymerization Processes Related to Early Forms of Life: Implications for a Prebiotic Aqueous Medium. *Astrobiology*, **2**(2), 139–152.
- [49] Chatterjee, A., Zhang, K., Rao, Y., Sharma, N., Giammar, D. E., and Parker, K. M. (March, 2022) Metal-Catalyzed Hydrolysis of RNA in Aqueous Environments. *Environmental Science & Technology*, **56**(6), 3564–3574.
- [50] Kawamura, K. (1999) Measurement of the rate of RNA hydrolysis in aqueous solution at elevated temperatures using a new monitoring method for hydrothermal reactions. *Nucleic Acids Symposium Series*, **42**(1), 289–290.
- [51] Lepper, C. P., Williams, M. A. K., Penny, D., Edwards, P. J. B., and Jameson, G. B. (March, 2018) Effects of Pressure and pH on the Hydrolysis of Cytosine: Implications for Nucleotide Stability around Deep-Sea Black Smokers. *ChemBiochem*, **19**(6), 540–544.
- [52] Tenhunen, J. (1989) Hydrolysis of single-stranded RNA in aqueous solutions—effect on quantitative hybridizations. *Molecular and Cellular Probes*, **3**(4), 391–396.
- [53] Zhang, K., Hodge, J., Chatterjee, A., Moon, T. S., and Parker, K. M. (June, 2021) Duplex Structure of Double-Stranded RNA Provides Stability against Hydrolysis Relative to Single-Stranded RNA. *Environmental Science & Technology*, **55**(12), 8045–8053.

- [54] Campbell, T. D., Hart, C. A., Febrian, R., Cheneler, M. L., and Bracher, P. J. (June, 2018) The opposite effect of K<sup>+</sup> and Na<sup>+</sup> on the hydrolysis of linear and cyclic dipeptides. *Tetrahedron Letters*, **59**(23), 2264–2267.
- [55] Rimola, A., Ugliengo, P., and Sodupe, M. (March, 2009) Formation versus Hydrolysis of the Peptide Bond from a Quantum-mechanical Viewpoint: The Role of Mineral Surfaces and Implications for the Origin of Life. *International Journal of Molecular Sciences*, **10**(3), 746–760.
- [56] Sibilska, I. K., Chen, B. M., Li, L. J., and Yin, J. (December, 2017) Effects of Trimetaphosphate on Abiotic Formation and Hydrolysis of Peptides. *Life-Basel*, **7**(4).
- [57] Gilbert, W. (February, 1986) Origin of life: The RNA world. *Nature*, **319**(6055), 618–618.
- [58] Higgs, P. G. and Lehman, N. (January, 2015) The RNA World: molecular cooperation at the origins of life. *Nature Reviews Genetics*, **16**(1), 7–17 Number: 1.
- [59] Walter, G. (1986) Origin of life: the RNA world. *Nature*, **319**(20), 618.
- [60] Westheimer, F. (1986) Biochemistry: Polyribonucleic acids as enzymes. *Nature*, **319**(6054), 534.
- [61] Cech, T. R. (2012) The RNA Worlds in Context. *Cold Spring Harbor Perspectives in Biology*, **4**(7), a006742–a006742.
- [62] Powner, M. W., Gerland, B., and Sutherland, J. D. (May, 2009) Synthesis of activated pyrimidine ribonucleotides in prebiotically plausible conditions. *Nature*, **459**(7244), 239–242.
- [63] Becker, S., Feldmann, J., Wiedemann, S., Okamura, H., Schneider, C., Iwan, K., Crisp, A., Rossa, M., Amatov, T., and Carell, T. (October, 2019) Unified prebiotically plausible synthesis of pyrimidine and purine RNA ribonucleotides. *Science*, **366**(6461), 76–82.
- [64] Teichert, J. S., Kruse, F. M., and Trapp, O. (July, 2019) Direct Prebiotic Pathway to DNA Nucleosides. *Angewandte Chemie International Edition*, **58**(29), 9944–9947.
- [65] Ritson, D. J. and Sutherland, J. D. (May, 2014) Conversion of Biosynthetic Precursors of RNA to Those of DNA by Photoredox Chemistry. *Journal of Molecular Evolution*, **78**(5), 245–250.
- [66] Steer, A. M., Bia, N., Smith, D. K., and Clarke, P. A. (2017) Prebiotic synthesis of 2-deoxy-ribose from interstellar building blocks promoted by amino esters or amino nitriles. *Chemical Communications*, **53**(75), 10362–10365.
- [67] Ritson, D. J., Battilocchio, C., Ley, S. V., and Sutherland, J. D. (2018) Mimicking the surface and prebiotic chemistry of early Earth using flow chemistry. *Nature communications*, **9**(1), 1821.
- [68] Fuller, W. D., Sanchez, R. A., and Orgel, L. E. (1972) Studies in prebiotic synthesis: VI. Synthesis of purine nucleosides. *Journal of molecular biology*, **67**(1), 25–33.
- [69] Anastasi, C., Buchet, F. F., Crowe, M. A., Parkes, A. L., Powner, M. W., Smith, J. M., and Sutherland, J. D. (2007) RNA: prebiotic product, or biotic invention?. *Chemistry & biodiversity*, **4**(4), 721–739.
- [70] Leslie E, O. (2004) Prebiotic chemistry and the origin of the RNA world. *Critical reviews in biochemistry and molecular biology*, **39**(2), 99–123.
- [71] Jørgensen, J. K., Favre, C., Bisschop, S. E., Bourke, T. L., Van Dishoeck, E. F., and Schmalzl, M. (2012) Detection of the simplest sugar, glycolaldehyde, in a solar-type protostar with ALMA. *The Astrophysical Journal Letters*, **757**(1), L4.
- [72] Jauker, M., Griesser, H., and Richert, C. (November, 2015) Spontaneous Formation of RNA Strands, Peptidyl RNA, and Cofactors. *Angewandte Chemie International Edition*, **54**(48), 14564–14569.

- [73] Ertem, G. and Ferris, J. P. (January, 1996) Synthesis of RNA oligomers on heterogeneous templates. *Nature*, **379**(6562), 238–240.
- [74] Verlander, M. S., Lohrmann, R., and Orgel, L. E. (December, 1973) Catalysts for the self-polymerization of adenosine cyclic 2',3'-phosphate. *Journal of Molecular Evolution*, **2**(4), 303–316.
- [75] Lohrmann, R. and Orgel, L. E. (August, 1973) Prebiotic Activation Processes. *Nature*, **244**(5416), 418–420.
- [76] Burcar, B. T., Jawed, M., Shah, H., and McGown, L. B. (June, 2015) In Situ Imidazole Activation of Ribonucleotides for Abiotic RNA Oligomerization Reactions. *Origins of Life and Evolution of Biospheres*, **45**(1-2), 31–40.
- [77] Kricheldorf, H. R. (2019) *Leben durch chemische Evolution?: Eine kritische Bestandsaufnahme von Experimenten und Hypothesen*, Springer Berlin Heidelberg, Berlin, Heidelberg.
- [78] Dirscherl, C. F., Ianeselli, A., Tetiker, D., Matreux, T., Queener, R. M., Mast, C. B., and Braun, D. (2023) A heated rock crack captures and polymerizes primordial DNA and RNA. *Physical Chemistry Chemical Physics*, **25**(4), 3375–3386.
- [79] Verlander, M. S. and Orgel, L. E. (June, 1974) Analysis of high molecular weight material from the polymerization of adenosine cyclic 2',3'-phosphate. *Journal of Molecular Evolution*, **3**(2), 115–120.
- [80] Dass, A. V., Wunnava, S., Langlais, J., Von Der Esch, B., Krusche, M., Ufer, L., Chrisam, N., Dubini, R. C. A., Gartner, F., Angerpointner, S., Dirscherl, C. F., Rovó, P., Mast, C. B., Šponer, J. E., Ochsenfeld, C., Frey, E., and Braun, D. (January, 2023) RNA Oligomerisation without Added Catalyst from 2',3'-Cyclic Nucleotides by Drying at Air-Water Interfaces\*\*. *ChemSystemsChem*, **5**(1), e202200026.
- [81] Morasch, M., Mast, C. B., Langer, J. K., Schilcher, P., and Braun, D. (April, 2014) Dry Polymerization of 3',5'-Cyclic GMP to Long Strands of RNA. *ChemBioChem*, **15**(6), 879–883.
- [82] Šponer, J. E., Šponer, J., Giorgi, A., Di Mauro, E., Pino, S., and Costanzo, G. (February, 2015) Untemplated Nonenzymatic Polymerization of 3',5'-cGMP: A Plausible Route to 3',5'-Linked Oligonucleotides in Primordia. *The Journal of Physical Chemistry B*, **119**(7), 2979–2989.
- [83] Šponer, J. E., Šponer, J., Výravský, J., Šedo, O., Zdráhal, Z., Costanzo, G., Di Mauro, E., Wunnava, S., Braun, D., Matyášek, R., and Kovařík, A. (November, 2021) Nonenzymatic, Template-Free Polymerization of 3',5' Cyclic Guanosine Monophosphate on Mineral Surfaces. *ChemSystemsChem*, **3**(6), e2100017.
- [84] Wunnava, S., Dirscherl, C. F., Výravský, J., Kovařík, A., Matyášek, R., Šponer, J., Braun, D., and Šponer, J. E. (December, 2021) Acid-Catalyzed RNA-Oligomerization from 3',5'-cGMP. *Chemistry – A European Journal*, **27**(70), 17581–17585.
- [85] Islam, S. and Powner, M. W. (April, 2017) Prebiotic Systems Chemistry: Complexity Overcoming Clutter. *Chem*, **2**(4), 470–501.
- [86] Islam, S., Bucar, D. K., and Powner, M. W. (June, 2017) Prebiotic selection and assembly of proteinogenic amino acids and natural nucleotides from complex mixtures. *Nature Chemistry*, **9**(6), 584–589.
- [87] Toner, J. D. and Catling, D. C. (January, 2020) A carbonate-rich lake solution to the phosphate problem of the origin of life. *Proceedings of the National Academy of Sciences*, **117**(2), 883–888.
- [88] Haas, S., Sinclair, K. P., and Catling, D. C. (January, 2024) Biogeochemical explanations for the world's most phosphate-rich lake, an origin-of-life analog. *Communications Earth & Environment*, **5**(1), 28.

- [89] O’Flaherty, D. K., Kamat, N. P., Mirza, F. N., Li, L., Prywes, N., and Szostak, J. W. (April, 2018) Copying of Mixed-Sequence RNA Templates inside Model Protocells. *Journal of the American Chemical Society*, **140**(15), 5171–5178.
- [90] Peng, H., Lelievre, A., Landenfeld, K., Müller, S., and Chen, I. A. (January, 2022) Vesicle encapsulation stabilizes intermolecular association and structure formation of functional RNA and DNA. *Current Biology*, **32**(1), 86–96.e6.
- [91] Smokers, I. B. A., van Haren, M. H. I., Lu, T., and Spruijt, E. (2022) Complex Coacervation and Compartmentalized Conversion of Prebiotically Relevant Metabolites\*\*. *ChemSystemsChem*, **4**(4), e202200004.
- [92] Biondi, E., Furukawa, Y., Kawai, J., and Benner, S. A. (2017) Adsorption of RNA on mineral surfaces and mineral precipitates. *Beilstein Journal of Organic Chemistry*, **13**, 393–404.
- [93] Guo, C. C. and Holland, G. P. (November, 2015) Alanine Adsorption and Thermal Condensation at the Interface of Fumed Silica Nanoparticles: A Solid-State NMR Investigation. *Journal of Physical Chemistry C*, **119**(45), 25663–25672.
- [94] Mignon, P., Corbin, G., Le Crom, S., Marry, V., Hao, J. H., and Daniel, I. (June, 2020) Adsorption of nucleotides on clay surfaces: Effects of mineral composition, pH and solution salts. *Applied Clay Science*, **190**.
- [95] Mast, C. B., Schink, S., Gerland, U., and Braun, D. (2013) Escalation of polymerization in a thermal gradient. *Proceedings of the National Academy of Sciences of the United States of America*, **110**(20), 8030–8035.
- [96] Mast, C. B. and Braun, D. (May, 2010) Thermal Trap for DNA Replication. *Physical Review Letters*, **104**(18), 188102.
- [97] Agerschou, E. D., Mast, C. B., and Braun, D. (January, 2017) Emergence of Life from Trapped Nucleotides? Non-Equilibrium Behavior of Oligonucleotides in Thermal Gradients. *Synlett*, **28**(1), 56–63.
- [98] Baaske, P., Weinert, F. M., Duhr, S., Lemke, K. H., Russell, M. J., and Braun, D. (May, 2007) Extreme accumulation of nucleotides in simulated hydrothermal pore systems. *Proceedings of the National Academy of Sciences*, **104**(22), 9346–9351.
- [99] Kreysing, M., Keil, L., Lanzmich, S., and Braun, D. (2015) Heat flux across an open pore enables the continuous replication and selection of oligonucleotides towards increasing length. *Nature Chemistry*, **7**(3), 203–208.
- [100] Pasek, M. A. (June, 2020) Thermodynamics of Prebiotic Phosphorylation. *Chemical Reviews*, **120**(11), 4690–4706.
- [101] Benner, S. A. and Hutter, D. (February, 2002) Phosphates, DNA, and the Search for Nonterrestrial Life: A Second Generation Model for Genetic Molecules. *Bioorganic Chemistry*, **30**(1), 62–80.
- [102] Ponnampertuma, C. and Mack, R. (May, 1965) Nucleotide Synthesis under Possible Primitive Earth Conditions. *Science*, **148**(3674), 1221–1223.
- [103] Lohrmann, R. and Orgel, L. E. (1968) Prebiotic Synthesis - Phosphorylation In Aqueous Solution. *Science*, **161**(3836), 64–&.
- [104] Fernandez-Garcia, C., Grefenstette, N. M., and Powner, M. W. (May, 2017) Prebiotic synthesis of aminooxazoline-5’-phosphates in water by oxidative phosphorylation. *Chemical Communications*, **53**(36), 4919–4921.
- [105] Coggins, A. J. and Powner, M. W. (April, 2017) Prebiotic synthesis of phosphoenol pyruvate by alpha-phosphorylation-controlled triose glycolysis. *Nature Chemistry*, **9**(4), 310–317.
- [106] Walton, C. R., Shorttle, O., Jenner, F. E., Williams, H. M., Golden, J., Morrison, S. M., Downs, R. T., Zerkle, A., Hazen, R. M., and Pasek, M. (October, 2021) Phosphorus

- mineral evolution and prebiotic chemistry: From minerals to microbes. *Earth-Science Reviews*, **221**, 103806.
- [107] Gull, M. and Pasek, M. (April, 2013) Is Struvite a Prebiotic Mineral?. *Life*, **3**(2), 321–330.
- [108] Schwartz, A. W. (October, 2006) Phosphorus in prebiotic chemistry. *Philosophical Transactions of the Royal Society B: Biological Sciences*, **361**(1474), 1743–1749.
- [109] Ding, Y., Lorenz, W. A., Dotu, I., Senter, E., and Clote, P. (2014) Computing the probability of RNA hairpin and multiloop formation. *Journal of Computational Biology*, **21**(3), 201–218.
- [110] Ding, T., Ma, D., Lu, J., and Zhang, R. (September, 2015) Apatite in granitoids related to polymetallic mineral deposits in southeastern Hunan Province, Shi–Hang zone, China: Implications for petrogenesis and metallogenesis. *Ore Geology Reviews*, **69**, 104–117.
- [111] Burcar, B., Pasek, M., Gull, M., Cafferty, B. J., Velasco, F., Hud, N. V., and Menor-Salván, C. (October, 2016) Darwin’s Warm Little Pond: A One-Pot Reaction for Prebiotic Phosphorylation and the Mobilization of Phosphate from Minerals in a Urea-Based Solvent. *Angewandte Chemie International Edition*, **55**(42), 13249–13253.
- [112] Budisa, N., Kubyshkin, V., and Schulze-Makuch, D. (August, 2014) Fluorine-Rich Planetary Environments as Possible Habitats for Life. *Life*, **4**(3), 374–385.
- [113] Maciá\*, E., Hernández, M. V., and Oró, J. (1997) Primary sources of phosphorus and phosphates in chemical evolution. *Origins of Life and Evolution of the Biosphere*, **27**(5/6), 459–480.
- [114] Bartlett, C. L., Hausrath, E. M., Adcock, C. T., Huang, S., Harrold, Z. R., and Udry, A. (December, 2018) Effects of Organic Compounds on Dissolution of the Phosphate Minerals Chlorapatite, Whitlockite, Merrillite, and Fluorapatite: Implications for Interpreting Past Signatures of Organic Compounds in Rocks, Soils and Sediments. *Astrobiology*, **18**(12), 1543–1558.
- [115] Hagan, W. J., Parker, A., Steuerwald, A., and Hathaway, M. (April, 2007) Phosphate Solubility and the Cyanate-Mediated Synthesis of Pyrophosphate. *Origins of Life and Evolution of Biospheres*, **37**(2), 113–122.
- [116] Arrhenius, G., Sales, B., Mojzsis, S., and Lee, T. (August, 1997) Entropy and Charge in Molecular Evolution—the Case of Phosphate. *Journal of Theoretical Biology*, **187**(4), 503–522.
- [117] Mojzsis, S. J. and Arrhenius, G. (November, 1998) Phosphates and carbon on Mars: Exobiological implications and sample return considerations. *Journal of Geophysical Research: Planets*, **103**(E12), 28495–28511.
- [118] Toner, J. D. and Catling, D. C. (September, 2019) Alkaline lake settings for concentrated prebiotic cyanide and the origin of life. *Geochimica Et Cosmochimica Acta*, **260**, 124–132.
- [119] Pearce, B. K. D., Pudritz, R. E., Semenov, D. A., and Henning, T. K. (October, 2017) Origin of the RNA world: The fate of nucleobases in warm little ponds. *Proceedings of the National Academy of Sciences of the United States of America*, **114**(43), 11327–11332.
- [120] Da Silva, L., Maurel, M. C., and Deamer, D. (February, 2015) Salt-Promoted Synthesis of RNA-like Molecules in Simulated Hydrothermal Conditions. *Journal of Molecular Evolution*, **80**(2), 86–97.
- [121] Maguire, O. R., Smokers, I. B. A., and Huck, W. T. S. (September, 2021) A physicochemical orthophosphate cycle via a kinetically stable thermodynamically activated intermediate enables mild prebiotic phosphorylations. *Nature Communications*, **12**(1), 5517.
- [122] Maguire, O. R., Smokers, I. B. A., Oosterom, B. G., Zheliezniak, A., and Huck, W. T. S. (March, 2024) A Prebiotic Precursor to Life’s Phosphate Transfer System with an ATP Analog and Histidyl Peptide Organocatalysts. *Journal of the American Chemical Society*, **146**(11), 7839–7849.

- [123] Becker, S., Schneider, C., Okamura, H., Crisp, A., Amatov, T., Dejmek, M., and Carell, T. (January, 2018) Wet-dry cycles enable the parallel origin of canonical and non-canonical nucleosides by continuous synthesis. *Nature Communications*, **9**(1), 163 Number: 1.
- [124] Dagar, S., Sarkar, S., and Rajamani, S. (2020) Geochemical influences on nonenzymatic oligomerization of prebiotically relevant cyclic nucleotides. *RNA (New York, N. Y.)*, **26**(6), 756–769 Number: 6.
- [125] Ervin, J. N., Bouza, M., Fernandez, F. M., and Forsythe, J. G. (August, 2020) Proline Behavior in Model Prebiotic Peptides Formed by Wet-Dry Cycling. *Acs Earth and Space Chemistry*, **4**(8), 1349–1359.
- [126] Forsythe, J. G., Yu, S. S., Mamajanov, I., Grover, M. A., Krishnamurthy, R., Fernandez, F. M., and Hud, N. V. (August, 2015) Ester-Mediated Amide Bond Formation Driven by Wet-Dry Cycles: A Possible Path to Polypeptides on the Prebiotic Earth. *Angewandte Chemie-International Edition*, **54**(34), 9871–9875.
- [127] Hassenkam, T. and Deamer, D. (June, 2022) Visualizing RNA polymers produced by hot wet-dry cycling. *Scientific Reports*, **12**(1), 10098 Number: 1.
- [128] Haugerud, I. S., Jaiswal, P., and Weber, C. A. (February, 2024) Nonequilibrium Wet–Dry Cycling Acts as a Catalyst for Chemical Reactions. *The Journal of Physical Chemistry B*,.
- [129] Martin, W., Baross, J., Kelley, D., and Russell, M. J. (November, 2008) Hydrothermal vents and the origin of life. *Nature Reviews Microbiology*, **6**(11), 805–814.
- [130] Sojo, V., Herschy, B., Whicher, A., Camprubi, E., and Lane, N. (February, 2016) The Origin of Life in Alkaline Hydrothermal Vents. *Astrobiology*, **16**(2), 181–197.
- [131] Helmbrecht, V., Weingart, M., Klein, F., Braun, D., and Orsi, W. D. (November, 2023) White and green rust chimneys accumulate RNA in a ferruginous chemical garden. *Geobiology*, **21**(6), 758–769.
- [132] Weingart, M., Chen, S., Donat, C., Helmbrecht, V., Orsi, W. D., Braun, D., and Alim, K. (September, 2023) Alkaline vents recreated in two dimensions to study pH gradients, precipitation morphology, and molecule accumulation. *Science Advances*, **9**(39), eadi1884.
- [133] Barge, L. M., Abedian, Y., Russell, M. J., Doloboff, I. J., Cartwright, J. H. E., Kidd, R. D., and Kanik, I. (July, 2015) From Chemical Gardens to Fuel Cells: Generation of Electrical Potential and Current Across Self-Assembling Iron Mineral Membranes. *Angewandte Chemie-International Edition*, **54**(28), 8184–8187.
- [134] Wang, Q., Barge, L. M., and Steinbock, O. (March, 2019) Microfluidic Production of Pyrophosphate Catalyzed by Mineral Membranes with Steep pH Gradients. *Chemistry – A European Journal*, **25**(18), 4732–4739.
- [135] Möller, F. M., Kriegel, F., Kieß, M., Sojo, V., and Braun, D. (2017) Steep pH Gradients and Directed Colloid Transport in a Microfluidic Alkaline Hydrothermal Pore. *Angewandte Chemie International Edition*, **56**(9), 2340–2344.
- [136] Hudson, R., de Graaf, R., Strandoo Rodin, M., Ohno, A., Lane, N., McGlynn, S. E., Yamada, Y. M. A., Nakamura, R., Barge, L. M., Braun, D., and Sojo, V. (September, 2020) CO<sub>2</sub> reduction driven by a pH gradient. *Proceedings of the National Academy of Sciences*, **117**(37), 22873–22879.
- [137] Yamaguchi, A., Yamamoto, M., Takai, K., Ishii, T., Hashimoto, K., and Nakamura, R. (September, 2014) Electrochemical CO<sub>2</sub> Reduction by Ni-containing Iron Sulfides: How Is CO<sub>2</sub> Electrochemically Reduced at Bisulfide-Bearing Deep-sea Hydrothermal Precipitates?. *Electrochimica Acta*, **141**, 311–318.
- [138] Sojo, V., Ohno, A., McGlynn, S. E., Yamada, Y. M. A., and Nakamura, R. (2019) Microfluidic Reactors for Carbon Fixation under Ambient-Pressure Alkaline-Hydrothermal-Vent Conditions. *Life (Basel, Switzerland)*, **9**(1).

- [139] Preiner, M., Igarashi, K., Muchowska, K. B., Yu, M., Varma, S. J., Kleinermaans, K., Nobu, M. K., Kamagata, Y., Tuysuz, H., Moran, J., and Martin, W. F. (April, 2020) A hydrogen-dependent geochemical analogue of primordial carbon and energy metabolism. *Nat Ecol Evol*, **4**(4), 534–542 Edition: 20200302.
- [140] Blank, J. G. (August, 2009) Delivery of Exogenous Materials from Comets and Asteroids to the Prebiotic Earth. *Origins of Life and Evolution of Biospheres*, **39**(3-4), 192–193.
- [141] Blank, J. G., Miller, G. H., Ahrens, M. J., and Winans, R. E. (February, 2001) Experimental shock chemistry of aqueous amino acid solutions and the cometary delivery of prebiotic compounds. *Origins of Life and Evolution of Biospheres*, **31**(1-2), 15–51.
- [142] Botta, O., Glavin, D. P., Dworkin, J. P., Matrajt, G., and Harvey, R. P. (August, 2009) Detection of AIB in Antarctic Ice Samples: Implications for Exogenous Delivery of Prebiotic Organic Compounds. *Origins of Life and Evolution of Biospheres*, **39**(3-4), 225–226.
- [143] Chyba, C. and Sagan, C. (January, 1992) Endogenous production, exogenous delivery and impact-shock synthesis of organic molecules: an inventory for the origins of life. *Nature*, **355**(6356), 125–132 Number: 6356.
- [144] Formaggio, F., Moretto, A., Toniolo, C., Broxterman, Q. B., Weber, A. L., and Pizzarello, S. (August, 2009) Exogenous Delivery and Molecular Evolution: Peptides Based on C-methylated alpha-Amino Acids as Asymmetric Catalysts in the Syntheses of Simple Sugars. *Origins of Life and Evolution of Biospheres*, **39**(3-4), 233–234.
- [145] Jenniskens, P., Wilson, M. A., Packan, D., Laux, C. O., Kruger, C. H., Boyd, I. D., Popova, O. P., and Fonda, M. (1998) Meteors: A delivery mechanism of organic matter to the early Earth. *Earth Moon and Planets*, **82-3**, 57–70.
- [146] Kwok, S. (July, 2009) Delivery of Complex Organic Compounds from Planetary Nebulae to the Solar System. *International Journal of Astrobiology*, **8**(3), 161–167.
- [147] Kwok, S. (December, 2011) Delivery of Complex Organic Compounds from Evolved Stars to the Solar System. *Origins of Life and Evolution of Biospheres*, **41**(6), 497–502.
- [148] Todd, Z. R. and Öberg, K. I. (2020) Cometary Delivery of Hydrogen Cyanide to the Early Earth. *Astrobiology*,.
- [149] Guillemin, J.-C., Trolez, Y., and Moncomble, A. (December, 2008) Synthesis, chemistry and photochemistry of cyanobutadiyne (HCCCCCN). *Advances in Space Research*, **42**(12), 2002–2007.
- [150] Niemann, H., Atreya, S., Bauer, S., Carignan, G., Demick, J., Frost, R., Gautier, D., Haberman, J., Harpold, D., Hunten, D., and others (2005) The abundances of constituents of Titan's atmosphere from the GCMS instrument on the Huygens probe. *Nature*, **438**(7069), 779.
- [151] Pasek, M. A., Dworkin, J. P., and Lauretta, D. S. (2007) A radical pathway for organic phosphorylation during schreibersite corrosion with implications for the origin of life. *Geochimica et Cosmochimica Acta*, **71**(7), 1721–1736.
- [152] Pasek, M. A. (March, 2017) Schreibersite on the early Earth: Scenarios for prebiotic phosphorylation. *Geoscience Frontiers*, **8**(2), 329–335.
- [153] La Cruz, N. L., Qasim, D., Abbott-Lyon, H., Pirim, C., McKee, A. D., Orlando, T., Gull, M., Lindsay, D., and Pasek, M. A. (2016) The evolution of the surface of the mineral schreibersite in prebiotic chemistry. *Physical Chemistry Chemical Physics*, **18**(30), 20160–20167.
- [154] Gull, M., Mojica, M. A., Fernández, F. M., Gaul, D. A., Orlando, T. M., Liotta, C. L., and Pasek, M. A. (November, 2015) Nucleoside phosphorylation by the mineral schreibersite. *Scientific Reports*, **5**(1), 17198.

- [155] Pallmann, S., Šteflová (Neé Svobod, J., Haas, M., Lamour, S., Henß, A., and Trapp, O. (May, 2018) Schreibersite: an effective catalyst in the formose reaction network. *New Journal of Physics*, **20**(5), 055003.
- [156] Aldersley, M. F. and Ferris, J. P. (August, 2009) The Further Development of RNA Synthesis with Mineral Catalysis. *Origins of Life and Evolution of Biospheres*, **39**(3-4), 297–297.
- [157] Arrhenius, G. (June, 2004) Mineral surface catalysis in models for the emergence of life. *Geochimica Et Cosmochimica Acta*, **68**(11), A117–A117.
- [158] Ferris, J. P., Joshi, P., Aldersley, M., Miyakawa, S., Huang, W. H., and Wang, K. J. (June, 2006) Mineral catalysis and prebiotic synthesis. *Origins of Life and Evolution of the Biosphere*, **36**(3), 212–212.
- [159] Wang, Q. P. and Steinbock, P. O. (January, 2020) Materials Synthesis and Catalysis in Microfluidic Devices: Prebiotic Chemistry in Mineral Membranes. *Chemcatchem*, **12**(1), 63–74.
- [160] Afrin, R., Ganbaatar, N., Aono, M., Cleaves, H. J., Yano, T., and Hara, M. (February, 2018) Size-Dependent Affinity of Glycine and Its Short Oligomers to Pyrite Surface: A Model for Prebiotic Accumulation of Amino Acid Oligomers on a Mineral Surface. *International Journal of Molecular Sciences*, **19**(2).
- [161] Zaia, D. A. M. (October, 2012) Adsorption of amino acids and nucleic acid bases onto minerals: a few suggestions for prebiotic chemistry experiments. *International Journal of Astrobiology*, **11**(4), 229–234.
- [162] Lambert, J. F. (June, 2008) Adsorption and polymerization of amino acids on mineral surfaces: A review. *Origins of Life and Evolution of Biospheres*, **38**(3), 211–242.
- [163] Banin, A., Lawless, J. G., Mazzurco, J., Church, F. M., Margulies, L., and Orenberg, J. B. (June, 1985) pH profile of the adsorption of nucleotides onto montmorillonite: II. Adsorption and desorption of 5'-AMP in iron-calcium montmorillonite systems. *Origins of life and evolution of the biosphere*, **15**(2), 89–101.
- [164] Cleaves, H. J., Crapster-Pregont, E., Jonsson, C. M., Jonsson, C. L., Sverjensky, D. A., and Hazen, R. A. (June, 2011) The adsorption of short single-stranded DNA oligomers to mineral surfaces. *Chemosphere*, **83**(11), 1560–1567.
- [165] Grunenwald, A., Keyser, C., Sautereau, A., Crubézy, E., Ludes, B., and Drouet, C. (February, 2014) Adsorption of DNA on biomimetic apatites: Toward the understanding of the role of bone and tooth mineral on the preservation of ancient DNA. *Applied Surface Science*, **292**, 867–875.
- [166] Mizuuchi, R., Blokhuis, A., Vincent, L., Nghe, P., Lehman, N., and Baum, D. (2019) Mineral surfaces select for longer RNA molecules. *Chemical Communications*, **55**(14), 2090–2093.
- [167] Chen, J., Bai, Q., Li, Y., Liu, Z., Li, Y., and Liang, D. (April, 2023) Coacervates Forming Coexisting Phases on a Mineral Surface. *Langmuir*, **39**(16), 5814–5824.
- [168] Dalai, P. and Sahai, N. (April, 2019) Mineral-Lipid Interactions in the Origins of Life. *Trends in Biochemical Sciences*, **44**(4), 331–341.
- [169] Kasting, J. F., Kopparapu, R., Ramirez, R. M., and Harman, C. E. (September, 2014) Remote life-detection criteria, habitable zone boundaries, and the frequency of Earth-like planets around M and late K stars. *Proceedings of the National Academy of Sciences*, **111**(35), 12641–12646.
- [170] Martín-Torres, F. J., Zorzano, M.-P., Valentín-Serrano, P., Harri, A.-M., Genzer, M., Kempainen, O., Rivera-Valentin, E. G., Jun, I., Wray, J., Bo Madsen, M., Goetz, W., McEwen, A. S., Hardgrove, C., Renno, N., Chevriér, V. F., Mischna, M., Navarro-González, R., Martínez-Frías, J., Conrad, P., McConnochie, T., Cockell, C., Berger, G., R. Vasavada, A., Sumner, D., and Vaniman, D. (May, 2015) Transient liquid water and water activity at Gale crater on Mars. *Nature Geoscience*, **8**(5), 357–361 Number: 5.



- [171] Frank, E. A., Meyer, B. S., and Mojzsis, S. J. (November, 2014) A radiogenic heating evolution model for cosmochemically Earth-like exoplanets. *Icarus*, **243**, 274–286.
- [172] Lineweaver, C. H. and Egan, C. A. (December, 2008) Life, gravity and the second law of thermodynamics. *Physics of Life Reviews*, **5**(4), 225–242.
- [173] Barnes, R., Jackson, B., Greenberg, R., and Raymond, S. N. (July, 2009) Tidal Limits To Planetary Habitability. *The Astrophysical Journal*, **700**(1), L30–L33 Number: 1.
- [174] Pirajno, F. (2010) Hydrothermal processes and mineral systems, Springer, Dordrecht reprinted with corr edition.
- [175] Takeuchi, Y., Furukawa, Y., Kobayashi, T., Sekine, T., Terada, N., and Kakegawa, T. (June, 2020) Impact-induced amino acid formation on Hadean Earth and Noachian Mars. *Scientific Reports*, **10**(1), 9220 Number: 1.
- [176] Osinski, G., Cockell, C., Pontefract, A., and Sapers, H. (September, 2020) The Role of Meteorite Impacts in the Origin of Life. *Astrobiology*, **20**(9), 1121–1149.
- [177] van Otterloo, J., Cas, R. A. F., and Scutter, C. R. (December, 2015) The fracture behaviour of volcanic glass and relevance to quench fragmentation during formation of hyaloclastite and phreatomagmatism. *Earth-Science Reviews*, **151**, 79–116.
- [178] Colombier, M., Scheu, B., Kueppers, U., Cronin, S. J., Mueller, S. B., Hess, K.-U., Wadsworth, F. B., Tost, M., Dobson, K. J., Ruthensteiner, B., and Dingwell, D. B. (January, 2019) In situ granulation by thermal stress during subaqueous volcanic eruptions. *Geology*, **47**(2), 179–182.
- [179] Montanaro, C., Mayer, K., Isaia, R., Gresse, M., Scheu, B., Yilmaz, T. I., Vandemeulebrouck, J., Ricci, T., and Dingwell, D. B. (November, 2017) Hydrothermal activity and subsoil complexity: implication for degassing processes at Solfatara crater, Campi Flegrei caldera. *Bulletin of Volcanology*, **79**(12), 83.
- [180] Bai, L., Baker, D. R., and Hill, R. J. (July, 2010) Permeability of vesicular Stromboli basaltic glass: Lattice Boltzmann simulations and laboratory measurements. *Journal of Geophysical Research*, **115**(B7), B07201.
- [181] Duhr, S. and Braun, D. (December, 2006) Why molecules move along a temperature gradient. *Proceedings of the National Academy of Sciences*, **103**(52), 19678–19682.
- [182] Baaske, P., Wienken, C. J., Reineck, P., Duhr, S., and Braun, D. (2010) Optical Thermophoresis for Quantifying the Buffer Dependence of Aptamer Binding. *Angewandte Chemie International Edition*, **49**(12), 2238–2241.
- [183] Wienken, C. J., Baaske, P., Rothbauer, U., Braun, D., and Duhr, S. (October, 2010) Protein-binding assays in biological liquids using microscale thermophoresis. *Nature Communications*, **1**(1), 100.
- [184] Clusius, K. and Dickel, G. (August, 1938) Neues Verfahren zur Gasentmischung und Isotopentrennung. *Die Naturwissenschaften*, **26**(33), 546–546.
- [185] Keil, L., Hartmann, M., Lanzmich, S., and Braun, D. (2016) Probing of molecular replication and accumulation in shallow heat gradients through numerical simulations. *Physical Chemistry Chemical Physics*, **18**(30), 20153–20159.
- [186] Debye, P. (January, 1939) Zur Theorie des Clusiuschen Trennungsverfahrens. *Annalen der Physik*, **428**(3-4), 284–294.
- [187] Pavlinova, P., Lambert, C. N., Malaterre, C., and Nghe, P. (February, 2023) Abiogenesis through gradual evolution of autocatalysis into template-based replication. *FEBS Letters*, **597**(3), 344–379.
- [188] Paul, N. and Joyce, G. F. (October, 2002) A self-replicating ligase ribozyme. *Proceedings of the National Academy of Sciences*, **99**(20), 12733–12740.

- [189] Horning, D. P. and Joyce, G. F. (August, 2016) Amplification of RNA by an RNA polymerase ribozyme. *Proceedings of the National Academy of Sciences*, **113**(35), 9786–9791.
- [190] Wochner, A., Attwater, J., Coulson, A., and Holliger, P. (April, 2011) Ribozyme-Catalyzed Transcription of an Active Ribozyme. *Science*, **332**(6026), 209–212.
- [191] Mutschler, H., Wochner, A., and Holliger, P. (June, 2015) Freeze–thaw cycles as drivers of complex ribozyme assembly. *Nature Chemistry*, **7**(6), 502–508.
- [192] Vaidya, N., Manapat, M. L., Chen, I. A., Xulvi-Brunet, R., Hayden, E. J., and Lehman, N. (November, 2012) Spontaneous network formation among cooperative RNA replicators. *Nature*, **491**(7422), 72–77.
- [193] Ameta, S., Arsène, S., Foulon, S., Saudemont, B., Clifton, B. E., Griffiths, A. D., and Nghe, P. (February, 2021) Darwinian properties and their trade-offs in autocatalytic RNA reaction networks. *Nature Communications*, **12**(1), 842.
- [194] Yeates, J. A., Nghe, P., and Lehman, N. (July, 2017) Topological and thermodynamic factors that influence the evolution of small networks of catalytic RNA species. *RNA*, **23**(7), 1088–1096.
- [195] Jeancolas, C., Matsubara, Y. J., Vybornyi, M., Lambert, C. N., Blokhuis, A., Alline, T., Griffiths, A. D., Ameta, S., Krishna, S., and Nghe, P. (2021) RNA diversification by a self-reproducing ribozyme revealed by deep sequencing and kinetic modelling. *Chemical Communications*, **57**(61), 7517–7520.
- [196] Arsène, S., Ameta, S., Lehman, N., Griffiths, A. D., and Nghe, P. (October, 2018) Coupled catabolism and anabolism in autocatalytic RNA sets. *Nucleic Acids Research*, **46**(18), 9660–9666.
- [197] Blokhuis, A., Lacoste, D., and Nghe, P. (October, 2020) Universal motifs and the diversity of autocatalytic systems. *Proceedings of the National Academy of Sciences*, **117**(41), 25230–25236.
- [198] Louis, A. A. (August, 2016) Contingency, convergence and hyper-astronomical numbers in biological evolution. *Studies in History and Philosophy of Science Part C: Studies in History and Philosophy of Biological and Biomedical Sciences*, **58**, 107–116.
- [199] Chizzolini, F., Passalacqua, L. F. M., Oumais, M., Dingilian, A. I., Szostak, J. W., and Lupták, A. (January, 2020) Large Phenotypic Enhancement of Structured Random RNA Pools. *Journal of the American Chemical Society*, **142**(4), 1941–1951.
- [200] Furuuchi, R., Imai, E. I., Honda, H., Hatori, K., and Matsuno, K. (August, 2005) Evolving lipid vesicles in prebiotic hydrothermal environments. *Origins of Life and Evolution of Biospheres*, **35**(4), 333–343.
- [201] Nader, S., Baccouche, A., Connolly, F., Abou-Ghanem, M., Styler, S. A., Lewis, J. D., Pink, D., and Mansy, S. S. (January, 2023) Model Atmospheric Aerosols Convert to Vesicles upon Entry into Aqueous Solution. *ACS Earth and Space Chemistry*, **7**(1), 252–259 Number: 1 Publisher: American Chemical Society.
- [202] Kindt, J. T., Szostak, J. W., and Wang, A. (November, 2020) Bulk Self-Assembly of Giant, Unilamellar Vesicles. *ACS Nano*, **14**(11), 14627–14634 Number: 11.
- [203] Gill, S. and Forterre, P. (January, 2016) Origin of life: LUCA and extracellular membrane vesicles (EMVs). *International Journal of Astrobiology*, **15**(1), 7–15.
- [204] Kudella, P. W., Preißinger, K., Morasch, M., Dirscherl, C. F., Braun, D., Wixforth, A., and Westerhausen, C. (December, 2019) Fission of Lipid-Vesicles by Membrane Phase Transitions in Thermal Convection. *Scientific Reports*, **9**(1), 1–11.
- [205] Sloatbeek, A. D., Van Haren, M. H. I., Smokers, I. B. A., and Spruijt, E. (2022) Growth, replication and division enable evolution of coacervate protocells. *Chemical Communications*, **58**(80), 11183–11200.

- [206] Jia, T. Z. and Fraccia, T. P. (November, 2020) Liquid Crystal Peptide/DNA Coacervates in the Context of Prebiotic Molecular Evolution. *Crystals*, **10**(11).
- [207] Le Vay, K. K., Salibi, E., Ghosh, B., Tang, T. D., and Mutschler, H. (June, 2023) Ribozyme activity modulates the physical properties of RNA-peptide coacervates. *eLife*, **12**, e83543.
- [208] Smokers, I., Visser, B., Lipiński, W., Nakashima, K., and Spruijt, E. Phase-separated droplets can direct the kinetics of chemical reactions including polymerization, self-replication and oscillating networks. (April, 2024).
- [209] Kühnlein, A. Selection and replication of oligonucleotides in early evolution: towards long functional sequences and motifs Doctoral dissertation LMU LMU (2021).
- [210] Morasch, M., Braun, D., and Mast, C. B. (2016) Heat-Flow-Driven Oligonucleotide Gelation Separates Single-Base Differences. *Angewandte Chemie International Edition*, **55**(23), 6676–6679.
- [211] Morasch, M., Liu, J., Dirscherl, C. F., Ianeselli, A., Kühnlein, A., Le Vay, K., Schwintek, P., Islam, S., Corpinot, M. K., Scheu, B., Dingwell, D. B., Schwillie, P., Mutschler, H., Powner, M. W., Mast, C. B., and Braun, D. (2019) Heated gas bubbles enrich, crystallize, dry, phosphorylate and encapsulate prebiotic molecules. *Nature chemistry*, **11**(9), 779–788.
- [212] Keil, L. M. R., Möller, F. M., Kieß, M., Kudella, P. W., and Mast, C. B. (2017) Proton gradients and pH oscillations emerge from heat flow at the microscale. *Nature communications*, **8**(1), 1897.
- [213] Salditt, A., Karr, L., Salibi, E., Le Vay, K., Braun, D., and Mutschler, H. (March, 2023) Ribozyme-mediated RNA synthesis and replication in a model Hadean microenvironment. *Nature Communications*, **14**(1), 1495.
- [214] Salditt, A., Keil, L. M., Horning, D., Mast, C., Joyce, G., and Braun, D. (July, 2020) Thermal Habitat for RNA Amplification and Accumulation. *Physical Review Letters*, **125**(4), 048104.
- [215] Ianeselli, A., Mast, C. B., and Braun, D. (September, 2019) Periodic Melting of Oligonucleotides by Oscillating Salt Concentrations Triggered by Microscale Water Cycles Inside Heated Rock Pores. *Angewandte Chemie-International Edition*, **58**(37), 13155–13160.
- [216] Yi, R., Tran, Q. P., Ali, S., Yoda, I., Adam, Z. R., Cleaves, H. J., and Fahrenbach, A. C. (June, 2020) A continuous reaction network that produces RNA precursors. *Proceedings of the National Academy of Sciences*, **117**(24), 13267–13274.
- [217] Cohen, S. and Michaud, D. (June, 1993) Synthesis of a Fluorescent Derivatizing Reagent, 6-Aminoquinolyl-N-Hydroxysuccinimidyl Carbamate, and Its Application for the Analysis of Hydrolysate Amino Acids via High-Performance Liquid Chromatography. *Analytical Biochemistry*, **211**(2), 279–287.
- [218] Muchowska, K. B., Varma, S. J., and Moran, J. (May, 2019) Synthesis and breakdown of universal metabolic precursors promoted by iron. *Nature*, **569**(7754), 104–107.
- [219] Jash, B., Tremmel, P., Jovanovic, D., and Richert, C. (August, 2021) Single nucleotide translation without ribosomes. *Nat Chem*, **13**(8), 751–757 Edition: 20210726.
- [220] Patel, B. H., Percivalle, C., Ritson, D. J., Duffy, C. D., and Sutherland, J. D. (April, 2015) Common origins of RNA, protein and lipid precursors in a cyanosulfidic protometabolism. *Nature Chemistry*, **7**(4), 301–307.
- [221] Schoffstall, A. M., Barto, R. J., and Ramos, D. L. (1982) Nucleoside and deoxynucleoside phosphorylation in formamide solutions. *Origins of Life*,.
- [222] Fahrenbach, A. C., Giurgiu, C., Tam, C. P., Li, L., Hongo, Y., Aono, M., and Szostak, J. W. (July, 2017) Common and Potentially Prebiotic Origin for Precursors of Nucleotide Synthesis and Activation. *Journal of the American Chemical Society*, **139**(26), 8780–8783.

- [223] Gibard, C., Bhowmik, S., Karki, M., Kim, E.-K., and Krishnamurthy, R. (February, 2018) Phosphorylation, oligomerization and self-assembly in water under potential prebiotic conditions. *Nature Chemistry*, **10**(2), 212–217.
- [224] Schuster, P. (July, 2000) Taming combinatorial explosion. *Proc Natl Acad Sci U S A*, **97**(14), 7678–80.
- [225] Anastasi, C., Crowe, M. A., Powner, M. W., and Sutherland, J. D. (2006) Direct Assembly of Nucleoside Precursors from Two- and Three-Carbon Units. *Angewandte Chemie*, **118**(37), 6322–6325 Section: 6322.
- [226] Ashe, K., Fernandez-Garcia, C., Corpinot, M. K., Coggins, A. J., Bucar, D. K., and Powner, M. W. (February, 2019) Selective prebiotic synthesis of phosphoroaminonitriles and aminothioamides in neutral water. *Communications Chemistry*, **2**.
- [227] Powner, M. W. and Sutherland, J. D. (2010) Phosphate-Mediated Interconversion of Ribo- and Arabino-Configured Prebiotic Nucleotide Intermediates. *Angewandte Chemie International Edition*, **49**(27), 4641–4643.
- [228] Todd, Z. R., Szabla, R., Szostak, J. W., and Sasselov, D. D. (2019) UV photostability of three 2-aminoazoles with key roles in prebiotic chemistry on the early earth. *Chemical communications (Cambridge, England)*, **55**(70), 10388–10391.
- [229] Springsteen, G. and Joyce, G. F. (August, 2004) Selective derivatization and sequestration of ribose from a prebiotic mix. *J Am Chem Soc*, **126**(31), 9578–83.
- [230] Sanchez, R., Ferris, J., and Orgel, L. E. (July, 1966) Conditions for purine synthesis: did prebiotic synthesis occur at low temperatures?. *Science*, **153**(3731), 72–3.
- [231] Le Vay, K. K., Song, E. Y., Ghosh, B., Tang, T.-Y. D., and Mutschler, H. (September, 2021) Enhanced ribozyme-catalyzed recombination and oligonucleotide assembly in peptide-RNA condensates. *Angewandte Chemie International Edition*,.
- [232] Mast, C. B. Accumulation and Selection of DNA in a Thermophoretic Trap PhD thesis LMU (2009).
- [233] Sehnem, A. L., Niether, D., Wiegand, S., and Figueiredo Neto, A. M. (April, 2018) Thermodiffusion of Monovalent Organic Salts in Water. *The Journal of Physical Chemistry B*, **122**(14), 4093–4100.
- [234] Petit, C. J., Hwang, M.-H., and Lin, J.-l. (1988) Thermal diffusion of dilute aqueous NH<sub>4</sub>Cl, Me<sub>4</sub>NCl, Et<sub>4</sub>NCl, n-Pr<sub>4</sub>NCl, and n-Bu<sub>4</sub>NCl solutions at 25°C. *Journal of Solution Chemistry*, **17**(1), 1–13.
- [235] Reichl, M., Herzog, M., Götz, A., and Braun, D. (2014) Why Charged Molecules Move Across a Temperature Gradient: The Role of Electric Fields. *Physical Review Letters*, **112**(19), 198101.
- [236] Dhont, J. K. G., Wiegand, S., Duhr, S., and Braun, D. (2007) Thermodiffusion of charged colloids: single-particle diffusion. *Langmuir : the ACS journal of surfaces and colloids*, **23**(4), 1674–1683.
- [237] Burelbach, J., Frenkel, D., Pagonabarraga, I., and Eiser, E. (2018) A unified description of colloidal thermophoresis. *The European physical journal. E, Soft matter*, **41**(1), 7.
- [238] Jerabek-Willemsen, M., Wienken, C. J., Braun, D., Baaske, P., and Duhr, S. (August, 2011) Molecular Interaction Studies Using Microscale Thermophoresis. *ASSAY and Drug Development Technologies*, **9**(4), 342–353.
- [239] Wiegand, S., Ning, H., and Kriegs, H. (December, 2007) Thermal diffusion forced Rayleigh scattering setup optimized for aqueous mixtures. *The Journal of Physical Chemistry. B*, **111**(51), 14169–14174.
- [240] Wang, Z., Kriegs, H., and Wiegand, S. (2012) Thermal Diffusion of Nucleotides. *The Journal of Physical Chemistry B*, **116**(25), 7463–7469.

- [241] Boigenzahn, H. and Yin, J. (December, 2022) Glycine to Oligoglycine via Sequential Trimetaphosphate Activation Steps in Drying Environments. *Origins of Life and Evolution of Biospheres*, **52**(4), 249–261.
- [242] Platten, J. K., Bou-Ali, M. M., Blanco, P., Madariaga, J. A., and Santamaria, C. (October, 2007) Soret Coefficients in Some Water-Methanol, Water-Ethanol, and Water-Isopropanol Systems. *The Journal of Physical Chemistry B*, **111**(39), 11524–11530.
- [243] Hennes, R.-C., Holm, N., and Engel, M. (1992) Abiotic synthesis of amino acids under hydrothermal conditions and the origin of life: a perpetual phenomenon?. *Naturwissenschaften*, **79**(8), 361–365.
- [244] Ring, D., Wolman, Y., Friedmann, N., and Miller, S. L. (1972) Prebiotic synthesis of hydrophobic and protein amino acids. *Proceedings of the National Academy of Sciences*, **69**(3), 765–768.
- [245] Levy, M., Miller, S. L., Brinton, K., and Bada, J. L. (2000) Prebiotic synthesis of adenine and amino acids under Europa-like conditions. *Icarus*, **145**(2), 609–613.
- [246] Marvel, C. (1941) dl-Valine. *Organic Syntheses*, pp. 106–106.
- [247] Sanchez, R., Ferris, J., and Orgel, L. (1966) Cyanoacetylene in prebiotic synthesis. *Science*, **154**(3750), 784–785.
- [248] Pizzarello, S. and Weber, A. L. (2004) Prebiotic amino acids as asymmetric catalysts. *Science*, **303**(5661), 1151–1151.
- [249] Ritson, D. J. and Sutherland, J. D. (2013) Synthesis of aldehydic ribonucleotide and amino acid precursors by photoredox chemistry. *Angewandte Chemie International Edition*, **52**(22), 5845–5847.
- [250] Liu, Z., Wu, L.-F., Xu, J., Bonfio, C., Russell, D. A., and Sutherland, J. D. (November, 2020) Harnessing chemical energy for the activation and joining of prebiotic building blocks. *Nature Chemistry*, **12**(11), 1023–1028.
- [251] Szostak, J. W., Bartel, D. P., and Luisi, P. L. (January, 2001) Synthesizing life. *Nature*, **409**(6818), 387–390.
- [252] Yeh Martín, N., Valer, L., and Mansy, S. S. (November, 2019) Toward long-lasting artificial cells that better mimic natural living cells. *Emerging Topics in Life Sciences*, **3**(5), 597–607.
- [253] Jia, H. and Schwille, P. (December, 2019) Bottom-up synthetic biology: reconstitution in space and time. *Current opinion in biotechnology*, **60**, 179–187.
- [254] Abil, Z. and Danelon, C. (August, 2020) Roadmap to Building a Cell: An Evolutionary Approach. *Frontiers in Bioengineering and Biotechnology*, **8**, 927.
- [255] Laohakunakorn, N., Grasemann, L., Lavickova, B., Michielin, G., Shahein, A., Swank, Z., and Maerkl, S. J. (March, 2020) Bottom-Up Construction of Complex Biomolecular Systems With Cell-Free Synthetic Biology. *Frontiers in Bioengineering and Biotechnology*, **8**, 213.
- [256] Aufinger, L. and Simmel, F. C. (October, 2019) Establishing Communication Between Artificial Cells. *Chemistry – A European Journal*, **25**(55), 12659–12670.
- [257] Noireaux, V. and Libchaber, A. (December, 2004) A vesicle bioreactor as a step toward an artificial cell assembly. *Proceedings of the National Academy of Sciences*, **101**(51), 17669–17674.
- [258] Elani, Y., Law, R. V., and Ces, O. (2015) Protein synthesis in artificial cells: using compartmentalisation for spatial organisation in vesicle bioreactors. *Physical Chemistry Chemical Physics*, **17**(24), 15534–15537.
- [259] Van Duppen, P., Daines, E., Robinson, W. E., and Huck, W. T. S. (April, 2023) Dynamic Environmental Conditions Affect the Composition of a Model Prebiotic Reaction Network. *Journal of the American Chemical Society*, **145**(13), 7559–7568.

- [260] Briš, A., Baltussen, M. G., Tripodi, G. L., Huck, W. T. S., Franceschi, P., and Roithová, J. (December, 2023) Direct Analysis of Complex Reaction Mixtures: Formose Reaction. *Angewandte Chemie International Edition*, p. e202316621.
- [261] Huck, W., Baltussen, M., De Jong, T., Duez, Q., and Robinson, W., Chemical reservoir computation in a self-organizing reaction network. preprint, In Review (November, 2023).
- [262] Simonov, A., Pestunova, O., Matvienko, L., and Parmon, V. (2007) The nature of autocatalysis in the Butlerov reaction. *Kinetics and Catalysis*, **48**(2), 245–254.
- [263] Chairat, C., Schott, J., Oelkers, E. H., Lartigue, J.-E., and Harouiya, N. (December, 2007) Kinetics and mechanism of natural fluorapatite dissolution at 25°C and pH from 3 to 12. *Geochimica et Cosmochimica Acta*, **71**(24), 5901–5912.
- [264] Parkhurst, D. L. and Appelo, C. (2013) Description of input and examples for PHREEQC version 3: a computer program for speciation, batch-reaction, one-dimensional transport, and inverse geochemical calculations. *US geological survey techniques and methods*, **6**(A43), 497.
- [265] Vitens PhreeqPython. (2021).
- [266] Yamagata, Y. and Inomata, K. (August, 1997) Condensation of glycyglycine to oligoglycines with trimetaphosphate in aqueous solution .2. Catalytic effect of magnesium ion. *Origins of Life and Evolution of Biospheres*, **27**(4), 339–344.
- [267] Ni, F., Sun, S., Huang, C., and Zhao, Y. (2009) N-phosphorylation of amino acids by trimetaphosphate in aqueous solution-learning from prebiotic synthesis. *Green Chemistry*, **11**(4), 569–573.
- [268] Sibilska, I., Feng, Y., Li, L. J., and Yin, J. (September, 2018) Trimetaphosphate Activates Prebiotic Peptide Synthesis across a Wide Range of Temperature and pH. *Origins of Life and Evolution of Biospheres*, **48**(3), 277–287.
- [269] Pasek, M. A., Kee, T. P., Bryant, D. E., Pavlov, A. A., and Lunine, J. I. (2008) Production of potentially prebiotic condensed phosphates by phosphorus redox chemistry. *Angewandte Chemie-International Edition*, **47**(41), 7918–7920.
- [270] Bezold, D., Durr, T., Singh, J., and Jessen, H. J. (February, 2020) Cyclotriphosphate: A Brief History, Recent Developments, and Perspectives in Synthesis. *Chemistry-a European Journal*, **26**(11), 2298–2308.
- [271] Britvin, S. N., Murashko, M. N., Vapnik, Y., Vlasenko, N. S., Krzhizhanovskaya, M. G., Vereshchagin, O. S., Bocharov, V. N., and Lozhkin, M. S. (2020) Cyclophosphates, a new class of native phosphorus compounds, and some insights into prebiotic phosphorylation on early Earth. *Geology*, **49**(4), 382–386 Section: 382.
- [272] Osterberg, R. and Orgel, L. E. (September, 1972) Polyphosphate and trimetaphosphate formation under potentially prebiotic conditions. *Journal of Molecular Evolution*, **1**(3), 241–248.
- [273] Morishita, T., Hattori, K. H., Terada, K., Matsumoto, T., Yamamoto, K., Takebe, M., Ishida, Y., Tamura, A., and Arai, S. (June, 2008) Geochemistry of apatite-rich layers in the Finero phlogopite–peridotite massif (Italian Western Alps) and ion microprobe dating of apatite. *Chemical Geology*, **251**(1-4), 99–111.
- [274] Ptáček, P. (April, 2016) Apatites and their Synthetic Analogues - Synthesis, Structure, Properties and Applications, InTech, .
- [275] Neveu, M., Kim, H.-J., and Benner, S. A. (April, 2013) The “Strong” RNA World Hypothesis: Fifty Years Old. *Astrobiology*, **13**(4), 391–403.
- [276] Hud, N. V. (December, 2018) Searching for lost nucleotides of the pre-RNA World with a self-refining model of early Earth. *Nature Communications*, **9**(1), 5171.
- [277] Bhowmik, S. and Krishnamurthy, R. (November, 2019) The role of sugar-backbone heterogeneity and chimeras in the simultaneous emergence of RNA and DNA. *Nature Chemistry*, **11**(11), 1009–1018.

- [278] Denesyuk, N. A. and Thirumalai, D. (October, 2015) How do metal ions direct ribozyme folding?. *Nature Chemistry*, **7**(10), 793–801.
- [279] Le Vay, K., Salibi, E., Song, E. Y., and Mutschler, H. (January, 2020) Nucleic Acid Catalysis under Potential Prebiotic Conditions. *Chemistry – An Asian Journal*, **15**(2), 214–230.
- [280] Freisinger, E. and Sigel, R. K. (July, 2007) From nucleotides to ribozymes—A comparison of their metal ion binding properties. *Coordination Chemistry Reviews*, **251**(13-14), 1834–1851.
- [281] Wu, Y.-Y., Zhang, Z.-L., Zhang, J.-S., Zhu, X.-L., and Tan, Z.-J. (July, 2015) Multivalent ion-mediated nucleic acid helix-helix interactions: RNA versus DNA. *Nucleic Acids Research*, **43**(12), 6156–6165.
- [282] Erat, M. C., Coles, J., Finazzo, C., Knobloch, B., and Sigel, R. K. (January, 2012) Accurate analysis of Mg<sup>2+</sup> binding to RNA: From classical methods to a novel iterative calculation procedure. *Coordination Chemistry Reviews*, **256**(1-2), 279–288.
- [283] Xi, K., Wang, F.-H., Xiong, G., Zhang, Z.-L., and Tan, Z.-J. (April, 2018) Competitive Binding of Mg<sup>2+</sup> and Na<sup>+</sup> Ions to Nucleic Acids: From Helices to Tertiary Structures. *Biophysical Journal*, **114**(8), 1776–1790.
- [284] Fischer, N. M., Polêto, M. D., Steuer, J., and van der Spoel, D. (June, 2018) Influence of Na<sup>+</sup> and Mg<sup>2+</sup> ions on RNA structures studied with molecular dynamics simulations. *Nucleic Acids Research*, **46**(10), 4872–4882.
- [285] Attwater, J., Tagami, S., Kimoto, M., Butler, K., Kool, E. T., Wengel, J., Herdewijn, P., Hirao, I., and Holliger, P. (2013) Chemical fidelity of an RNA polymerase ribozyme. *Chemical Science*, **4**(7), 2804.
- [286] Heilman-Miller, S. L., Thirumalai, D., and Woodson, S. A. (March, 2001) Role of counterion condensation in folding of the Tetrahymena ribozyme. I. Equilibrium stabilization by cations. *Journal of Molecular Biology*, **306**(5), 1157–1166.
- [287] Koculi, E., Hyeon, C., Thirumalai, D., and Woodson, S. A. (March, 2007) Charge Density of Divalent Metal Cations Determines RNA Stability. *Journal of the American Chemical Society*, **129**(9), 2676–2682.
- [288] Gangidine, A., Havig, J. R., Hannon, J. S., and Czaja, A. D. (January, 2020) Silica Precipitation in a Wet–Dry Cycling Hot Spring Simulation Chamber. *Life*, **10**(1), 3.
- [289] Damer, B. and Deamer, D. (April, 2020) The Hot Spring Hypothesis for an Origin of Life. *Astrobiology*, **20**(4), 429–452.
- [290] Attwater, J., Wochner, A., Pinheiro, V. B., Coulson, A., and Holliger, P. (September, 2010) Ice as a protocellular medium for RNA replication. *Nature Communications*, **1**(1), 76.
- [291] Monnard, P.-A., Kanavarioti, A., and Deamer, D. W. (November, 2003) Eutectic Phase Polymerization of Activated Ribonucleotide Mixtures Yields Quasi-Equimolar Incorporation of Purine and Pyrimidine Nucleobases. *Journal of the American Chemical Society*, **125**(45), 13734–13740.
- [292] Shellnutt, J. G. (March, 2018) Derivation of intermediate to silicic magma from the basalt analyzed at the Vega 2 landing site, Venus. *PLOS ONE*, **13**(3), e0194155.
- [293] Verney-Carron, A., Vigier, N., and Millot, R. (June, 2011) Experimental determination of the role of diffusion on Li isotope fractionation during basaltic glass weathering. *Geochimica et Cosmochimica Acta*, **75**(12), 3452–3468.
- [294] Allègre, C. J., Louvat, P., Gaillardet, J., Meynadier, L., Rad, S., and Capmas, F. (March, 2010) The fundamental role of island arc weathering in the oceanic Sr isotope budget. *Earth and Planetary Science Letters*, **292**(1-2), 51–56.

- [295] Dessert, C., Dupré, B., Gaillardet, J., François, L. M., and Allègre, C. J. (December, 2003) Basalt weathering laws and the impact of basalt weathering on the global carbon cycle. *Chemical Geology*, **202**(3-4), 257–273.
- [296] Gislason, S. R. and Oelkers, E. H. (October, 2003) Mechanism, rates, and consequences of basaltic glass dissolution: II. An experimental study of the dissolution rates of basaltic glass as a function of pH and temperature. *Geochimica et Cosmochimica Acta*, **67**(20), 3817–3832.
- [297] Robertson, M. and Joyce, G. (February, 2014) Highly Efficient Self-Replicating RNA Enzymes. *Chemistry & Biology*, **21**(2), 238–245.
- [298] Dibrova, D. V., Galperin, M. Y., Koonin, E. V., and Mulkidjanian, A. Y. (May, 2015) Ancient systems of sodium/potassium homeostasis as predecessors of membrane bioenergetics. *Biochemistry (Moscow)*, **80**(5), 495–516.
- [299] Palmgren, M. (October, 2023) Evolution of the sodium pump. *Biochimica et Biophysica Acta (BBA) - Molecular Cell Research*, **1870**(7), 119511.
- [300] Takeyama, N. and Nakashima, K. (April, 1988) Proportionality of intrinsic heat of transport to standard entropy of hydration for aqueous ions. *Journal of Solution Chemistry*, **17**(4), 305–325.
- [301] Miller, S. L. (May, 1955) Production of Some Organic Compounds under Possible Primitive Earth Conditions1. *Journal of the American Chemical Society*, **77**(9), 2351–2361.
- [302] Orgel, L. E. (2004) Prebiotic chemistry and the origin of the RNA world. *Critical reviews in biochemistry and molecular biology*, **39**(2), 99–123.
- [303] Xu, S., Hutchinson, A. J., Taheri, M., Corry, B., and Torres, J. F. (April, 2024) Thermodiffusive desalination. *Nature Communications*, **15**(1), 2996.
- [304] Kosmidis Papadimitriou, A., Chong, S. W., Shen, Y., Lee, O. S., Knowles, T. P. J., Grover, L., and Vigolo, D. (February, 2024) Fabrication of gradient hydrogels using a thermophoretic approach in microfluidics. *Biofabrication*,.
- [305] Saiki, T., Ono, N., Matsumoto, S., and Watanabe, S. (December, 2020) Separation of a binary gas mixture by thermal diffusion in a two-dimensional cascade of many small cavities. *International Journal of Heat and Mass Transfer*, **163**, 120394.
- [306] Weiss, M. C., Sousa, F. L., Mrnjavac, N., Neukirchen, S., Roettger, M., Nelson-Sathi, S., and Martin, W. F. (July, 2016) The physiology and habitat of the last universal common ancestor. *Nature Microbiology*, **1**(9), 16116.
- [307] Mitchell, P. (1961) Coupling of phosphorylation to electron and hydrogen transfer by a chemi-osmotic type of mechanism. *Nature*, **191**(4784), 144–148.
- [308] Mariani, A., Bonfio, C., Johnson, C. M., and Sutherland, J. D. (2018) pH-Driven RNA strand separation under prebiotically plausible conditions. *Biochemistry*,.
- [309] Pino, S., Di Mauro, E., Costanzo, G., Saladino, R., Šedo, O., Zdráhal, Z., Šponer, J., and Šponer, J. E. (November, 2019) Stabilization of Short Oligonucleotides in the Prebiotic Mix: The Potential Role of Amino Alcohols. *ChemSystemsChem*, **1**(4), e1900006.
- [310] Ferris, J. P. (October, 2006) Montmorillonite-catalysed formation of RNA oligomers: the possible role of catalysis in the origins of life. *Philosophical Transactions of the Royal Society B: Biological Sciences*, **361**(1474), 1777–1786.
- [311] Bonfio, C., Godino, E., Corsini, M., Fabrizi de Biani, F., Guella, G., and Mansy, S. S. (August, 2018) Prebiotic iron–sulfur peptide catalysts generate a pH gradient across model membranes of late protocells. *Nature Catalysis*, **1**(8), 616–623.
- [312] Lane, N. and Martin, W. (December, 2012) The Origin of Membrane Bioenergetics. *Cell*, **151**(7), 1406–1416.
- [313] Lane, N. (June, 2017) Proton gradients at the origin of life. *BioEssays*, **39**(6), 1600217.



- [314] Huber, C. and Wächtershäuser, G. (July, 1998) Peptides by Activation of Amino Acids with CO on (Ni,Fe)S Surfaces: Implications for the Origin of Life. *Science*, **281**(5377), 670–672.
- [315] Chittenden, G. and Schwartz, A. W. (January, 1981) Prebiotic photosynthetic reactions. *Biosystems*, **14**(1), 15–32.
- [316] Moret, S., Dyson, P. J., and Laurenczy, G. (June, 2014) Direct synthesis of formic acid from carbon dioxide by hydrogenation in acidic media. *Nature Communications*, **5**(1), 4017.
- [317] Inoue, T., Fujishima, A., Konishi, S., and Honda, K. (February, 1979) Photoelectrocatalytic reduction of carbon dioxide in aqueous suspensions of semiconductor powders. *Nature*, **277**(5698), 637–638.
- [318] Saladino, R. (May, 2001) A possible prebiotic synthesis of purine, adenine, cytosine, and 4(3H)-pyrimidinone from formamide implications for the origin of life. *Bioorganic & Medicinal Chemistry*, **9**(5), 1249–1253.
- [319] Saladino, R., Crestini, C., Pino, S., Costanzo, G., and Di Mauro, E. (March, 2012) Formamide and the origin of life. *Physics of Life Reviews*, **9**(1), 84–104.
- [320] Choughuley, A., Subbaraman, A., Kazi, Z., and Chadha, M. (September, 1977) A possible prebiotic synthesis of thymine: Uracil-formaldehyde-formic acid reaction. *Biosystems*, **9**(2-3), 73–80.
- [321] Becker, S., Thoma, I., Deutsch, A., Gehrke, T., Mayer, P., Zipse, H., and Carell, T. (2016) A high-yielding, strictly regioselective prebiotic purine nucleoside formation pathway. *Science (New York, N)*, **352**(6287), 833–836.
- [322] Wächtershäuser, G. (August, 2000) Life as We Don't Know It. *Science*, **289**(5483), 1307–1308.
- [323] Pine, S. H. and Sanchez, B. L. (March, 1971) Formic acid-formaldehyde methylation of amines. *The Journal of Organic Chemistry*, **36**(6), 829–832.
- [324] Bennett, C. J., Hama, T., Kim, Y. S., Kawasaki, M., and Kaiser, R. I. (January, 2011) Laboratory studies on the formation of formic acid (HCOOH) in interstellar and cometary ices. *The Astrophysical Journal*, **727**(1), 27.
- [325] Bockelée-Morvan, D., Lis, D. C., Wink, J. E., Despois, D., Crovisier, J., Bachiller, R., Benford, D. J., Biver, N., Colom, P., Davies, J. K., Gérard, E., Germain, B., Houde, M., Mehringer, D., Moreno, R., Paubert, G., Phillips, T. G., and Rauer, H. (January, 2000) New molecules found in comet C/1995 O1 (Hale-Bopp). Investigating the link between cometary and interstellar material. *Astronomy and Astrophysics*, **353**, 1101–1114.
- [326] Biver, N., Bockelée-Morvan, D., Debout, V., Crovisier, J., Boissier, J., Lis, D. C., Dello Russo, N., Moreno, R., Colom, P., Paubert, G., Vervack, R., and Weaver, H. A. (June, 2014) Complex organic molecules in comets C/2012 F6 (Lemmon) and C/2013 R1 (Lovejoy): detection of ethylene glycol and formamide. *Astronomy & Astrophysics*, **566**, L5.
- [327] Szopa, C., Sternberg, R., Coscia, D., Raulin, F., and Vidal-Madjar, C. (December, 2000) Gas chromatography for in situ analysis of a cometary nucleus. *Journal of Chromatography A*, **904**(1), 73–85.
- [328] Lide, D. R. (2001) CRC handbook of chemistry and physics, CRC Press, Boca Raton 82nd, ed., 2001-2001. edition.
- [329] Domonkos, L. and Liszi, J. (January, 2000) Thermal Diffusion of Weak Electrolytes III. The Soret Coefficients of Normal Carboxylic Acids. *Zeitschrift für Physikalische Chemie*, **214**(1).
- [330] Winkelmann, J. (2018) Diffusion coefficient of formic acid in water at infinite dilution. In Lechner, M. D., (ed.), *Diffusion in Gases, Liquids and Electrolytes*, pp. 1946–1946 Springer Berlin Heidelberg Berlin, Heidelberg.

- [331] Rubio-Sánchez, R., O’Flaherty, D. K., Wang, A., Coscia, F., Petris, G., Di Michele, L., Cicuta, P., and Bonfio, C. (October, 2021) Thermally Driven Membrane Phase Transitions Enable Content Reshuffling in Primitive Cells. *Journal of the American Chemical Society*, **143**(40), 16589–16598.
- [332] Steenbergh, A. K., Bodelier, P. L. E., Hoogveld, H. L., Slomp, C. P., and Laanbroek, H. J. (November, 2011) Phosphatases relieve carbon limitation of microbial activity in Baltic Sea sediments along a redox-gradient. *Limnology and Oceanography*, **56**(6), 2018–2026.
- [333] Mateo-Alonso, A., Ehli, C., Guldi, D. M., and Prato, M. (November, 2008) Charge Transfer Reactions along a Supramolecular Redox Gradient. *Journal of the American Chemical Society*, **130**(45), 14938–14939.
- [334] Selby, T. D. and Blackstock, S. C. (1998) Preparation of a redox-gradient dendrimer. Polyamines designed for one-way electron transfer and charge capture. *Journal of the American Chemical Society*, **120**(46), 12155–12156.
- [335] Frederix, P. W., Idé, J., Altay, Y., Schaeffer, G., Surin, M., Beljonne, D., Bondarenko, A. S., Jansen, T. L., Otto, S., and Marrink, S. J. (2017) Structural and Spectroscopic Properties of Assemblies of Self-Replicating Peptide Macrocycles. *ACS nano*, **11**(8), 7858–7868.
- [336] Moore, K. R., Gong, J., Pajusalu, M., Skoog, E. J., Xu, M., Feliz Soto, T., Sojo, V., Matreux, T., Baldes, M. J., Braun, D., Williford, K., and Bosak, T. (September, 2021) A new model for silicification of cyanobacteria in Proterozoic tidal flats. *Geobiology*, **19**(5), 438–449.
- [337] Moore, K. R., Pajusalu, M., Gong, J., Sojo, V., Matreux, T., Braun, D., and Bosak, T. (September, 2020) Biologically mediated silicification of marine cyanobacteria and implications for the Proterozoic fossil record. *Geology*, **48**(9), 862–866.
- [338] Jensen, P., Matreux, T., Cambe, J., Larralde, H., and Bertin, E. (May, 2018) Giant Catalytic Effect of Altruists in Schelling’s Segregation Model. *Physical Review Letters*, **120**(20), 208301.

# List of figures

1.1	Dimensions of heat-flow-driven effects . . . . .	4
2.1	Parts of thermo-microfluidic chamber . . . . .	8
2.2	Temperature profile in the experimental setup . . . . .	9
2.3	Implementation of large convective fluxes for experiments and sample recovery . . . . .	11
2.4	Freeze extraction procedure . . . . .	12
2.5	Depiction of leaching and dissolution experiments . . . . .	15
3.1	Graphical abstract chapter 3 - Separation and purification of molecules and boosting of reactions . . . . .	17
3.2	Enrichment of 2-aminoazoles . . . . .	19
3.3	Enrichment of amino acids . . . . .	20
3.4	Separation in a 3-chamber-network . . . . .	20
3.5	Determination of Soret coefficients . . . . .	21
3.6	Simulated large network . . . . .	22
3.7	TMP-catalysed dimerization of glycine . . . . .	23
4.1	Graphical abstract chapter 4 - Solubilization of apatite and local enrichment of phosphate . . . . .	25
4.2	Leaching experiment on natural apatite samples . . . . .	27
4.3	Dissolution of apatite and thermally driven separation . . . . .	28
4.4	pH-neutralization of solution and accessibility for prebiotic chemistry . . . . .	29
4.5	Saturation indices for different databases . . . . .	29
4.6	Impact of temperature and inflow pH on neutralization and precipitation . . . . .	30
4.7	Flow setting for heat-flow-driven enrichment of phosphate from dilute sources . . . . .	31
4.8	Compatibility of phosphate polymerization with geomaterial . . . . .	32
4.9	Experimental setup for flow retention experiment . . . . .	32
4.10	Selective precipitation of magnesium phosphates . . . . .	33
5.1	Graphical abstract chapter 5 - Ribozyme habitats from basalt leachates . . . . .	35
5.2	Leaching from basaltic rock . . . . .	37
5.3	Separation of magnesium versus sodium in a thermophoretic flow cell . . . . .	38
5.4	Ribozyme activity for various salt conditions . . . . .	39
5.5	Salty pH gradients . . . . .	40
5.6	General principle of separation cells . . . . .	40
5.7	Thermodiffusive versus thermogravitational separation . . . . .	41
5.8	Example of 2D burgers network . . . . .	42
5.9	Thermodiffusive salt concentration and desalination . . . . .	42

---

6.1	Graphical abstract chapter 6 - Formation mechanism of thermally controlled pH gradients . . . . .	43
6.2	Experimental setup for measurement of pH gradients . . . . .	45
6.3	Resulting pH gradients . . . . .	46
6.4	Calculation of initially present species . . . . .	48
6.5	Finite-element simulation of thermophoretic retention in a flow . . . . .	49
6.6	Step factor for varied thermophoretic parameters of formate . . . . .	51
6.7	Comparison of inflow and outflow pHs for different equivalents of sodium hydroxide . . . . .	51
6.8	Difference in pH for multiple initial concentrations of formic acid . . . . .	52

# List of tables

4.1	Composition of natural apatites . . . . .	27
4.2	Phosphate content of various geomaterials . . . . .	30
6.1	Values of Soret and diffusion coefficients. . . . .	49



# List of my publications

## PhD-related first author publications

Matreux, T.\*, Schmid, A.\*, Rappold, M., Weller, D., Çalışkanoglu, A.Z., Moore, K.R., Bosak, T., Dingwell, D. B., Karaghiosoff, K., Guyot, F., Scheu, B., Braun, D. & Mast, C. B. *Heat flows solubilize apatite to boost phosphate availability for prebiotic chemistry*. [2]

Matreux, T.\*, Aikkila, P.\*, Scheu, B., Braun, D. & Mast, C. B. *Heat flows enrich prebiotic building blocks and enhance their reactivity*. **Nature**, 2024, 628, 110–116. [1]

Matreux, T.\*, Altaner, B.\*, Raith, J.\*, Braun, D., Mast, C. B. & Gerland, U. *Formation mechanism of thermally driven pH gradients*. **Communications Physics**, 2023 6, 14. [4]

Matreux, T.\*, Le Vay, K.\*, Schmid, A., Aikkila, P., Belohlavek, L., Çalışkanoglu, A.Z., Salibi, E., Kühnlein, A., Springsklee, C., Scheu, B., Dingwell, D. B., Braun, D., Mutschler, H. & Mast, C. B. *Heat flows in rock cracks naturally optimize salt compositions for ribozymes*. **Nature Chemistry**, 2021, 13, 1038–1045. [3]

## PhD-related contributing author publications

(Manuscript under review) Floroni, A.\*, Yeh Martin, N.\*, Matreux, T., Weise, L.I., Mansy, S.S., Mutschler, H., Mast, C.B. & Braun, D. *Membraneless self-feeding cell created by a heat flow*.

Dirscherl, C. F., Ianeselli, A., Tetiker, D., Matreux, T., Queener, R. M., Mast, C. B. & Braun, D. *A heated rock crack captures and polymerizes primordial DNA and RNA*. **Physical Chemistry Chemical Physics**, 2023, 25, 3375–3386. [78]

## Other publications

Moore, K. R., Gong, J., Pajusalu, M., Skoog, E. J., Xu, M., Feliz Soto, T., Sojo, V., Matreux, T., Baldes, M. J., Braun, D., Williford, K. & Bosak, T. *A new model for silicification of cyanobacteria in Proterozoic tidal flats*. **Geobiology**, 2021, 1472–4677. [336]

Moore, K. R., Pajusalu, M., Gong, J., Sojo, V., Matreux, T., Braun, D., & Bosak, T. *Biologically mediated silicification of marine cyanobacteria and implications for the Proterozoic fossil record.* **Geology**, 2020, 48(9), 862-866. [337]

Jensen, P., Matreux, T., Cambe, J., Larralde, H., & Bertin, E. *Giant catalytic effect of altruists in Schelling's segregation model.* **Physical Review Letters**, 2018, 120(20), 208301. [338]



# Acknowledgements

There are a lot of people I want to thank because without them all this thesis would not have been possible and the last few years would have been a lot less fun.

First of all, a huge thank you goes to **Christof**, for everything. Thank you for your trust and support, all discussions and projects and for the degree of freedom to pursue my own ideas (even if there was no room for new ideas), all while being supportive and always available for discussions and help.

Thank you **Dieter** for living the love of science (and coffee) and your trust. The atmosphere in the lab and the vision and passion you have are very special, and the path you have taken for equality and creating opportunities is impressive.

Many thanks to all the collaborations inside the lab and the great team work. **Paula**, I could not have gone through all the experiments and suffering for Nature without you. I think when you came to the lab for the first time, neither of us knew where the journey would go, but it was a pleasure to work together for the last 5 years. **Almuth** for sharing a taste of what good music is and many coffee breaks together. Thank you for all the work together and your help and support for any chemistry (and not only) questions and problems. **Alex**, thank you for taking me under your wing when I did not even have a project yet and for a great time as Mastschweinchen (or whatever the name was). **Meggie** for all your help and many interesting discussions. **Max**, thank you for your trust and for taking me on as a supervisor even before my own PhD had started, **Noël**, thank you for a lot interesting discussions and (like for many of the Braunies) lots of kickers. And of course, now already quite some long time ago, **Fiona**, for teaching me the first basics of chemistry, **David**, for suffering together in learning chemistry on the flight and **Vivian** for the help in a time when it was needed.

Heartfelt thanks to the whole BraunLab with all the great people who have been here over the years. It's a great atmosphere and spirit - with lots of shared coffee and lunch breaks, plenty of kicker and always someone around to discuss with, be it in the mornings, evenings or weekends. I will definitely miss this lab! **Georg** and **Zhenya** for Senf, I look forward to seeing you again soon, **Victor** for being open to any idea. **Julian** for interesting discussions about everything late into the night. **Patta** for breakfasts and for a lot of kicker, the same also to **Alan** and **Chrissy** and for many shared lunch breaks. **Avinash** for your curiosity and open-mindedness and of course for lots of kickers. **Adriana** for the shared journey, starting the PhD at the same time. **Annalena**, we even started the Bachelor's together and both of us ended up here. It is impressive, how you managed to handle everything (and still finished half a year faster). **Sree** for your willingness and openness to discuss everything and at any time, **Philipp** reliably turning on good music

(even if I sometimes might have changed it) **Juliette** for living the French spirit in the lab - and a lot of good food and discussion, **Saroj** for your passion for amyloids - and Indian cuisine. I'm sure our paths will cross again.

Thanks to everyone who has been in the lab over the years (and I'm sorry if I'm forgetting some), **André, Lonzo, Matze, Alex, Ninos, Felix, Riccardo, Julian, Damla, Lea, Joachim, Adam, Leo, Jara, Nico, Sabrina, Bobby, Emma, Katharina, Barbara** - and **Zsófi** and **Francesco** for the small ESM meeting at BraunLab.

All my projects were collaborations and I think science would have been a lot less fun without all the great people I got the chance to work with. **Daniel** for an amazing collaboration, it was a great chance to get to work together. Thanks to **Betty, Zeynep, Christina** and **Lukas** for explaining the different phases to me for the 100th time and figuring out what we can do. **Kris** and **Hannes**, thank you for making my very first project a lot of good memories. **Bernhard** and **Uli** for the many interesting discussions, I learned a lot from the project and about science. **Jo**, the discussions and writing sessions in Leone will definitely stay in my memory. Thank you **Francois** for your enthusiasm and openness. **Ludovic** for always being super-helpful. Thanks to **Conny** for being so open-minded and helpful about any project. **Kelsey** for your generosity and samples that were very useful years later.

Thanks to the Huck&Spruijt groups for making me feel very welcome during my stay in Nijmegen. **Iris** for many nice conversations, **Wilhelm** and **Evan** for making me feel part of the lab and your warm welcome. **Thijs** and **Will** for intense, but also very funny and productive 6 weeks. I look forward to coming back at some point.

Many thanks to **Filiz** and **Andrea** for organizing all the CRC events and to **Mandy** and **Margrit** for all the help in the background. In all the years of doing the contracts, thanks a lot to all people of the 4th floor who being super helpful and nice: **Anna, Christian, Risa, Jakob, Ina** and **Ulla**.

Special thanks go to **Paula, Almuth, Christof, Sree** and **Clara** for proofreading this thesis.

Last but not least, I would also like to say a special thank you to my **family**.

**Clara**, words cannot describe how I feel about you, thank you for your support and your love.